Treatment strategies for experimental melanoma brain metastases

Synnøve Nymark Aasen

Dissertation for the degree philosophiae doctor (PhD)

at the University of Bergen

June 2019

Scientific environment

The work introduced in this thesis was carried out at the Kristian Gerhard Jebsen Brain Tumour Research Centre, Department of Biomedicine, Faculty of Medicine, University of Bergen.

I have also been affiliated with the Department of Oncology and Medical Physics, Haukeland University Hospital and taken part in the Bergen Biomedical Research School.

The PhD project was funded by the Western Norway Regional Health Authority.

UNIVERSITETET I BERGEN
Det medisinske fakultet

HELSE BERGEN
Haukeland University Hospital

Acknowledgements

All things considered, I have my late grandfather to thank for piquing my scientific curiosity. After what seems like an unplanned route into academia, I consider myself extremely lucky being given the opportunity to contribute to the research field on brain metastases. During the years as a PhD candidate at the University of Bergen I have met some of the world's leading people in the field and the studies have been educational and consuming on so many levels.

I am truly grateful to my all my wonderful colleagues at the Translational Cancer Research Group at Institute of Biomedicine. In particular I would like to thank the brain metastasis group led by professor Frits Thorsen, who has been an inspiring mentor for me since he introduced me to the field in 2014. You are a great supervisor who is always supportive and including, and I am sincerely grateful for the opportunity you have given me. Further, all current and former group members, Tuyen, Agathe, Christina, Trond Are, Ole, Emma, Himal, Krister, Zichao, Jiwei, Anna, Christopher and Kislay (and more), have all contributed to an excellent working environment. Thank you to each and every one of you! Thanks to my co-supervisor Terje for always taking the time to share some of your wisdom in your busy days and for reminding me what is important in a clinical perspective. Thanks to Rolf for critical feedback on papers, motivating meetings and valuable input on the projects throughout the scholarship.

A special thanks to Heidi, who I have learned a lot from. From the first time I met you and witnessed your flawless microsurgical skills, you have remained my biggest lab idol.

Thank you to Tuyen, Marzieh, Halala and Sandra for creating a sanctuary site when life in the lab is tough. Your company always improves my day – also, thank you for everything you do in the lab organizing and overseeing all of us.

I would also like to direct a big thank you to my fantastic office team, Kathrine and Andrea. If someone gave us the chance, we really could solve world problems together!

Thank you to Cecilie for raising the bar for radiographers taking a PhD (because of you everyone who knows you assumes I am brilliant too) and also thanks for recruiting me to valuable teaching experience at Høgskulen på Vestlandet.

I am also grateful to the Western Norway Regional Health for funding the PhD project, collaborating partners and co-authors on the papers for making the project possible. I would also like to thank the staff and patients at the Department for Neurosurgery for making indispensable tissue samples available. Thanks to the staff (and mice) at the Animal Facility for making the inevitable preclinical investigations carried out throughout this project possible. I am also grateful for the excellent imaging facilities and technical assistance at MIC located at our institute. Thanks to Margarethe for all your help with administrative things.

Finally, to all my fantastic friends and family, thank you for your support. Mom and dad, Kristine and Vegard you encourage me on a daily basis in your own ways. To my fiancé Steffen and daughter Alva, you are a wonderful family. Thank you for keeping up with my unpredictably long working days seeing the project through. Alva, you add a new dimension to being a PhD candidate and even though this is my dream job, you have taught me what is really important in life.

Synnøve – June 14th 2019

List of abbreviations

Abbreviation	Full name
2-DG	2-deoxyglucose
5-ALA	5-aminolevulinic acid
ABC	ATP-binding cassette
AIF	Arterial input function
AKT	Protein kinase B (PKB)
ALK	Anaplastic lymphoma kinase
ATP	Adenosine triphosphate
AUC	Area under curve
BBB	Blood-brain barrier
BCRP	Breast cancer resistance protein
BRAF	Serine/threonine protein kinase B-raf
BTB	Blood-tumour barrier
CDKN2A/B	Cyclin-dependent kinase inhibitor 2A/B
CEST	Chemical exchange saturation transfer
CNS	Central nervous system
CT	Computer tomography
CTLA-4	T–lymphocyte–associated antigen 4
CXCR4	Chemokine receptor type 4
DCE-MRI	Dynamic contrast enhanced magnetic resonance imaging
DMSO	Dimethyl sulfoxide
ECAR	Extracellular acidification rate
EES	Extravascular, extracellular space
EGFR	Epidermal growth factor receptor
EMT	Epithelial-mesenchymal transition
EPR	Enhanced permeability and retention effect
ER	Estrogen receptor
ETC	Electron transport chain
FADD	Fas-associated death domain
FCCP	Carbonyl cyanide-p-trifluoromethoxyphenyl-hydrazon
FGF	Fibroblast growth factor
FLAIR	Fluid-attenuated inversion recovery
FLASH	Fast low angle shot
GEMM	Genetically engineered mouse models
GLUT-1	Glucose transporter 1
GPA	Graded prognostic assessment
HER2	Human epidermal growth factor receptor 2
KPS	Karnofsky performance score
K_{ep}	Reversed transfer constant
K^{trans}	Transfer constant
LDH	Lactate dehydrogenase
LINAC	Linear accelerator

MAPK	Mitogen-activated protein kinase
MDCK	Mabin-Darby Canine Kidney cells
MEK	MAPK/Erk kinase
MITF	Melanocyte inducing transcription factor
MMP	Matrix metalloproteinase
MRI	Magnetic resonance imaging
MRS	Magnetic resonance spectroscopy
MRP2	Multidrug-resistance protein
mTOR	Mammalian target of rapamycin
NOD/SCID	Non-obese diabetic/severe compromised immunodeficiency
NRAS	Neuroblastoma RAS viral oncogene homolog
NSCLC	Non-small cell lung carcinoma
OCR	Oxygen consumption rate
PET/CT	Positron emission tomography/computer tomography
PD-1	Programmed cell death protein 1
PD-L1	Programmed death ligand 1
PGC1α	Peroxisome proliferator-activated receptor gamma coactivator 1α
PI3K	Phosphoinisotide 3-kinase
PR	Progesterone receptor
PTEN	Phosphatase and tensin homolog
P-gp	P-glycoprotein
QUARTZ	Quality of life after treatment for brain metastases
RBE4	Rat brain endothelial 4 cells
ROS	Reactive oxygen species
RTOG	Radiation therapy oncology group
SRS	Stereotactic radiosurgery
TGFβ	Transforming growth factor β
TGFR	Transforming growth factor receptor
VEGF	Vascular endothelial growth factor
WBRT	Whole-brain radiotherapy
ZO	Zonula occludens

Abstract

Despite major scientific discoveries in the last decades, the survival rates for cancer patients suffering from brain metastases are quite divergent. Survival times have traditionally been measured in weeks to months regardless of implementing aggressive treatment. New treatment strategies have improved the average prognosis; however, brain metastasis is a heterogenous disease and still the therapeutic efficacy varies. Thus, further research is needed in order to improve the treatment options offered to the patients today. The major aim of this thesis was to contribute to the molecular understanding of brain metastasis, in particular from melanoma, and further to integrate our findings towards new treatment strategies. In **Paper I**, we assessed the applicability of a novel glycogen nanoprobe on melanoma cells *in vitro*. We further carried out a proof-of-concept experiment *in vivo* and found corresponding contrast enhancement to a clinically used contrast agent by MRI. In **Paper II**, we reported on the mechanistic properties of a synthetic peptide called K16ApoE. Moreover, we assessed its blood-brain barrier permeabilizing effects, and showed improved drug delivery into brain metastases beyond an intact barrier. In **Paper III**, a melanoma brain metastasis-specific 108-gene signature was determined by RNA sequencing and subsequent bioinformatics. These results were then used in an *in silico* analysis, to identify therapeutic compounds with the potential to revert the gene signature, thus inhibiting brain metastatic development. We identified β-sitosterol as a promising drug candidate, and carried out *in vitro* studies, followed by *in vivo* experiments to validate the hypothesis. The results indicated that β-sitosterol inhibited brain metastatic growth by restricting mitochondrial respiration. In **Paper IV**, we assessed the therapeutic potential of two targeted therapies inhibiting effectors in signaling pathways often upregulated in melanoma; the phosphoinisotide 3-kinase (PI3K) and mitogen activated protein kinase (MAPK) signaling pathways. By this, we were able to effectively treat human, metastatic melanoma cells and overcome acquired drug resistance, which is often reported when using single, targeted therapy. In conclusion, in **Paper I**, we show that nanomedicine could be a promising, future treatment modality for melanoma,

however, further studies in preclinical brain metastases models are needed. In **Papers II**, **III** and **IV** we demonstrate promising new treatment strategies for metastatic melanoma, using a blood-brain barrier permeabilizing peptide, a brain permeable compound or a combinatorial systemic therapy approach, respectively.

List of Papers

Paper I: Aasen SN, Pospisilova A, Eichler TW, Panek J, Hruby M, Stepanek P, Spriet E, Jirak D, Skaftnesmo KO and Thorsen F. *«A Novel Nanoprobe for Multimodal Imaging Is Effectively Incorporated into Human Melanoma Metastatic Cell Lines»* International Journal of Molecular Sciences 2015 16(9): 21658-80.

Paper II: Aasen SN, Espedal H, Holte CF, Keunen O, Karlsen TV, Tenstad O, Maherally Z, Miletic H, Hoang T, Eikeland AV, Baghirov H, Olberg DE, Pilkington GJ, Sarkar G, Jenkins R, Sundstrøm T, Bjerkvig R and Thorsen F. *«Improved drug delivery to brain metastases by peptide-mediated permeabilization of the blood-brain barrier»* Molecular Cancer Therapeutics 2019 (In 2nd Review).

Paper III: Sundstrøm T, Prestegarden L, Azuaje F, Aasen SN, Røsland GV, Varughese JK, Bernatz S, Braun Y, Harter PN, Skaftnesmo KO, Ingham ES, Mahakian LM, Tam S, Tepper CG, Petersen K, Ferrara KW, Tronstad KJ, Lund-Johansen M, Bjerkvig R and Thorsen F. *«Inhibition of mitochondrial respiration prevents BRAF-mutant melanoma brain metastasis»* Acta Neuropathologica Communications 2019 7(1): 55.

Paper IV: Aasen SN†, Parajuli H†, Roy K, Hoang T, Stokke K, Wang J, Feng Z, Bjerkvig R and Thorsen F. *«Dual targeting of the MAPK and PI3K signalling pathways in the treatment of metastatic melanoma»* Manuscript. †Equal contributions.

Contents

1. Introduction

1.1 Cancer

The first documentation of cancer in the history of medicine can be dated back to the Edwin Smith Papyrus from approximately 3000 BC[1,2]. Here, a tumour growing in the breast of a patient was described as an incurable, grave disease[2,3]. Almost three millennia later, Hippocrates introduced the terms «carcinoma» and «cancer» (latin for crab), owing to the fact that the malignant growth patterns of tumours reminded him of a moving crab that adhered its claws to the surrounding environment[2,4]. Already in this era, physicians concluded that early detection and complete surgical removal of the lesions was associated with a better prognosis[2]. Today we know that cancer is a genetic disease that develops gradually in a multistep process[5]. The tumour acquires an increasing degree of malignancy as the neoplastic cells obtain characteristics commonly known as the «hallmarks of cancer»[6,7]: Sustained proliferative signalling[8], resistance of cell death[9], induced angiogenesis[10], activation of invasion and metastasis[11], evasion of growth suppressors[12] and enabled replicative immortality[13]. The updated publication also included the so-called emerging hallmarks of cancer: Deregulated cellular energetics[14], avoided immune destruction[15], genome instability and mutations[16] and tumour-promoting inflammation[17,18] (Figure 1).

Tumour cells fail to comply with many basic rules in cell biology[5]. The overview in Figure 1 eases to some extent our understanding cancer. The hallmarks of cancer also indicate how the different properties can be exploited for treatment purposes[6]. For instance, it has been shown that the intracellular mitogen-activated protein kinase (MAPK) signalling pathway, which is regulated, among others, by the protein RAF, carries a mutation in 40-60% of all melanomas. This results in a constitutive activation of the pathway leading to continued cell proliferation. Several inhibitors of the mutated protein v-Raf murine sarcoma viral oncogene homolog B (BRAF) have been clinically investigated, such as vemurafenib and dabrafenib[19,20]. Both of these drugs are examples of utilization of targeted therapy towards cell proliferation (Figure 1). However, the

reality is often not that straight-forward. Despite initial clinical activity and subsequent drug responses, the tumour cells commonly develop treatment resistance, which will be further discussed in chapters 1.4.4.1, 1.4.4.2 and 4.

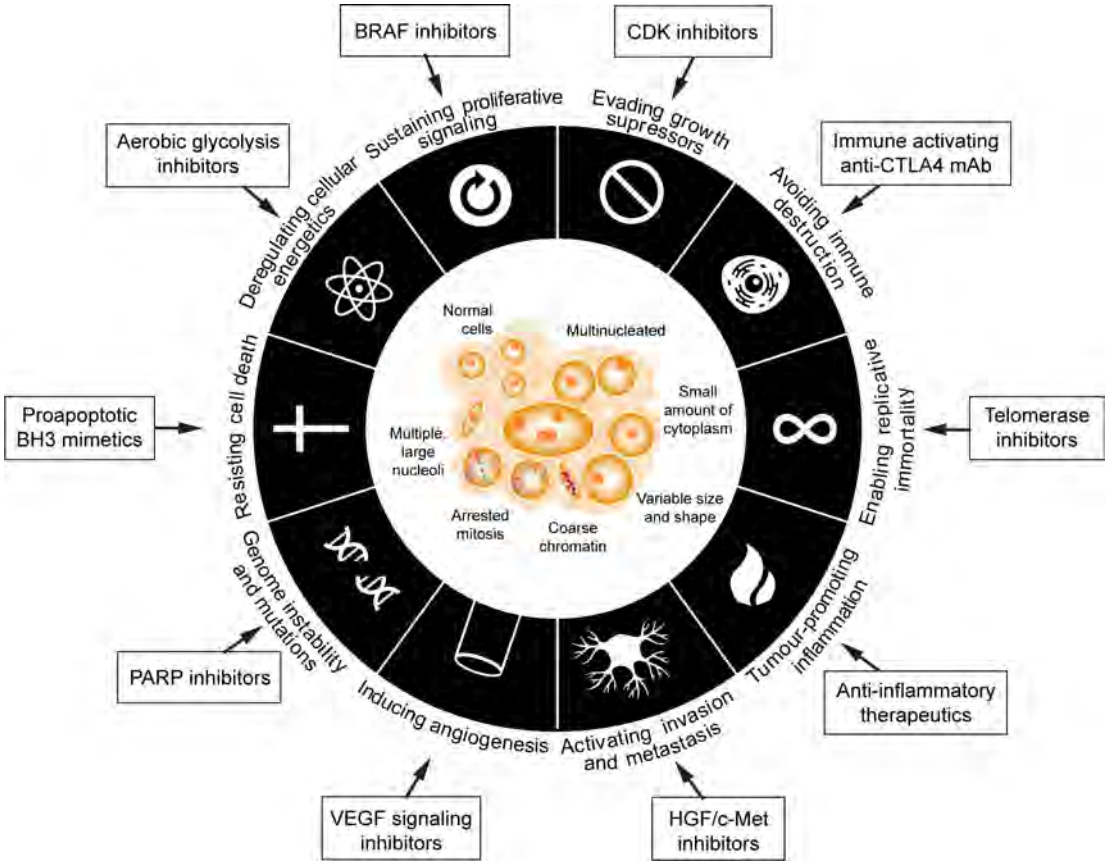

Figure 1: **The hallmarks of cancer and examples of therapeutic targets**. A summary of the ten characteristics that are typical of tumour cells. Several drugs are currently under preclinical investigation or in clinical trials aiming to exploit the different properties, exemplified by the drug types listed in circumferential boxes. Modified from Hanahan and Weinberg, 2011[6].

1.2 Metastasis

Metastasis is the result of an intricate, multistage process where tumour cells disseminate from their primary site, whereupon they colonize and grow as secondary tumours in remote organs[21]. The initial stages of metastasis include migration through the local stroma, which represents a network of connective tissue and blood vessels[22].

In metastatic cells, this is powered by among others secretion of metalloproteinases (MMPs) and cathepsins, a reorganization of the cytoskeleton and adhesive actions of tumour cells[23,24]. An acknowledged mechanism of migration and local invasion is the initial rearrangement of extracellular matrix components[25-27]. It has also been shown that single tumour cells can move throughout the length of actin collections[28] or migrate as multicellular colonies[29]. During the initial steps, many disseminating tumour cells undergo epithelial-to-mesenchymal transition (EMT) upon signalling from e.g. transforming growth factor β (TGFβ). In this morphological transformation, cells lose their epithelial polarization by down-regulating E-cadherine. Thus, they lose their intercellular adhesive properties, and become increasingly mobile[30]. EMT is therefore an important factor in tumour cell intravasation.

After successful dispersal via the vascular system, there is a need for adaptation to a new tissue micro-environment[31]. Colonization of tumour cells at distant sites necessitates extravasation of the tumour cells across different barriers from the circulatory system, such as the tight endothelium in the lungs and fenestrated endothelium in bone and liver tissue. Further colonization at the distant site can result in metastatic growth (Figure 2)[32]. A unique challenge for cells that metastasize to the brain, is the encounter with the blood-brain barrier (BBB), discussed further in chapter 1.6, before entry into brain tissue is possible (Figure 2)[22].

Further growth at the secondary site following extravasation and tumour cell attachment, requires the construction of a sufficient blood supply to obtain nutrients. This can occur by several mechanisms. In angiogenesis, new blood vessels are created by sprouting from pre-existing ones[33], whereas in vascular co-option, the tumour cells grow along pre-existing blood vessels[34]. In vasculogenesis, new blood vessels are created from precursor endothelial cells[35], whereas vasculogenic mimicry denotes *de novo* creation of tumour vascular networks, organized in tubular structures[36]. By employing a mechanism for angiogenic growth, it is believed that angiogenesis is triggered by hypoxia in tumour lesions between 1-3 mm^3. This leads to the formation of macro-metastases[37]. Angiogenesis depends on the expression of several angiogenic factors such as vascular endothelial growth factors (VEGF), Tie-2 and Angiopoetin.

Angiopoetin-2 is an angiogenic growth factor critical for co-option, vessel remodelling and angiogenic sprouting[38]. Several attempts to inhibit angiopoetin and VEGF signalling aiming to hamper the development of metastases, have been carried out[39-42]. Yet, few attempts at this dual treatment have been carried out on brain metastasis[38].

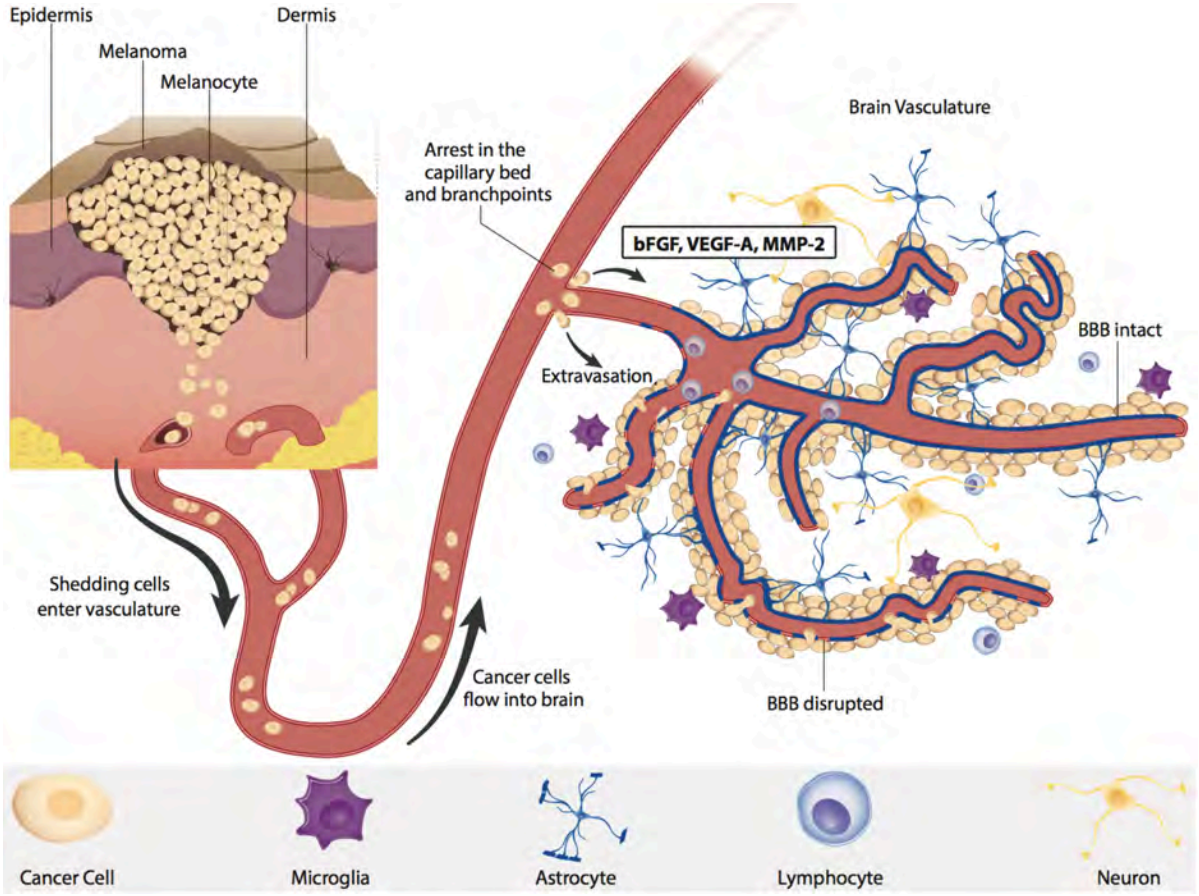

Figure 2: **Illustration of the multistage process of metastasis, exemplified by malignant melanoma.** After the tumour cells at the primary site (such as for instance in the skin) have managed to extravasate into the circulation, it follows the blood flow towards the brain, at which point the cells encounter capillary branch points and are physically constrained. At this point the tumour cells faces and extravasates the BBB and into the brain parenchyma, a process which involves components such as VEGF, fibroblast growth factors (FGF) and metalloproteinases (MMP). Following extravasation into the brain, the tumour cells adhere to and continue proliferation along the blood vessels. At the same time, VEGF secretion by tumour cells favours tumour angiogenesis. Most likely, there is at this stage a simultaneous interplay between tumour and glia cells promoting tumour growth[43]. Reprinted with permission from Oxford University Press.

1.3 Brain metastasis

Metastatic disease is the most threatening feature of cancer, accounting for more than 90% of cancer-related deaths[44-46]. This is often ascribed to the fact that metastases cannot be surgically resected in the same manner as many solitary, primary tumours[47]. Metastatic spread to the brain represents a major health problem, which substantially affects the quality of life and the length of patient survival[48]. The patients often experience symptoms such as headache, focal weaknesses, mental disturbances, seizures, difficulties to speak, visual impairments and sensory disruptions, all of which greatly reduces the performance status[49-52].

1.3.1 Occurrence

Even with a major influence on quality of life and high mortality rates, there is a lack of statistics summarizing the incidence of brain metastases. This is in part due to a previously used diagnostic coding system that did not specifically distinguish between primary and secondary brain tumours[53]. Interestingly, more than half of all malignant, intracranial tumours are brain metastases, making them the most common type of brain malignancies in the adult population[54].

The annual incidence of brain metastases appears to be increasing[55-57], and it has been estimated that around 10-40% of all cancer patients develop brain metastases[54,58]. For instance, in the US, it is estimated that around 200 000 patients will develop brain metastases at an annual basis[37,59-61]. This approximation has, however, been described as speculative, as the incidence of brain metastases is difficult to report[62]. Specific incidence rates describing the number of individuals diagnosed with brain metastases per 100 000 populations have been reported as low as 2.8 on Iceland to 14.3 in Scotland (different studies conducted between the years of 1935 to 2006)[63-71].

1.3.2 Causes and risk factors

The growing incidence of brain metastases is significantly related to improvements in systemic cancer therapies; patients live longer with their cancers and the inherent risks of brain metastasis thus increase[55,72]. Also, neuroimaging tools have substantially improved. Traditionally, computed tomography (CT) has been used to detect brain metastases. However, magnetic resonance imaging (MRI) modalities, which have superior imaging quality, have become increasingly more available, and this has contributed to increased detection[73,74]. The growing incidence is also presumably a consequence of the steadily increasing frequency of primary cancer types that establish brain metastases[75]. The risk factors of developing brain metastases are in part dependent on the causative primary tumour. In principle, all tumour types can metastasize to the brain[76]. However, the majority of brain metastases originate from lung cancer (∼50%), breast cancer (∼25%) and melanoma (∼20%)[77]. Out of these, melanomas have the strongest tendency to metastasize to the brain[73,78]. Their central nervous system (CNS) involvement has been found to be up to 75% by post mortem analysis[73,79,80].

For melanoma patients, individuals with primary tumours restricted to the skin without involvement of the lymph nodes, have low chances of developing brain metastases[81]. It has also been shown that men over 60 years of age have higher probabilities of developing brain metastases[82]. Patients with involvement of more than three regional lymph nodes[83], aberrant MAPK signalling[84,85] or elevated lactate dehydrogenase (LDH) have been shown to be at enlarged risks[82].

For patients with non-small-cell lung cancer (NSCLC), two genetic alterations are predictive for the development of and treatment response of brain metastases. Mutations in the epidermal growth factor receptor (EGFR) occur in 40% of patients with East-Asian descent and 10-15% of Caucasians with metastatic NSCLC. The mutation status of EGFR predicts the response to therapy of brain metastases. Rearrangements in the anaplastic lymphoma kinase (ALK) gene are seen in some cases of NSCLC and is also a predictor of treatment response and thus survival[86,87].

The risk of developing brain metastases from breast cancer is highly dependent on the tumour subtype: Luminal A tumours have high levels of the estrogen receptor (ER) and progesterone receptor (PR) and are negative for human epidermal growth factor receptor 2 (HER2). These tumours have a low cell proliferation rate, which is defined by Ki67 staining below 20%. Luminal B patients carry ER positive, PR negative and HER2 positive tumours with a high proliferation rate (Ki67 above 20%). HER2 non-luminal patients have HER2 positive tumours and lack steroid receptor expression (ER and PR). Triple-negative tumours are HER2 and steroid receptor negative[88]. The risk of developing metastases is highest among the patients that carry highly proliferative hormone receptor negative tumours or HER2 overexpressing tumours[89].

The incidence of brain metastases from colorectal cancer is in general low. However, a subgroup of this patient group is at enlarged risk of developing metastatic lesions in the brain. Risk factors include progressive pulmonary involvement, placement of the primary tumour in the left colon and chemokine receptor type 4 (CXCR4) expression in the tumour cells[90]. Also, a subgroup of patients with renal cell carcinoma have a greater risk of developing brain metastases. Risk factors include tumour measurements greater than 10 cm, lymph node involvement, clear cell histology and sarcomatoid differentiation, i.e. tumours with aggressive growth patterns and poor responsiveness to immunotherapy[91].

1.3.3 Diagnosis

As established by Hippocrates over 2 000 years ago, early detection is key to improve the patient's treatment response and thus the chances of survival[92,93]. Today, contrast enhanced MRI is primarily used to diagnose brain metastases[94]. In contrast-enhanced T_1 weighted MRI scans (i.e. light grey white matter and darker grey cortex[95]), brain metastases are usually hyperintense[96], but can also be ring-enhancing[97] or punctate[98] (Figures 3A and B). In both T_2 (i.e. dark grey white matter and light grey cortex[95]; Figure 3C) and fluid-attenuated inversion recovery (FLAIR; i.e. dark grey white matter

and light grey cortex[95]) weighted MRI scans (Figure 3D), brain metastases are usually hyperintense[99].

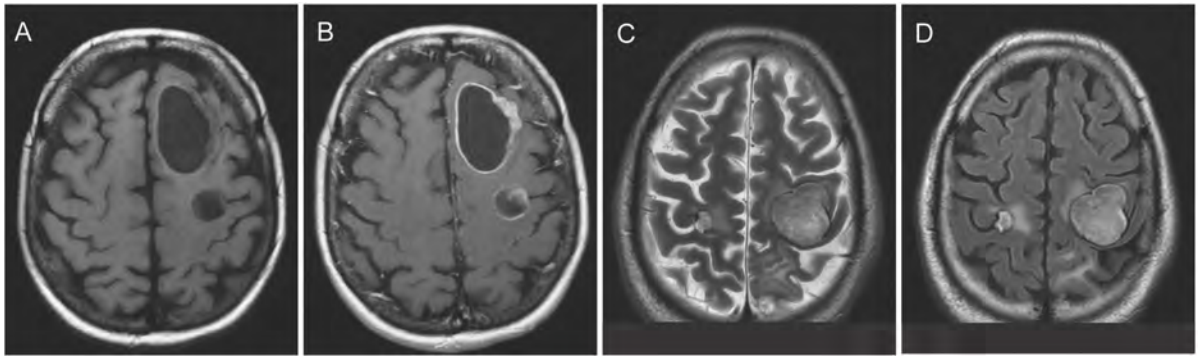

Figure 3: Radiographical assessment of brain metastases. A, B: Axial T_1 weighted MRI scans with (B) and without (A) contrast agent of a patient with brain metastatic lung cancer. The lesions had a cystic appearance with ring-enhancing contrast agent effect (B) (case courtesy of Prof F Gaillard, Radiopaedia.org, rID: 3972). C, D: Axial T_2 (C) and FLAIR (D) scans of a 60-year-old man with brain metastasis from colorectal cancer (case courtesy of Dr M Shebl, Radiopaedia.org, rID: 19894).

By using magnetic resonance spectroscopy (MRS) it is feasible to investigate the proton spectrum of healthy and diseased CNS tissue. Brain metastases express dissimilar metabolites than for instance abscesses or glioblastoma, and can thus be used to distinguish between varying cerebral pathological conditions[100,101]. Although the radiographical evaluation is important, the final diagnosis is made by histopathological assessments and molecular features of the resected tumour material.

1.3.4 Placement and number of metastases

The number, appearance and placement of brain metastases is often indicative of the causative primary tumour[54]. A previous study with 729 patients has shown that 47% of the patients receiving treatment had more than one metastatic lesion[102]. Multiple brain metastases are often linked to lung carcinoma and melanoma, whereas patients with breast, colon or renal cell carcinoma frequently present with solitary metastasis[103]. Metastases from melanoma or kidneys are often hemorrhagic and metastases from lung adenocarcinomas appear cystic[104]. The anatomical placement of brain metastases is typically correlated to blood flow and tissue volume; cerebral hemispheres (80%),

cerebellum (15%) or in the brainstem (5%). Interestingly, breast and lung cancers are more susceptible to colonize in the cerebellum[105].

1.3.5 Prognosis

The survival times for patients with brain metastases varies substantially[106], but the prognosis has traditionally been poor[103,107-109]. Standard treatment strategies have commonly involved surgery, radiation therapy and/or chemotherapies[110]. For patients with brain metastases from melanoma, recent advances resulting in novel targeted systemic therapies have extended the median patient survival from around six to nine months with chemotherapy[111,112], to close to two years with new drug strategies[113-115]. However, not all patients are candidates or respond as expected to these novel therapies[110]. Relatively long median survival times are seen in other brain metastases subgroups as well, such as for instance patients with HER2-positive breast cancer[116].

The Radiation Therapy Oncology Group (RTOG) developed a prognostic categorization with three patient classes based on age, disease status and Karnofsky performance score (KPS). Patients younger than 65 years and KPS above 70 are assigned to Class I, individuals with KPS below 70 to Class III and the remaining patients to Class II[117]. The significance of these predicting classes was reviewed by analysing 1200 patients enrolled in three RTOG brain metastasis trials[118], and further validated in a second RTOG trial[117]. The prognostic classes and patient outcome correlated with median survival: Class I patients had a median survival of 7.1 months, class II 4.2 months and class III 2.3 months. Several other prognostic models have been developed since[62]. The Graded Prognostic Assessment (GPA) model described by Sperduto et al. remains one of the most prominent prognostic tools. A refined diagnosis-specific GPA model underpins that the prognosis additionally depends on the unique properties of the causative primary tumour[119].

1.4 Treatment strategies for brain metastases

The therapeutic strategy for patients with brain metastases is usually multidisciplinary, and depends on the primary tumour, anatomical location, number and sizes of the metastases, mutation status, comorbidity, age, performance status and extent of systemic disease burden of the patient[107]. The treatment strategies are discussed in more detail below. For patients with brain metastases from melanoma, a summary is included in Figure 4.

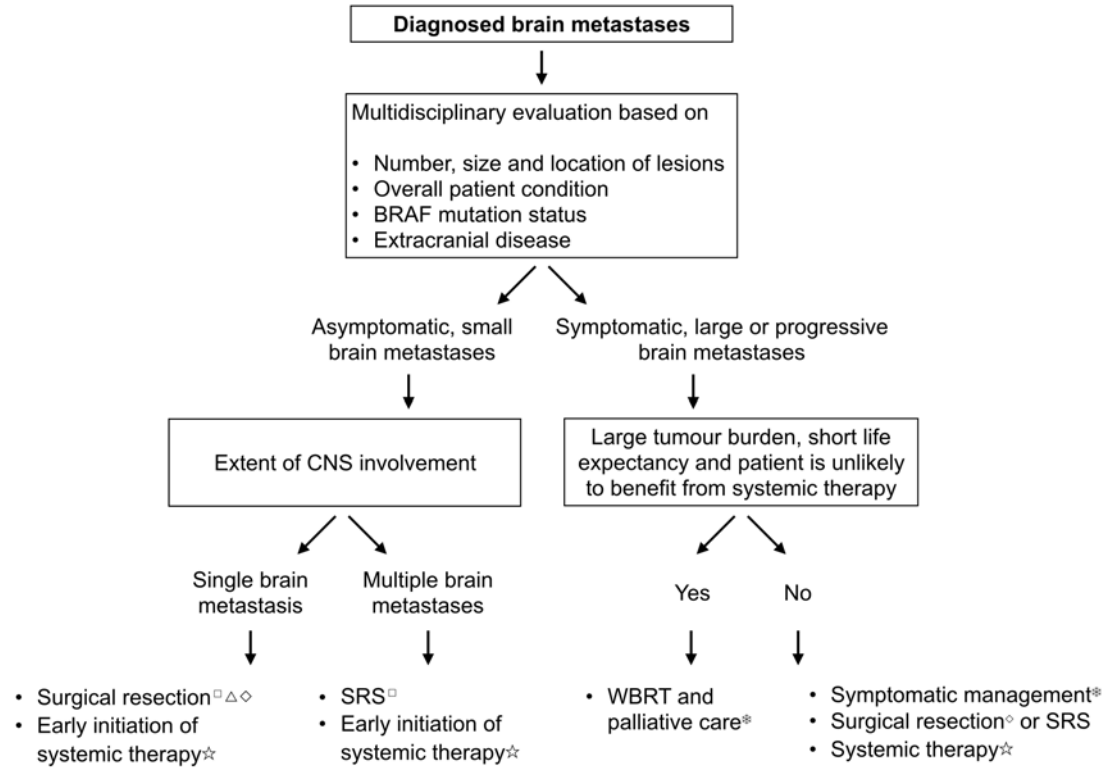

Figure 4. Treatment algorithm for patients with brain metastases, here exemplified by metastases from melanoma. The therapeutic approach depends on a number of variables, such as the number, size and location of the metastatic lesions, mutational status and the degree of CNS involvement. Symbols: □As an alternative to surgery or SRS, some patients may be better suited for systemic therapy, however, close follow-up with imaging is required. △For patients with unoperable metastases, SRS is an option. ◇Postoperative SRS into the resection cavity is only done if the patient is not a candidate for systemic treatment. The risk of radiation necrosis and tumour recurrence must be balanced. ☆Options for systemic therapy include immune checkpoint inhibitors or targeted therapies. The latter may worsen radiation toxicity. ❋Corticosteroids or anticonvulsants. Adapted from Samlowski et al., 2018[120].

Briefly, solitary, asymptomatic, small lesions are usually resected surgically and treated with systemic therapy. Multiple, asymptomatic lesions are treated using stereotactic radiosurgery (SRS) and systemic therapy. Patients with large and symptomatic metastases and low performance status are treated with whole-brain radiation therapy (WBRT) and palliation[120]. In chapters 1.4.1, 1.4.2 and 1.4.3 the discussion is focused on brain metastases in general, whereas in chapter 1.4.4 the systemic treatment strategies of the brain metastases from different causative primary cancers are described in detail.

1.4.1 Surgical resection

The importance of adjuvant treatment of brain metastases consisting of surgical removal and WBRT was demonstrated in two major clinical trials published in the early 1990s[121,122]. Patchell et al. showed in a randomized clinical trial that the recurrence rate of a single brain metastasis was reduced from 52 to 20% when surgery was combined with WBRT. The overall survival was extended from 15 to 40 weeks[121]. These findings were verified by Vecht et al.[122]. Standard surgery involves using conventional white-light microscopy to remove the lesion and perform circumferential stripping from the surrounding brain tissue[123]. Although dependent on anatomical placement and lesion volume, it has been indicated that *en bloc* resections are beneficial with respect to local recurrence, as opposed to piecemeal resections[124]. According to Ahn et al. there is a risk of post-surgical, leptomeningeal spread if piecemeal resections methods are used, in particular if the tumour is located within close proximity to the ventricles[125]. Further, Yoo et al. concluded that surgical removal with tumour cell free resection margins improved local tumour control[126].

In addition to white-light microscopy-guided surgery, fluorescence-guided resection methods may also be used, in which case traceable agents are employed to visualize the tumours and refine the neurosurgical resection. For instance, fluorescein can overcome a compromised blood-brain barrier and 5-ALA (e.g. 5-aminolevulinic acid) takes advantage of the altered metabolism present in tumour tissue for visualization[127,128]. Schebesch et al. carried out a retrospective study with 30 patients

who received 200 mg of fluorescein sodium intravenously prior to brain metastases resection. 90% of the patients showed a fluorescence signal in the tumour tissue. Total resection was confirmed by postoperative MRI for 83.3% of the patients. Although fluorescein sodium was well tolerated and safe, they concluded that additional, larger studies are needed to evaluate potential benefits over conventional white-light guided surgery[129].

Although surgery is the first treatment of choice, additional treatments are needed, as described below[123]. Neurosurgical intervention can be associated with postoperative complications such as infections, neurological aggravation, intracranial haemorrhage and stroke. Despite this, the outcomes after surgical treatment are commonly improved or unchanged for nine out of ten patients[54]. Surgery should, however, be balanced between the potential harms and benefits.

1.4.2 Whole-brain radiotherapy (WBRT)

WBRT has been part of the standard treatment strategy of brain metastases since the 1970s. With the increased survival from improved systemic treatments, the adverse effects of WBRT have become more apparent. Hence, it has become more and more common to give SRS and/or postpone WBRT. For patients with multiple brain metastases, WBRT is normally the treatment of choice[130].

Ionizing radiation produced through linear accelerators (LINACs) damages DNA either directly or indirectly. The high energy photons may interact directly with the DNA, causing single- and double strand breaks[131]. The energy of the ionizing radiation may also discharge orbital electrons of molecules in the irradiated tissue, producing intracellular ionized water molecules ($H_2O^{+\bullet}$), which further interact with water molecules and yield hydroxyl radicals ($^{\bullet}OH$). These will in turn react with and damage the DNA strands (indirect damage).

The aim of radiation treatment is to kill tumour cells and at the same time limit damage to surrounding, healthy cells. Since the radiation has to travel through healthy tissues to reach the tumour cells, non-cancerous cells will inevitably be damaged. However,

tumour cells are harmed to a larger extent, as they have dysfunctional DNA repair mechanisms. Examples of repair pathways involve base excision repair, nucleotide excision repair, mismatch repair, transcription coupled repair, homologous recombination repair and non–homologous end joining repair[131]. Normal cells can normally repair DNA damages within six hours, whereas more than 90% of radiation sensitive tumour cells may die from each radiation fraction[132].

Although associated with adverse effects, WBRT is in general well tolerated among patients. Predictors of tolerance include tumour oedema, number and location of brain metastatic lesions and age. Short-term toxicities of WBRT are fatigue, alopecia, dermatitis, nausea and cerebral oedema. Most of these are either self-limiting or can be treated pharmaceutically. Late toxicity occurs at least 90 days after treatment onset and include neurocognitive decline, leukoencephalopathy and radiation necrosis. In contrast to the acute toxicities listed above, late toxic adverse effects are not self-limiting, and can be quite challenging to manage medically[130].

Patients with brain metastases from NSCLC, have traditionally been treated with WBRT in combination with steroids, commonly dexamethasone[133]. Interestingly, this strategy was based on reports from the 1950 and 60s, and for a long time, there was a lack of randomized clinical trials specifically addressing the efficacy of WBRT in brain metastatic NSCLC. Mulvenna et al. investigated whether WBRT could be excluded from the clinical approach without a major effect on survival time on 538 patients in the Quality of Life after Treatment for Brain Metastases (QUARTZ) study. They found no difference in the frequency of serious adverse events between the two treatment groups. Most importantly, they did not detect any improvement in overall survival or quality of life in the WBRT group, and concluded that WBRT did not provide any significant benefit for this patient group[134].

1.4.3 Stereotactic radiosurgery

Due to the poor outcomes for many patients receiving WBRT, increasing attention has been given to more focused radiation approaches[120]. Stereotactic radiosurgery (SRS) is

a technique for delivering focused radiation[135] and has become an attractive treatment alternative[136]. SRS can either be used alone or in combination with WBRT. However, one of them is usually favoured based on the clinical picture of the individual patient[137]. SRS is typically provided to patients with one or a few relatively small and asymptomatic brain metastases. It can also be administered in combination with systemic treatment to patients with a relatively good prognosis, who have larger, progressive and symptomatic metastases[120].

In SRS, numerous focused radiation beams enter through the skull of the patient from several different angles, and meet in a defined target, thereby achieving a high radiation dose within the target volume. The individual radiation beams will deposit low radiation doses towards the target, thus sparing the normal brain from radiation effects. Normally, SRS is administered as one single fraction, however, the treatment can also be administered in several fractions, commonly once a day for five days in total (fractionated SRS). The radiation can be administered either through a LINAC system, which produces x-rays, or by The Leksell Gamma Knife, which produces γ-rays[137].

Due to its specificity, SRS has been described as one of the most effective treatment options for brain metastases[138-140]. In 2006, Aoyama and colleagues randomized 132 patients with one to four brain metastatic lesions smaller than 3 cm in diameter and compared patients receiving WBRT + SRS with patients receiving SRS only. No difference in median overall survival between the WBRT + SRS and SRS groups were found (7.5 and 8 months, respectively). Also, there was no difference in deterioration in neurological function, however, the tumour recurrence was significantly greater in the SRS arm[49]. On the other hand, in a phase III trial with 213 patients either receiving SRS alone or SRS + WBRT, the latter group presented with more pronounced cognitive decline than the patients in the first treatment arm[141]. Yamamoto et al. studied 1194 brain metastatic cases with a KPS over 70 treated with SRS. Their results questioned the need for WBRT in patients with multiple brain metastatic lesions, and suggested that the number of lesions might be less important than formerly anticipated[142]. Also, the comparison of pre- versus post-operative delivery of SRS is gaining increasing interest. For instance, Patel et al. studied the outcome of 180 patients receiving SRS

either before or after surgery, and found similar outcomes with regard to overall survival, and distant and local recurrence rates[143].

Taken together, the current approaches involve SRS as single treatment, combined treatment with WBRT, surgery or systemic therapies, and radiation delivery either before or after surgery. For the latter, more research is needed to determine its clinical value.

A frequently reported complication from radiation therapy is the occurrence of radiation necrosis, seen on T_1 weighted MRI as a contrast enhancing inflammatory lesion (often with associated oedema) six to 24 months after treatment. Radiation necrosis can be difficult to discriminate from tumour progression. In this context, clinical symptoms can be challenging to manage[144]. Kim et al. enrolled 1650 patients in a clinical trial aiming to map late toxicity in patients with brain metastases treated with WBRT or SRS. They found that the frequency of radiation necrosis increased when patients were treated with systemic therapies, WBRT and SRS at the same time, however this was not the case when patients received systemic treatment and SRS only. This adds to the previous statement that WBRT may be omitted from the treatment of brain metastases[145].

1.4.4 Systemic therapy

The therapeutic agent selected for individual patients with brain metastases depends on the mutation status and the origin of the causative tumour. Several chemotherapies have traditionally been used for the treatment of brain metastases and some can even cross the BBB such as topotecan, irinotecan, carboplatin and procarbazine[146]. Another example is temozolomide, which is an alkylating, lipid-soluble orally administered chemotherapeutic agent[147]. Phase II clinical trials combining temozolomide + WBRT have shown varying outcomes[148-151]. New and more targeted therapies have been actively investigated based on divergent efficacies of chemotherapeutic drugs. In the case of metastatic melanoma, a range of novel drug-related discoveries has

predominated the field with the introduction of more targeted therapies as discussed below[152].

1.4.4.1 Brain metastases from melanoma

Brain metastases have previously been diagnosed in 10-40% of melanoma patients. However, autopsy studies have revealed that as many as 75% have brain metastases, and frequently more than one lesion is found[81,102,153,154]. Around 90% of the previously mentioned BRAF mutations frequently found in melanoma (chapter 1.1) result in a replacement of valine with glutamate at amino acid position 600 (V600E), i.e. the $BRAF^{V600E}$ mutation[155]. The first attempt to systemically inhibit BRAF mutated melanoma with the multikinase inhibitor sorafenib was not successful[156]. Later, a more selective BRAF inhibitor, vemurafenib, targeting the specific $BRAF^{V600E}$ mutation was introduced[157]. In a phase II clinical trial, the response rate was 53% and the mean duration of response was 6.8 months[158].

A second selective BRAF inhibitor, dabrafenib (GSK2118436), showed high intracranial response rates in $BRAF^{V600E}$ mutated metastatic melanomas in a phase I clinical trial[20]. In a multicentre phase II clinical trial, 172 patients with $BRAF^{V600E}$ or $BRAF^{V600K}$ mutated brain metastases were enrolled and treated with dabrafenib; for patients with $BRAF^{V600E}$ mutations, response rates were similar for previously untreated patients (39%) and pre-treated patients (31%)[159].

Treatment with BRAF inhibitors is normally associated with an initial treatment response, followed by acquired drug resistance and subsequent tumour progression after approximately six months. In order to overcome acquired drug resistance, BRAF inhibitors have been combined with inhibitors of downstream targets in the MAPK pathway, such as MEK1 or MEK2[160]. Long et al. used a combination of dabrafenib and trametinib, showing lower recurrence risks in patients with metastatic $BRAF^{V600E}$ mutated melanoma, with no additional toxic effects by the combined therapy[161]. Figure 5A summarizes some of the existing systemic inhibitors of targets in the MAPK pathway.

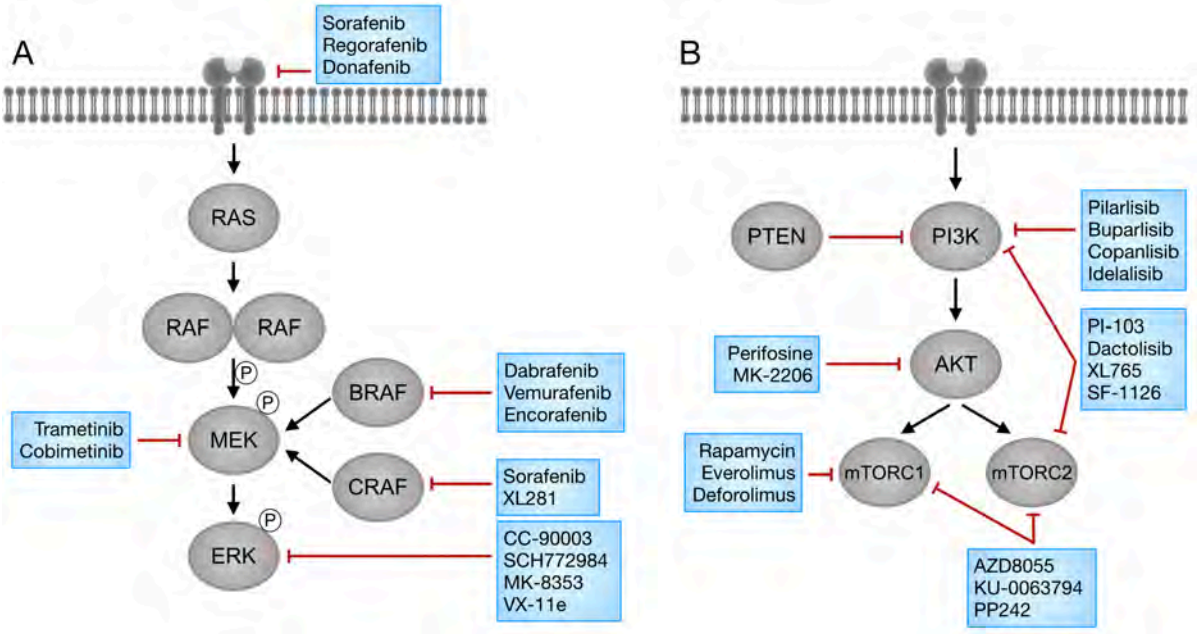

Figure 5: **Inhibitors of targets in the MAPK and PI3K signalling pathways**. A: Upon activation of RAS, RAF dimers are created, and RAF phosphorylates the downstream protein MEK. MEK in turn phosphorylates ERK, which regulate targets both in the cytosol and inside the nucleus. In this way ERK promotes tumour cell survival and further proliferation. Downstream ERK activity is regulated at the level of receptor tyrosine kinases, RAS, RAF and ERK proteins. The BRAF inhibitors dabrafenib, vemurafenib and encorafenib inhibit ERK activation in tumours that are BRAF mutant, whereas sorafenib and XL281 are more active against CRAF mutations. Agents that target ERK directly include CC-90003, SCH772984, MK-8353 and VX-11e. In contrast to BRAF inhibitors, ERK inhibitors downregulate ERK activity in both tumour and normal cells. Adapted from Nissan et al., 2013[162]. B: The MAPK pathway coincides with the PI3K pathway by growth factor receptor activation and can function as an alternative mTOR activation mechanism. Upon activation and phosphorylation of phosphoinositide 3 (PI3K) by activated growth factor receptors such as HER2 or EGFR, the second messenger PIP3 is produced. PIP3 signals through AKT to activate downstream targets such as mTOR. PTEN is a negative regulator of the signaling pathway by preventing phosphorylation of AKT. Several agents target different levels in the signaling pathway, such as buparlisib which targets PI3K, and rapamycin which targets mTOR. Adapted from Majchrzak et al., 2014[163].

Another frequently mutated signalling pathway in melanoma is the phospho-inositide-3 kinase (PI3K) pathway, illustrated in Figure 5B[164]. Around 10-30% of patients with metastatic melanoma have an activating PI3K mutation, and this is often associated with BRAF mutations[165,166].

Altered PI3K signalling may cause loss of function in the phosphatase and tensin homolog (PTEN) protein, which is a negative regulator of AKT and subsequent downstream effectors[164]. Other causative mechanisms that can activate PI3K signalling are PIK3CA or RAS mutations and mutated receptor tyrosine kinases such as EGFR and HER2[167,168]. Thus, the PI3K protein is an attractive target due to its connectivity and central position in the signalling pathway[168]. Previously, PI3K pathway inhibitors have been associated with acquired drug resistance, illustrating a potential beneficial effect of adding for instance MAPK inhibitors as an adjuvant treatment to PI3K inhibitors[169].

Rapamycin, or sirolimus, was the first small-molecule drug that was used to therapeutically inhibit mTOR, a downstream target of AKT in the PI3K signalling pathway. Everolimus (RAD001) is a newer rapamycin analog, but still belongs to the first-generation of rapamycin drugs. Second-generation inhibitors function by competing with adenotriphosphate (ATP) for the catalytically active site of mTOR. There are two subgroups of this class of drugs: Selective mTORC1 and mTORC2 inhibitors, and dual mTOR and PI3K inhibitors. Unlike the first-generation rapamycin-based drugs, the dual targeting of mTOR and PI3K inhibits reactivation of PI3K signalling[169]. As this inhibition results in induction of apoptosis and diminished cell proliferation[170], inhibiting agents of the PI3K signalling pathway are currently under clinical investigation for patients with brain metastases[171]. However, because of the intricate characteristics of the PI3K signalling pathway with considerable cross-talk with other signalling pathways, it is challenging to predict which patients will benefit from the treatment[172].

Since treatment resistance is a major concern when targeting intracellular signalling pathways, supplemental targeting strategies are needed. Melanoma is one of the most immunogenic tumours, which can be exploited for treatment purposes. Several immunomodulatory mechanisms have been shown to be downregulated in melanomas, preventing immune cells from identifying and attacking tumour cells. Therapeutic strategies aiming to take advantage of these mechanisms and overcome the immune system evasion have been pursued[173]. The immune checkpoint inhibitor ipilimumab is

a monoclonal antibody that blocks cytotoxic T–lymphocyte–associated antigen 4 (CTLA–4), which a negative stimulant of T–cells. By inhibiting CTLA–4, the inhibiting effects on the T–cell is removed and it becomes hyper-responsive. Ipilimumab thus improves the activity of T–cells, which again encourages anti-tumour activity[174]. However, the results from two phase III clinical trials evaluating ipilimumab in metastatic melanoma showed only minor effects, with response rates around 10–15%[174,175]. Despite this, a major benefit is that the toxicities after treatment with ipilimumab alone is controllable[156]. Schadendorf et al. reviewed the overall survival from 12 phase II and III clinical trials with a total number of 1 861 patients. The overall survival was 11.4 months, and the overall three-year survival rate was 22% (26% for treatment-naïve and 20% for pre-treated patients). The survival was seen to plateau around three years after treatment[176].

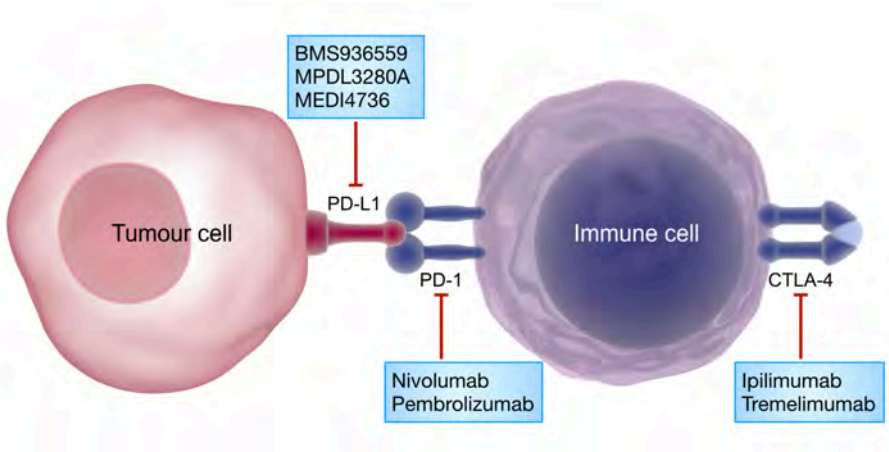

Figure 6: The interaction between tumour cells and immune cells. PD-L1 is abundantly present on the surface of tumour cells, and when bound to the PD-1 receptor on immune cells, the tumour cell is camouflaged from immune cell attacks. The PD-1 receptor thus serves as an on-switch that prevents attacking. CTLA-4 is a negative stimulant of T-cells and when inhibitied, promotes anti-tumour activity.

Attempts to combine BRAF/MEK inhibitors with ipilimumab have unfortunately been associated with high toxicities[177]. Thus, combined targeted therapy with other immunomodulators, such as programmed cell death protein 1 (PD-1) and programmed death ligand 1 (PD–L1) have been evaluated[178]. PD-1 is a receptor present on T–cells, and functions as an off-switch, that prevents T cells from exerting their immunogenic

function. PD–L1 is a receptor abundantly present on tumour cells, and when bound to PD-1, the tumour cell is concealed from immune cell attacks[179]. Figure 6 shows an illustration of the interplay between these receptors.

A phase II clinical trial combining ipilimumab with fotemustine, which is a lipophilic alkylating agent, showed a response rate of 47% in patients with brain metastases[180]. Several other clinical trials are ongoing, investigating the effects of immunotherapy combined with other targeting agents against brain metastases[171] (Table 1).

In a phase I clinical trial (NCT02027961), a combination of MEDI4736, an antagonist to PD–L1, and dabrafenib and/or trametinib in BRAF mutated and BRAF wildtype melanoma patients was studied. The patients with BRAF mutated tumours who received a combination of MEDI4736 and the two signalling pathway inhibitors, showed a response rate of 69% and a disease control rate, which comprised patients with complete or partial response as well as stable disease, of 79%. The patients with BRAF wildtype tumours treated with trametinib and MEDI4736 had a response rate of 21% and a disease control rate of 80%. In the other, wildtype BRAF tumour group, the patients initially received trametinib as monotherapy, before they received a combination of trametinib and MEDI4736, and finally MEDI4736 as monotherapy. These patients had a response rate of 21% and a disease control rate of 80%. However, the treatment regimens showed high toxicity, and grade 3 and 4 adverse events were recorded for 17 to 40% of all patients[181].

Regarding treatment resistance, the molecular profiles of primary melanoma and patient-matched metastases are receiving increasing attention. Hannan et al. found a 14% discordance in BRAF mutation status between primary tumours and brain metastases among 42 melanoma patients with spread to distant sites[182]. Chen et al. concluded that there was a 100% concordance in patient-matched samples regarding BRAF and NRAS mutation status[183]. Niessner et al. found hyperactivated AKT expression in brain metastases compared to the matched samples, implicating the PI3K signalling pathway in treatment of brain metastases[184]. Further, Fischer et al. identified

metabolic and immunologic discordances between extracranial and intracranial melanoma brain metastases, which could be a contributing factor to drug resistance[185].

1.4.4.2 Brain metastases from NSCLC

Regarding brain metastases from NSCLC, EGFR tyrosine kinase inhibitors such as the first generation agents gefitinib and erlotinib[186] and the second generation agents afatinib and dacomitinib[187] have shown clinical activity, resulting in an improved survival for patients with EGFR-mutated tumours. However, a common mechanism of drug resistance is mediated by the T790M EGFR mutation. Thus, third generation agents have been developed to bypass this resistance mechanism: Osimertinib[188,189], rociletinib[190] and olmutinib[191]. These drugs inhibit the T790M EGFR mutation in an irreversible manner, and at the same time do not affect the wildtype EGFR[192]. Also, inhibitors of the ALK rearrangement mutations have shown clinical activity in metastatic NSCLC. For the first-generation drugs, progression of brain metastases was seen in most of the patients, likely due to acquired resistance. The second-generation ALK inhibitor ceritinib has shown to overcome resistance to first-generation agents, however, not in brain metastases[106]. Third-generation ALK inhibitors have demonstrated substantially improved intracranial activity. For instance, in the ALUR clinical trial, it was shown that the the ALK inhibitor alectinib had a CNS objective response rate of 54.2% compared to the chemotherapy group[193].

1.4.4.3 Brain metastases from breast cancer

Although traditional chemotherapies have resulted in improved survival rates, targeted therapy is becoming increasingly more important also for patients with brain metastases from breast cancer[171]. Phase II clinical trials combining the tyrosine kinase inhibitor lapatinib with the chemotherapeutic agent capecitabine showed an objective CNS treatment response of 65% in previously untreated patients[194], however, in a corresponding clinical trial with previously treated patients, the response rate was only 6%[195]. Also, the combination treatment was associated with severe degrees of adverse

events[194]. Lapatinib + capecitabine has also been evaluated in combination with everolimus in a phase Ib/II trial including pretreated patients with HER2 positive brain metastatic breast cancer (NCT01783756). 27% showed a partial CNS response, whereas 64% had stable disease, and the treatment was well tolerated[196]. For patients with brain metastases originating from triple negative breast cancer, the management of the disease has been particularly challenging, and the prognosis is poor. In such cases, the patients are usually offered WBRT. Cause of death is usually from extracranial disease, reflecting the need for therapeutic agents targeting both intra- and extracranial metastatic lesions[171].

Previous studies have highlighted a phenotypic discordance between primary breast cancer and distant metastases[171,197]. Most commonly, these alterations involve loss of hormone receptors such as ER and PR[198-202], but also altered HER2 status[198,203]. Further, Manson et al. found a discordance in PD-1 and PD-L1 expression between primary breast cancers and distant metastases in more than one third of the patients investigated[204]. This molecular divergence clearly illustrates the need for updated molecular information (biopsy or re-biopsy) prior to initiation of systemic treatment with targeted agents[205]. Also, dysregulation in the PI3K signalling pathway has been associated with brain metastases from breast cancer[206,207].

1.4.4.4 Antiangiogenic therapies

The antiangiogenic therapeutic agent bevacizumab, which targets VEGF, has shown promising results alone and in an adjuvant setting with several other therapeutic agents in clinical trials and case reports[208-210]. Previous preclinical research has shown that the development from micro- to macro-metastases is hampered by bevacizumab in brain metastases originating from lung cancer, in contrast to melanoma-derived brain metastases, which often grow in a more co-optive pattern[211,212]. This is also in line with autopsy studies[213]. However, targeting the brain vasculature, is associated with a risk of «pseudoresponse», which is a false impression of tumour regression because of reduced MRI contrast agent uptake. In such instances, chemical exchange saturation

transfer (CEST) MRI can aid in the evaluation of true versus false treatment responses[214].

1.4.4.5 Metabolic targeting therapies

It has been shown that molecular drivers of tumour progression may have the ability to reprogram cellular metabolism to favour further tumour growth, drug resistance and metastasis[215]. Thus, additional treatment strategies besides those targeting molecular drivers, immune checkpoints and angiogenesis should be exploited. It is well known that tumour cells have a higher energy demand than normal, healthy cells due to, among others, cell division[216]. This demand implies reprogrammed tumour cell metabolism, which represents several attractive therapeutic targets. The adaptation from oxidative phosphorylation to aerobic glycolysis, «the Warburg effect», is a phenomenon that occurs in most tumour cells[217].

Some metastatic melanoma cells are metabolically altered to a more neuronal-like phenotype characterized by increased glutamate and calcium signalling during the initial stages of metastatic development. These cells have been shown to be particularly prone to colonize the brain[218]. Also, some cells lose the expression of the tight junction protein claudin-1, which further favours brain metastatic development[219]. When melanoma cells encounter S100 calcium-binding protein A4 (S100A4), a shift towards aerobic, glycolytic activity takes place (the Warburg effect). Upregulation of these pathways favours invasiveness and increased cell proliferation, and illustrates how reprogrammed metabolism is linked to metastases[220].

A problem related to targeting metabolic reprogramming in brain metastatic cells, is that normal brain tissue utilizes the similar metabolic pathways, and off-target toxic effects can arise[91]. One promising candidate where this can be bypassed, is dichloroacetate, which obstructs pyruvate dehydrogenase kinase, and is well tolerated in both mice and humans. Dichloroacetate makes malignant cells with hyperpolarized mitochondria susceptible to apoptosis, and leave healthy cells with normal metabolism unaffected[221-223]. Dichloroacetate is a small molecule (150 kDa) that has been used in

the clinic for more than 30 years, and is relatively inexpensive in use. Michelakis et al. showed that dichloroacetate activates pyruvate dehydrogenase in mitochondria, thereby causing increased delivery of pyruvate. In this way, glucose oxidation was increased and brought the membrane potential back to homeostasis without influencing the healthy, surrounding cells. During this situation, ROS increased and apoptosis was commenced. Therefore, this represents a potential way of exploiting altered metabolic pathways in brain metastases[224].

Haq et al. showed that the melanocyte inducing transcription factor (MITF) peroxisome proliferator-activated receptor gamma coactivator 1-α (PGC1α), the master regulator of mitochondrial biogenesis, is upregulated following treatment with the BRAF inhibitor vemurafenib. The net result is elevated mitochondrial respiration[225]. This is an example of another acquired survival mechanism resulting from reprogrammed cell metabolism in melanoma cells, also in the context of treatment.

β-sitosterol is an example of another compound that is known to act on the mitochondria of tumour cells and promote apoptosis through the production of reactive oxygen species (ROS)[226,227]. β-sitosterol is the most abundant phytosterol, i.e. plant sterol; the analogue of animal cholesterol. It has a molecular weight of ~414.71 Da and crosses the intact BBB[228]. However, β-sitosterol is not used for treatment of cancer in the clinic as of today.

Fischer et al. showed that an inhibitor of oxidative phosphorylation, IACS-010759, improved the survival of mice with melanoma brain metastases resistant to MAPK inhibitors. They hypothesized that metabolic and immunologic differences between extracranial and intracranial melanoma metastases may contribute to resistance to targeted therapies[185].

Table 1. Selected systemic therapies targeting brain metastases in ≥ phase II clinical trials registered the last decade with more than ten enrolled patients.

Registered	Clinical trial ID	Phase	Therapy	Target	Status
2009	NCT00949702, BRIM-2[229]	II	Vemurafenib	BRAF	Completed (Clinical activity in previously treated $BRAF^{V600E}$ mutant metastases)
2009	NCT01006980 BRIM-3[230]	III	Vemurafenib or dacarbazine	BRAF or DNA	Completed (Vemurafenib contributed to prolonged patient survival)
2010	NCT01266967, BREAK-MB[159]	II	Dabrafenib	BRAF	Completed (Dabrafenib has clinical activity regardless of previous treatment)
2010	NCT01253564	II	RO5185426 (vemurafenib)	BRAF	Completed (Stopped due to progressing disease or serious adverse events)
2011	NCT01378975[231]	II	Vemurafenib	BRAF	Completed (Few patients completed the trial due to death)
2012	NCT01682083, COMBI-AD[161,232,233]	III	Dabrafenib + trametinib	BRAF + MEK1/2	Active, not recruiting (Treatment resulted in a lower risk of recurrence than placebo treatment)
2012	NCT01689519, coBRIM[114]	III	Vemurafenib + cobimetinib	BRAF + MEK1	Active, not recruiting (Adjuvant treatment improved survival, but increased toxicity)
2014	NCT02085070[234-236]	II	MK-3475 (Pembrolizumab)	PD-1	Active, not recruiting
2014	NCT02308020	II	Abemaciclib (LY2835219)	CDK4/6	Active, not recruiting
2014	NCT02039947, COMBI-MB[237]	II	Dabrafenib + trametinib	BRAF + MEK1/2	Completed (Short duration of response, but safe)
2015	NCT02460068, NIBIT-M2	III	Fotemustine + ipilimumab + nivolumab	Chemotherapy + CTLA-4 + PD-1	Recruiting
2015	NCT02374242, ABC	II	Nivolumab + ipilimumab	PD-1 + CTLA-4	Active, not recruiting
2015	NCT02452294, BUMPER	II	Buparlisib	PI3K	Unknown status
2015	NCT02537600, CONVERCE	II	Cobimetinib + Vemurafenib	MEK1 + BRAF	Active, not recruiting
2016	NCT02700763	NA	^{18}F-dabrafenib + PET	^{18}F-dabrafenib molecular imaging	Recruiting
2017	NCT03175432, BEAT-MBM	II	Bevacizumab + atezolizumab	VEGF + PD-L1	Recruiting
2019	NCT03911869, POLARIS	II	Encorafenib + binimetinib	BRAF + MEK1/2	Recruiting
2018	NCT03430947, RadioCoBRIM	II	Vemurafenib + cobimetinig	MEK1	Recruiting
2018	NCT03520634	NA	^{18}F-PD-L1 PET imaging	Gain pharmacokinetic information on the tracer for patients treated with anti-PD-1.	Recruiting
2019	NCT03911869, POLARIS	II	Encorafenib + binimetinib	BRAF + MEK1/2	Recruiting

1.4.4.6 Concluding remarks on systemic therapies

The introduction of systemic therapies targeting molecular drivers, metabolism and immune checkpoints have revolutionized the treatment of brain metastates[120]. Although drugs such as vemurafenib and ipilimumab have their limitations, they have paved the way for further investigations of targeted therapies and immune modulators. Based on this, it is expected that major treatment improvements will originate from the evolution of current systemic therapy strategies[156]. Moreover, it has been argued that due to the properties of melanoma brain metastases, it is the perfect candidate for personalized medicine and that such an individual plan will significantly improve the outcome for this patient group as a whole[127]. Also, the current treatment group should be prioritized in clinical trials which can contribute to improved knowledge and subsequently better therapies, which has not always been the case in the past[43].

1.5 The role of apoptosis in tumours

Apoptosis is a mechanism where cells undergo programmed cell death. It plays an important role in cancer, not only after treatment as discussed above, but also during tumour development. During tumour growth there is an imbalance between normal cell proliferation and cell death (lack of signals for cells to undergo apoptosis)[238], as illustrated in the hallmarks of cancer[6,239]. A mechanism in which this often occurs is through downregulation of the tumour suppressor gene p53, which leads to increased cell proliferation and reduced levels of apoptosis[240-242].

Apoptosis is characterized by cell size reduction, membrane blebbing, nuclear degradation, chromatin condensation and chromosomal disruptions, mediated by one of two pathways; intrinsic or extrinsic[243], as summarized in Figure 7.

The external pathway involves cell membrane receptors and downstream effectors. The intrinsic pathway is mediated by the mitochondria involving a number of pro- and anti-apoptotic factors[244]. Bax, Bak, Bad, Bcl-Xs, Bid, Bik, Bim and Hrk are proteins belonging to the group promoting apoptosis, whereas Bcl-2, Bcl-X_L, Bcl-W, Bfl-1 and

Mcl-1 are examples of anti-apoptotic proteins. These function by inhibiting the release of cytochrome-c, a protein located in the inner mitochondrial membrane, while apoptotic proteins stimulate cytochrome-c release to inhibit apoptosis[245].

When cells undergo apoptosis, they are usually engulfed by macrophages or neighbouring cells upon phosphatidylserine signalling on the cell membrane. Thus, apoptotic cells are in contrast to necrotic cells quickly cleared from the tissue without inducing inflammation[5].

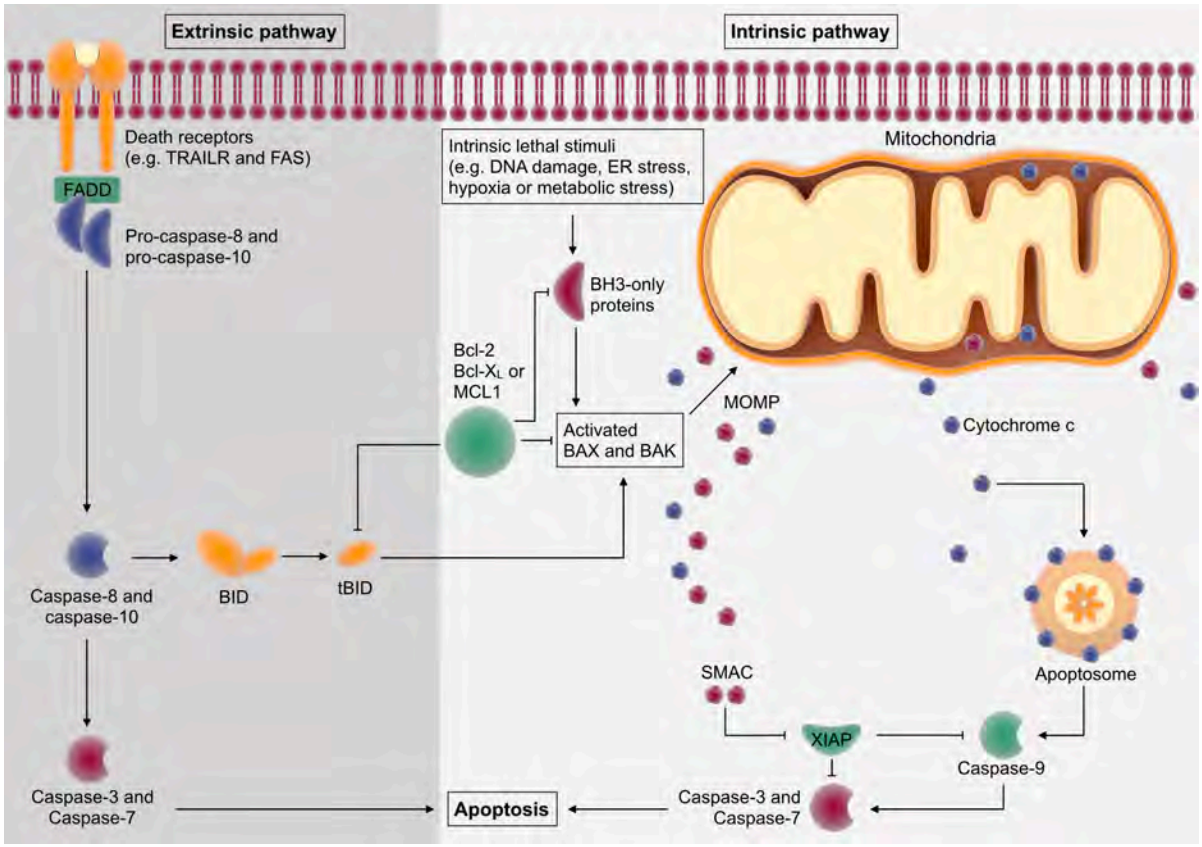

Figure 7: Illustration of the extrinsic and intrinsic apoptotic pathways. Upon extracellular signal, the cell is instructed to initiate apoptosis through receptor binding. Activation of fas-associated death domain (FADD) further activates pro-caspases-8 and -10, which further are matured into caspases-8 and -10. This also activates BID, Bax and Bak, the latter two represent a crossing point between the extrinsic and intrinsic apoptotic pathways. The activation causes mitochondrial outer membrane permeability (MOMP), which is essential for cytochrome c release into the cytoplasm. This promotes the formation of a protein complex refered to as the apoptosome, which matures pro-caspase-9, further advancing apoptosis by amongst others activating caspases-3 and -7, which initiates DNA destruction. Modified from BiologyDictionary.net, made using symbols from www.somersault1824.com.

The objective of many systemic therapies is to induce cell death of the tumour cells, preferentially without harming adjacent, healthy cells and tissue. Whether killing tumour cells directly by administering chemotherapy or manipulating cells to undergo apoptosis by targeted therapies is the optimal approach, is debated[246,247]. Previous attempts at generating a mouse model deficient of caspases for this purpose have been unsuccessful since lack of caspase 8 is deadly. Thus, the role of apoptosis as a stress response secondary to chemotherapy is not fully understood[248]. Although apoptosis of tumour cells is an attractive feature induced by many systemic therapies, the importance of apoptosis versus direct toxic effects is not known[246].

1.6 The blood-brain barrier (BBB)

A complicating factor that challenges the systemic treatment of not only brain metastases, but essentially all diseases in the brain, is the BBB. This is a multicellular network that primarily consists of a vascular endothelial monolayer connected by tight junctions, the basement membrane, supporting pericytes and encircling astrocytic end-feet, as illustrated in Figure 8. This complex configuration makes the BBB a physical barrier that hampers the access of nearly all compounds into the brain, in order to protect the brain tissue[249].

Circulating compounds can enter into the healthy brain by passive diffusion or active transport[250]. When substances are transported into the brain between the endothelial cells, the passage is paracellular, which is the case for ions and solutes that depend on a concentration gradient. If the passage occurs through the cells, this is referred to as transcellular. This usually takes place with passive diffusion upon stimuli of specific receptors. For instance, many proteins and peptides rely on the endothelial cell membrane receptor GLUT-1 (Figure 9E).

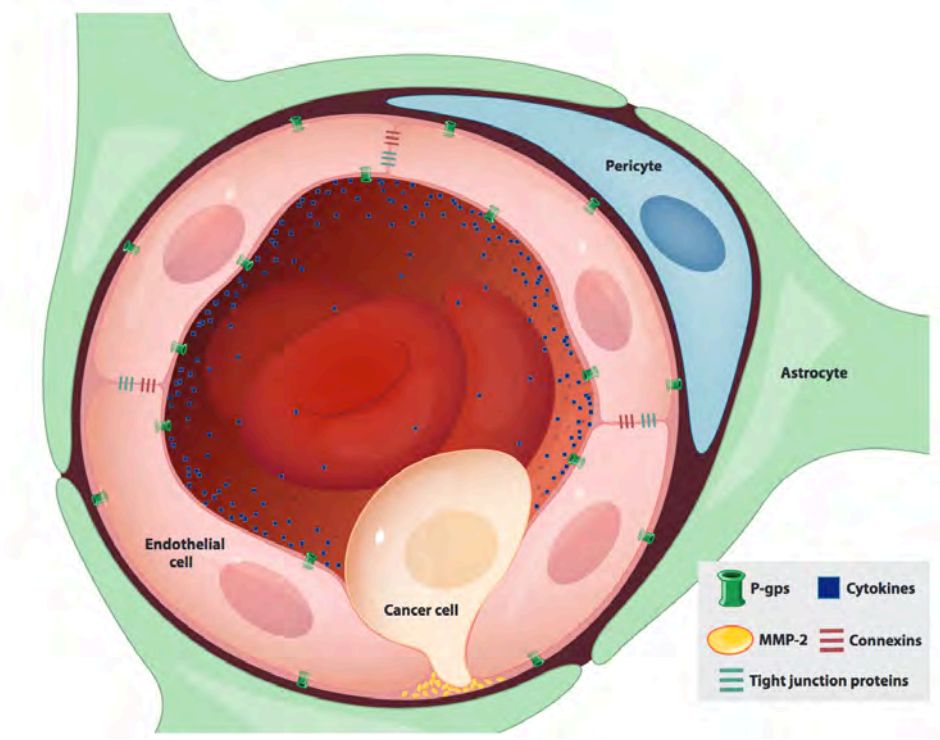

Figure 8: **A cross-section of the components of the neurovascular unit in the BBB involved in haematogenous metastatic spread**. Cytokines secreted in the neurovascular area favour adhesion of the spreading tumour cell, which will extravasate through the endothelial monolayer and into the brain. The presence of the physical barrier in itself as well as certain proteins, such as for instance P-glycoprotein (P-gp), hampers the delivery of systemic therapies as described previously. Reproduced from Glitza Oliva et al., 2018[43]. Reprinted with permission from Oxford University Press.

Some compounds can also induce invaginations of the endothelial plasma membrane, and subsequently form an intracellular membrane-bound vesicle and enter the brain by for instance transcytosis (Figure 9E and F)[251]. However, as a general rule, all molecules larger than 400–500 Da and with a greater quantity than 8–10 hydrogen bonds are unable to enter the brain through the BBB. In other words, 100% of large molecule drugs and 98% of small molecule drugs are precluded from entering[252].

A number of strategies to bypass the BBB for improved drug delivery in a non-permanent way has been reported previously. One of the earliest attempts were carried out by Rapoport et al. already in 1972[253], involving the use of osmotic permeabilization of the brain. Also, several successful preclinical attempts have been conducted using focused ultrasound and microbubble contrast agents[254-256]. Cao et al. reported on the use of radiotherapy for opening the BBB and the blood-tumour barrier (BTB)[257].

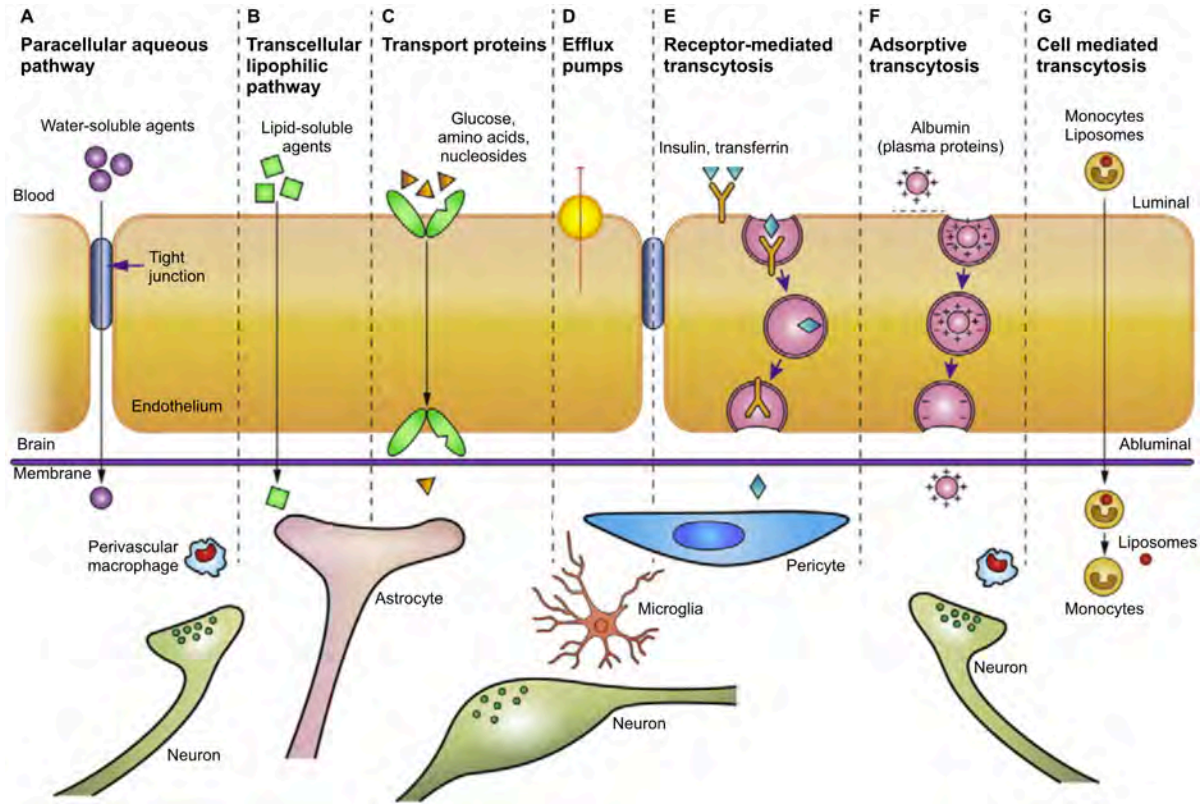

Figure 9: Different transport routes and mechanisms across the BBB. A through D represent typical transport paths for molecules needed to maintain brain homeostasis. The transcytosis pathways illustrated in E-G are examples of routes that can be used for drug-delivery by conjugating the compounds to for instance insulin, transferrin, albumin or immune cells. Adapted from Chen and Liu, 2012[258]. Reprinted with permission from Elsevier.

Other strategies have aimed to circumvent the BBB rather than directly disrupting parts of its constituents, such as viral-mediated or liposomal delivery[259,260], carrier molecules[261] and polymer wafers[262]. It is also possible to use convection-enhanced delivery to increase the diffusion and improve the dissemination of drugs[263]. These strategies have both strengths and limitations, and some are associated with serious side effects. However, more than one clinical trial have failed to meet the intended aim to permeabilize the BBB for improved drug delivery[264]. Thus, new methods to improve drug delivery to brain metastases are needed.

Different nanoplatforms have been used previously to ease the delivery of large drugs into the brain. Many represent hybrid theranostic systems, i.e. they combine diagnostic

and therapeutic purposes. Such nanoparticles or -probes are usually multicomponent particles composed of either organic or inorganic materials[265].

The nano-constructs can enter the brain by permeabilizing tight junction proteins between endothelial cells, or cause a local toxic effect resulting in increased permeability in the exposed area, by endocytosis or transcytosis, or a combination thereof[251]. Hamilton et al. showed in 2015 that nanoparticles coated with the tumour-penetrating peptide iRDG reduced the brain metastatic burden of breast cancer in mice[266]. Patil et al. engineered polymeric nanoimaging agents conjugated to either a gadolinium-based contrast agent or molecular signalling pathway inhibitors. These constructs were able to cross the BBB and targeted tumour cells for efficient imaging as well as treatment[267].

In addition to the physical properties of the BBB, generating a passive barrier, a number of active drug efflux proteins are located on the luminal side of brain capillary endothelial cells (Figure 9D). These efflux proteins belong to the ATP-binding cassette (ABC) transporters, including P-gp, multidrug-resistance protein (MRP2) and breast cancer resistance protein (BCRP). These and others are expressed on endothelial cells, and collectively contribute to challenging the efflux of many drugs. Thus, the BBB represents both a passive and active fence between the circulation and the brain[268]. The brain is consequently often considered to be a sanctuary site for metastatic growth[269].

In tumour tissue, the barrier acquires a heterogenous permeability. In micro-metastases, i.e. in metastatic lesions smaller than ~1 mm^3, the BTB is usually impermeable. For this reason, micro-metastases are not taking up contrast agents, and are radiographically occult[270]. Metastases of considerable sizes usually have a heterogenous BTB with areas of degradation[271]. These lesions are often visible by contrast enhanced MRI, whereas micro-metastases are not[272]. A challenge is thus to detect the brain metastases early to initiate treatment before the disease becomes too advanced.

2. Aim and objectives

The overall aim of this thesis was to improve the molecular understanding of metastatic melanoma, primarily to the brain, and subsequently to implement this towards the development of new treatment principles. Listed below are the specific objectives of each paper.

Paper I: To evaluate the properties of a glycogen nanoprobe on metastatic melanoma cells. The main aim was to provide data which could establish the nanoprobe as a «theranostics» platform in future melanoma brain metastases research.

Paper II: To improve the mechanistic understanding of the synthetic peptide K16ApoE, and further to evaluate its BBB permeabilizing capacity for increased drug-delivery and improved treatment efficacy.

Paper III: To identify candidate drugs specific for melanoma brain metastases, and establish their potential, clinical efficacy.

Paper IV: To evaluate the combined effect of MEK and PI3K inhibition in metastatic melanoma cells as a proof-of-concept for later use in the treatment of melanoma brain metastases.

3. Methodological considerations

3.1 Cell culture

Cell culture represents an easy, inexpensive and useful method in the field of biological research, and despite methodological limitations associated with the technique, cell culture has provided valuable knowledge in tumour biology. Despite the lack of a straight forward translation of results obtained from cell cultures to an *in vivo* setting, it is usually the starting point when testing a new hypothesis. Cell culture was used for varying purposes throughout **Papers I-IV** in this thesis.

The H1 cell line is derived from a melanoma brain metastasis and was used in all four papers in this thesis. It harbours the $BRAF^{V600E}$ mutation, which is representative for melanoma. Further, H1 cells carry MITF amplification and loss of PTEN and CDKN2A/B. The melanoma brain metastatic H2 and H10 cells are also $BRAF^{V600E}$ mutated, whereas H3 cells carry a $BRAF^{L577F}$ mutation, which has not been described in the literature previously. Melmet 1 and Melmet 5 cells are derived from metastatic melanoma in subcutaneous and lymph tissue, respectively, and both carry the $BRAF^{V600E}$ mutation. We also used a range of different endothelial cell lines with the aim to mimic the endothelial monolayer at the BBB (RBE4, MDCK, MDCK II, hCMEC/D3). In addition, SC-1800 astrocytes were used as part of the *in vitro* BBB model system. The primary epidermal melanocytes HEMa cells were used in the extracellular flux analysis as a basis for comparison to the malignant H1_DL2 cells.

3.2 Animal models

To be able to develop new treatment strategies for brain metastases, preclinical animal models are a prerequisite. Models need to demonstrate reproducibility, in which tumour cells repeatedly grow into metastatic lesions after inoculation. Tumour cell lines or

biopsies are usually injected or inoculated into either the same organ they came from originally, i.e. orthotopic, or into a different site, i.e. ectopic. The material may be derived from either human (xenograft) or rodent (syngeneic) tumour tissue, and xenograft models require the use of immunodeficient animals[273].

Throughout this thesis, we have used human-derived H1_DL2 cells in non-obese severe compromised immunodeficiency (NOD/SCID) mice as a model system for brain metastases. NOD/SCID mice carry a mutation in the Prkdc gene, which encodes a protein kinase needed for DNA repair and sealing of double-stranded DNA breaks that may take place upon recombination of T-cell receptor and immunoglobulin genes. In the absence of the Prkdc protein, these cannot rearrange, which culminates in a B- and T-cell deficient genotype. This makes the NOD/SCID mice more immunecompromised than for instance nude mice[274].

The model used in **Papers II** and **III** has been showed to be reproducible and predictive, and is based on intracardial injection of H1_DL2 cells into NOD/SCID mice[275].

The animal models used in brain metastasis research do not fully reflect the clinical picture seen in patients with brain metastases. Genetically engineered mouse models (GEMMs) can provide a more complete model system, e.g. by including oncogene mutations for metastasis modelling. However, such models have not yet been extensively used in brain metastases research[273]. Rarely, spontaneous melanomas can occur in rodents, and one well known example of this was the precursor of the B16 cell lines, frequently used in brain metastasis models over many years[276].

In 2009 Kienast et al. reported that they were able to track single metastasizing cells in real-time using cranial windows[277]. In this manner, they were able to study the dissemination steps of the primary tumour tissue over time, instead of one or two cross sectional measurements during metastatic development. However, in their experiments, the long-term imaging of disseminating tumour cells was only possible for a proportion of all the injected mice, and the experimental layout is advanced and requires expensive equipment. Thus, new experimental models to mimic the early

stages of the metastatic cascade are needed to complement the current knowledge on metastatic disease.

Despite the reproducible properties of many of these animal models, they usually mirror only parts of the metastatic process and they all have significant limitations compared to human tumours; thus, the usefulness of animal models are debated[273]. Moreover, some cancer types show dormancy with disease-free intervals before late recurrences occur years after the primary diagnosis and treatment. Also, whether metastatic spread is an early or late event of malignancy is not fully understood[273]. Together, these aspects of the metastatic dissemination are difficult to model.

In both **Paper I** and **Paper IV** we used a subcutaneous tumour model in NOD/SCID mice as a proof-of-principle experiment on metastatic melanoma. In **Paper IV**, this was done as the MEK inhibitor trametinib does not to cross an intact BBB[278]. To deliver trametinib across an intact BBB, permeabilizing agents need to be employed.

All experiments were approved by the National Research Authority (#8093), the Regional Ethical Committee (#013.09) and the Norwegian Directorate of Health (#9634). We acquired written consent from patients before tumour tissue was collected.

The mice were bred and maintained in animal facilities at the University of Bergen accredited by the Association for Assessment and Accreditation of Laboratory Animal Care International.

3.3 Ultrasound-guided intracardial tumour injections

The ectopic xenograft H1_DL2 model is illustrated in Figure 10. To assure that we are injecting the tumour cells into the left ventricle, we use ultrasound-guidance with a cross-sectional overview of the heart (Figure 10B). Given accurate injections, the tumour take in this experimental model is 100% and a reproducible number of metastases can be achieved by injecting the same number of cells in a similar passage number range.

Bioluminescence imaging can be carried out within the next couple of days to confirm successful injections. At four or six weeks after tumour cell injections, we quantitatively assess the brain metastatic burden using T_2 and contrast enhanced T_1 weighted MRI.

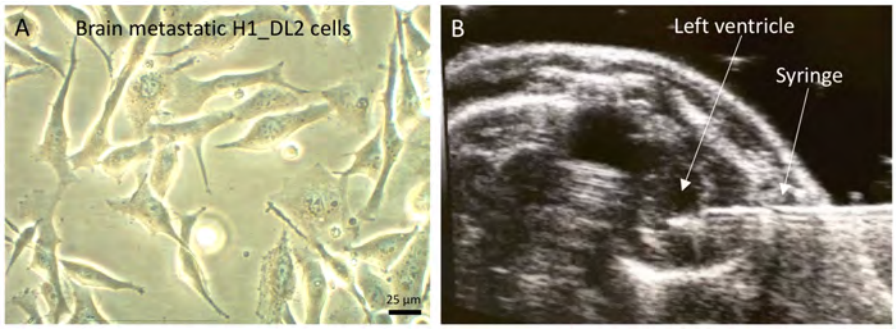

Figure 10: Ultrasound guided intracardial tumour cell injections. A: H1_DL2 cells. B: Axial ultrasound frame of the left cardiac ventricle and the insulin syringe while injecting tumour cells.

The experimental layout allows us to study various treatment strategies in a situation where the tumour cells are already present in the circulation and are starting to extravasate and colonize the brain. For instance, we have employed it to study the *in vivo* efficacy of β-sitosterol, which is a compound that is able to cross the BBB (**Paper III**) and combining drugs that do not readily cross an intact BBB in combination with K16ApoE, a BBB permeabilizing peptide (**Paper II**). For such treatment efficacy purposes, the model is highly relevant and useful.

3.4 DCE-MRI

DCE-MRI is an advanced MRI technique in which a series of images are acquired prior to, during and after a bolus injection of a traceable contrast agent. This technique can be readily used to study the temporary effects of contrast agents by means of relaxation rates in a quantitative manner. Thus, when using DCE-MRI, we can measure the perfusion of contrast agent within the brain tissue, and gain quantitative information on BBB permeabilization. In **Paper II**, the DCE-MRI data are based on calculations

using the two-compartment model proposed by Tofts et al[279]. In this model, a few simplifications are made. First, it is assumed that the contrast agent used is evenly distributed in the circulatory system at the time of injection and secondly, that there is a gradual leakage into the extravascular, extracellular space (EES) after the initial distribution (Figure 11).

The diffusion of compounds from the blood circulatory system to the EES is described by the transfer constant, K^{trans}, whereas the reverse leakage is described by K_{ep} (Figure 12A). If the BBB is completely closed, as is usually the case during normal conditions, the K^{trans} should be 0. By interrupting the BBB with K16ApoE or other methods for temporary permeabilization, the K^{trans} will increase[279]. Since the BBB commonly is degraded and has a heterogenous permeability in brain metastases[272], higher K^{trans} values are often seen here.

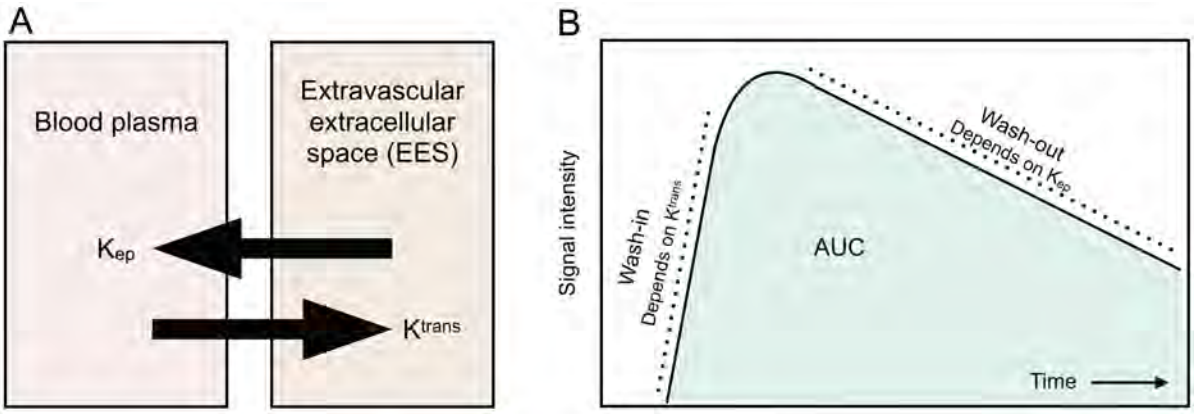

Figure 11: The principles of Tofts two-compartment model. The connection between the two parameters K^{trans} and K_{ep} in Tofts two-compartment model. K^{trans} is the transfer constant that describes the flow of a traceable agent from blood plasma into EES, whereas K_{ep} depicts the reverse transport (A). The area under curve (AUC) parameter depends on the steepness of the wash-in curve, i.e. how disrupted the BBB is and how much contrast agent is thus washed into EES, and the wash-out curve.

Also, area under the curve (AUC) can be calculated from DCE-MRI data, which says something about the accumulation of contrast agent over time. The principles for both parameters are summarized in Figure 11. In addition to being dependent on the permeability of the BBB, the rate of diffusion is also dependent on the blood flow to the tissue as well as the surface area of the blood vessels. In the case of a global BBB

permeabilization, one can expect immediate contrast agent accumulation in the brain parenchyma during the cardiac cycle[279].

In our DCE-MRI experiments, we injected K16ApoE at different time intervals before the bolus injection of Omniscan, a Gadolinium-based agent chelated to DTPA-BMA. For the perfusion imaging, the middle slice in the coronal oriented slice package was selected. First, six fast low-angle shot (FLASH) sequences were acquired with flip angles increasing from 5 to 30 degrees. FLASH images, or other ultrafast sequences, are frequently used to quantify the amount of contrast agent within a tissue of interest. The reason is that these have a high temporal resolution, adequate T_1 sensitivity and volume coverage, as well as the ability to measure the arterial input function (AIF). AIFs are used to correct for the heterogenous temporal distribution of contrast agent that arises due to delays from passage through the cardiac system. The shape of the measured contrast agent concentration in tissue depends on the AIF. The easiest way to identify AIFs is to place a region of interest over an artery and then apply the obtained curve shape to all voxels in the slice, referred to as global AIF. Instead, we identified local AIFs from the neck muscle close to the tissue voxels of question for a more accurate AIF interrogation[280]. 900 repetitions of the FLASH sequence were then acquired, and the contrast agent was injected 15 seconds after initiation of the sequence. These dynamic T_1 data were then used to gain information on the course of the contrast agent during 15 minutes of scan time (Figure 12).

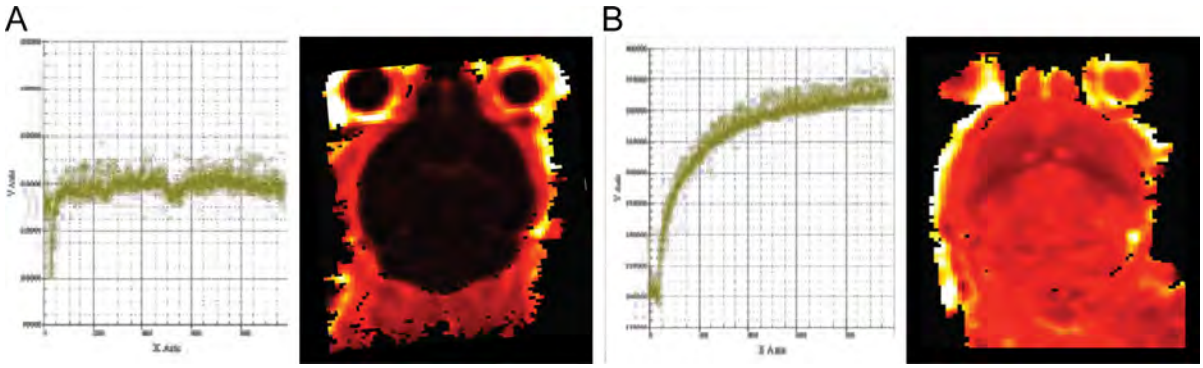

Figure 12: Examples of temporal signal intensity curves and associated parametric AUC images. A: A healthy NOD/SCID mouse injected with 9 mg/mL saline 10 minutes prior to DCE-MRI scans. B: A healthy NOD/SCID mouse injected with 200 µg K16ApoE 10 minutes prior to DCE-MRI scans.

Although compartment models in DCE-MRI have been widely used both in preclinical settings and in the clinic, it suffers from weaknesses due to their simplicity, as mentioned above. Also, they assume a rapid contrast agent transit, followed by an even distribution throughout the compartment upon contrast agent arrival. In other words, equivalent models consider the temporal, but not spatial distribution[281]. For this purpose more sophisticated models have been developed, such as for instance the model proposed by Johnson and Wilson[282].

3.5 Extracellular flux analysis

Preliminary results in **Paper III** raised questions as to whether β-sitosterol interfers with basic cellular functions such as metabolism and apoptosis. And, since it is already known that mitochondrial respiration is altered in melanoma cells, this topic was explored using an extracellular flux analyzer. We treated healthy melanocytes (HEMa) and metastatic melanoma cells (H1_DL2) with 50 μM β-sitosterol or 0.05% DMSO (negative control) for 24 hours and acquired real-time metabolic information from live cells in culture.

Extracellular flux experiments, also known as a «seahorse assay», was carried out to determine the mitochondrial and glycolytic functions of the cells during induced states of stress. In both experiments, the basal respiration was determined initially before modulators of cellular respiration that target specific components of the electron transport chain were added.

In the mitochondrial stress test assay, essential variables of mitochondrial activity were evaluated by measuring the oxygen consumption rate (OCR) of cells upon serial-addition of four modulators: Oligomycin, FCCP, rotenone and antimycin A.

After initial measurements of basal mithochondrial respiration for 20 minutes, the first modulator, oligomycin, was added. Oligomycin targets and inhibits the enzyme ATP synthase in mitochondrial complex V in the electron transport chain (ETC). The net

result is a reduction in OCR corresponding to the amount of basal respiration used to produce ATP. Thus, the next segment on the graph gives information about proton leak. The presence of proton leak can indicate mitochondrial damage or activation of an alternative regulatory mechanism to produce ATP.

Following the oligomycin, FCCP is added, which targets the inner mitochondrial membrane and stimulates the respiration to run at maximum capacity. The OCR thus increases.

Rotenone and antimycin A are the last two modulators and can be added simultaneously or sequentially. Rotenone and antimycin A targets complex I and III, respectively. This terminates mitochondrial respiration and indicates non-mitochondrial respiration[283]. See Figure 13A.

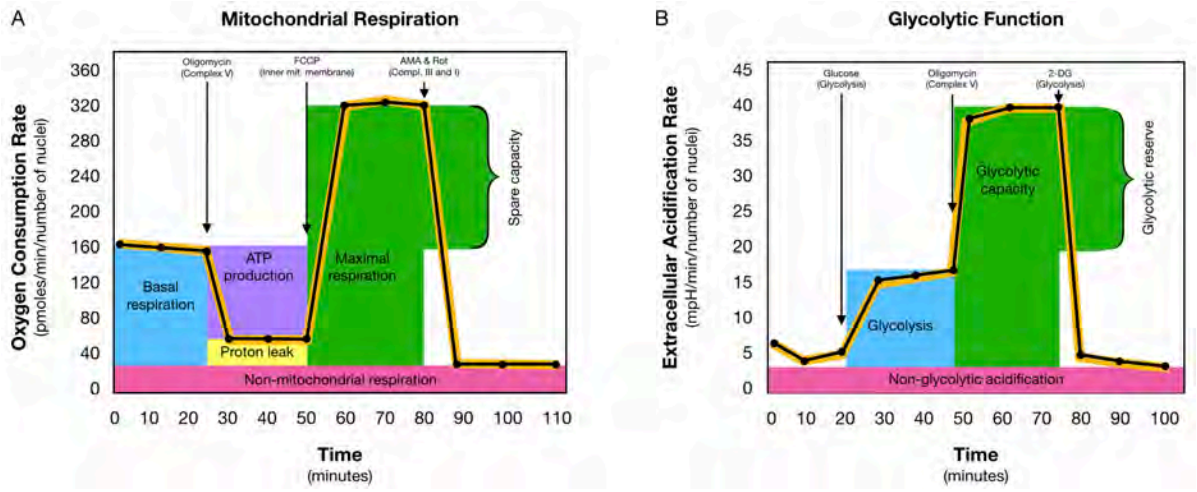

Figure 13: An illustration of extracellular flux analysis of key mitochondrial modulators. A: Mitochondrial respiration of cells upon serial-addition of four mitochondrial modulators. Initially, the basal respiration is measured, before oligomycin is added to address proton leak, FCCP to study maximum respiratory capacity and rotenone and antimycin A to study mitochondrial complex I and III dependency, respectively. B: Glycolytic activity of cells upon serial-addition of three modulators. The basal respiration is measured initially, before glucose is added to determine basal glycolysis. Then, oligomycin is added also here, to study glycolytic capacity and finally 2-DG to determine glycolysis dependency. Modified from Agilent Technologies[283].

Glycolytic respiration was measured as the extracellular acidification rate (ECAR). Three different modulators of glycolytic activity were serial-added as the ECAR was monitored; glucose, oligomycin and 2-deoxyglucose (2-DG).

Glucose targets and fuels glycolytic activity and the readout gives information on the basal glycolysis of the cells. Oligomycin is then added to inhibit ATP production in complex V, similarly as in the mitochondrial stress experiments described above and in Figure 13A. This increases the ECAR, as the metabolim of the cells is shifted towards higher glycolytic activity, and the capacity is evaluated. By adding 2-DG, a competitive inhibitor of glucose, this is bound to glucose-6-phosphate, the first component of the glycolytic cycle and ECAR decreases[283]. See Figure 13B. Throughout our experiments we were able to identify mitochondrial complex I as a likely target of β-sitosterol on metatatic melanoma cells.

There are however, a few disadvantages with the extracellular flux analysis. Despite the high amount of information provided on mitochondrial respiration with a relatively low number of cells required, the assay is quite expensive, especially when taken into consideration the initial optimization steps. Furthermore, the compound in question during the experiment may interfere with the ETC, necessitating further optimization. The injected compounds can also interfere with the sensors in the equipment and subsequently give erroneous results[284].

4. Results and discussion

Paper I – A novel nanoprobe for multimodal imaging is effectively incorporated into human melanoma metastatic cell lines. In **Paper I**, we had access to a newly developed nanoprobe for multimodal imaging consisting of a backbone of glycogen. In its current configuration, it was conjugated to chelated (DOTA) Gadolinium MRI contrast agent and a red fluorescent marker (dyomics-615-NHS). We carried out a range of different *in vitro* assays to evaluate how labelling affected three different metastatic melanoma cell lines.

Initially, we studied cellular proliferation rate and cell death of melanoma cells upon labelling with the nanoprobe, and found no difference in viability compared to unlabelled cells. This indicated that the glycogen nanoprobe did not alter basic cellular functions. Furthermore, we also found that the migratory capacity of the cells was unaffected by nanoprobe labelling. We then studied the intracellular location of the nanoprobe using confocal microscopy, and found an accumulation of the nanoprobe in lysosomes, in line with lysosomal degradation and indicative of nanoprobe clearance from the cells. We also verified this by imaging the cells over a time period of five days, after which we found an abolished fluorescence signal after labelling with the nanoprobe.

Metastatic melanoma cells pre-labelled with the nanoprobe in culture flasks were trypsinized and casted in agar in Eppendorf tubes and subsequently analysed by relaxometry measurements on the MRI. During these experiments, we found an association between measured T_1 relaxation and age of the prepared phantoms. Thus, all phantoms were prepared within the same time frame to minimize factors producing divergent results. Despite this, we still found differences in T_1 relaxation between different cell lines. For Melmet 1 cells, we were able to detect a lower number of labelled cells compared to the other cells. This indicates biological internalization differences between cells and that more nanoprobe is accumulated in some cell lines.

Finally, we carried out a proof-of-concept experiment on two NOD/SCID mice with subcutaneous tumours of cells from brain metastatic origin. We injected either Omniscan, a clinically accepted gadolinium-based contrast agent, or the glycogen nanoprobe intravenously and performed T_1 weighted MRI before and after contrast agent administration. We found that the contrast enhancing effect was comparable between the two agents. These findings suggest that the nanoprobe is able to accumulate in tumour tissue, likely as a result of the enhanced permeability and retention (EPR) effect present in many tumours.

Although of brain metastatic origin, we carried out the proof-of-concept experiment on subcutaneous tumours. Despite drug uptake after systemic injections, we have not evaluated BBB penetrance of the nanoprobe. Also, the molecular weight of the construct is currently unknown, further challenging the prediction of its penetrating abilities. It has previously been shown that a nanoparticle with a size of 10 nm was well distributed in brain tissue upon injection through the internal carotid artery. However, when corresponding nanoparticles with increased sizes were injected (50 or 100 nm), they were primarily observed near the blood vessels in immunofluorescence sections, and not in brain parenchyma. Thus, nanoparticle size might be indicative of its ability to cross the BBB[285].

Given BBB permeabilization, the nanoprobe has the potential to also carry therapeutic agents for delivery into brain metastatic lesions and thus be extended to a theranostic nanoprobe, which can be evaluated in future experiments.

Paper II – Improved drug delivery to brain metastasis by peptide-mediated permeabilization of the blood-brain barrier. In **Paper II**, our objective was to test the capacity of a synthetic peptide to permeabilize the BBB for increased drug delivery, with subsequent improvements in treatment efficacy. Initially, the BBB opening effect was quantified using DCE-MRI, and the toxicity profile of the peptide was evaluated on healthy NOD/SCID mice. Furthermore, we carried out a range of *in vitro* assays aiming to elucidate the mechanistic effects of the peptide on cells and tissue. Based on

flow cytometry, we confirmed the current view that K16ApoE promotes endocytosis in endothelial cells, but also that in high concentrations, i.e. >IC_{50}, the peptide induces nonspecific disruptions of cell membranes in culture. Moreover, we used *in vitro* BBB models, and found that both a mono- and a co-layer of endothelial cells and astrocytes restored the integrity, given time for the cells to recover after 45 minutes of peptide exposure. In an *in vivo* treatment study on NOD/SCID mice with brain metastases, K16ApoE increased the delivery of a molecularly targeted compound, that otherwise do not cross the intact BBB, resulting in a decreased tumour burden in the mice. Thus, the peptide has a translational value in a drug delivery setting.

As immune checkpoint inhibitors are sometimes considered more clinically relevant than molecular targeting therapies, we also wanted to check whether K16ApoE could facilitate the delivery of compounds in the size range of such compounds (nivolumab has a size of approximately 143 kDa and ipilimumab around 148 kDa[286]). It should be emphasized that size is not the only crucial factor regarding BBB permeability. However, it is still of major concern, and the *in vivo* positron emission tomography/computer tomography (PET/CT) scans colleting dynamic data clearly show that the peptide induced a BBB permeabilizing effect, which was sufficient to deliver IgG antibodies into the brain. Thus, the use of K16ApoE could also be of interest when delivering immune checkpoint inhibitors.

Although not included in **Paper II**, we started looking into the integrity of the tight junction proteins occludin, claudins and zonula occludens (ZO) after exposing normal human endothelial cells to the peptide. There was a tendency of slight reduction in some of the tight junction proteins at increasing peptide concentrations, however at varying degrees and with varying results between cell lines. Some of our findings corresponded with previous work, however, the significance of these data was somewhat obscure. Nevertheless, it seems that in addition to the endocytic uptake as seen by flow cytometry, there is a degree of paracellular transport as well as a result of loss in integrity of tight junction proteins.

As briefly touched upon in the introduction of **Paper II**, there are several methods to transiently permeabilize the BBB for treatment delivery purposes. Peptides represent an attractive method of BBB permeabilization which can be modified to possess a wide range of different properties. However, the mechanisms are still not fully understood for the peptides described in the literature today[287]. Currently, there are ongoing clinical trials aiming to study the effect of focused ultrasound together with an intravenous ultrasound contrast agent (NCT02343991 as an example). The functionality of this method has thus not been fully elucidated[288], however, the technique is targeted and focal, and scattered BBB permeabilizatin is thus avoided. Also, the effect is similarly to the K16ApoE approach, reversible and non-invasive[289]. Nevertheless, further experiments to evaluate toxicity are needed before K16ApoE can be utilized clinically.

Paper III – Inhibition of mitochondrial respiration prevents BRAF-mutant melanoma brain metastasis. In **Paper III**, it was sought to identify repurposeable compounds with therapeutic activity against BRAF mutated brain metastases. mRNA sequencing of metastatic cells harvested from brains, adrenals, ovaries and bone of NOD/SCID mice was carried out, corresponding gene lists were produced, and differentially expressed genes (brains versus adrenals, adrenals and bone) were determined, generating a list of 54 upregulated and 54 downregulated genes. A bioinformatic analysis (Connectivity Map) was then carried out to identify small molecules that would induce an opposing gene signature. These were then hypothesized to have an inhibitory effect on the gene signature identified. The top ten candidate drugs were then evaluated on brain metastases cells *in vitro*, before the three most promising candidates were tested on mice with brain metastases. The most promising drug from this study was β-sitosterol, which was validated in an extensive *in vivo* treatment study on mice with brain metastases, as well as in a subcutaneous melanoma model. Inhibitory effects of β-sitosterol on brain metastases was demonstrated. When β-sitosterol was given in combination with the BRAF inhibitor PLX4720, the treatment resistance of PLX4720 was inhibited.

To study the putative mechanisms behind these finding, we evaluated whether β-sitosterol interfered with the metabolism of the cells. For this purpose, we used extracellular flux analysis, as described in chapter 3.5 on healthy melanocytes, HEMa, and brain metastatic melanoma cells, H1_DL2 treated with 50 μM β-sitosterol or vehicle (0.05% DMSO). Inhibiting the ATP synthase (oligomycin) had a similar effect both for vehicle and β-sitosterol treated cells, across both cell lines. This indicates that β-sitosterol does not induce proton-leakage (or uncoupling) through the inner mitochondrial membrane. Inhibiting complex I showed that most of the respiratory activity was linked to this complex in H1_DL2 cells, and indicates that β-sitosterol targets mitochondrial complex I in the tumour cells. The basal glycolysis respiration and glycolytic capacity was not affected by β-sitosterol in either of the cell lines or treatment groups. Simultaneously with the reduced mitochondrial respiration through complex I inhibition, β-sitosterol also induced apoptosis by activating reactive oxygen species. This is in line with previous research showing that increased mitochondrial oxidative capacity mediates resistance to MAPK targeting therapeutic compounds and can also prevent apoptosis[225,290,291].

Considering that acquired resistance is a common problem with such drugs, our findings suggest that it should be tested in clinical trials combined with adjuvant β-sitosterol early in metastatic development or in patients at risk of developing brain metastases.

Paper IV – Dual targeting of the MAPK and PI3K signalling pathways in the treatment of metastatic melanoma. It is not uncommon that the MAPK and the PI3K signalling pathways are dysregulated in melanoma. These pathways are often intertwined in tumour development by compensating feedback loops, and the development of treatment resistance in one or the other pathway has been observed. However, it has also been shown that targeting the PI3K and MAPK signalling pathways simultaneously can eliminate treatment resistance[292]. In **Paper IV**, we

therefore sought to target these two pathways simultaneously, as we hypothesized that this could abrogate resistance mechanisms.

Three clinical trials have been registered, aiming to treat brain metastases with buparlisib: The STAR Cape+BKM120 trial (NCT02000882) is a phase II with ten enrolled patients who were treated with buparlisib in combination with capecitabine (a chemotherapy). The BUMPER trial (NCT02452294) sought to treat $BRAF^{WT}$ brain metastases from melanoma on patients with unoperable tumours and a final phase Ib/II trial combined buparlisib with trastuzumab and capecitabine in patients with HER2 overexpressing breast cancer with brain metastases (NCT01132664). None of these have today led to any sensible results due to restricting factors such as low patient participation. There are five clinical trials aiming to treat brain metastases by applying trametinib, four of them in combination with dabrafenib. Only one clinical trial has been registered aiming to combine buparlisib + trametinib on a variety of solid tumours (NCT01155453). However, no patients with metastases were enrolled in this study and the results were disappointing for patients with primary non-small cell lung cancer, which tends to metastasize to the brain[293].

Our results from *in vitro* experiments indicate that the combinatorial therapy outlined represents a promising approach for melanoma, since it appears that buparlisib and trametinib have varying efficacies dependent on the *in vitro* experiment in question. For instance, in pre-treated cells allowed to migrate towards a chemoattractant, there was a tendency that trametinib inhibited migration more than buparlisib in three of four cell lines. However, during constant exposure to drug, buparlisib showed a stronger inhibitory effect on the cells than trametinib. Cells pre-treated with drugs and seeded in low numbers had a low capacity of regrowth, indicative of a limited tumour cell reproduction potential after treatment.

With the limited research on the promising combinatorial approach of buparlisib + trametinib, we further sought to evaluate whether the combination could reduce tumour burden in a subcutaneous melanoma model of metastatic cells. Buparlisib is BBB penetrable, and it has even been found that the accumulation is higher in the brain than

in other organs. Thus, buparlisib is an attractive targeted therapy for treating intracranial tumours, however, the longitudinal plasma concentration is highly different in humans and mice and conclusions from preclinical experiments cannot be directly drawn to patients[294]. Furthermore, there have been cases with adverse events associated with PI3K inhibitors, also challenging the direct translation of the combinatorial approach into the clinic. More balanced PI3K inhibitors are thus under development[295]. Nevertheless, the we show that the principle of PI3K signalling pathway inhibition is a useful approach in melanoma serving as a proof-of-principle also for metastatic melanomas.

As mentioned above, trametinib has been extensively tested in clinical settings, but is associated with acquired resistance. Also, it does not readily cross the intact BBB, challenging the translation from metastatic melanoma cell lines to brain metastatic melanoma. We thus used a subcutaneous *in vivo* model to ensure drug distribution into the tumours upon peroral administrations. A drawback is accordingly that the intracranial activity has not been elucidated in our experiments.

Also, since subcutaneous tumours from H1_DL2 cells do not metastasize, all mice were sacrificed at end-point, and no survival curves were subsequently drawn from these experiments.

5. Conclusions

Paper I – A novel nanoprobe for multimodal imaging is effectively incorporated into human melanoma metastatic cell lines. The glycogen nanoprobe is effectively internalized by metastatic melanoma cells and visualization of the nanoprobe is enabled both *in vitro* and *in vivo*.

Paper II – Improved drug delivery to brain metastasis by peptide-mediated permeabilization of the blood-brain barrier. K16ApoE mediates a transient BBB permeabilization that increases drug delivery and decreases tumour burden in an animal model of brain metastases.

Paper III – Inhibition of mitochondrial respiration prevents BRAF-mutant melanoma brain metastasis. β-sitosterol can serve as adjuvant treatment to targeted therapies in the treatment of brain metastases.

Paper IV – Dual targeting of the MAPK and PI3K signalling pathways in the treatment of metastatic melanoma. Combining PI3K and MAPK signalling pathway inhibitors improves treatment of metastatic melanoma.

6. Future perspectives

The stated aim of this thesis was to contribute new knowledge to the current molecular understanding of metastatic dissemination and subsequently to implement this towards new therapeutic strategies. **Papers I-IV** represent different methods of tackling this particular task: Using nanomedicine for improved treatment of metastatic melanoma (**Paper I**), implementing a BBB permeabilizing peptide for improved drug-delivery into the brain (**Paper II**), treatment of brain metastases using brain permeable compounds (**Paper III**) and combinatorial targeted therapy aiming to treat metastatic melanoma cells as a proof-of-principle for brain metastases (**Paper IV**). Each strategy is associated with strengths and weaknesses and further work is needed to validate any of them towards a clinical context.

In the field of brain metastatic research, we are frequently faced with challenges related to the translational relevance of our results. Implementing promising preclinical results to use on patients requires years of work, which is time we do not posess taken into consideration the low survival times traditionally seen for patients with brain metastases. However, the field is progressing: The average survival times for patients with melanoma brain metastases increased substantially after the introduction of more targeted therapies. Within the field, it seems there is a collective anticipation that further improvements will come as targeted therapies with enhanced efficacy, less adverse events and improved BBB permeabilization; and that the treatment strategies will be more personalized. Regarding BBB permeabilization, as discussed in **Paper II**, there are ongoing clinical trials aiming to use techniques to improve the intracranial drug delivery to patients. Furthermore, the number of clinical trials using targeted therapies and immune checkpoint inhibitors as discussed in **Paper IV** (and summarized in Table 1) has markedly increased during the last years.

Regarding specific future prospects, we aim to study the usability of the glycogen nanoprobe from **Paper I** and the drug combination used in **Paper IV** in brain metastatic animal models, expecting this to provide useful information regarding their

translational potential. Multidisciplinary research on brain metastases is a prerequisite for the development of new treatment strategies that eventually will increase the survival times for all patients.

Source of data

1. Breasted JHe. The Edwin Smith Surgical Papyrus. *University of Chicago Press* 1930; **1**: 283-7.

2. Hajdu SI. A note from history: landmarks in history of cancer, part 1. *Cancer* 2011; **117**(5): 1097-102.

3. Lakhtakia R. A Brief History of Breast Cancer: Part I: Surgical domination reinvented. *Sultan Qaboos Univ Med J* 2014; **14**(2): e166-9.

4. Pemherton O. Observations on the History, Pathology and Treatment of Cancerous Diseases. *J Churchill* 1858.

5. Alberts B, Johnson A, Lewis J, Raff M, Roberts K, Walter P. Molecular Biology of the Cell. 5th ed. New York NY 10016, USA: Garland Science; 2008.

6. Hanahan D, Weinberg RA. Hallmarks of cancer: the next generation. *Cell* 2011; **144**(5): 646-74.

7. Hanahan D, Weinberg RA. The hallmarks of cancer. *Cell* 2000; **100**(1): 57-70.

8. Feitelson MA, Arzumanyan A, Kulathinal RJ, et al. Sustained proliferation in cancer: Mechanisms and novel therapeutic targets. *Semin Cancer Biol* 2015; **35 Suppl**: S25-S54.

9. Adams JM, Cory S. The Bcl-2 apoptotic switch in cancer development and therapy. *Oncogene* 2007; **26**(9): 1324-37.

10. Petrovic N. Targeting Angiogenesis in Cancer Treatments: Where do we Stand? *J Pharm Pharm Sci* 2016; **19**(2): 226-38.

11. Mareel MM, Bracke ME, Boghaert ER. Tumour invasion and metastasis: therapeutic implications? *Radiother Oncol* 1986; **6**(2): 135-42.

12. Burkhart DL, Sage J. Cellular mechanisms of tumour suppression by the retinoblastoma gene. *Nat Rev Cancer* 2008; **8**(9): 671-82.

13. Blasco MA. Telomeres and human disease: ageing, cancer and beyond. *Nat Rev Genet* 2005; **6**(8): 611-22.

14. Hsu CC, Tseng LM, Lee HC. Role of mitochondrial dysfunction in cancer progression. *Exp Biol Med (Maywood)* 2016; **241**(12): 1281-95.

15. Messerschmidt JL, Prendergast GC, Messerschmidt GL. How Cancers Escape Immune Destruction and Mechanisms of Action for the New Significantly Active Immune Therapies: Helping Nonimmunologists Decipher Recent Advances. *Oncologist* 2016; **21**(2): 233-43.

16. Tubbs A, Nussenzweig A. Endogenous DNA Damage as a Source of Genomic Instability in Cancer. *Cell* 2017; **168**(4): 644-56.

17. Pages F, Galon J, Dieu-Nosjean MC, Tartour E, Sautes-Fridman C, Fridman WH. Immune infiltration in human tumors: a prognostic factor that should not be ignored. *Oncogene* 2010; **29**(8): 1093-102.

18. Kumar V, Abbas A, Aster J. Robbins Basic Pathology. 9 ed. Canada: Elsevier Saunders; 2013.

19. Chapman PB, Hauschild A, Robert C, et al. Improved survival with vemurafenib in melanoma with BRAF V600E mutation. *N Engl J Med* 2011; **364**(26): 2507-16.

20. Falchook GS, Long GV, Kurzrock R, et al. Dabrafenib in patients with melanoma, untreated brain metastases, and other solid tumours: a phase 1 dose-escalation trial. *The Lancet* 2012; **379**(9829): 1893-901.

21. Cheung KJ, Ewald AJ. A collective route to metastasis: Seeding by tumor cell clusters. *Science* 2016; **352**(6282): 167-9.

22. Massague J, Obenauf AC. Metastatic colonization by circulating tumour cells. *Nature* 2016; **529**(7586): 298-306.

23. Hall A. The cytoskeleton and cancer. *Cancer Metastasis Rev* 2009; **28**(1-2): 5-14.

24. Kessenbrock K, Plaks V, Werb Z. Matrix metalloproteinases: regulators of the tumor microenvironment. *Cell* 2010; **141**(1): 52-67.

25. Giampieri S, Manning C, Hooper S, Jones L, Hill CS, Sahai E. Localized and reversible TGFbeta signalling switches breast cancer cells from cohesive to single cell motility. *Nat Cell Biol* 2009; **11**(11): 1287-96.

26. Yamaguchi H, Wyckoff J, Condeelis J. Cell migration in tumors. *Curr Opin Cell Biol* 2005; **17**(5): 559-64.

27. Varani J. Interaction of tumor cells with the extracellular matrix. *Revis Biol Celular* 1987; **12**: 1-113.

28. Roh-Johnson M, Bravo-Cordero JJ, Patsialou A, et al. Macrophage contact induces RhoA GTPase signaling to trigger tumor cell intravasation. *Oncogene* 2014; **33**(33): 4203-12.

29. Friedl P, Gilmour D. Collective cell migration in morphogenesis, regeneration and cancer. *Nat Rev Mol Cell Biol* 2009; **10**(7): 445-57.

30. Thiery JP, Acloque H, Huang RY, Nieto MA. Epithelial-mesenchymal transitions in development and disease. *Cell* 2009; **139**(5): 871-90.

31. Akhtar M, Haider A, Rashid S, Al-Nabet A. Paget's "Seed and Soil" Theory of Cancer Metastasis: An Idea Whose Time has Come. *Adv Anat Pathol* 2019; **26**(1): 69-74.

32. Wan L, Pantel K, Kang Y. Tumor metastasis: moving new biological insights into the clinic. *Nat Med* 2013; **19**(11): 1450-64.

33. MacKeil JL, Brzezinska P, Burke-Kleinman J, Craig AW, Nicol CJB, Maurice DH. A PKA/cdc42 Signaling Axis Restricts Angiogenic Sprouting by Regulating Podosome Rosette Biogenesis and Matrix Remodeling. *Sci Rep* 2019; **9**(1): 2385.

34. Kuczynski EA, Vermeulen PB, Pezzella F, Kerbel RS, Reynolds AR. Vessel co-option in cancer. *Nature Reviews Clinical Oncology* 2019.

35. Davidson CD, Wang WY, Zaimi I, Jayco DKP, Baker BM. Cell force-mediated matrix reorganization underlies multicellular network assembly. *Scientific Reports* 2019; **9**(1): 12.

36. Hendrix MJ, Seftor EA, Seftor RE, Chao JT, Chien DS, Chu YW. Tumor cell vascular mimicry: Novel targeting opportunity in melanoma. *Pharmacol Ther* 2016; **159**: 83-92.

37. Eichler AF, Chung E, Kodack DP, Loeffler JS, Fukumura D, Jain RK. The biology of brain metastases-translation to new therapies. *Nat Rev Clin Oncol* 2011; **8**(6): 344-56.

38. Scholz A, Harter PN, Cremer S, et al. Endothelial cell-derived angiopoietin-2 is a therapeutic target in treatment-naive and bevacizumab-resistant glioblastoma. *EMBO Mol Med* 2016; **8**(1): 39-57.

39. Holopainen T, Saharinen P, D'Amico G, et al. Effects of angiopoietin-2-blocking antibody on endothelial cell-cell junctions and lung metastasis. *J Natl Cancer Inst* 2012; **104**(6): 461-75.

40. Thomas M, Kienast Y, Scheuer W, et al. A novel angiopoietin-2 selective fully human antibody with potent anti-tumoral and anti-angiogenic efficacy and superior side effect profile compared to Pan-Angiopoietin-1/-2 inhibitors. *PLoS One* 2013; **8**(2): e54923.

41. Kienast Y, Klein C, Scheuer W, et al. Ang-2-VEGF-A CrossMab, a novel bispecific human IgG1 antibody blocking VEGF-A and Ang-2 functions simultaneously, mediates potent antitumor, antiangiogenic, and antimetastatic efficacy. *Clin Cancer Res* 2013; **19**(24): 6730-40.

42. Rigamonti N, Kadioglu E, Keklikoglou I, Wyser Rmili C, Leow CC, De Palma M. Role of angiopoietin-2 in adaptive tumor resistance to VEGF signaling blockade. *Cell Rep* 2014; **8**(3): 696-706.

43. Glitza Oliva IC, Schvartsman G, Tawbi H. Advances in the systemic treatment of melanoma brain metastases. *Ann Oncol* 2018; **29**(7): 1509-20.

44. Seyfried TN, Huysentruyt LC. On the origin of cancer metastasis. *Crit Rev Oncog* 2013; **18**(1-2): 43-73.

45. Guan X. Cancer metastases: challenges and opportunities. *Acta Pharm Sin B* 2015; **5**(5): 402-18.

46. Chaffer CL, Weinberg RA. A perspective on cancer cell metastasis. *Science* 2011; **331**(6024): 1559-64.

47. Valastyan S, Weinberg RA. Tumor metastasis: molecular insights and evolving paradigms. *Cell* 2011; **147**(2): 275-92.

48. Tsao MN, Xu W, Wong RKS, et al. Whole brain radiotherapy for the treatment of newly diagnosed multiple brain metastases. *Cochrane Database of Systematic Reviews* 2018.

49. Aoyama H, Shirato H, Tago M, et al. Stereotactic radiosurgery plus whole-brain radiation therapy vs stereotactic radiosurgery alone for treatment of brain metastases: a randomized controlled trial. *JAMA* 2006; **295**(21): 2483-91.

50. Kocher M, Soffietti R, Abacioglu U, et al. Adjuvant whole-brain radiotherapy versus observation after radiosurgery or surgical resection of one to three cerebral

metastases: results of the EORTC 22952-26001 study. *J Clin Oncol* 2011; **29**(2): 134-41.

51. Gallego Perez-Larraya J, Hildebrand J. Brain metastases. *Handb Clin Neurol* 2014; **121**: 1143-57.

52. Patel CK, Vemaraju R, Glasbey J, et al. Trends in peri-operative performance status following resection of high grade glioma and brain metastases: The impact on survival. *Clin Neurol Neurosurg* 2018; **164**: 67-71.

53. Cagney DN, Martin AM, Catalano PJ, et al. Incidence and prognosis of patients with brain metastases at diagnosis of systemic malignancy: a population-based study. *Neuro Oncol* 2017; **19**(11): 1511-21.

54. Loeffler JS, Wen PY. Epidemiology, clinical manifestations, and diagnosis of brain metastases. Wolters Kluwer: UpToDate, Inc., 2018.

55. Bollig-Fischer A, Michelhaugh S, Ali-Fehmi R, Mittal S. The molecular genomics of metastatic brain tumours. *OA Mol Oncol* 2013; **1**(1).

56. Norden AD, Wen PY, Kesari S. Brain metastases. *Curr Opin Neurol* 2005; **18**(6): 654-61.

57. Caffo O, Veccia A, Russo L, Galligioni E. Brain metastases from prostate cancer: an emerging clinical problem with implications for the future therapeutic scenario. *Future Oncol* 2012; **8**(12): 1585-95.

58. Wong J, Hird A, Kirou-Mauro A, Napolskikh J, Chow E. Quality of life in brain metastases radiation trials: a literature review. *Curr Oncol* 2008; **15**(5): 25-45.

59. Pruitt AA. Epidemiology, Treatment, and Complications of Central Nervous System Metastases. *Continuum (Minneap Minn)* 2017; **23**(6, Neuro-oncology): 1580-600.

60. Patchell RA. The management of brain metastases. *Cancer Treat Rev* 2003; **29**(6): 533-40.

61. Posner JB. Management of brain metastases. *Rev Neurol (Paris)* 1992; **148**(6-7): 477-87.

62. Arvold ND, Lee EQ, Mehta MP, et al. Updates in the management of brain metastases. *Neuro Oncol* 2016; **18**(8): 1043-65.

63. Fox BD, Cheung VJ, Patel AJ, Suki D, Rao G. Epidemiology of metastatic brain tumors. *Neurosurg Clin N Am* 2011; **22**(1): 1-6, v.

64. Guomundsson KR. A survey of tumors of the central nervous system in Iceland during the 10-year period 1954-1963. *Acta Neurol Scand* 1970; **46**(4): 538-52.

65. Smedby KE, Brandt L, Backlund ML, Blomqvist P. Brain metastases admissions in Sweden between 1987 and 2006. *Br J Cancer* 2009; **101**(11): 1919-24.

66. Materljan E, Materljan B, Sepcic J, Tuskan-Mohar L, Zamolo G, Erman-Baldini I. Epidemiology of central nervous system tumors in Labin area, Croatia, 1974-2001. *Croat Med J* 2004; **45**(2): 206-12.

67. Fogelholm R, Uutela T, Murros K. Epidemiology of central nervous system neoplasms. A regional survey in Central Finland. *Acta Neurol Scand* 1984; **69**(3): 129-36.

68. Counsell CE, Collie DA, Grant R. Incidence of intracranial tumours in the Lothian region of Scotland, 1989-90. *J Neurol Neurosurg Psychiatry* 1996; **61**(2): 143-50.

69. Percy AK, Elveback LR, Okazaki H, Kurland LT. Neoplasms of the central nervous system. Epidemiologic considerations. *Neurology* 1972; **22**(1): 40-8.

70. Barnholtz-Sloan JS, Sloan AE, Davis FG, Vigneau FD, Lai P, Sawaya RE. Incidence proportions of brain metastases in patients diagnosed (1973 to 2001) in the Metropolitan Detroit Cancer Surveillance System. *J Clin Oncol* 2004; **22**(14): 2865-72.

71. Walker AE, Robins M, Weinfeld FD. Epidemiology of brain tumors: the national survey of intracranial neoplasms. *Neurology* 1985; **35**(2): 219-26.

72. Villano JL, Durbin EB, Normandeau C, Thakkar JP, Moirangthem V, Davis FG. Incidence of brain metastasis at initial presentation of lung cancer. *Neuro Oncol* 2015; **17**(1): 122-8.

73. Eichler AF, Loeffler JS. Multidisciplinary management of brain metastases. *Oncologist* 2007; **12**(7): 884-98.

74. Fink KR, Fink JR. Imaging of brain metastases. *Surg Neurol Int* 2013; **4**(Suppl 4): S209-19.

75. Tabouret E, Chinot O, Metellus P, Tallet A, Viens P, Goncalves A. Recent trends in epidemiology of brain metastases: an overview. *Anticancer Res* 2012; **32**(11): 4655-62.

76. Lin X, DeAngelis LM. Treatment of Brain Metastases. *J Clin Oncol* 2015; **33**(30): 3475-84.

77. Chamberlain MC, Baik CS, Gadi VK, Bhatia S, Chow LQ. Systemic therapy of brain metastases: non-small cell lung cancer, breast cancer, and melanoma. *Neuro Oncol* 2017; **19**(1): i1-i24.

78. Zhang D, Wang Z, Shang D, Yu J, Yuan S. Incidence and prognosis of brain metastases in cutaneous melanoma patients: a population-based study. *Melanoma Res* 2019; **29**(1): 77-84.

79. Amer MH, Al-Sarraf M, Baker LH, Vaitkevicius VK. Malignant melanoma and central nervous system metastases. Incidence, diagnosis, treatment and survival. *Cancer* 1978; **42**(2): 660-8.

80. Davies MA, Liu P, McIntyre S, et al. Prognostic factors for survival in melanoma patients with brain metastases. *Cancer* 2011; **117**(8): 1687-96.

81. Zakrzewski J, Geraghty LN, Rose AE, et al. Clinical variables and primary tumor characteristics predictive of the development of melanoma brain metastases and post-brain metastases survival. *Cancer* 2011; **117**(8): 1711-20.

82. Bedikian AY, Wei C, Detry M, et al. Predictive factors for the development of brain metastasis in advanced unresectable metastatic melanoma. *Am J Clin Oncol* 2011; **34**(6): 603-10.

83. Ballo MT, Ross MI, Cormier JN, et al. Combined-modality therapy for patients with regional nodal metastases from melanoma. *Int J Radiat Oncol Biol Phys* 2006; **64**(1): 106-13.

84. El-Osta H, Falchook G, Tsimberidou A, et al. BRAF mutations in advanced cancers: clinical characteristics and outcomes. *PLoS One* 2011; **6**(10): e25806.

85. Thumar J, Shahbazian D, Aziz SA, Jilaveanu LB, Kluger HM. MEK targeting in N-RAS mutated metastatic melanoma. *Mol Cancer* 2014; **13**: 45.

86. Witlox WJA, Ramaekers BLT, Zindler JD, et al. The Prevention of Brain Metastases in Non-Small Cell Lung Cancer by Prophylactic Cranial Irradiation. *Front Oncol* 2018; **8**: 241.

87. Rangachari D, Yamaguchi N, VanderLaan PA, et al. Brain metastases in patients with EGFR-mutated or ALK-rearranged non-small-cell lung cancers. *Lung Cancer* 2015; **88**(1): 108-11.

88. Berghoff AS, Bartsch R, Wohrer A, et al. Predictive molecular markers in metastases to the central nervous system: recent advances and future avenues. *Acta Neuropathol* 2014; **128**(6): 879-91.

89. Furet E, El Bouchtaoui M, Feugeas JP, et al. Increased risk of brain metastases in women with breast cancer and p16 expression in metastatic lymph-nodes. *Oncotarget* 2017; **8**(23): 37332-41.

90. Mongan JP, Fadul CE, Cole BF, et al. Brain metastases from colorectal cancer: risk factors, incidence, and the possible role of chemokines. *Clin Colorectal Cancer* 2009; **8**(2): 100-5.

91. Sun M, De Velasco G, Brastianos PK, et al. The Development of Brain Metastases in Patients with Renal Cell Carcinoma: Epidemiologic Trends, Survival, and Clinical Risk Factors Using a Population-based Cohort. *Eur Urol Focus* 2018.

92. Hiom SC. Diagnosing cancer earlier: reviewing the evidence for improving cancer survival. *Br J Cancer* 2015; **112 Suppl 1**: S1-5.

93. Blandin Knight S, Crosbie PA, Balata H, Chudziak J, Hussell T, Dive C. Progress and prospects of early detection in lung cancer. *Open Biol* 2017; **7**(9).

94. Zakaria R, Das K, Bhojak M, Radon M, Walker C, Jenkinson MD. The role of magnetic resonance imaging in the management of brain metastases: diagnosis to prognosis. *Cancer Imaging* 2014; **14**: 8.

95. Westbrook C, Roth CK, Talbot J. MRI in practice. 4 ed: Wiley-Blackwell; 2011.

96. Shah S, Desai N, Upadhyay A. Clinical Review: Cerebral Metastases - Variable Appearance on MRI. *GCSMC J Med Sci* 2015; **4**.

97. Holtås S, Geijer B, Strömblad LG, Maly-Sundgren P, Burtscher IM. A ring-enhancing metastasis with central high signal on diffusion-weighted imaging and low apparent diffusion coefficients. *Neuroradiology* 2000; **42**(11): 824-27.

98. Pope WB. Brain metastases: neuroimaging. *Handb Clin Neurol* 2018; **149**: 89-112.

99. Terae S, Yoshida D, Kudo K, Tha KK, Fujino M, Miyasaka K. Contrast-enhanced FLAIR imaging in combination with pre- and postcontrast magnetization

transfer T1-weighted imaging: usefulness in the evaluation of brain metastases. *J Magn Reson Imaging* 2007; **25**(3): 479-87.

100. Crisi G, Orsingher L, Filice S. Lipid and macromolecules quantitation in differentiating glioblastoma from solitary metastasis: a short-echo time single-voxel magnetic resonance spectroscopy study at 3 T. *J Comput Assist Tomogr* 2013; **37**(2): 265-71.

101. Tsougos I, Svolos P, Kousi E, et al. Differentiation of glioblastoma multiforme from metastatic brain tumor using proton magnetic resonance spectroscopy, diffusion and perfusion metrics at 3 T. *Cancer Imaging* 2012; **12**: 423-36.

102. Nussbaum ES, Djalilian HR, Cho KH, Hall WA. Brain metastases. Histology, multiplicity, surgery, and survival. *Cancer* 1996; **78**(8): 1781-8.

103. Khuntia D, Brown P, Li J, Mehta MP. Whole-brain radiotherapy in the management of brain metastasis. *J Clin Oncol* 2006; **24**(8): 1295-304.

104. Donato J, Campigotto F, Uhlmann EJ, et al. Intracranial hemorrhage in patients with brain metastases treated with therapeutic enoxaparin: a matched cohort study. *Blood* 2015; **126**(4): 494-9.

105. Graf AH, Buchberger W, Langmayr H, Schmid KW. Site preference of metastatic tumours of the brain. *Virchows Arch A Pathol Anat Histopathol* 1988; **412**(5): 493-8.

106. Berghoff AS, Preusser M. New developments in brain metastases. *Ther Adv Neurol Disord* 2018; **11**: 1-14.

107. Fidler IJ. Reviews: Part III: Cancer Metastasis: Biology and Treatment. *The Cancer Journal* 2015; **21**(4): 284-93.

108. Alsidawi S, Malek E, Driscoll JJ. MicroRNAs in brain metastases: potential role as diagnostics and therapeutics. *Int J Mol Sci* 2014; **15**(6): 10508-26.

109. Suh JH, Stea B, Nabid A, et al. Phase III study of efaproxiral as an adjunct to whole-brain radiation therapy for brain metastases. *J Clin Oncol* 2006; **24**(1): 106-14.

110. Vosoughi E, Lee JM, Miller JR, et al. Survival and clinical outcomes of patients with melanoma brain metastasis in the era of checkpoint inhibitors and targeted therapies. *BMC Cancer* 2018; **18**(1): 490.

111. Middleton MR, Grob JJ, Aaronson N, et al. Randomized phase III study of temozolomide versus dacarbazine in the treatment of patients with advanced metastatic malignant melanoma. *J Clin Oncol* 2000; **18**(1): 158-66.

112. Bedikian AY, Millward M, Pehamberger H, et al. Bcl-2 antisense (oblimersen sodium) plus dacarbazine in patients with advanced melanoma: the Oblimersen Melanoma Study Group. *J Clin Oncol* 2006; **24**(29): 4738-45.

113. Robert C, Karaszewska B, Schachter J, et al. Improved overall survival in melanoma with combined dabrafenib and trametinib. *N Engl J Med* 2015; **372**(1): 30-9.

114. Larkin J, Ascierto PA, Dreno B, et al. Combined vemurafenib and cobimetinib in BRAF-mutated melanoma. *N Engl J Med* 2014; **371**(20): 1867-76.

115. Long GV, Stroyakovskiy D, Gogas H, et al. Dabrafenib and trametinib versus dabrafenib and placebo for Val600 BRAF-mutant melanoma: a multicentre, double-blind, phase 3 randomised controlled trial. *Lancet* 2015; **386**(9992): 444-51.

116. Yuan P, Gao SL. Management of breast cancer brain metastases: Focus on human epidermal growth factor receptor 2-positive breast cancer. *Chronic Dis Transl Med* 2017; **3**(1): 21-32.

117. Gaspar LE, Scott C, Murray K, Curran W. Validation of the RTOG recursive partitioning analysis (RPA) classification for brain metastases. *Int J Radiat Oncol Biol Phys* 2000; **47**(4): 1001-6.

118. Gaspar L, Scott C, Rotman M, et al. Recursive partitioning analysis (RPA) of prognostic factors in three Radiation Therapy Oncology Group (RTOG) brain metastases trials. *Int J Radiat Oncol Biol Phys* 1997; **37**(4): 745-51.

119. Sperduto PW, Kased N, Roberge D, et al. Summary report on the graded prognostic assessment: an accurate and facile diagnosis-specific tool to estimate survival for patients with brain metastases. *J Clin Oncol* 2012; **30**(4): 419-25.

120. Samlowski WE, Oh K, Wu JK, Editor: Eichler AF. Management of brain metastases in melanoma. *Up to date* 2018.

121. Patchell RA, Tibbs PA, Walsh JW, et al. A randomized trial of surgery in the treatment of single metastases to the brain. *N Engl J Med* 1990; **322**(8): 494-500.

122. Vecht CJ, Haaxma-Reiche H, Noordijk EM, et al. Treatment of single brain metastasis: radiotherapy alone or combined with neurosurgery? *Ann Neurol* 1993; **33**(6): 583-90.

123. Kamp MA, Dibue M, Santacroce A, et al. The tumour is not enough or is it? Problems and new concepts in the surgery of cerebral metastases. *Ecancermedicalscience* 2013; **7**: 306.

124. Patel AJ, Suki D, Hatiboglu MA, et al. Factors influencing the risk of local recurrence after resection of a single brain metastasis. *J Neurosurg* 2010; **113**(2): 181-9.

125. Ahn JH, Lee SH, Kim S, et al. Risk for leptomeningeal seeding after resection for brain metastases: implication of tumor location with mode of resection. *J Neurosurg* 2012; **116**(5): 984-93.

126. Yoo H, Kim YZ, Nam BH, et al. Reduced local recurrence of a single brain metastasis through microscopic total resection. *J Neurosurg* 2009; **110**(4): 730-6.

127. Hardesty DA, Nakaji P. The Current and Future Treatment of Brain Metastases. *Front Surg* 2016; **3**: 30.

128. Kamp MA, Grosser P, Felsberg J, et al. 5-aminolevulinic acid (5-ALA)-induced fluorescence in intracerebral metastases: a retrospective study. *Acta Neurochir (Wien)* 2012; **154**(2): 223-8; discussion 8.

129. Schebesch KM, Hoehne J, Hohenberger C, et al. Fluorescein sodium-guided resection of cerebral metastases-experience with the first 30 patients. *Acta Neurochir (Wien)* 2015; **157**(6): 899-904.

130. McTyre E, Scott J, Chinnaiyan P. Whole brain radiotherapy for brain metastasis. *Surg Neurol Int* 2013; **4**(Suppl 4): S236-44.

131. Symonds P, Deehan C, Mills JA, Meredith C. Walter and Miller's Textbook of Radiotherapy. Radiation physics, Therapy and Oncology. 7 ed: Elsevier Churchill Livingstone; 2012.

132. Degerfält J, Moegelin I-M, Sharp L. Strålbehandling. 2 ed: Studentlitteratur; 2008.

133. Owen S, Souhami L. The management of brain metastases in non-small cell lung cancer. *Front Oncol* 2014; **4**: 248.

134. Mulvenna P, Nankivell M, Barton R, et al. Dexamethasone and supportive care with or without whole brain radiotherapy in treating patients with non-small cell lung cancer with brain metastases unsuitable for resection or stereotactic radiotherapy (QUARTZ): results from a phase 3, non-inferiority, randomised trial. *The Lancet* 2016; **388**(10055): 2004-14.

135. Nieder C, Grosu AL, Gaspar LE. Stereotactic radiosurgery (SRS) for brain metastases: a systematic review. *Radiat Oncol* 2014; **9**: 155.

136. Nieder C, Spanne O, Mehta MP, Grosu AL, Geinitz H. Presentation, patterns of care, and survival in patients with brain metastases: what has changed in the last 20 years? *Cancer* 2011; **117**(11): 2505-12.

137. Badiyan SN, Regine WF, Mehta M. Stereotactic Radiosurgery for Treatment of Brain Metastases. *J Oncol Pract* 2016; **12**(8): 703-12.

138. Linskey ME, Andrews DW, Asher AL, et al. The role of stereotactic radiosurgery in the management of patients with newly diagnosed brain metastases: a systematic review and evidence-based clinical practice guideline. *J Neurooncol* 2010; **96**(1): 45-68.

139. Matsunaga S, Shuto T, Kawahara N, Suenaga J, Inomori S, Fujino H. Gamma Knife surgery for brain metastases from colorectal cancer. Clinical article. *J Neurosurg* 2011; **114**(3): 782-9.

140. Hasegawa T, Kato T, Yamamoto T, et al. Multisession gamma knife surgery for large brain metastases. *J Neurooncol* 2017; **131**(3): 517-24.

141. Paul D. Brown PD, Asher AL, Ballman KV, et al. NCCTG N0574 (Alliance): A phase III randomized trial of whole brain radiation therapy (WBRT) in addition to radiosurgery (SRS) in patients with 1 to 3 brain metastases. *Journal of Clinical Oncology* 2017; **33**(18).

142. Yamamoto M, Serizawa T, Shuto T, et al. Stereotactic radiosurgery for patients with multiple brain metastases (JLGK0901): a multi-institutional prospective observational study. *Lancet Oncol* 2014; **15**(4): 387-95.

143. Patel KR, Burri SH, Asher AL, et al. Comparing Preoperative With Postoperative Stereotactic Radiosurgery for Resectable Brain Metastases: A Multi-institutional Analysis. *Neurosurgery* 2016; **79**(2): 279-85.

144. Song YP, Colaco RJ. Radiation Necrosis - A Growing Problem in a Case of Brain Metastases Following Whole Brain Radiotherapy and Stereotactic Radiosurgery. *Cureus* 2018; **10**(1): e2037.

145. Kim JM, Miller JA, Kotecha R, et al. The risk of radiation necrosis following stereotactic radiosurgery with concurrent systemic therapies. *J Neurooncol* 2017; **133**(2): 357-68.

146. Owonikoko TK, Arbiser J, Zelnak A, et al. Current approaches to the treatment of metastatic brain tumours. *Nat Rev Clin Oncol* 2014; **11**(4): 203-22.

147. Newlands ES, Stevens MF, Wedge SR, Wheelhouse RT, Brock C. Temozolomide: a review of its discovery, chemical properties, pre-clinical development and clinical trials. *Cancer Treat Rev* 1997; **23**(1): 35-61.

148. Kouvaris JR, Miliadou A, Kouloulias VE, et al. Phase II study of temozolomide and concomitant whole-brain radiotherapy in patients with brain metastases from solid tumors. *Onkologie* 2007; **30**(7): 361-6.

149. Addeo R, De Rosa C, Faiola V, et al. Phase 2 trial of temozolomide using protracted low-dose and whole-brain radiotherapy for nonsmall cell lung cancer and breast cancer patients with brain metastases. *Cancer* 2008; **113**(9): 2524-31.

150. Trudeau ME, Crump M, Charpentier D, et al. Temozolomide in metastatic breast cancer (MBC): a phase II trial of the National Cancer Institute of Canada - Clinical Trials Group (NCIC-CTG). *Ann Oncol* 2006; **17**(6): 952-6.

151. Siena S, Crino L, Danova M, et al. Dose-dense temozolomide regimen for the treatment of brain metastases from melanoma, breast cancer, or lung cancer not amenable to surgery or radiosurgery: a multicenter phase II study. *Ann Oncol* 2010; **21**(3): 655-61.

152. Schadendorf D, van Akkooi ACJ, Berking C, et al. Melanoma. *Lancet* 2018; **392**(10151): 971-84.

153. Raizer JJ, Hwu WJ, Panageas KS, et al. Brain and leptomeningeal metastases from cutaneous melanoma: survival outcomes based on clinical features. *Neuro Oncol* 2008; **10**(2): 199-207.

154. Sampson JH, Carter JH, Jr., Friedman AH, Seigler HF. Demographics, prognosis, and therapy in 702 patients with brain metastases from malignant melanoma. *J Neurosurg* 1998; **88**(1): 11-20.

155. Davies H, Bignell GR, Cox C, et al. Mutations of the BRAF gene in human cancer. *Nature* 2002; **417**(6892): 949-54.

156. Finn L, Markovic SN, Joseph RW. Therapy for metastatic melanoma: the past, present and future. *BMC Medicine* 2012; **10**(23): 10.

157. Flaherty KT, Puzanov I, Kim KB, et al. Inhibition of mutated, activated BRAF in metastatic melanoma. *N Engl J Med* 2010; **363**(9): 809-19.

158. Ribas A, Kim KB, Schuchter LM, et al. BRIM-2: An open-label, multicenter phase II study of vemurafenib in previously treated patients with BRAF V600E mutation-positive metastatic melanoma. 2011; **29**(15_suppl): 8509-.

159. Long GV, Trefzer U, Davies MA, et al. Dabrafenib in patients with Val600Glu or Val600Lys BRAF-mutant melanoma metastatic to the brain (BREAK-MB): a multicentre, open-label, phase 2 trial. *Lancet Oncol* 2012; **13**(11): 1087-95.

160. Villanueva J, Vultur A, Lee JT, et al. Acquired resistance to BRAF inhibitors mediated by a RAF kinase switch in melanoma can be overcome by cotargeting MEK and IGF-1R/PI3K. *Cancer Cell* 2010; **18**(6): 683-95.

161. Long GV, Hauschild A, Santinami M, et al. Adjuvant Dabrafenib plus Trametinib in Stage III BRAF-Mutated Melanoma. *N Engl J Med* 2017; **377**(19): 1813-23.

162. Nissan MH, Rosen N, Solit DB. ERK pathway inhibitors: how low should we go? *Cancer Discov* 2013; **3**(7): 719-21.

163. Majchrzak A, Witkowska M, Smolewski P. Inhibition of the PI3K/Akt/mTOR signaling pathway in diffuse large B-cell lymphoma: current knowledge and clinical significance. *Molecules* 2014; **19**(9): 14304-15.

164. Daphu I, Horn S, Stieber D, et al. In Vitro Treatment of Melanoma Brain Metastasis by Simultaneously Targeting the MAPK and PI3K Signaling Pathways. *International Journal of Molecular Sciences* 2014; **15**(5): 8773-94.

165. Davies MA, Stemke-Hale K, Lin E, et al. Integrated Molecular and Clinical Analysis of AKT Activation in Metastatic Melanoma. *Clin Cancer Res* 2009; **15**(24): 7538-46.

166. Tsao H, Zhang X, Fowlkes K, Haluska FG. Relative reciprocity of NRAS and PTEN/MMAC1 alterations in cutaneous melanoma cell lines. *Cancer Res* 2000; **60**(7): 1800-4.

167. Dienstmann R, Rodon J, Serra V, Tabernero J. Picking the point of inhibition: a comparative review of PI3K/AKT/mTOR pathway inhibitors. *Mol Cancer Ther* 2014; **13**(5): 1021-31.

168. Massacesi C, Di Tomaso E, Urban P, et al. PI3K inhibitors as new cancer therapeutics: implications for clinical trial design. *Onco Targets Ther* 2016; **9**: 203-10.

169. Zaytseva YY, Valentino JD, Gulhati P, Evers BM. mTOR inhibitors in cancer therapy. *Cancer Lett* 2012; **319**(1): 1-7.

170. Zhou HY, Huang SL. Current development of the second generation of mTOR inhibitors as anticancer agents. *Chin J Cancer* 2012; **31**(1): 8-18.

171. Brastianos HC, Cahill DP, Brastianos PK. Systemic therapy of brain metastases. *Curr Neurol Neurosci Rep* 2015; **15**(2): 518.

172. Massacesi C, di Tomaso E, Fretault N, Hirawat S. Challenges in the clinical development of PI3K inhibitors. *Ann N Y Acad Sci* 2013; **1280**: 19-23.

173. Passarelli A, Mannavola F, Stucci LS, Tucci M, Silvestris F. Immune system and melanoma biology: a balance between immunosurveillance and immune escape. *Oncotarget* 2017; **8**(62): 106132-42.

174. Robert C, Thomas L, Bondarenko I, et al. Ipilimumab plus dacarbazine for previously untreated metastatic melanoma. *N Engl J Med* 2011; **364**(26): 2517-26.

175. Hodi FS, O'Day SJ, McDermott DF, et al. Improved survival with ipilimumab in patients with metastatic melanoma. *N Engl J Med* 2010; **363**(8): 711-23.

176. Schadendorf D, Hodi FS, Robert C, et al. Pooled Analysis of Long-Term Survival Data From Phase II and Phase III Trials of Ipilimumab in Unresectable or Metastatic Melanoma. *J Clin Oncol* 2015; **33**(17): 1889-94.

177. Eroglu Z, Ribas A. Combination therapy with BRAF and MEK inhibitors for melanoma: latest evidence and place in therapy. *Ther Adv Med Oncol* 2016; **8**(1): 48-56.

178. Mackiewicz J, Mackiewicz A. BRAF and MEK inhibitors in the era of immunotherapy in melanoma patients. *Contemp Oncol (Pozn)* 2018; **22**(1A): 68-72.

179. Riley JL. PD-1 signaling in primary T cells. *Immunol Rev* 2009; **229**(1): 114-25.

180. Di Giacomo AM, Ascierto PA, Pilla L, et al. Ipilimumab and fotemustine in patients with advanced melanoma (NIBIT-M1): an open-label, single-arm phase 2 trial. *Lancet Oncol* 2012; **13**(9): 879-86.

181. Ribas A, Butler M, Lutzky J, et al. Phase I study combining anti-PD-L1 (MEDI4736) with BRAF (dabrafenib) and/or MEK (trametinib) inhibitors in advanced melanoma. *Journal of Clinical Oncology* 2015; **33**(15_suppl): 3003-.

182. Hannan EJ, O'Leary DP, MacNally SP, et al. The significance of BRAF V600E mutation status discordance between primary cutaneous melanoma and brain

metastases: The implications for BRAF inhibitor therapy. *Medicine (Baltimore)* 2017; **96**(48): e8404.

183. Chen G, Chakravarti N, Aardalen K, et al. Molecular profiling of patient-matched brain and extracranial melanoma metastases implicates the PI3K pathway as a therapeutic target. *Clin Cancer Res* 2014; **20**(21): 5537-46.

184. Niessner H, Forschner A, Klumpp B, et al. Targeting hyperactivation of the AKT survival pathway to overcome therapy resistance of melanoma brain metastases. *Cancer Med* 2013; **2**(1): 76-85.

185. Fischer GM, Jalali A, Kircher DA, et al. Molecular Profiling Reveals Unique Immune and Metabolic Features of Melanoma Brain Metastases. *Cancer Discov* 2019.

186. Pesce GA, Klingbiel D, Ribi K, et al. Outcome, quality of life and cognitive function of patients with brain metastases from non-small cell lung cancer treated with whole brain radiotherapy combined with gefitinib or temozolomide. A randomised phase II trial of the Swiss Group for Clinical Cancer Research (SAKK 70/03). *Eur J Cancer* 2012; **48**(3): 377-84.

187. Paz-Ares L, Tan EH, O'Byrne K, et al. Afatinib versus gefitinib in patients with EGFR mutation-positive advanced non-small-cell lung cancer: overall survival data from the phase IIb LUX-Lung 7 trial. *Ann Oncol* 2017; **28**(2): 270-7.

188. Uchino J, Nakao A, Tamiya N, et al. Treatment rationale and design of the SPIRAL study: A phase II trial of osimertinib in elderly epidermal growth factor receptor T790M-positive nonsmall-cell lung cancer patients who progressed during prior EGFR-TKI treatment. *Medicine (Baltimore)* 2018; **97**(23): e11081.

189. Janne PA, Yang JC, Kim DW, et al. AZD9291 in EGFR inhibitor-resistant non-small-cell lung cancer. *N Engl J Med* 2015; **372**(18): 1689-99.

190. Sequist LV, Soria JC, Goldman JW, et al. Rociletinib in EGFR-mutated non-small-cell lung cancer. *N Engl J Med* 2015; **372**(18): 1700-9.

191. Kim ES. Olmutinib: First Global Approval. *Drugs* 2016; **76**(11): 1153-7.

192. Yun J, Hong MH, Kim SY, et al. YH25448, an Irreversible EGFR-TKI with Potent Intracranial Activity in EGFR Mutant Non-Small Cell Lung Cancer. *Clin Cancer Res* 2019.

193. Novello S, Mazieres J, Oh IJ, et al. Alectinib versus chemotherapy in crizotinib-pretreated anaplastic lymphoma kinase (ALK)-positive non-small-cell lung cancer: results from the phase III ALUR study. *Ann Oncol* 2018; **29**(6): 1409-16.

194. Bachelot T, Romieu G, Campone M, et al. Lapatinib plus capecitabine in patients with previously untreated brain metastases from HER2-positive metastatic breast cancer (LANDSCAPE): a single-group phase 2 study. *Lancet Oncol* 2013; **14**(1): 64-71.

195. Lin NU, Dieras V, Paul D, et al. Multicenter phase II study of lapatinib in patients with brain metastases from HER2-positive breast cancer. *Clin Cancer Res* 2009; **15**(4): 1452-9.

196. Hurvitz S, Singh R, Adams B, et al. Phase Ib/II single-arm trial evaluating the combination of everolimus, lapatinib and capecitabine for the treatment of HER2-positive breast cancer with brain metastases (TRIO-US B-09). *Ther Adv Med Oncol* 2018; **10**: 1758835918807339.

197. Duchnowska R, Dziadziuszko R, Trojanowski T, et al. Conversion of epidermal growth factor receptor 2 and hormone receptor expression in breast cancer metastases to the brain. *Breast Cancer Res* 2012; **14**(4): R119.

198. Guarneri V, Giovannelli S, Ficarra G, et al. Comparison of HER-2 and hormone receptor expression in primary breast cancers and asynchronous paired metastases: impact on patient management. *Oncologist* 2008; **13**(8): 838-44.

199. Hoefnagel LD, van de Vijver MJ, van Slooten HJ, et al. Receptor conversion in distant breast cancer metastases. *Breast Cancer Res* 2010; **12**(5): R75.

200. Curigliano G, Bagnardi V, Viale G, et al. Should liver metastases of breast cancer be biopsied to improve treatment choice? *Ann Oncol* 2011; **22**(10): 2227-33.

201. Gong Y, Han EY, Guo M, Pusztai L, Sneige N. Stability of estrogen receptor status in breast carcinoma: a comparison between primary and metastatic tumors with regard to disease course and intervening systemic therapy. *Cancer* 2011; **117**(4): 705-13.

202. Liedtke C, Broglio K, Moulder S, et al. Prognostic impact of discordance between triple-receptor measurements in primary and recurrent breast cancer. *Ann Oncol* 2009; **20**(12): 1953-8.

203. Gaedcke J, Traub F, Milde S, et al. Predominance of the basal type andHER-2/neu type in brain metastasisfrom breast cancer. *Modern Pathology* 2007; **20**: 864-70.

204. Manson QF, Schrijver W, Ter Hoeve ND, Moelans CB, van Diest PJ. Frequent discordance in PD-1 and PD-L1 expression between primary breast tumors and their matched distant metastases. *Clin Exp Metastasis* 2018.

205. Brastianos PK, Carter SL, Santagata S, et al. Genomic Characterization of Brain Metastases Reveals Branched Evolution and Potential Therapeutic Targets. *Cancer Discov* 2015; **5**(11): 1164-77.

206. Adamo B, Deal AM, Burrows E, et al. Phosphatidylinositol 3-kinase pathway activation in breast cancer brain metastases. *Breast Cancer Res* 2011; **13**(6): R125.

207. Sobhani N, Roviello G, Corona SP, et al. The prognostic value of PI3K mutational status in breast cancer: A meta-analysis. *J Cell Biochem* 2018; **119**(6): 4287-92.

208. Labidi SI, Bachelot T, Ray-Coquard I, et al. Bevacizumab and paclitaxel for breast cancer patients with central nervous system metastases: a case series. *Clin Breast Cancer* 2009; **9**(2): 118-21.

209. Lin NU, Gelman RS, Younger WJ, et al. Phase II trial of carboplatin (C) and bevacizumab (BEV) in patients (pts) with breast cancer brain metastases (BCBM). 2013; **31**(15_suppl): 513-.

210. Lu Y-S, Chen W-W, Lin C-H, et al. Bevacizumab, etoposide, and cisplatin (BEEP) in brain metastases of breast cancer progressing from radiotherapy: Results of the first stage of a multicenter phase II study. *Journal of Clinical Oncology* 2012; **30**.

211. Berghoff AS, Preusser M. Anti-angiogenic therapies in brain metastases. *Memo* 2018; **11**(1): 14-7.

212. Kienast Y, von Baumgarten L, Fuhrmann M, et al. Real-time imaging reveals the single steps of brain metastasis formation. *Nat Med* 2010; **16**(1): 116-22.

213. Berghoff AS, Rajky O, Winkler F, et al. Invasion patterns in brain metastases of solid cancers. *Neuro Oncol* 2013; **15**(12): 1664-72.

214. Desmond KL, Mehrabian H, Chavez S, et al. Chemical exchange saturation transfer for predicting response to stereotactic radiosurgery in human brain metastasis. *Magn Reson Med* 2017; **78**(3): 1110-20.

215. Roesch A, Vultur A, Bogeski I, et al. Overcoming intrinsic multidrug resistance in melanoma by blocking the mitochondrial respiratory chain of slow-cycling JARID1B(high) cells. *Cancer Cell* 2013; **23**(6): 811-25.

216. Boroughs LK, DeBerardinis RJ. Metabolic pathways promoting cancer cell survival and growth. *Nat Cell Biol* 2015; **17**(4): 351-9.

217. Vander Heiden MG, Cantley LC, Thompson CB. Understanding the Warburg effect: the metabolic requirements of cell proliferation. *Science* 2009; **324**(5930): 1029-33.

218. Nygaard V, Prasmickaite L, Vasiliauskaite K, Clancy T, Hovig E. Melanoma brain colonization involves the emergence of a brain-adaptive phenotype. *Oncoscience* 2014; **1**(1): 82-94.

219. Izraely S, Sagi-Assif O, Klein A, et al. The metastatic microenvironment: Claudin-1 suppresses the malignant phenotype of melanoma brain metastasis. *Int J Cancer* 2015; **136**(6): 1296-307.

220. Ciminera AK, Jandial R, Termini J. Metabolic advantages and vulnerabilities in brain metastases. *Clin Exp Metastasis* 2017; **34**(6-7): 401-10.

221. Bonnet S, Archer SL, Allalunis-Turner J, et al. A mitochondria-K+ channel axis is suppressed in cancer and its normalization promotes apoptosis and inhibits cancer growth. *Cancer Cell* 2007; **11**(1): 37-51.

222. Stacpoole PW, Kerr DS, Barnes C, et al. Controlled clinical trial of dichloroacetate for treatment of congenital lactic acidosis in children. *Pediatrics* 2006; **117**(5): 1519-31.

223. Kinnaird A, Dromparis P, Saleme B, et al. Metabolic Modulation of Clear-cell Renal Cell Carcinoma with Dichloroacetate, an Inhibitor of Pyruvate Dehydrogenase Kinase. *Eur Urol* 2016; **69**(4): 734-44.

224. Michelakis ED, Webster L, Mackey JR. Dichloroacetate (DCA) as a potential metabolic-targeting therapy for cancer. *Br J Cancer* 2008; **99**(7): 989-94.

225. Haq R, Shoag J, Andreu-Perez P, et al. Oncogenic BRAF regulates oxidative metabolism via PGC1alpha and MITF. *Cancer Cell* 2013; **23**(3): 302-15.

226. Sook SH, Lee HJ, Kim JH, et al. Reactive oxygen species-mediated activation of AMP-activated protein kinase and c-Jun N-terminal kinase plays a critical role in beta-sitosterol-induced apoptosis in multiple myeloma U266 cells. *Phytother Res* 2014; **28**(3): 387-94.

227. Sundstrom T, Prestegarden L, Azuaje F, et al. Inhibition of mitochondrial respiration prevents BRAF-mutant melanoma brain metastasis. *Acta Neuropathol Commun* 2019; **7**(1): 55.

228. Vanmierlo T, Weingartner O, van der Pol S, et al. Dietary intake of plant sterols stably increases plant sterol levels in the murine brain. *J Lipid Res* 2012; **53**(4): 726-35.

229. Sosman JA, Kim KB, Schuchter L, et al. Survival in BRAF V600-mutant advanced melanoma treated with vemurafenib. *N Engl J Med* 2012; **366**(8): 707-14.

230. McArthur GA, Chapman PB, Robert C, et al. Safety and efficacy of vemurafenib in BRAF(V600E) and BRAF(V600K) mutation-positive melanoma (BRIM-3): extended follow-up of a phase 3, randomised, open-label study. *Lancet Oncol* 2014; **15**(3): 323-32.

231. McArthur GA, Maio M, Arance A, et al. Vemurafenib in metastatic melanoma patients with brain metastases: an open-label, single-arm, phase 2, multicentre study. *Ann Oncol* 2017; **28**(3): 634-41.

232. Hauschild A, Dummer R, Schadendorf D, et al. Longer Follow-Up Confirms Relapse-Free Survival Benefit With Adjuvant Dabrafenib Plus Trametinib in Patients With Resected BRAF V600-Mutant Stage III Melanoma. *J Clin Oncol* 2018: JCO1801219.

233. Schadendorf D, Hauschild A, Santinami M, et al. Patient-reported outcomes in patients with resected, high-risk melanoma with BRAF(V600E) or BRAF(V600K) mutations treated with adjuvant dabrafenib plus trametinib (COMBI-AD): a randomised, placebo-controlled, phase 3 trial. *Lancet Oncol* 2019; **20**(5): 701-10.

234. Goldberg SB, Gettinger SN, Mahajan A, et al. Pembrolizumab for patients with melanoma or non-small-cell lung cancer and untreated brain metastases: early analysis of a non-randomised, open-label, phase 2 trial. *Lancet Oncol* 2016; **17**(7): 976-83.

235. Kluger HM, Chiang V, Mahajan A, et al. Long-Term Survival of Patients With Melanoma With Active Brain Metastases Treated With Pembrolizumab on a Phase II Trial. *J Clin Oncol* 2019; **37**(1): 52-60.

236. Qian JM, Mahajan A, Yu JB, et al. Comparing available criteria for measuring brain metastasis response to immunotherapy. *J Neurooncol* 2017; **132**(3): 479-85.

237. Davies MA, Saiag P, Robert C, et al. Dabrafenib plus trametinib in patients with BRAF(V600)-mutant melanoma brain metastases (COMBI-MB): a multicentre, multicohort, open-label, phase 2 trial. *Lancet Oncol* 2017; **18**(7): 863-73.

238. Wong RS. Apoptosis in cancer: from pathogenesis to treatment. *J Exp Clin Cancer Res* 2011; **30**: 87.

239. Green DR. Cancer and Apoptosis: Who Is Built to Last? *Cancer Cell* 2017; **31**(1): 2-4.

240. Wawryk-Gawda E, Chylinska-Wrzos P, Lis-Sochocka M, et al. P53 protein in proliferation, repair and apoptosis of cells. *Protoplasma* 2014; **251**(3): 525-33.

241. Wang X, Simpson ER, Brown KA. p53: Protection against Tumor Growth beyond Effects on Cell Cycle and Apoptosis. *Cancer Res* 2015; **75**(23): 5001-7.

242. Chen J. The Cell-Cycle Arrest and Apoptotic Functions of p53 in Tumor Initiation and Progression. *Cold Spring Harb Perspect Med* 2016; **6**(3): a026104.

243. Su Z, Yang Z, Xu Y, Chen Y, Yu Q. Apoptosis, autophagy, necroptosis, and cancer metastasis. *Mol Cancer* 2015; **14**: 48.

244. Fridman JS, Lowe SW. Control of apoptosis by p53. *Oncogene* 2003; **22**(56): 9030-40.

245. Reed JC. Bcl-2 family proteins: regulators of apoptosis and chemoresistance in hematologic malignancies. *Semin Hematol* 1997; **34**(4 Suppl 5): 9-19.

246. Gerl R, Vaux DL. Apoptosis in the development and treatment of cancer. *Carcinogenesis* 2005; **26**(2): 263-70.

247. Tannock IF, Lee C. Evidence against apoptosis as a major mechanism for reproductive cell death following treatment of cell lines with anti-cancer drugs. *Br J Cancer* 2001; **84**(1): 100-5.

248. Zheng TS, Flavell RA. Divinations and surprises: genetic analysis of caspase function in mice. *Exp Cell Res* 2000; **256**(1): 67-73.

249. Weidle UH, Niewohner J, Tiefenthaler G. The Blood-Brain Barrier Challenge for the Treatment of Brain Cancer, Secondary Brain Metastases, and Neurological Diseases. *Cancer Genomics Proteomics* 2015; **12**(4): 167-77.

250. Pardridge WM. Blood-brain barrier biology and methodology. *J Neurovirol* 1999; **5**(6): 556-69.

251. Saraiva C, Praca C, Ferreira R, Santos T, Ferreira L, Bernardino L. Nanoparticle-mediated brain drug delivery: Overcoming blood-brain barrier to treat neurodegenerative diseases. *J Control Release* 2016; **235**: 34-47.

252. Pardridge WM. The blood-brain barrier: bottleneck in brain drug development. *NeuroRx* 2005; **2**(1): 3-14.

253. Rapoport SI, Hori M, Klatzo I. Testing of a hypothesis for osmotic opening of the blood-brain barrier. *Am J Physiol* 1972; **223**(2): 323-31.

254. McDannold N, Arvanitis CD, Vykhodtseva N, Livingstone MS. Temporary disruption of the blood-brain barrier by use of ultrasound and microbubbles: safety and efficacy evaluation in rhesus macaques. *Cancer Res* 2012; **72**(14): 3652-63.

255. Alkins R, Burgess A, Ganguly M, et al. Focused ultrasound delivers targeted immune cells to metastatic brain tumors. *Cancer Res* 2013; **73**(6): 1892-9.

256. Hynynen K, McDannold N, Vykhodtseva N, Jolesz FA. Noninvasive MR imaging-guided focal opening of the blood-brain barrier in rabbits. *Radiology* 2001; **220**(3): 640-6.

257. Cao Y, Tsien CI, Shen Z, et al. Use of Magnetic Resonance Imaging to Assess Blood-Brain/Blood-Glioma Barrier Opening During Conformal Radiotherapy. *Journal of Clinical Oncology* 2005; **23**(18): 4127-36.

258. Chen Y, Liu L. Modern methods for delivery of drugs across the blood-brain barrier. *Adv Drug Deliv Rev* 2012; **64**(7): 640-65.

259. Allen C, Paraskevakou G, Liu C, et al. Oncolytic measles virus strains in the treatment of gliomas. *Expert Opin Biol Ther* 2008; **8**(2): 213-20.

260. Gupta B, Levchenko TS, Torchilin VP. TAT peptide-modified liposomes provide enhanced gene delivery to intracranial human brain tumor xenografts in nude mice. *Oncol Res* 2007; **16**(8): 351-9.

261. Saenz del Burgo L, Hernandez RM, Orive G, Pedraz JL. Nanotherapeutic approaches for brain cancer management. *Nanomedicine* 2014; **10**(5): 905-19.

262. Bregy A, Shah AH, Diaz MV, et al. The role of Gliadel wafers in the treatment of high-grade gliomas. *Expert Rev Anticancer Ther* 2013; **13**(12): 1453-61.

263. Bobo RH, Laske DW, Akbasak A, Morrison PF, Dedrick RL, Oldfield EH. Convection-enhanced delivery of macromolecules in the brain. *Proc Natl Acad Sci U S A* 1994; **91**(6): 2076-80.

264. Azad TD, Pan J, Connolly ID, Remington A, Wilson CM, Grant GA. Therapeutic strategies to improve drug delivery across the blood-brain barrier. *Neurosurg Focus* 2015; **38**(3): E9.

265. Silva CO, Pinho JO, Lopes JM, Almeida AJ, Gaspar MM, Reis C. Current Trends in Cancer Nanotheranostics: Metallic, Polymeric, and Lipid-Based Systems. *Pharmaceutics* 2019; **11**(1).

266. Hamilton AM, Aidoudi-Ahmed S, Sharma S, et al. Nanoparticles coated with the tumor-penetrating peptide iRGD reduce experimental breast cancer metastasis in the brain. *J Mol Med (Berl)* 2015; **93**(9): 991-1001.

267. Patil R, Ljubimov AV, Gangalum PR, et al. MRI Virtual Biopsy and Treatment of Brain Metastatic Tumors with Targeted Nanobioconjugates: Nanoclinic in the Brain. *ACS Nano* 2015; **9**(5): 5594-608.

268. Loscher W, Potschka H. Blood-brain barrier active efflux transporters: ATP-binding cassette gene family. *NeuroRx* 2005; **2**(1): 86-98.

269. Palmieri D, Chambers AF, Felding-Habermann B, Huang S, Steeg PS. The biology of metastasis to a sanctuary site. *Clin Cancer Res* 2007; **13**(6): 1656-62.

270. Osswald M, Blaes J, Liao Y, et al. Impact of Blood-Brain Barrier Integrity on Tumor Growth and Therapy Response in Brain Metastases. *Clin Cancer Res* 2016; **22**(24): 6078-87.

271. Lockman PR, Mittapalli RK, Taskar KS, et al. Heterogeneous blood-tumor barrier permeability determines drug efficacy in experimental brain metastases of breast cancer. *Clin Cancer Res* 2010; **16**(23): 5664-78.

272. Thorsen F, Fite B, Mahakian LM, et al. Multimodal imaging enables early detection and characterization of changes in tumor permeability of brain metastases. *J Control Release* 2013; **172**(3): 812-22.

273. Daphu I, Sundstrom T, Horn S, et al. In vivo animal models for studying brain metastasis: value and limitations. *Clin Exp Metastasis* 2013; **30**(5): 695-710.

274. Prochazka M, Gaskins HR, Shultz LD, Leiter EH. The nonobese diabetic scid mouse: model for spontaneous thymomagenesis associated with immunodeficiency. *Proc Natl Acad Sci U S A* 1992; **89**(8): 3290-4.

275. Sundstrom T, Daphu I, Wendelbo I, et al. Automated tracking of nanoparticle-labeled melanoma cells improves the predictive power of a brain metastasis model. *Cancer Res* 2013; **73**(8): 2445-56.

276. Stephenson EM, Stephenson NG. Karyotype analysis of the B16 mouse melanoma with reassessment of the normal mouse idiogram. *J Natl Cancer Inst* 1970; **45**(4): 789-800.

277. Kienast Y, von Baumgarten L, Fuhrmann M, et al. Real-time imaging reveals the single steps of brain metastasis formation. *Nature Medicine* 2009; **16**(1): 116-22.

278. Vaidhyanathan S, Mittapalli RK, Sarkaria JN, Elmquist WF. Factors influencing the CNS distribution of a novel MEK-1/2 inhibitor: implications for combination therapy for melanoma brain metastases. *Drug Metab Dispos* 2014; **42**(8): 1292-300.

279. Tofts P. Quantitative MRI of the brain: Measuring changes caused by disease. West Sussex, England: John Wiley & Sons Ltd; 2003.

280. Calamante F, Morup M, Hansen LK. Defining a local arterial input function for perfusion MRI using independent component analysis. *Magn Reson Med* 2004; **52**(4): 789-97.

281. Khalifa F, Soliman A, El-Baz A, et al. Models and methods for analyzing DCE-MRI: a review. *Med Phys* 2014; **41**(12): 124301.

282. Johnson JA, Wilson TA. A model for capillary exchange. *Am J Physiol* 1966; **210**(6): 1299-303.

283. AgilentTechnologies. Agilent Seahorse XF Cell Mito Stress Test Kit. In: Technologies A, editor. 1st ed. 2850 Centerville Road, Wilmington DE 19808-1610 USA: Agilent Technologies Inc.; 2017.

284. Horan MP, Pichaud N, Ballard JW. Review: quantifying mitochondrial dysfunction in complex diseases of aging. *J Gerontol A Biol Sci Med Sci* 2012; **67**(10): 1022-35.

285. Kang JH, Cho J, Ko YT. Investigation on the effect of nanoparticle size on the blood-brain tumour barrier permeability by in situ perfusion via internal carotid artery in mice. *J Drug Target* 2019; **27**(1): 103-10.

286. Patel SP, Woodman SE. Profile of ipilimumab and its role in the treatment of metastatic melanoma. *Drug Des Devel Ther* 2011; **5**: 489-95.

287. Ghosh D, Peng X, Leal J, Mohanty R. Peptides as drug delivery vehicles across biological barriers. *J Pharm Investig* 2018; **48**(1): 89-111.

288. Ghanouni P, Pauly KB, Elias WJ, et al. Transcranial MRI-Guided Focused Ultrasound: A Review of the Technologic and Neurologic Applications. *AJR Am J Roentgenol* 2015; **205**(1): 150-9.

289. Etame AB, Diaz RJ, Smith CA, Mainprize TG, Hynynen K, Rutka JT. Focused ultrasound disruption of the blood-brain barrier: a new frontier for therapeutic delivery in molecular neurooncology. *Neurosurg Focus* 2012; **32**(1): E3.

290. Wheaton WW, Weinberg SE, Hamanaka RB, et al. Metformin inhibits mitochondrial complex I of cancer cells to reduce tumorigenesis. *Elife* 2014; **3**: e02242.

291. Vazquez F, Lim JH, Chim H, et al. PGC1alpha expression defines a subset of human melanoma tumors with increased mitochondrial capacity and resistance to oxidative stress. *Cancer Cell* 2013; **23**(3): 287-301.

292. Greger JG, Eastman SD, Zhang V, et al. Combinations of BRAF, MEK, and PI3K/mTOR inhibitors overcome acquired resistance to the BRAF inhibitor GSK2118436 dabrafenib, mediated by NRAS or MEK mutations. *Mol Cancer Ther* 2012; **11**(4): 909-20.

293. Bedard PL, Tabernero J, Janku F, et al. A phase Ib dose-escalation study of the oral pan-PI3K inhibitor buparlisib (BKM120) in combination with the oral MEK1/2 inhibitor trametinib (GSK1120212) in patients with selected advanced solid tumors. *Clin Cancer Res* 2015; **21**(4): 730-8.

294. de Gooijer MC, Zhang P, Buil LCM, et al. Buparlisib is a brain penetrable pan-PI3K inhibitor. *Sci Rep* 2018; **8**(1): 10784.

295. Cintas C, Guillermet-Guibert J. Heterogeneity of Phosphatidylinositol-3-Kinase (PI3K)/AKT/Mammalian Target of Rapamycin Activation in Cancer: Is PI3K Isoform Specificity Important? *Front Oncol* 2017; **7**: 330.

Int. J. Mol. Sci. **2015**, *16*, 21658-21680; doi:10.3390/ijms160921658

OPEN ACCESS
International Journal of
Molecular Sciences
ISSN 1422-0067
www.mdpi.com/journal/ijms

Article

A Novel Nanoprobe for Multimodal Imaging Is Effectively Incorporated into Human Melanoma Metastatic Cell Lines

Synnøve Nymark Aasen [1], Aneta Pospisilova [2], Tilo Wolf Eichler [3], Jiri Panek [2], Martin Hruby [2], Petr Stepanek [2], Endy Spriet [4], Daniel Jirak [5,6], Kai Ove Skaftnesmo [1] and Frits Thorsen [1,4,7,*]

1 NorLux Neuro-Oncology Laboratory, Department of Biomedicine, University of Bergen, 5020 Bergen, Norway; E-Mails: synnovenymarkaasen@gmail.com (S.N.A.); kaioveskaftnesmo@gmail.com (K.O.S.)
2 Institute of Macromolecular Chemistry, Academy of Sciences of the Czech Republic, 162 06 Prague, Czech Republic; E-Mails: pospisilova-a@seznam.cz (A.P.); panek@imc.cas.cz (J.P.); mhruby@centrum.cz (M.H.); ppetr.stepanek@gmail.com (P.S.)
3 Department of Clinical Medicine, University of Bergen, 5020 Bergen, Norway; E-Mail: tilo.eichler@k1.uib.no
4 Molecular Imaging Center, Department of Biomedicine, University of Bergen, 5020 Bergen, Norway; E-Mail: endy.spriet@uib.no
5 Department of Diagnostic and Interventional Radiology, Institute for Clinical and Experimental Medicine, 140 21 Prague, Czech Republic; E-Mail: daji@medicon.cz
6 Institute of Biophysics and Informatics, 1st Medicine Faculty, Charles University, 120 00 Prague, Czech Republic
7 Kristian Gerhard Jebsen Brain Tumour Research Centre, Department of Biomedicine, University of Bergen, 5020 Bergen, Norway

* Author to whom correspondence should be addressed; E-Mail: frits.thorsen@uib.no or frits.thorsen@biomed.uib.no; Tel.: +47-5558-6272; Fax: +47-5558-6360.

Academic Editor: John T. McDevitt

Received: 19 June 2015 / Accepted: 25 August 2015 / Published: 8 September 2015

Abstract: To facilitate efficient drug delivery to tumor tissue, several nanomaterials have been designed, with combined diagnostic and therapeutic properties. In this work, we carried out fundamental *in vitro* and *in vivo* experiments to assess the labeling efficacy of our novel theranostic nanoprobe, consisting of glycogen conjugated with a red fluorescent probe and gadolinium. Microscopy and resazurin viability assays were used to study cell labeling and cell viability in human metastatic melanoma cell lines. Fluorescence lifetime

correlation spectroscopy (FLCS) was done to investigate nanoprobe stability. Magnetic resonance imaging (MRI) was performed to study T_1 relaxivity *in vitro*, and contrast enhancement in a subcutaneous *in vivo* tumor model. Efficient cell labeling was demonstrated, while cell viability, cell migration, and cell growth was not affected. FLCS showed that the nanoprobe did not degrade in blood plasma. MRI demonstrated that down to 750 cells/μL of labeled cells in agar phantoms could be detected. *In vivo* MRI showed that contrast enhancement in tumors was comparable between Omniscan contrast agent and the nanoprobe. In conclusion, we demonstrate for the first time that a non-toxic glycogen-based nanoprobe may effectively visualize tumor cells and tissue, and, in future experiments, we will investigate its therapeutic potential by conjugating therapeutic compounds to the nanoprobe.

Keywords: melanoma brain metastasis; nanoprobe; theranostics; magnetic resonance imaging; fluorescence microscopy; high throughput microscopy; fluorescence lifetime correlation spectroscopy; zeta potential

1. Introduction

Around 90% of cancer patients die of tumor metastasis [1]. A detailed and accurate diagnosis of cancer metastasis is therefore necessary in the management of metastatic disease [2]. Commonly used imaging techniques in the clinic, such as magnetic resonance imaging (MRI), computerized tomography (CT) and positron emission tomography (PET), play a critical role in diagnosis and therapy of cancer metastasis [2–4]. A combined use of imaging modalities (*i.e.*, multimodal imaging) has the potential of combining anatomical and physiological image information, thereby improving our understanding of tumor development and therapeutic responses [5,6].

Recently, increased attention has been given to the establishment of functional nano-scaled materials for the application of combined cancer therapy and diagnostics, also named "nano-theranostics" [7–9]. By using such systems, multimodal imaging is able to confirm delivery of therapeutic substances to the tumors and provides a superior visualization of treatment efficacy by real-time monitoring of treatment response [10,11]. An ideal nanoscale drug delivery platform should be biodegradable and non-toxic. The drug load should also occur locally within tumor tissue and reach therapeutic concentrations for a sufficient period of time [12]. Recent developments have advanced the use of theranostic nanomaterials on neoplasms also within the central nervous system (CNS), which may improve treatment of brain metastatic disease in future [13,14]. Polysaccharide-based nanomaterials have drawn notable attention, as they are biocompatible *in vivo* and have the potential to traverse physiological obstacles [15–18]. Further, optimization of size and surface coating of the nanomaterial may extend the circulation time after intravenous administration compared to standard delivery methods of chemotherapeutic drugs [19]. Moreover, solid tumors spontaneously accumulate biocompatible polymers, polymer micelles, liposomes and nanoparticles less than 200 nm in diameter due to the leaky nature of the newly formed tumor neovasculature. This enhanced permeability and retention (EPR) effect is

relatively universal for many solid tumors and allows concentrating nanoparticles to more than one order of magnitude compared to surrounding tissue [20,21].

We have recently developed a nanoprobe for multimodal imaging, composed of glycogen conjugated with gadolinium (Gd-DOTA) and the red fluorescent marker Dyomics-615-NHS (Dy-615) [22]. D-Glucose is normally stored as glycogen in the human body (for instance in muscle and liver tissue), and the use of glycogen as the backbone of a nanoprobe offers several advantages. It is biodegradable and non-toxic to human cells. Furthermore, the abundance, low cost, and wide range of modification possibilities makes glycogen attractive for use in an imaging nanoprobe.

We report here for the first time the application of a glycogen nanoprobe, used to image tumor cells. We demonstrate that the nanoprobe effectively labeled human metastatic melanoma cells *in vitro*, and cellular properties such as viability and migration was not affected after labeling. T_1 weighted *in vivo* MRI scans showed that the contrast enhancement in subcutaneous tumors obtained by the nanoprobe was comparable to using a contrast agent commonly used in the clinic. Our data suggest that the nanoprobe may likely accumulate in solid tumor tissue due to the EPR effect. The nanoprobe may easily be expanded to a nano-theranostic entity, by conjugating it with a therapeutic substance. The main aim of this study was, however, to show proof-of-principle that the nanoprobe is an effective contrast agent for multimodal imaging, while future experiments will address its theranostic utility, where therapeutic agents will be conjugated to the nanoprobe, and the *in vivo* effects will be studied in our mouse models of metastatic melanoma.

2. Results and Discussion

2.1. The Glycogen Nanoprobe Is Efficiently Internalized into the Metastatic Melanoma Cell Lines

We first evaluated the uptake of the glycogen nanoprobe into H1_DL2 human melanoma metastatic cells and two normal human fibroblast cell lines (SV-80 and NSF3) by intracellular fluorescence intensity from Dy-615 after labeling the cells with nanoprobe doses ranging from 10 to 100 μg/mL (Figure 1A). After 6 h, H1_DL2 cells incubated with 10 μg/mL nanoprobe had internalized a minor amount of the nanoprobe. Increased concentration of labeling solution resulted in increased uptake of nanoprobe, as seen by elevated fluorescence intensity. Further, incubation for 24 h with the same concentrations showed stronger uptake of the nanoprobe (Figure 1A). We could not detect any uptake of nanoprobe into the two fibroblast cell lines, even at a labeling concentration of 100 μg/mL (Figure S1).

A detailed inspection of the fluorescence images revealed that all the cells were labeled already when using 10 μg/mL of the nanoprobe. However, a rather weak fluorescence was observed for all labeling concentrations, except 100 μg/mL, indicating that higher concentrations should also be evaluated.

Therefore, we increased the labeling concentrations of nanoprobe to between 100–400 μg/mL. Micrographs obtained from live-cell high-throughput imaging indicated that during an incubation time of 24 h all of the cells were effectively and strongly labeled at these concentrations (Figure 1B). The fluorescence intensities from the micrographs were then quantified (Figure 1C–E). In general, there was a dose-dependent as well as a time-dependent increase in mean fluorescence intensities for all cell lines. For the H1_DL2 cells (Figure 1C) and the Melmet 5 pGFI cells (Figure 1E), a statistically

significant increase in fluorescence was seen after increasing the labeling concentration to 200 µg/mL. For the Melmet 1 pGF1 cells (Figure 1D), there was no increase in labeling efficacy in the range of 100 to 300 µg/mL (24 h labeling time). Based on these results, we continued to investigate cell viability using a nanoprobe labeling concentration of 200 µg/mL.

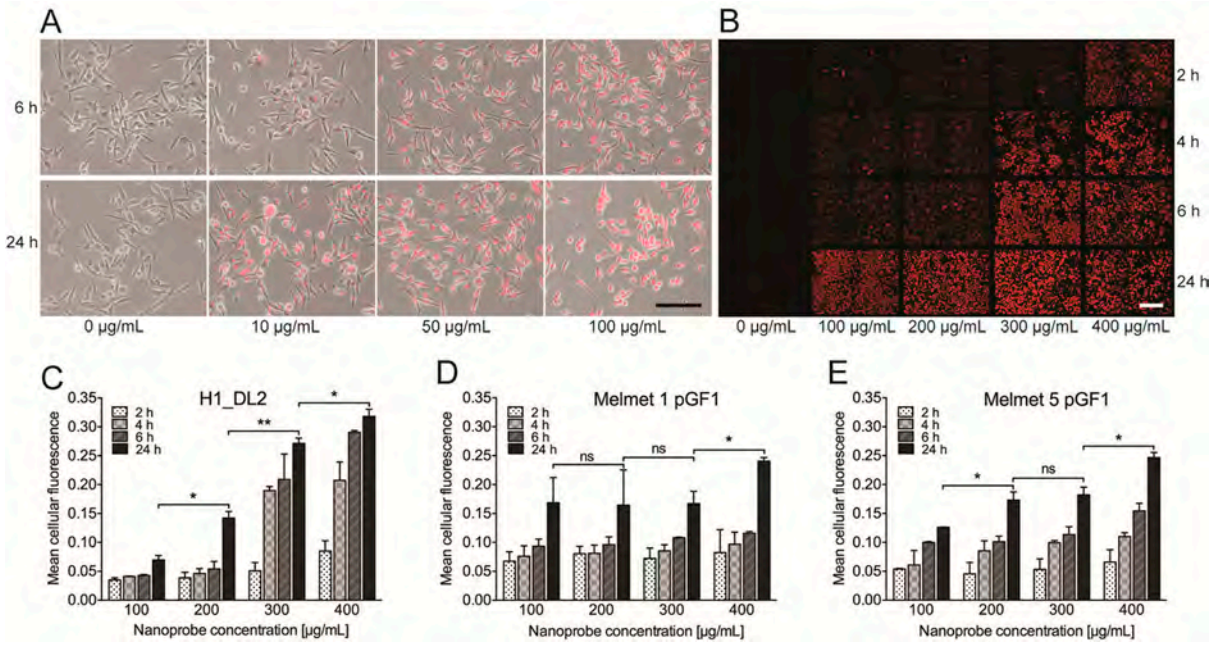

Figure 1. Cellular uptake of the glycogen nanoprobe. (**A**) Fluorescence micrographs overlaid light microscopy images, showing the H1_DL2 cells after being labeled with the glycogen nanoprobe for 6 or 24 h. Scale bar, 100 µm; (**B**) Representative fluorescence micrographs, showing the H1_DL2 cells after being labeled with the glycogen nanoprobe for 2, 4, 6 or 24 h. Similar high throughput experiments were performed for all three cell lines. Scale bar: 100 µm; (**C**–**E**) Quantification of mean fluorescence intensity in the images acquired of the three cell lines by high throughput microscopy. ns: not significant; * $p < 0.05$; ** $p < 0.01$: (**C**) H1_DL2 cell line; (**D**) Melmet 1 pGF1 cell line; and (**E**) Melmet 5 pGF1 cell line.

2.2. The Glycogen Nanoprobe Does Not Affect Short-Term Cell Viability in Vitro

The survival of cells labeled with 200 µg/mL glycogen nanoprobe was studied using a resazurin viability assay (Figure 2A). From 72 h onwards, Melmet 1 pGF1 cells showed reduced proliferative capacity compared to the unlabeled cell population. This was also seen for Melmet 5 pGF1 cells labeled with 200 µg/mL after 24 h. However, subsequent measurements showed no significant differences at later time points. H1_DL2 cells did not show decreased viability until 120 h of exposure to the glycogen nanoprobe (Figure 2A).

Viability was also assessed by counting live and dead cells, after incubation with 200 µg/mL glycogen nanoprobe for up to 72 h. We found no significant differences in viability between labeled and unlabeled cells for any of the cell lines (Figure 2B–G). Thus, based on the internalization and viability studies, a labeling time of 24 h using a concentration of 200 µg/mL nanoprobe was chosen for subsequent experiments.

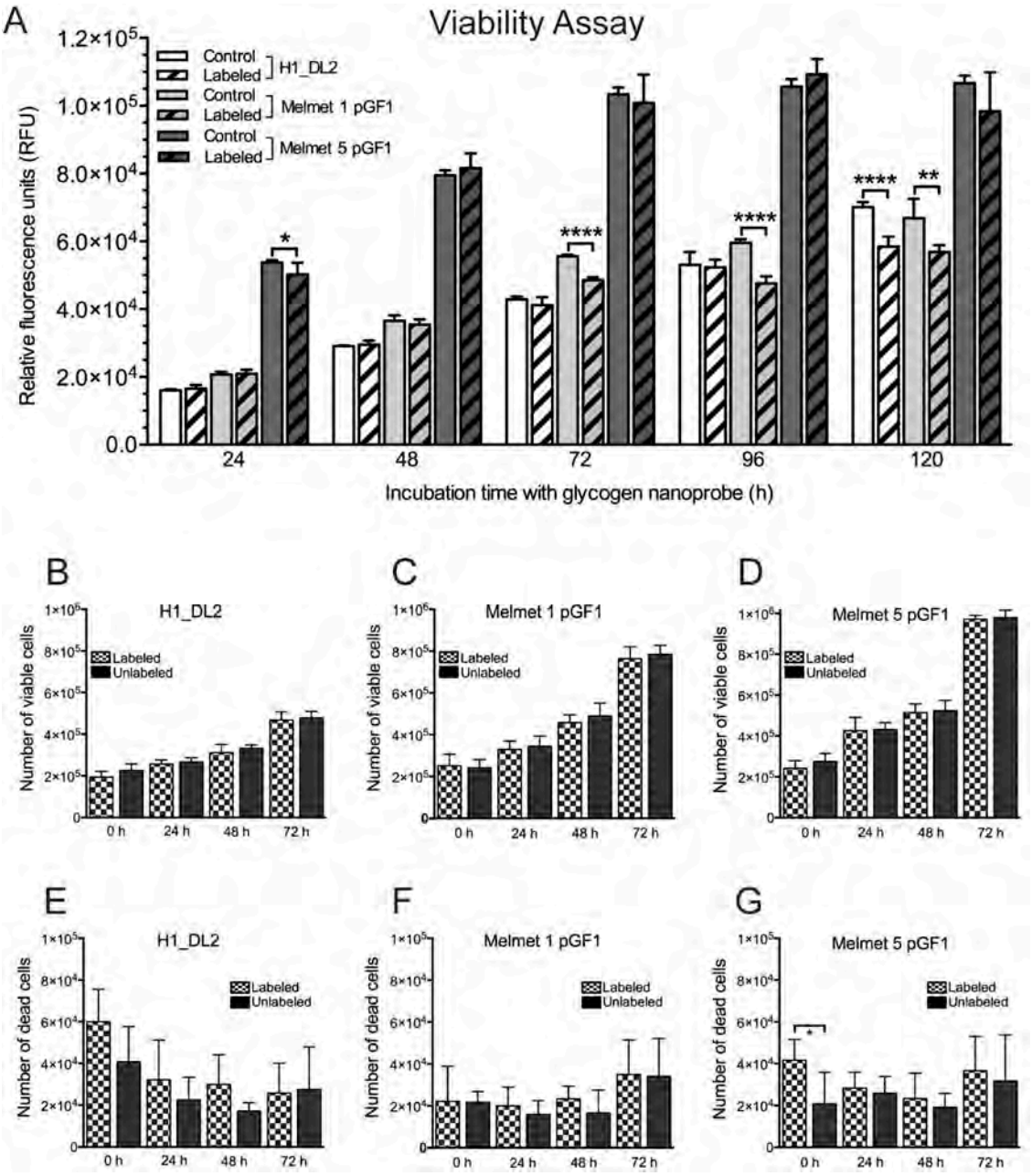

Figure 2. Cell viability in monolayer cultures. (**A**) Monolayer resazurin assay to determine viability of labeled and unlabeled melanoma metastatic cell lines for 120 h. The labeled cells were exposed to 200 μg/mL of the glycogen nanoprobe during the whole time period (for all experiments, $n = 8$; mean ± SD). The relative fluorescence units (vertical axis) were proportional to the number of viable cells. * $p < 0.05$, ** $p < 0.01$, **** $p < 0.0001$; (**B**–**D**) Cell counting assay to determine the number of viable cells in monolayer cultures of labeled and unlabeled cell lines during 72 h. The labeled cells were exposed to 200 μg/mL of the glycogen nanoprobe during the whole time period (for all experiments, $n = 6$; mean ± SD): (**B**) H1_DL2 cells; (**C**) Melmet 1 pGF1 cells; and (**D**) Melmet 5 pGF1 cells; (**E**–**G**) Cell counting assay to determine the number of dead cells in monolayer cultures of labeled and unlabeled cell lines during 72 h. The labeled cells were exposed to 200 μg/mL of the glycogen nanoprobe during the whole time period (for all experiments, $n = 6$; mean ± SD): (**E**) H1_DL2 cells; (**F**) Melmet 1 pGF1 cells; and (**G**) Melmet 5 pGF1 cells.

2.3. The Glycogen Nanoprobe Is Localized in Cytoplasm and Lysosomes

To investigate the subcellular localization of the nanoprobe, H1 human metastatic melanoma cells were labeled with the nanoprobe and incubated with markers for different cellular organelles (Figure 3, Table 1). In general, the nanoprobe was localized within the cytoplasm of the cells. Our analysis showed that the only organelle able to internalize the nanoprobe were the lysosomes (Figure 3C, $R = 0.5614$). All other organelles investigated had a random co-distribution with the nanoprobe, and no co-localization could be detected ($R < 0.5$, Table 1).

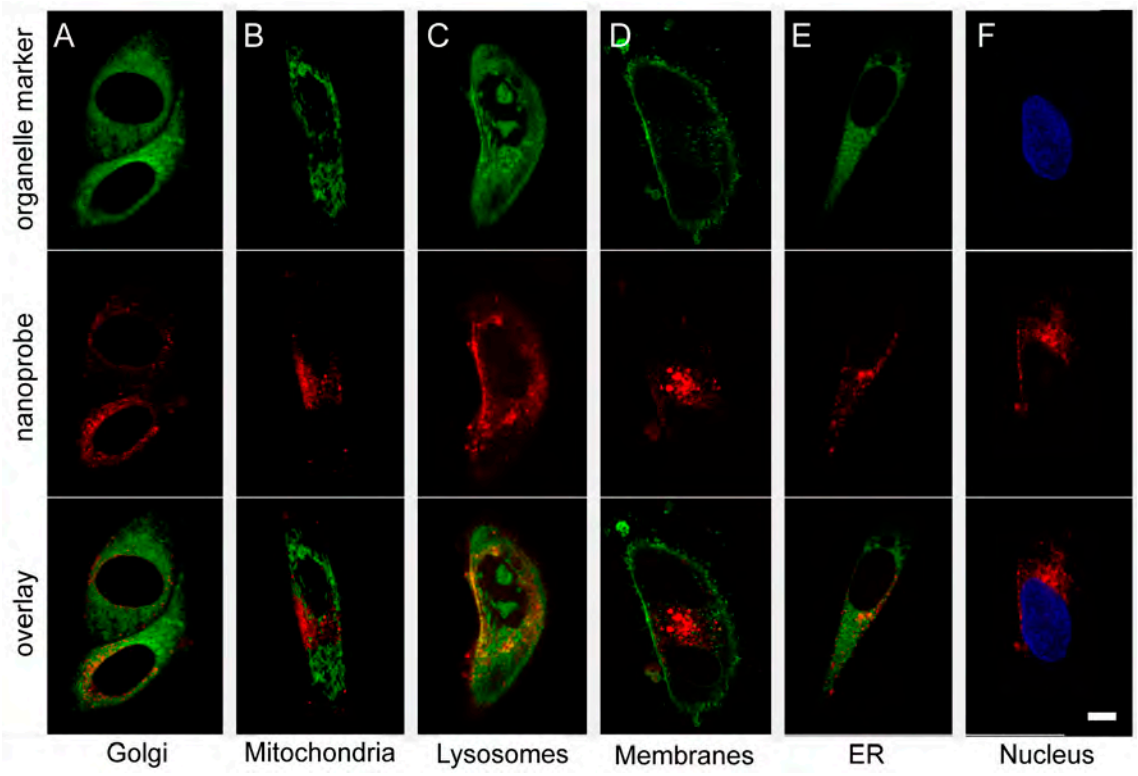

Figure 3. Internalization of the glycogen nanoprobe into organelles within the H1 cells. All organelle probes were conjugated to a green fluorescent dye (**top row**, **A**–**E**) or Hoechst (**F**), while the red fluorescent probe Dyomics-615 was incorporated into the nanoprobe (**middle row**, **A**–**F**). In order to determine co-localization of the nanoprobe with the organelles and thus showing internalization, the red fluorescent images were overlaid the green fluorescent images (**bottom row**, **A**–**E**) or the Hoechst (blue) images (**bottom row**, **F**). (**A**) Staining of Golgi apparatus using the CytoPainter Golgi Staining Kit (Abcam); (**B**) staining of mitochondria using MitoTracker Green (Invitrogen); and (**C**) staining of lysosomes using CytoPainter LysoGreen (Abcam). Areas of co-localization (yellow areas in the overlay picture) could be found; (**D**) Staining of membranes using Wheat Germ Agglutinin Alexa Fluor Conjugate (Thermo Fisher Scientific); (**E**) staining of endoplasmic reticulum using the CytoPainter ER Staining Kit (Abcam); and (**F**) staining of nuclei using Hoechst 33342 (Life Technologies). Scale bar, 10 μm.

Table 1. Co-localization of nanoprobe to organelles.

Organelle	Mean Pearson's Correlation Coefficient	*n*	SD
Golgi apparatus	0.0283	2	0.0063
Mitochondria	0.0574	1	0
Lysosome	0.5614	5	0.0849
Plasma membrane	0.0166	5	0.1003
Endoplasmatic reticulum	0.2839	3	0.0535
Nucleus	0.1117	11	0.2049

2.4. Intracellular Glycogen Nanoprobe Can Be Detected up to 96 h after Labeling

Nanoprobe clearance was assessed by measuring the decrease in cellular fluorescence intensity over 96 h, after an incubation period of 24 h with 200 µg/mL nanoprobe (Figure 4). In general, the cellular fluorescence intensity declined with increased time (Figure 4A,C). Cellular fluorescence within the cells was measured after outlining the cells, as shown in Figure 4B. In total, 64 cells were measured at each time point for each cell line, and the mean intensity value was calculated. This analysis verified a gradual decrease in fluorescence intensity for all cell lines over a time period of 96 h (Figure 4C). However, around 9% of the nanoprobe was still internalized at that time point. Our study showed an inverse relationship between cell proliferation (Figure 4D) and clearance (Figure 4C), indicating an elevated dilution of nanoprobe in more rapidly proliferating cell lines.

2.5. Labeling with the Glycogen Nanoprobe Does Not Influence in Vitro Cell Migration

To study whether labeling with the nanoprobe affected cell migration, a standardized monolayer wound healing assay was carried out (Figure 5). Labeled and unlabeled Melmet 1 pGF1 cells demonstrated similar wound healing capacities, and cell labeling did not influence migration (Figure 5A,B). The wound was closed after 18 h, both for labeled and unlabeled cells (Figure 5D). Similar results were also found for the H1_DL2 and Melmet 5 pGF1 cell lines (Figure 5C,E), as there were no differences in migration between labeled and unlabeled cells. The wounds were closed after 45 h for the H1_DL2 cells, while 15% of the initial area was still open after 45 h for the Melmet 5 pGF1 cell line.

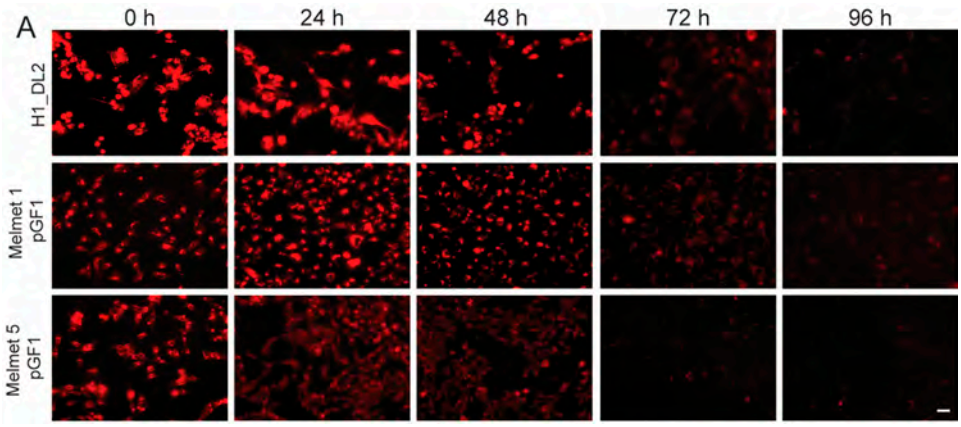

Figure 4. *Cont.*

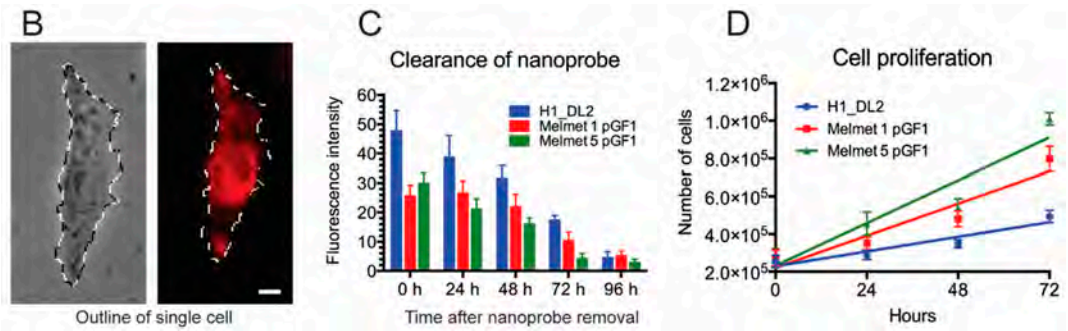

Figure 4. Clearance of the glycogen nanoprobe from cells after removing the labeling solution. (**A**) Representative micrographs demonstrating a gradual decrease in cellular fluorescence intensity for H1_DL2 (**top row**), Melmet 1 pGF1 (**middle row**) and Melmet 5 pGF1 (**bottom row**) cells during four days in culture. Scale bar: 50 µm; (**B**) For each time point, the cellular area of 64 cells (from each cell line) was outlined in Photoshop, as shown in this example. Scale bar: 10 µm; (**C**) The mean fluorescence intensity for each cell was determined, and the mean values of all 64 cells were calculated and plotted for each time point (mean ± SD); (**D**) Cell proliferation for each cell line was determined over a time period of 72 h (mean ± SD). The curves were obtained by linear regression (Graphpad Prism v6).

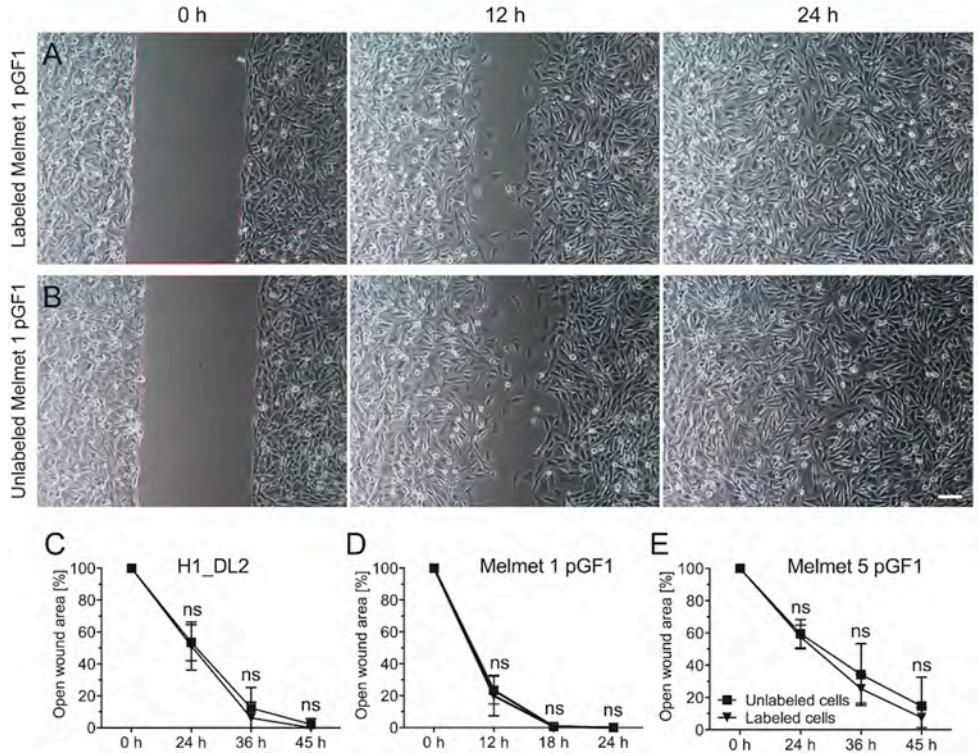

Figure 5. *In vitro* wound healing assay to determine migration capacity. (**A**) Melmet 1 pGF1 cells labeled with 200 µg/mL of nanoprobe; (**B**) unlabeled Melmet 1 pGF1 cells; (**C**) quantification of open wound area of unlabeled and labeled H1_DL2 cells for 45 h; (**D**) quantification of open wound area of unlabeled and labeled Melmet 1 pGF1 cells for 24 h; and (**E**) quantification of open wound area of unlabeled and labeled Melmet 5 pGF1 cells for 45 h. Scale bar: 100 µm; (**C**–**E**) n = 8, mean ± SD. ns: not significant.

2.6. The Surface Charge of the Nanoprobe Is Minimally Affected by pH

The subcellular uptake of the glycogen nanoprobe (Figure 3) could in theory be affected by changes in its surface charge, due to differences in pH within the different cytosolic compartments. Therefore, we measured the zeta-potential of the nanoprobe as a function of pH. We found that the zeta-potential of the glycogen nanoprobe was slightly positive and decreased with increasing pH (obtained values of zeta-potential were 16.7 ± 0.85, 13.8 ± 0.72, 7.28 ± 0.47 and 5.10 ± 0.74 mV, for pH 5.03, 6.00, 6.99 and 7.39, respectively). This can be explained by presence of unreacted amino groups.

2.7. The Nanoprobe Is Stable in Blood Plasma for at Least 60 min

We measured nanoprobe stability over time by fluorescence lifetime correlation spectroscopy (FLCS). In general, our results consistently indicated that the glycogen nanoparticles were stable for at least 60 min in human blood plasma.

We first measured the labeled glycogen in physiological saline, and obtained a recovered diffusion constant of about 4 $\mu m^2/s$, which is around two orders of magnitude lower than what a free dye of the size of Dy-615 would have in water. A closer inspection of the FLCS curve revealed that there was a small fraction of faster diffusing particles, with a diffusion coefficient D around 30–40 $\mu m^2/s$, likely due to a fraction of unbound Dy-615 diffusing in the solution. That means that a small fraction of Dy-615 was non-covalently linked to the glycogen particles and preserved partly its mobility.

We then measured pure human blood plasma, and showed that the autofluorescence intensity after 640 nm laser excitation was very small, less than 5% of the intensity of labeled glycogen under the same conditions, and could therefore be neglected in the subsequent measurements of plasma–glycogen mixtures. The average diffusion coefficient was around 60 $\mu m^2/s$.

The labeled glycogen and blood plasma were then mixed directly in a one-chamber microscope dish, and FLCS was performed. The observed diffusion clearly consisted of two major components. One component was practically identical to the major component of the labeled glycogen in physiological saline (D around 4 $\mu m^2/s$). The other component was faster with a diffusion constant similar to plasma (D around 60 $\mu m^2/s$), and was likely due to a non-covalently linking of a small Dy-615 fraction released from the labeled glycogen to plasma proteins (as seen in saline).

Most importantly, the diffusion of the glycogen nanoparticles themselves (fraction with diffusion constant of about 4 $\mu m^2/s$) did not show any change during 60 min after mixing.

2.8. The Glycogen Nanoprobe Is an Effective Contrast Agent in Vitro

To study whether cell labeling with the glycogen nanoprobe reduced the T_1 relaxation times, we conducted an *in vitro* relaxometry experiment with MRI phantoms (Figure 6A). For Melmet 1 pGF1 cells, we detected a statistically significant reduction in T_1 relaxation times for labeled cells (with 200 μg/mL nanoprobe) down to 750 cells/μL, as compared to the phantoms with unlabeled cells. For phantoms with H1_DL2 and Melmet 5 pGF1 cells, labeled cells reduced the T_1 relaxation down to cell concentrations of 1500 cells/μL, as compared to the control phantoms (Figure 6A). The data also suggested that a concentration of 750 cells/μL of labeled H1_DL2 and Melmet 5 pGFI cells could reduce the relaxation times, however this was not statistically significant.

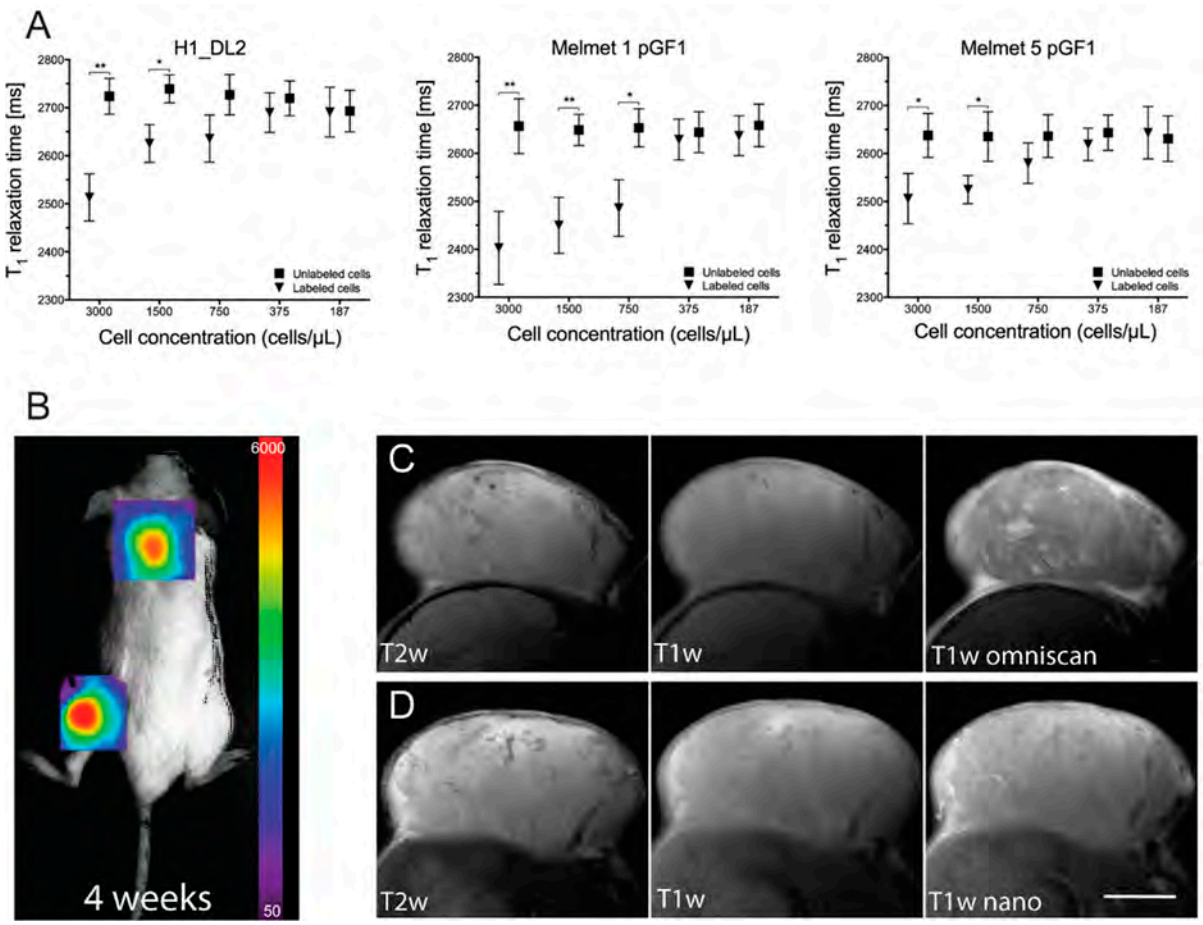

Figure 6. *In vitro* relaxometry and *in vivo* tumor imaging. (**A**) T_1 relaxation times for phantoms containing labeled and unlabeled H1_DL2 cells (**left**), labeled and unlabeled Melmet 1 pGF1 cells (**middle**), and labeled and unlabeled Melmet 5 pGF1 cells (**right**). The different cell concentrations used are shown on the horizontal axis. Mean ± SD, $n = 3$. * $p < 0.05$; ** $p < 0.01$; ms: milliseconds; (**B**) Representative bioluminescence image of tumor growth in one of the NOD/SCID mice four weeks after injection of H1_DL2 cells in the neck and flank area; (**C**) Representative axial MR images of the neck tumors in the same mouse as shown in (**B**), eight weeks after tumor cell injection. T_2 weighted image (**left**), T_1 weighted image before contrast injection (**middle**), and T_1 weighted image after injecting Omniscan (**right**); (**D**) Magnetic resonance (MR) images of the same mouse as in (**C**), using the nanoprobe as contrast agent. T_2 weighted image (**left**), T_1 weighted image before contrast injection (**middle**), and T_1 weighted image after injecting nanoprobe (**right**). Scale bar, 5 mm.

2.9. The Glycogen Nanoprobe Effectively Enhances MRI T_1 Contrast in Subcutaneous Tumors

Tumor take and development was verified by bioluminescence imaging (BLI) four weeks after subcutaneous injection of H1_DL2 cells into the mice, and tumor necrosis was not observed at that time point (Figure 6B). T_2 weighted MRI images acquired eight weeks after tumor cell injections showed tumor edema and necrotic areas within the tumors (Figure 6C-left, Figure 6D-left). Administration of Omniscan showed enhanced tumor contrast on T_1 weighted images (Figure 6D-right),

most likely due to leaky tumor blood vessels, compared to T_1 weighted images obtained before contrast injections (Figure 6D-middle). In addition, contrast enhancement of the tumors on T_1 weighted scans was clearly detected after administration of the nanoprobe (Figure 6D-middle, right).

We then used the T_1 weighted images to calculate the contrast noise ratio (CNR) in tumor *versus* normal tissue adjacent to the tumor on two mice scanned with both contrast agents. We found that the mean CNR value was 42.8 after administration of Omniscan, and 49.5 after administration of the glycogen nanoprobe. This indicated that the contrast efficiency was comparable between Omniscan and the nanoprobe.

2.10. Discussion

In the current study, we show that our novel theranostic, glycogen based nanoprobe effectively and safely labeled several different human melanoma metastatic cell lines. Nanoprobe labeling did not influence the cellular behavior, labeled cells could easily be visualized *in vitro* with microscopy and MRI, and used as an effective *in vivo* MRI contrast agent. To our knowledge, the use of glycogen in a multimodal imaging nanoprobe has not been reported previously in tumor cell imaging.

The fluorescence microscopy experiments showed that our nanoprobe was efficiently internalized into three different human melanoma metastatic cell lines, and the cellular uptake increased with elevated incubation times and doses (Figure 1). The amount of cellular internalization is commonly dependent on cell type, labeling time, and also on several properties of nanomaterials such as size, surface characteristics, morphology and charge [23–25]. Cellular uptake is reported to be dependent on the size of the nanoparticles, and materials around 50 nm (our nanoprobe is 54.4 nm in diameter) are efficiently endocytosed by cells [24,26,27]. We observed variations in fluorescence intensity and thus nanoprobe uptake among the three cell lines investigated. Others have also demonstrated varying internalization rates, using a gadolinium-based nanomaterial to label a larynx cancer cell line, a glioblastoma cell line and healthy lymphocytes [28]. The observed variations in cellular uptake were ascribed to differences in cell membrane permeability among the cell lines, which could also be the case in our experiments.

The uptake of nanoprobe by the cells is likely due to a combination of nonspecific adsorptive endocytosis, clathrin-mediated endocytosis, macropinocytosis and dynamin-dependent endocytosis, as previously described for such materials [29]. These uptake mechanisms do not require specific receptors on the cells, and the zeta potential plays eventually an important role in the uptake. Molecules with positive zeta potential (our nanoprobe is weakly positive) would be more effectively internalized into the cells than neutral or negatively charged particles [29].

In general, labeling of our metastatic melanoma cell lines did not affect cell viability, indicating that the nanoprobe itself was not toxic to the cells (Figure 2). Labeled Melmet 5 pGF1 cells exhibited a slightly reduced capacity to reduce the non-fluorescent resazurin to the highly fluorescent resorufin at 24 h. However, no differences were observed at later time-points. Melmet 1 pGF1 cells showed a slightly reduced viability after 72 h of incubation with the nanoprobe by the resazurin assay. It is likely that cells exposed to the nanoprobe may replace intracellular glycogen with the nanoprobe [22]. Our findings may indicate that the glucose cycle in the Melmet 1 pGF1 cell line was not as effective in utilizing the glycogen as well as in the other two cell lines.

Our nanoprobe was mainly localized in the cytoplasm of the cells, which is in agreement with other studies showing localization of native glycogen within mammalian cells [30]. The signal from Dy-615 was concentrated around the nucleus and scattered throughout the cells in focal areas of varying sizes (Figure 3). In confocal images, co-localization between red and green stained particles would be observed as yellow areas. Since we commonly observed weak yellow areas in our images, a more thorough analysis was performed. The analysis of the subcellular localization of the nanoprobe demonstrated accumulation in lysosomes after 24 h. The nanoprobe was only randomly co-localized with the other markers investigated (Table 1). Accumulation of glycogen into lysosomes is in line with previous *in vivo* experiments on rats [31], and lysosomes have been referred to as the most common organelle involved in intracellular degradation of nanomaterials [26,32].

Our study showed a gradual clearance of the nanoprobe during 96 h (Figure 4). After 72 h, a relatively high amount of fluorescent signal could still be detected, indicating that therapeutic compounds attached to the nanoprobe in future experiments also may be internalized and exert its effects within the cells for several hours. Due to limitations in resolution of our confocal instruments, we could not investigate whether Dy-615 was still attached to the probe at this time point, or if the nanoprobe had been degraded inside the cytoplasm.

Our measurements of the zeta potential showed that the nanoprobe itself exerted a relatively stable, very slightly positive charge (in fact nearly electroneutral—within the range ±30 mV) at different pH levels. According to the manufacturers information on Dyomics probes in general, the fluorescence intensities from these probes are not dependent on variations in pH, as the structure of carboxyl group-conjugated Dyomics 615 does not contain acidobasically active groups that would have pK close to physiological pH range 5–7.4 (the amino groups have very low basicity due to aromatic conjugation). Taken together, the observed decrease in fluorescence intensity over 96 h is likely not due to quenching of the fluorescent signal, but due to clearance of the nanoprobe from the cells. The nanoprobe may be entrapped within secretory vesicles in the Golgi apparatus, before being exocytosed by the cells [20], although we did not observe co-localization between Golgi and nanoprobe in our experiments.

In addition to the suggested lysosomal degradation of the nanoprobe, we also showed that there was a negative correlation between the cell proliferation rate (Figure 4D) and temporal decrease in fluorescence intensity (Figure 4C), indicating that the observed decrease in fluorescence was also caused by dilution of the nanoprobe due to cell proliferation.

There were no differences in migration between unlabeled and labeled cells. This indicates that cellular features such as cytoskeletal structure and cell polarization are not affected due to exposure of the nanoprobe [33,34]. This finding is in line with other studies investigating effects of nanomaterials on cancer cell lines [35].

The *in vitro* MRI study showed that we were able to detect 750 labeled cells/μL after labeling with 200 μg/mL nanoprobe. Terreno and colleagues evaluated the number of Gd-HPDO3A labeled rat hepatocarcinoma cells visible by MRI in agar phantoms [36]. They incubated the cells with contrast agent in standard culture conditions for 16 h (5–100 mM), and showed that the minimum number of cells they were able to detect by MRI was 5000 cells/μL. Thus, our nanoprobe was up to 6.7 times more sensitive *in vitro*, at the concentrations we used.

We observed by fluorescence microscopy that a nanoprobe dose of only 10 μg/mL in the growth medium labeled all cells, however the fluorescence intensity was too low to be effective in further *in vitro* experiments. We did not study if other labeling concentrations would improve the detection limit by MRI, although it is likely that higher labeling concentrations could improve the sensitivity of the MRI methods.

In vivo MRI showed that the glycogen nanoprobe increased contrast on T_1 weighted images after administering the nanoprobe intravenously, which was comparable to what was seen after administering Omniscan to the same tumor. This was also confirmed by the CNR analysis. Thus, we demonstrated a proof-of-principle that our nanoprobe can be used as a contrast agent in MRI, in addition to being an excellent probe for fluorescent imaging.

We have previously described that a 200 μm diameter brain metastasis in our animal/tumor model consists of around 350–400 tumor cells [4]. Here, we show that we were able to detect down to 750 cells/μL in the agar phantoms. In our animal/brain metastasis model [34], brain lesions with a diameter of 300 μm would thus contain around 1300 tumor cells, and should likely be detected by T_1 weighted MRI in experiments *in vivo*, if successfully labeled with our nanoprobe.

We did not investigate by *ex vivo* fluorescence whether the nanoprobe was internalized in the tumor cells *in vivo*, as we did not possess suitable tumor tissue for such analysis, and the main focus in this work was to perform a detailed *in vitro* characterization of the novel nanoprobe. Future studies will address this issue.

Glycogen is relatively inactive to amylase present in the blood, and can thus survive transportation in the bloodstream without being immediately eliminated, as the molecular weight is above the renal threshold [22], which our FLCS study also supports. The FLCS allowed us to track the size of the fluorescently labeled nanoparticles even in a complex environment such as blood plasma. We observed that the slow-moving fraction of the fluorescence (*i.e.*, the intact nanoprobe) did not change its diffusion coefficient within 60 min incubation with blood plasma, implying that the nanoprobe did not change its size due to degradation within this time frame. Our data, however, suggests that when the nanoprobe is internalized in cells, degradation within the lysosomes may occur. Due to the enhanced permeability and retention effects present in most tumors, the nanoprobe may be retained within tumor tissue for several hours after its arrival. Thus, any pharmaceuticals incorporated into the nanoprobe would likely be located within the tumor cells for a corresponding period of time, offering a benefit over conventional chemotherapeutical approaches.

The glycogen nanoprobe would be of particular interest to us in future studies of drug delivery to brain metastasis in our animal brain tumor models [4,35]. The blood brain barrier (BBB) plays an important role in the treatment of brain metastasis, as delivery of chemotherapeutics to small tumors is inefficient due to an intact vascular barrier in the brain. We have previously shown that a wide variety of imaging tracers, with molecular weights ranging between 0.24 and 65.55 kDa, are able to leak across the BBB at various stages of brain metastasis development [2,4]. Even if the size of our nanoprobe is in the order of 10 MDa [22], further modifications of the probe by, for instance, attaching suitable antibodies to the surface, could facilitate receptor-mediated transcytosis of the nanoprobe through the vascular endothelium of the brain [37].

In this study, we show that two different normal human fibroblast cell lines (SV-80 and NSF3) did not accumulate the nanoprobe at labeling concentrations up to 100 μg/mL. This is in line with other

studies, which have shown that nanoparticles may accumulate to more than one order of magnitude in tumors compared to surrounding tissue, due to the EPR effect [20,21]. This implies that while in normal tissues the probe is in the vessels (in blood volume) physically separated from the surrounding tissue by the vessel wall, in tumor tissue it is present mainly in interstitial space in close touch with the tumor cells that subsequently may take up the nanoprobe.

Uptake of nanoprobe into different animal organs, and clearance *in vivo* was not evaluated. Others have injected glycogen into rabbits and found that within a few hours, glycogen had diffused from the bloodstream to other organs. Further, it was suggested that glycogen used by this route of administration could hold a clinical value, as it was considered harmless [38]. It has been demonstrated previously by MRI that our glycogen nanoprobe was eliminated through the mouse kidneys. Six hours after intravenous injections, only a negligible amount of the nanoprobe was found within the kidney of the animals, which suggested minimal renal burden [22].

3. Experimental Section

3.1. Glycogen Nanoprobe

The process of synthesis as well as a detailed characterization of our glycogen nanoprobe has been described previously [22]. Briefly, natural glycogen was modified to an amino group-bearing derivative, and then it was conjugated with 0.33 wt % fluorochrome Dyomics-615-NHS ester (Dy-615) with a fluorescence emission maximum at 643 nm [39] and 3.19 wt % of the MRI T_1 contrast agent gadolinium (Gd-DOTA). It was demonstrated that the nanoprobe holds a spherical shape with a mean diameter at 54.4 nm, has a weakly positive charge and a uniform distribution of contrast agent.

3.2. Cell Lines and Cell Culture

The H1 cell line was developed in our laboratory from a resected brain tumor obtained from a patient with metastatic melanoma [40]. The H1 cells were transduced with two lentiviral vectors, encoding Dendra (a GFP variant) and Luciferase, to obtain the H1_DL2 cell line [35]. The Melmet 1 and Melmet 5 cell lines were established from human metastatic melanomas in subcutaneous tissue and a lymph node, respectively [41]. The Melmet 1 and Melmet 5 cells were transduced with a lentiviral vector, encoding CopGFP (a GFP variant, Systems Biosciences, Inc., Mountain View, CA, USA) and Luciferase, resulting in the Melmet 1 pGF1 and Melmet 5 pGF1 cell lines. Two normal human fibroblast cell lines were also used, the SV-80 lung fibroblast cell line (obtained from CLS Cell Line Services GmbH, Eppelheim, Germany) and the NSF3 skin fibroblast cell line (developed in our lab). We obtained written consent before tumor material was collected. The Regional Ethical Committee (#013.09) and the Norwegian Directorate of Health (#9634) approved the tissue collection and storage.

All cells were grown in Dulbecco's Modified Eagle Medium (DMEM, Sigma-Aldrich Inc., St. Louis, MO, USA) supplemented with 10% heat-inactivated newborn calf serum (Thermo Fisher Scientific, Waltham, MA, USA), 4 times the prescribed concentration of nonessential amino acids (BioWhittaker, Verviers, Belgium), 2% L-glutamine (BioWhittaker), penicillin (100 IU/mL, BioWhittaker), and streptomycin (100 μL/mL, BioWhittaker), hereafter referred to as complete

DMEM. The cells were kept in a standard tissue culture incubator at 37 °C with 100% humidity and 5% CO_2. The growth medium was exchanged twice a week.

3.3. Cellular Internalization of the Nanoprobe

The Melmet 1 pGF1, Melmet 5 pGF1, H1_DL2, SV-80 and NSF3 cell lines were grown in 6-well plates (Nunc, Roskilde, Denmark) at a density of 10^5 cells/mL in a total volume of 2 mL complete DMEM. After 24 h of incubation, the growth medium was replaced with complete DMEM containing the glycogen nanoprobe at final concentrations of 10, 50 or 100 μg/mL. Dishes with unlabeled cells were used as negative controls. After 6 or 24 h of incubation with the nanoprobe, the cells were fixed using 4% paraformaldehyde (PFA, Thermo Fisher Scientific) diluted in phosphate-buffered saline (PBS, Sigma-Aldrich). Subsequently, the cells were studied by fluorescence microscopy with a Nikon TE2000 inverted microscope (Nikon Instruments Inc., Melville, NY, USA) using a 20× ELWD Plan Fluor objective. Micrographs were acquired using the NIS Elements software (64 bit version, Nikon Instruments Inc.), with identical settings (gain 1.7, exposure time 600 ms) for all fluorescence images. The micrographs were processed using Photoshop CS5 (Adobe Systems Inc., San Jose, CA, USA).

In a second internalization study, the three melanoma cell lines were seeded into the wells of three 96-well plates (Nunc) at a density of 4×10^3 cells/mL in a total volume of 100 μL complete DMEM and incubated for 24 h. The medium was then substituted with growth medium containing the nanoprobe at concentrations of 100, 200, 300 or 400 μg/mL (n = 8 wells per concentration), and incubated for 2, 4, 6 or 24 h. Wells with unlabeled cells were used as negative controls. At the different time points, the wells were washed with preheated complete DMEM (37 °C), and imaged with a BD Pathway 855 high content imager (BD Biosciences, San Diego, CA, USA) using the 10× objective. The mean cellular fluorescence within each image was determined using CellProfiler v2.1.1 (Broad Institute, Cambridge, MA, USA).

3.4. Cell Viability

We performed a monolayer resazurin cell viability assay to study cell proliferation during incubation with the nanoprobe. The Melmet 1 pGF1, Melmet 5 pGF1 and H1_DL2 cells were each seeded into the wells of a 96-well dish (Nunc) at a density of 5×10^3 cells per well in 100 μL complete DMEM. After 24 h, the growth medium was exchanged with complete DMEM containing the nanoprobe in final concentrations of 100, 200, 300 or 400 μg/mL. Unlabeled cells were used as negative controls. After another 24 h of incubation, Resazurin solution (0.1 mg/mL, Sigma-Aldrich) was added at a volume corresponding to 10% of the total volume within each well. Following incubation for 4 h, the absorbance was measured at dual mode 560/590 nm with a scanning multiwell spectrophotometer (Victor 3 1420 multi-label counter, Perkin Elmer, Waltham, MA, USA), using WorkOut v2.0 software (Dazdaq Solutions Ltd., East Sussex, UK). This procedure was repeated on Days 2, 3, 4 and 5. The obtained measurements were in relative fluorescence units (RFUs) and based on six parallel samples. Monolayer cell viability was also determined by counting live and dead cells after incubating the cells with the nanoprobe. The cell lines were seeded into three six-well plates (Nunc) at a cell density of 1×10^5 cells/mL in 2 mL of complete DMEM. After an incubation period of 24 h, the growth medium was replaced with complete DMEM containing nanoprobe at a concentration

of 200 μg/mL. Unlabeled cells were used as negative controls. The numbers of live and dead cells were then counted 24, 48 and 72 h after labeling, by adding 0.5 mL trypsin EDTA (BioWhittaker) and mixing 1:1 with growth medium. The cell numbers were determined using a Countess Automated Cell Counter (Invitrogen, Paisley, UK), according to the manufacturer's instructions. The experiment was done in triplicate.

3.5. Subcellular Internalization of the Nanoprobe

We then studied whether organelles within the tumor cells were able to internalize the nanoprobe. In total, 5×10^4 H1 cells were distributed into five poly-L-lysine coated (Sigma-Aldrich Inc.) 25 mm μ-Dishes (Ibidi GmbH, Munich, Germany) and incubated for 24 h. The growth medium was then exchanged with 1 mL 200 μg/mL glycogen nanoprobe diluted in complete DMEM and incubated for another 24 h. We stained the Golgi apparatus using the following method: A 1× Assay Solution (Abcam ab139483, Cambridge, UK) was prepared, containing 1 mL 10× Assay Buffer 1 (Abcam), 0.2 mL 50× Assay Buffer 2 (Abcam) and 8.8 mL milliQ water. 100 μL of this solution was then mixed with 50 nM Golgi Green Detection Reagent (Abcam), before 100 μL of the solution was preheated (37 °C) and added directly into the dish containing adhered cells. The lysosomes were stained by mixing 20 μL LysoGreen Indicator (Abcam ab112136) with 10 mL Live Cell Staining Buffer (Abcam), heated to 37 °C and 100 μL of the solution was added to the cell sample. The plasma membrane was stained using Wheat Germ Agglutinin (WGA), by dissolving 1 mg of Alexa Fluor® 488 Conjugate (Thermo Fisher Scientific) in 1 mL PBS (Sigma-Aldrich), before diluting this to a working solution of 5 μg/mL. 100 μL of this solution was then preheated (37 °C) and added to the cell sample. We stained the endoplasmatic reticulum (ER) by mixing 1 mL Green Detection Reagent (Abcam ab139481) with 1× Assay Solution (Abcam) and adding 100 μL of this preheated (37 °C) solution to the cell sample. For staining of the nucleus, the cells were incubated at room temperature for 30 min in growth medium containing 1 μg/mL Hoechst 33342 (Life Technologies). All cells were then washed twice with PBS and fixed with 2 mL 4% PFA (Thermo Scientific).

Mitochondria staining was carried out by incubating the cells with 150 nM MitoTracker® Green FM (Invitrogen) for 30 min before the labeling solution was replaced with complete DMEM. Live cell imaging was performed using a Leica TCS SP5 confocal microscope (Leica Microsystems, Wetzlar, Germany), with excitation wavelengths of 408, 488 and 633 nm, and a 63× HCX PL Apo objective with NA 1.4. All images were processed using Imaris V 7.6.3 (Bitplane AG, Zürich, Switzerland). Co-localization was investigated in 3D image stacks with the co-localization plugin after the cells were cropped to optimal size and the auto-threshold function was applied. The Pearson's correlation coefficient was measured and the average of all values for each organelle marker was determined. The Pearson's correlation coefficient, R, describes the relationship in intensity distribution between two color channels, and the value ranges from −1 to 1. Values between −1 and 0.5 suggest no co-localization, $R > 0.5$ suggest some degree of co-localization and $R = 1$ suggests complete co-localization [42].

3.6. Nanoprobe Clearance

The Melmet 1 pGF1, Melmet 5 pGF1 and H1_DL2 cells were seeded into six-well plates at a density of 1×10^5 cells/mL in 2 mL complete DMEM, and incubated for 24 h. The growth medium was then replaced with complete DMEM containing nanoprobe at a concentration of 200 μg/mL. After a further incubation period of 24 h, the labeling solution was exchanged with complete DMEM without nanoprobe. Four micrographs of the labeled cells were captured every 24 h for four days using a Nikon TE2000 inverted microscope (Nikon Instruments Inc., NY, USA) with a 20× objective. In each micrograph, 16 single cells were processed to find the average cellular fluorescence intensity using Photoshop CS5 (Adobe Systems Inc., San Jose, CA, USA).

3.7. Study of in Vitro Cell Migration

To study the effects of the nanoprobe on cell migration, a monolayer wound healing assay was performed. A silicone culture insert (Ibidi GmbH, Martinsried, Germany) was positioned into each well of a 4-well μ-Slide (Ibidi GmbH). 70 μL of H1_DL2, Melmet 1 pGF1 and Melmet 5 pGF1 cell solution at a concentration of 5×10^5 cells/mL was then added into each half of the culture inserts. The cells were allowed to grow to confluence before the culture insert was removed, resulting in a cell free gap with a width of 500 μm within the culture. All chambers were washed twice with preheated (37 °C) complete DMEM before the chambers were filled with 500 μL growth medium containing 200 μg/mL nanoprobe. As negative control, chambers were filled with 500 μL growth medium without the nanoprobe. Immediately afterwards, cell migration into the wound was studied by time lapse microscopy for 60 h using a Nikon TE2000 inverted microscope (Nikon Instruments Inc., Melville, NY, USA) equipped with an incubator holding 37 °C, 100% humidity and 5% CO_2. Images were then processed and analyzed using ImageJ v1.46a freeware (National Institutes of Health, Bethesda, MA, USA).

3.8. Measurement of Zeta-Potential

The glycogen nanoprobe was diluted in 0.01 M phosphate buffer to obtain 0.1% (wt) solution. The pH of each sample was adjusted to accurate value using few microliters of diluted HCl or NaOH solution. Measurement was performed with Zetasizer Nano-ZS instrument (Malvern Instruments Ltd., Malvern, UK) that computes the zeta potential through the Henry equation.

3.9. Measurement of Stability of the Glycogen Nanoprobe in Blood Plasma by Fluorescence Lifetime Correlation Spectroscopy (FLCS)

FLCS is a variant of fluorescence correlation spectroscopy (FCS), which uses differences in rates of fluorescence intensity decays to obtain separate FCS autocorrelation functions (ACFs) of individual fluorophore populations in a mixture [43]. We used this technique to study the stability of the labeled glycogen nanoprobe in human blood plasma. The FLCS experiments were performed using an Olympus IX83 confocal laser scanning microscope with FluoView 1200 software (Olympus Corporation, Tokyo, Japan), extended with a FLIM/FLCS upgrade kit and SymphoTime64 software (PicoQuant

GmbH, Berlin, Germany). The measurements were performed with a 640 nm pulsed laser with repetition frequency of 40 MHz and with PMA hybrid detectors.

First, a reference measurement of the labeled glycogen nanoprobe with a concentration of 500 μg/mL in physiological saline was performed; Second, a measurement of human blood plasma (obtained from Sigma-Aldrich Ltd., Prague, Czech Republic) was performed with the same setup as for the reference experiment. The labeled glycogen nanoprobe and blood plasma were then mixed directly in a one-chamber microscope dish (with the same final nanoprobe concentration, *i.e.*, 125 μg/mL). Several measurements were performed, one immediately after mixing, and then 20, 40 and 60 min later. For the measurements in blood plasma, the FLCS curves were fitted with a two component model, to obtain the recovered diffusion constants.

3.10. In Vitro MR Relaxometry

The Melmet 1 pGF1, Melmet 5 pGF1 and H1_DL2 cells were prelabeled with nanoprobe (200 μg/mL) in monolayer for 24 h, as described in previous sections. A 2% Difco Agar Noble solution (BD, Franklin Lakes, NJ, USA) was prepared in autoclaved water, microwaved and placed in a preheated waterbath (50 °C). The agar solution was further mixed 1:1 with growth medium containing prelabeled cells. The agar/cell solution was then aliquoted into five different 2 mL eppendorf tubes (Eppendorf Instrumente GmbH, Hamburg, Germany), at concentrations 3000, 1500, 750, 375 or 187 cells/μL. As negative controls, unlabeled cells were introduced into five additional 2 mL eppendorf tubes, with the same cell concentrations as above.

The tubes were examined at 21 °C using a 7 T small animal MRI scanner (Bruker Biospin MRI GmbH, Ettlingen, Germany) equipped with a 40 mm quadrature volume coil. A T_2 weighted turbo spin echo scan was performed (repetition time (TR) 4000 ms, echo time (TE) 48 ms, field of view (FOV) 2.0 cm, matrix size 256 × 256, slice thickness 1 mm, 15 slices, number of acquisitions (NEX) 4, axial sectioning) to verify homogeneity of the agar/cell solution. Then, a spin echo T_1 mapping sequence was obtained (TR 5000, 3000, 1500, 800, 400 and 200 ms, TE 33 ms, FOV 3.5 cm, matrix size 256 × 256, slice thickness 1 mm, 1 slice NEX 1). Within the image of each tube, a region of interest (ROI) covering 75% of the surface area of the tube was defined in the scan software (ParaVision 5.1), and T_1 relaxation values of the tubes were calculated.

3.11. Animal Model and Tumor Cell Injections

Twelve-week-old female NOD/SCID mice were bred and maintained in animal facilities under standard conditions, being fed a standard pellet diet and provided water *ad libitum*. The National Animal Research Authority approved all animal procedures (Application No. 20135046, approved 7 May 2013).

H1_DL2 cells were cultured in 175 cm^2 flasks (Nunc), trypsinated and centrifuged at 900 rpm for four min. The medium was removed, and the cell pellet was dissolved in PBS (Sigma-Aldrich Inc.) at a concentration of 10^7 cells/mL. The cells were kept on ice prior to injections. Two anaesthetized mice (2% isoflurane) were injected subcutaneously with 0.1 mL cell solution (10^6 cells) in their left flank or neck using a 30G insulin syringe (Omnican50, B. Brain Melsungen AG, Melsungen, Germany). This is an animal model that is already in use and thus well tested and highly standardized [4,40,44].

3.12. Bioluminescence Imaging (BLI) of Tumor Development

After 4 weeks, bioluminescence imaging (BLI) was performed to verify tumor take and growth. This would also suggest that contrast enhancement by MRI could be achieved after administrating the glycogen nanoprobe. Briefly, anaesthetized mice (2% isoflurane) were injected intraperitoneally with 150 mg/kg D-luciferin 10 min prior to whole body imaging, performed with an Optix® MX2 Small Animal Molecular Imager (ART Inc., Saint-Laurent, QC, Canada). Bioluminescent images were acquired with Optix® OptiviewTM (ART Inc.) acquisition software (version 2.00) using an integration time of 0.3 s and a scan resolution of 1.5 mm, and analyzed using Optix® OptiviewTM (version 2.00.01, ART Inc.).

3.13. Pilot in Vivo MRI Experiment

In vivo MRI experiments were carried out on the mice 8 weeks after tumor cell injection, at which time the tumor sizes were approximately 16 × 9 mm. A 7 T small animal MRI scanner (Bruker Biospin MRI GmbH) equipped with a 72 mm quadrature transmit coil and a mouse brain array receive coil was used. T_2 weighted spin echo scans were initially acquired with a region of interest over the subcutaneous neck tumors of the mice (TR 4300 ms, TE 36 ms, FOV 2 cm, matrix size 256 × 256, slice thickness 1.5 mm, number of slices 25, NEX 3, axial sectioning). Tumor contrast agent uptake was then studied by T_1 weighted spin echo scans (TR 1000/740 ms, TE 9 ms, FOV 2 cm, matrix size 256 × 256, slice thickness 1.5 mm, number of slices 11, NEX 6, axial sectioning) before and immediately after administrating 0.5 μmol glycogen nanoprobe or Omniscan (GE Healthcare, Fairfield, CT, USA) through the tail veins. Each animal was first studied with Omniscan, and, after 24 h, the same animal was studied using nanoprobe. T_1 mapping studies were not performed, to minimize scan time and thus lower the burden to the animals.

The MR images were processed using the ImageJ freeware (version 1.46r, National Institute of Health, Bethesda, MD, USA). Briefly, the regions of interests were carefully outlined around the area containing tumor excluding necrotic tissue and CNR was assessed. CNR in T_1 weighted MR images obtained after contrast injections were calculated according to the formula: $CNR = (ST - SN)/SD$, where ST represents mean signal intensity from tumor tissue, SN means signal intensity from normal tissue directly outside the tumor, and SD is the standard deviation of the noise.

3.14. Statistical Analysis

Linear regressions and statistical analyses were performed using GraphPad Prism v7 for Mac OS X (GraphPad Software, Inc., La Jolla, CA, USA). Unpaired two-tailed Students *t*-tests were used. Values are presented as mean ± standard deviation (SD). For all tests, a p value < 0.05 was considered statistically significant.

4. Conclusions

In summary, we have robust data indicating that the nontoxic glycogen nanoprobe is a highly functional imaging probe, both for fluorescence microscopy and MRI. Our data show that the nanoprobe is taken up into the cytoplasm of the tumor cells, and that the probe is likely degraded

inside the lysosomes. We now have an excellent foundation upon which we can base further experiments in studies on combined therapeutic and diagnostic issues in metastatic melanoma, including brain metastasis.

Supplementary Materials

Supplementary materials can be found at http://www.mdpi.com/1422-0067/16/09/21658/s1.

Acknowledgments

This study was funded by the University of Bergen, the Norwegian Cancer Society, the Norwegian Research Council, the Kristian Gerhard Jebsen Foundation, the Grant Agency of the Czech Republic (grant # 13-08336S), the Academy of Sciences of the Czech Republic (grant # M200501201), the Ministry of Health, Czech Republic (grant # 15-25781A) and funds for development of research organization 00023001 (IKEM, Prague, Czech Republic). The Melmet 1 and Melmet 5 cell lines were generously provided by Øystein Fodstad at the Oslo University Hospital, Norway. We thank Bodil Hansen and Tove Johansen for technical assistance, Hege Dale for assisting with the MitoTracker confocal experiments, and Ian Pryme for correcting the English language.

Author Contributions

Synnøve Nymark Aasen performed monolayer experiments on internalization, nanoprobe localization, cell viability and nanoprobe clearance, wound healing, *in vitro* MRI, and *in vivo* MRI and BLI. Aneta Pospisilova did the synthesis of the nanoprobe. Tilo Wolf Eichler performed the subcellular internalization study. Jiri Panek performed FLCS. Martin Hruby did a physico-chemical characterization of the nanoprobe, data evaluation, and writing the corresponding parts of the text. Petr Stepanek performed data interpretation. Endy Spriet performed *in vitro* wound healing experiments. Daniel Jirak did pilot testing of the nanoprobe by MRI and data evaluation. Kai Ove Skaftnesmo transfected the cell lines with reporter genes. Frits Thorsen was responsible for the design of this study, contributed to the *in vivo* experiments, and made all figures. Synnøve Nymark Aasen and Frits Thorsen wrote the manuscript. All authors read and approved the manuscript.

Conflicts of Interest

The authors declare no conflict of interest.

References

1. Spano, D.; Zollo, M. Tumor microenvironment: A main actor in the metastasis process. *Clin. Exp. Metastasis* **2012**, *29*, 381–395.
2. Fink, K.R.; Fink, J.R. Imaging of brain metastases. *Surg. Neurol. Int.* **2013**, *4* (Suppl. 4), S209–S219.
3. Giovannini, E.; Lazzeri, P.; Milano, A.; Gaeta, M.C.; Ciarmiello, A. Clinical applications of choline PET/CT in brain tumors. *Curr. Pharm. Des.* **2015**, *21*, 121–127.

4. Thorsen, F.; Fite, B.; Mahakian, L.M.; Seo, J.W.; Qin, S.; Harrison, V.; Johnson, S.; Ingham, E.; Caskey, C.; Sundstrøm, T.; *et al.* Multimodal imaging enables early detection and characterization of changes in tumor permeability of brain metastases. *J. Control. Release* **2013**, *172*, 812–822.
5. Jang, E.S.; Lee, S.Y.; Cha, E.J.; Sun, I.C.; Kwon, I.C.; Kim, D.; Kim, Y.I.; Kim, K.; Ahn, C.H. Fluorescent dye labeled iron oxide/silica core/shell nanoparticle as a multimodal imaging probe. *Pharm. Res.* **2014**, *12*, 3371–3378.
6. Xing, Y.; Zhao, J.; Conti, P.S.; Chen, K. Radiolabeled nanoparticles for multimodality tumor imaging. *Theranostics* **2014**, *4*, 290–306.
7. Khemtong, C.; Kessinger, C.W.; Gao, J. Polymeric nanomedicine for cancer MR imaging and drug delivery. *Chem. Commun.* **2009**, *24*, 3497–3510.
8. Lee, D.E.; Koo, H.; Sun, I.C.; Ryu, J.H.; Kim, K.; Kwon, I.C., Multifunctional nanoparticles for multimodal imaging and theragnosis. *Chem. Soc. Rev.* **2012**, *41*, 2656–2672.
9. Sumer, B.; Gao, J. Theranostic nanomedicine for cancer. *Nanomedicine* **2008**, *3*, 137–140.
10. Li, N.; Yang, H.; Pan, W.; Diao, W.; Tang, B. A tumour mRNA-triggered nanocarrier for multimodal cancer cell imaging and therapy. *Chem. Commun.* **2014**, *50*, 7473–7476.
11. Laurent, S.; Saei, A.A.; Behzadi, S.; Panahifar, A.; Mahmoudi, M. Superparamagnetic iron oxide nanoparticles for delivery of therapeutic agents: Opportunities and challenges. *Exp. Opin. Drug Deliv.* **2014**, *9*, 1449–1470.
12. Jain, K.K. Nanobiotechnology-based strategies for crossing the blood-brain barrier. *Nanomedicine* **2012**, *7*, 1225–1233.
13. Horowitz, P.M.; Chiocca, E.A. Nanotechnology-based strategies for the diagnosis and treatment of intracranial neoplasms. *World Neurosurg.* **2013**, *80*, 53–55.
14. Wang, T.; Kievit, F.M.; Veiseh, O.; Arami, H.; Stephen, Z.R.; Fang, C.; Liu, Y.; Ellenbogen, R.G.; Zhang, M. Targeted cell uptake of a noninternalizing antibody through conjugation to iron oxide nanoparticles in primary central nervous system lymphoma. *World Neurosurg.* **2013**, *80*, 134–141.
15. Yuk, S.H.; Oh, K.S.; Cho, S.H.; Lee, B.S.; Kim, S.Y.; Kwak, B.K.; Kim, K.; Kwon, I.C. Glycol chitosan/heparin immobilized iron oxide nanoparticles with a tumor-targeting characteristic for magnetic resonance imaging. *Biomacromolecules* **2011**, *12*, 2335–2343.
16. Chung, Y.I.; Kim, J.C.; Kim, Y.H.; Tae, G.; Lee, S.Y.; Kim, K.; Kwon, I.C. The effect of surface functionalization of PLGA nanoparticles by heparin- or chitosan-conjugated pluronic on tumor targeting. *J. Control. Release* **2010**, *143*, 374–382.
17. Mansa, R.; Detellier, C. Preparation and characterization of guar-montmorillonite nanocomposites. *Materials* **2013**, *6*, 5199–5216.
18. Wanga, C.; Huang, Y. Facile preparation of fluorescent Ag-clusters–chitosan-hybrid nanocomposites for bio-applications. *New J. Chem.* **2014**, *38*, 657–662.
19. Win, K.Y.; Feng, S.S. Effects of particle size and surface coating on cellular uptake of polymeric nanoparticles for oral delivery of anticancer drugs. *Biomaterials* **2005**, *26*, 2713–2722.
20. Sakhtianchi, R.; Minchin, R.F.; Lee, K.B.; Alkilany, A.M.; Serpooshan, V.; Mahmoudi, M. Exocytosis of nanoparticles from cells: Role in cellular retention and toxicity. *Adv. Colloid Interface Sci.* **2013**, *201–202*, 18–29.

21. Ridley, A.J.; Schwartz, M.A.; Burridge, K.; Firtel, R.A.; Ginsberg, M.H.; Borisy, G.; Parsons, J.T.; Horwitz, A.R. Cell migration: Integrating signals from front to back. *Science* **2003**, *302*, 1704–1709.
22. Filippov, S.K.; Sedlacek, O.; Bogomolova, A.; Vetrik, M.; Jirak, D.; Kovar, J.; Kucka, J.; Bals, S.; Turner, S.; Stepanek, P.; *et al.* Glycogen as a biodegradable construction nanomaterial for *in vivo* use. *Macromol. Biosci.* **2012**, *12*, 1731–1738.
23. Naahidi, S.; Jafari, M.; Edalat, F.; Raymond, K.; Khademhosseini, A.; Chen, P. Biocompatibility of engineered nanoparticles for drug delivery. *J. Control. Release* **2013**, *166*, 182–194.
24. Zhang, S.; Li, J.; Lykotrafitis, G.; Bao, G.; Suresh, S. Size-dependent endocytosis of nanoparticles. *Adv. Mater.* **2009**, *21*, 419–424.
25. Barua, S.; Rege, K. Cancer-cell-phenotype-dependent differential intracellular trafficking of unconjugated quantum dots. *Small* **2009**, *5*, 370–376.
26. Kelf, T.A.; Sreenivasan, V.K.; Sun, J.; Kim, E.J.; Goldys, E.M.; Zvyagin, A.V. Non-specific cellular uptake of surface-functionalized quantum dots. *Nanotechnology* **2010**, *21*, 285105.
27. Chithrani Devika, B.; Chan, W.C.W. Elucidating the mechanism of cellular uptake and removal of protein-coated gold nanoparticles of different sizes and shapes. *Nano Lett.* **2007**, *7*, 1542–1550.
28. Rima, W.; Sancey, L.; Aloy, M.T.; Armandy, E.; Alcantara, G.B.; Epicier, T.; Malchere, A.; Joly-Pottuz, L.; Mowat, P.; Lux, F.; *et al.* Internalization pathways into cancer cells of gadolinium-based radiosensitizing nanoparticles. *Biomaterials* **2013**, *34*, 181–195.
29. Liu, J.; Bauer, H.; Callahan, J.; Kopečková, P.; Pan, H.; Kopeček, J. Endocytic uptake of a large array of HPMA copolymers: Elucidation into the dependence on the physicochemical characteristics. *J. Control. Release* **2010**, *143*, 71–79.
30. Ferrer, J.C.; Favre, C.; Gomis, R.R.; Fernández-Novell, J.M.; García-Rocha, M.; de la Iglesia, N.; Cid, E.; Guinovart, J.J. Control of glycogen deposition. *FEBS Lett.* **2003**, *546*, 127–132.
31. Glaumann, H.; Fredzell, J.; Jubner, A.; Ericsson, J.L.E. Uptake and degradation of glycogen by Kupffer cells. *Exp. Mol. Pathol.* **1979**, *31*, 70–80.
32. Rejman, J.; Oberle, V.; Zuhorn, I.S.; Hoekstra, D. Size-dependent internalization of particles via the pathways of clathrin- and caveolae-mediated endocytosis. *Biochem. J.* **2004**, *377 Pt 1*, 159–169.
33. Fenouille, N.; Tichet, M.; Dufies, M.; Pottier, A.; Mogha, A.; Soo, J.K.; Rocchi, S.; Mallavialle, A.; Galibert, M.D.; Khammari, A.; *et al.* The epithelial-mesenchymal transition (EMT) regulatory factor SLUG (SNAI2) is a downstream target of SPARC and AKT in promoting melanoma cell invasion. *PLoS ONE* **2012**, *7*, e40378.
34. Eikenes, L.; Bruland, O.S.; Brekken, C.; Davies Cde, L. Collagenase increases the transcapillary pressure gradient and improves the uptake and distribution of monoclonal antibodies in human osteosarcoma xenografts. *Cancer Res.* **2004**, *64*, 4768–4773.
35. Sundstrøm, T.; Daphu, I.; Wendelbo, I.; Hodneland, E.; Lundervold, A.; Immervoll, H.; Skaftnesmo, K.O.; Babic, M.; Jendelova, P.; Syková, E.; *et al.* Automated tracking of nanoparticle-labeled melanoma cells improves the predictive power of a brain metastasis model. *Cancer Res.* **2013**, *73*, 2445–2456.
36. Terreno, E.; Geninatti Crich, S.; Belfiore, S.; Biancone, L.; Cabella, C.; Esposito, G.; Manazza, A.D.; Aime, S. Effect of the intracellular localization of a Gd-based imaging probe on the relaxation enhancement of water protons. *Magn. Res. Med.* **2006**, *55*, 491–497.

37. Chacko, A.-M.; Li, C.; Pryma, D.A.; Brem, S.; Coukos, G.; Muzykantov, V. Targeted delivery of antibody-based therapeutic and imaging agents to CNS tumors: Crossing the blood-brain barrier divide. *Exp. Opin. Drug Deliv.* **2013**, *10*, 907–926.
38. Morris, D.L. Some effects of the intravenous injection of corn glycogen into rabbits. *J. Biol. Chem.* **1943**, *148*, 699–706.
39. Czerney, P. Dyomics—Colours for life. In *Fluorescent Dyes for Bioanalytical and Hightech Applications*, 7th ed.; Dyomics GmbH, Jena, Germany, 2011; Volume 7, p. 84.
40. Wang, J.; Daphu, I.; Pedersen, P.H.; Miletic, H.; Hovland, R.; Mørk, S.; Bjerkvig, R.; Tiron, C.; McCormack, E.; Micklem, D.; *et al.* A novel brain metastases model developed in immunodeficient rats closely mimics the growth of metastatic brain tumours in patients. *Neuropathol. Appl. Neurobiol.* **2011**, *37*, 189–205.
41. Prasmickaite, L.; Skrbo, N.; Høifødt, H.K.; Suo, Z.; Engebraten, O.; Gullestad, H.P.; Aamdal, S.; Fodstad, Ø.; Maelandsmo, G.M. Human malignant melanoma harbours a large fraction of highly clonogenic cells that do not express markers associated with cancer stem cells. *Pigment Cell Melanoma Res.* **2010**, *23*, 449–451.
42. Pawley, J.B. *Handbook of Biological Confocal Microscopy*, 3rd ed.; Springer Science + Business Media: New York, NY, USA, 2006.
43. Kapusta, P.; Macháň, R.; Benda, A.; Hof, M. Fluorescence lifetime correlation spectroscopy (FLCS): Concepts, applications and outlook. *Int. J. Mol. Sci.* **2012**, *13*, 12890–12910.
44. Daphu, I.; Sundstrøm, T.; Horn, S.; Huszthy, P.C.; Niclou, S.P.; Sakariassen, P.Ø.; Immervoll, H.; Miletic, H.; Bjerkvig, R.; Thorsen, F. *In vivo* animal models for studying brain metastasis: Value and limitations. *Clin. Exp. Metastasis* **2013**, *30*, 695–710.

Improved drug delivery to brain metastases by peptide-mediated permeabilization of the blood-brain barrier

List of authors

Synnøve Nymark Aasen[1,2], Heidi Espedal[2,3], Christopher Florian Holte[2], Olivier Keunen[4], Tine Veronika Karlsen[5], Olav Tenstad[5], Zaynah Maherally[6], Hrvoje Miletic[2,7], Tuyen Hoang[2], Anne Vaag Eikeland[8], Habib Baghirov[9], Dag Erlend Olberg[10,11], Geoffrey J. Pilkington[7], Gobinda Sarkar[12], Robert Jenkins[12], Terje Sundstrøm[2,13,14], Rolf Bjerkvig[2,4,*] and Frits Thorsen[2,3,*]

Affiliations

[1] Department of Oncology and Medical Physics, Haukeland University Hospital, Bergen, Norway.

[2] Kristian Gerhard Jebsen Brain Tumor Research Centre, Department of Biomedicine, University of Bergen, Bergen, Norway.

[3] Molecular Imaging Center, Department of Biomedicine, University of Bergen, Bergen, Norway.

[4] Department of Oncology, Luxembourg Institute of Health, Luxembourg, Luxembourg.

[5] Department of Biomedicine, University of Bergen, Bergen, Norway.

[6] Brain Tumor Research Centre, Institute of Biomedical and Biomolecular Sciences, University of Portsmouth, Portsmouth, PO1 2DT, UK.

[7] Department of Pathology, Haukeland University Hospital, Bergen, Norway.

[8] Department of Radiology, Haukeland University Hospital, Bergen, Norway.

[9] Department of Physics, Norwegian University of Science and Technology, Trondheim, Norway.

[10] Department of Pharmaceutical Chemistry, University of Oslo, Oslo, Norway.

[11] Norwegian Cyclotron Center, Oslo University Hospital, Oslo, Norway.

[12] Department of Experimental Pathology, Mayo Clinic, Rochester MN, USA.

[13] Department of Neurosurgery, Haukeland University Hospital, Bergen, Norway.

[14] Department of Clinical Medicine, University of Bergen, Bergen, Norway.

[*] Equal contributions

Running title: Peptide-mediated drug delivery to experimental brain metastasis

Keywords: Brain metastases, K16ApoE, blood-brain barrier (BBB), drug delivery, targeted therapy

Financial support: The study was funded by the Western Norway Regional Health Authority, the Kristian Gerhard Jebsen Foundation, the Norwegian Cancer Society, Animal Free Research UK and Brain Tumor Research.

Correspondence to: Frits Thorsen, Department of Biomedicine, University of Bergen, Jonas Lies vei 91, N-5009, BERGEN, Norway. Phone: +47 95749681. E-mail: Frits.Thorsen@uib.no

Disclosure of potential conflict of interest: The authors declare no potential conflict of interest.

Abstract

Melanoma patients have a high risk of developing brain metastasis, which is associated with a dismal prognosis. During early stages of metastasis development, the blood-brain barrier (BBB) is likely intact, which inhibits sufficient drug delivery into the metastatic lesions. We investigated the ability of the peptide, K16ApoE, to permeabilize the BBB for improved treatment with targeted therapies preclinically. DCE-MRI was carried out on NOD/SCID mice to study the therapeutic window of peptide-mediated BBB permeabilization. Further, both *in vivo* and *in vitro* assays were used to determine K16ApoE toxicity and to obtain mechanistic insight into its action on the BBB. The therapeutic impact of K16ApoE on metastases was evaluated combined with the mitogen-activated protein kinase pathway inhibitor dabrafenib, targeting BRAF mutated melanoma cells, which is otherwise known not to cross the intact BBB. Our results from the DCE-MRI experiments showed effective K16ApoE-mediated BBB permeabilization lasting for at least one hour. Mechanistic studies showed a dose-dependent effect of K16ApoE caused by induction of endocytosis. At concentrations above IC_{50}, the peptide additionally showed nonspecific disturbances on plasma membranes. Combined treatment with K16ApoE and dabrafenib reduced the brain metastatic burden in mice and increased animal survival, and PET/CT showed that the peptide also facilitated the delivery of compounds with molecular weights as large as 150 kDa into the brain. To conclude, we demonstrate a transient permeabilization of the BBB, caused by K16ApoE, that facilitates enhanced drug delivery into the brain. This improves the efficacy of drugs that otherwise do not cross the intact BBB.

Introduction

Brain metastasis is a frequently reported complication for patients with cutaneous melanoma where the average survival time, if untreated, is 3–5 months. Current treatment strategies involve surgery, systemic therapy, radiotherapy and/or radiosurgery (1). This can to some extent increase the survival time, yet with a divergent treatment efficacy, emphasizing the need for new treatment options.

It is well known that melanomas are molecularly heterogeneous (2) and immunogenic tumors (3), properties that have been exploited for drug development (4). For instance, it has been shown that the serine/threonine kinase protein BRAF is a key molecular driver of metastatic melanoma, which has led to the development of several BRAF inhibitors (BRAFi). Furthermore, immune checkpoint inhibitors such as PD-1/PD-L1 have shown a strong clinical efficacy in clinical trials for melanoma (5-7). However, a recurring issue is that many of these drugs are too large to cross the intact interface between circulating blood and the brain parenchyma, i.e. the blood-brain barrier (BBB) (8,9). The BBB consists of vascular endothelial cells linked by tight junctions, encircled by astrocytic end-feet and pericytes leading to a selective barrier that determines the entry of molecules into the brain (10). This barrier represents in many instances a major obstacle for systemic brain metastasis treatment. Compounds that consist of more than eight to ten hydrogen bonds and are larger than 400–500 Da are prohibited from entering the brain. All large molecular drugs, such as antibodies, and 98% of small molecular drugs are excluded from the brain by the BBB (11). The brain is thus considered as a sanctuary site for metastatic growth (12) and the exposure to drugs is lower in brain metastases than systemic metastases. This is not only ascribed to the presence of the BBB but also the blood-tumor barrier (BTB) (13). The BTB differs from the BBB in that the vascular system is no longer surrounded by the other, normal BBB components, but tumor cells. Due to this structural difference, the BTB is proposed to be more permeable than the BBB (14). Micro-metastases, i.e. lesions smaller than 1 mm^3, usually have a lower permeability than larger metastases, in which the BTB might be compromised as a result of tumor growth (15). Systemic therapy may therefore show

efficacy on larger metastatic lesions, whereas micro-metastases receive subtherapeutic drug concentrations, which can contribute to treatment resistance (16). However, it has also been shown that there is not necessarily a straightforward association between brain metastasis size and drug uptake. Within the same lesion, the distribution can vary up to 10-folds (17). Also, melanoma patients with advanced disease can present with multiple brain metastases of different sizes with varying BTB integrities, further challenging the systemic treatment (18). Several strategies have therefore been developed to temporarily disrupt the BBB for improved drug delivery such as focused ultrasound combined with circulating microbubble contrast agents (19-21), hyperosmotic opening (22-24) and radiotherapy (25). Other strategies involve the circumvention of the BBB by convection-enhanced delivery (26), viral-mediated or liposomal delivery (27), carrier molecules (28) and polymer wafers (29). These strategies have shown both strengths and weaknesses, but with limited success and many with apparent side effects (30,31).

It has previously been reported that the synthetic peptide K16ApoE can carry relatively large compounds into the mouse brain through the low-density lipoprotein receptor (LDLR) pathway (32). The use of K16ApoE in a therapeutic setting *in vivo*, however, has not been investigated. Here we determined, using advanced magnetic resonance imaging (MRI) techniques, the length of the therapeutic time window of K16ApoE BBB permeabilization in NOD/SCID mice and also its *in vivo* toxicity profile. Moreover, the morphological and functional effects of the peptide on cells and tissues were elucidated. In addition, we assessed the ability of K16ApoE to enhance drug delivery of a clinically active BRAFi (dabrafenib) on preclinical brain metastases, which was our main objective with this study. Finally, using PET/CT as an *in vivo* biodistribution tool for studying brain penetration, we assessed the potential of the peptide to deliver compounds to the brain with a size range corresponding to clinically relevant immune checkpoint inhibitors.

Materials and methods

K16ApoE peptide design and production

The K16ApoE peptide has the following amino acid sequence: KKKK-KKKK-KKKK-KKKK-LRVR-LASH-LRKL-RKRL-LRDA with a molecular weight (M_W) of 4 521.79 Da. The synthesis and characterization of the peptide is elaborated in Supplementary Materials. Briefly, a series of 16 lysine residues (K16) was covalently linked to the 20 amino acid part of the low-density lipoprotein receptor binding segment of apolipoprotein E (ApoE).

Cell culture

Five cell lines were used as constituents of the *in vitro* model system of the BBB, namely Mabin-Darby Canine Kidney (MDCK) cells, MDCK II, rat brain endothelial cells 4 (RBE4), human brain endothelial cells (hCMEC/D3) and human brain astrocytes (SC-1800). In addition, two brain metastatic melanoma cell lines were used; H1 (or H1_DL2) and H2. See Supplementary Materials.

Animals

Female non-obese diabetic/severe combined immunodeficient (NOD/SCID) mice were purchased from Envigo (Gannat, France). The animals were bred and maintained in our animal facility certified by the Association for Assessment and Accreditation of Laboratory Animal Care International. They were fed a standard pellet diet and provided water *ad libitum*. The National Animal Research Authority approved all animal procedures (Application #8093, approved February 13th, 2016). Anaesthesia was induced with 3% sevoflurane (Abbott Laboratories Ltd., Berkshire, UK) in oxygen and maintained with 1.5% sevoflurane in oxygen during all procedures unless stated otherwise. The mice were monitored daily and sacrificed when significant morbidity symptoms were observed.

Evaluation of the *in vivo* toxicity of K16ApoE

The toxicity of K16ApoE was evaluated by intravenous tail vein injections of increasing concentrations of peptide into 38 NOD/SCID mice as described in Supplementary Materials and Supplementary Figure S1A.

Dynamic Contrast Enhanced Magnetic Resonance Imaging (DCE-MRI)

DCE-MRI was carried out using a 7 Tesla small-animal horizontal scanner (Bruker BioSpin GmbH, Ettlingen, Germany), using a 72 mm quadrature transmit coil and a 4-channel mouse brain array receive coil. The animals were placed in prone position and body temperature was maintained at 37 °C.

T_1 and T_2 weighted spin echo scans were acquired to provide anatomical references by using fast spin echo (FSE) protocols as described in Supplementary Materials. The mice received a dose of 50 (n=5), 100 (n=11) or 200 μg (n=5) of K16ApoE dissolved in 100 μL 9 mg/mL NaCl administered through the tail vein 10, 30, 60, 120 or 240 minutes before the start of the perfusion scans. Mice in the negative control group received 100 μL 9 mg/mL NaCl.

The perfusion scans were performed using dynamic contrast enhanced MRI (DCE-MRI) and analyzed using the Extended Tofts model implemented in nordicICE v2.3 (Nordic NeuroLab, Bergen, Norway) as described in Supplementary Materials.

Flow cytometry

RBE4 cells were pre-treated with 20 μg/mL rhodamine-conjugated K16ApoE for 45 minutes and exposed to inhibitors of dynamin- and clathrin-mediated endocytosis and studied by flow cytometry. RBE4, MDCK, hCMEC/D3, H1 and H2 cells were incubated with endocytosis inhibitors and pre-treated with 20 μg/mL K16ApoE and Alexa Fluor 647-conjugated BSA prior to flow cytometry. Both experiments are elaborated in Supplementary Materials.

In vitro cell viability

The viability of MDCK, MDCK II, RBE4 and hCMEC/D3 endothelial cells and H1 brain metastasis cells after treatment with K16ApoE was evaluated *in vitro* using a resazurin proliferation assay and for MDCK cells also a Live/Dead assay. The procedures are described in Supplementary Materials.

Scanning electron microscopy

RBE4 and MDCK II cells were incubated with 0, 20, 40 or 80 μg/mL K16ApoE for 45 minutes before they were fixed and prepared for scanning electron microscopy to study the morphology of the endothelial monolayers after peptide exposure. The protocol is described in Supplementary Materials.

In vitro human BBB models

The procedure for the cell adhesion assay carried out prior to *in vitro* BBB modelling experimental set-ups is described in the Supplementary Materials.

Mono- and co-culture BBB models were constructed using the human astrocyte cell line SC-1800 and the endothelial cell line hCMEC/D3. The resistance values, indicating increased BBB permeability, were recorded using the Electric Cell Substrate Impedance Sensing (ECIS) system and CellZScope® for 2D and 3D modelling respectively, as reported previously (33). The mono- and co-cultures were treated with 0, 20, 40 or 80 μg/mL of K16ApoE and resistance was recorded until recovery of the barrier was observed. Resistance values were obtained in Ω from the ECIS system and $\Omega.cm^2$ from the automated sensing system, CellZScope®. See Supplementary Materials for a detailed description of the protocol.

In vivo biodistribution of ^{125}I–K16ApoE

To study the biodistribution of the peptide, we injected ^{125}I-K16ApoE intravenously into NOD/SCID mice and collected blood samples and a selection of organs and measured these for radioactivity. See Supplementary Materials for further details.

In vivo treatment study

In an initial control experiment, nine NOD/SCID mice (eight weeks old) were injected with 5×10^5 H1_DL2 cells intracardially in 0.1 mL PBS as described in Supplementary Materials and divided into two groups by simple randomization: Four animals were injected with 200 µg K16ApoE and five with 9 mg/mL NaCl, to exclude any treatment effects of the peptide.

36 female NOD/SCID mice (eight weeks old) were then injected with 5×10^5 H1_DL2 cells intracardially as described in Supplementary Materials. The next day, mice were by simple randomization divided into three treatment groups: The first group received 200 µg K16ApoE followed by 10 mg/kg dabrafenib (free base, CT-DABRF, ChemieTek, Indianapolis, IN, USA) five minutes later. The next group received 10 mg/kg dabrafenib and the third group received 9 mg/mL NaCl (vehicle).

All solutions were administered intravenously. The mice were treated twice a week for six weeks. See Supplementary Figure S1B for a detailed description of the animals used.

Contrast enhanced T_1 and T_2 weighted MRI was conducted four and six weeks after as described in Supplementary Materials.

Histology assessments

Mouse organs such as lungs, heart, liver, kidneys, colon, stomach, spleen, skin, muscle and brain were harvested after treatment with K16ApoE and fixed using 4% formaldehyde. Paraffin embedded organs were sectioned and mounted on slides. The sections were deparaffinized and stained with Hematoxylin and Eosin (H&E) for histological assessments.

Mass spectrometry

A mass spectrometry experiment was performed to confirm the presence of dabrafenib in K16ApoE combination treated NOD/SCID mice from the *in vivo* treatment experiment. The procedures are described in Supplementary Materials.

Dynamic PET/CT

The capacity of BBB permeability from K16ApoE was further evaluated by PET/CT using ^{18}F-albumin (~67 kDa) and ^{18}F-IgG (~150 kDa) to study if also these compounds could enter the brain after administration of K16ApoE. The albumin and IgG labelling procedure prior to PET/CT as well as the dynamic scanning procedures are described in Supplementary Materials.

Statistical analysis

The statistical analyses were carried out in Prism 7 for Mac, Version 7.0b (La Jolla, CA, USA). Unpaired t-tests were used to evaluate two normally distributed groups, whereas Mann-Whitney tests were used to compare nonparametric data. A Mantel-Cox log-rank test was used to analyze survival data from the in vivo treatment experiment. The results are displayed as individual points with mean ± SEM or mean ± SEM. A two-tailed *P*-value ≤0.05 was considered significant.

Results

Nontoxic doses of K16ApoE increase BBB permeability

To determine the maximum tolerated dose of K16ApoE, mice were injected intravenously with increasing concentrations of peptide (50 to 1,000 μg). For peptide doses up to 400 μg, the mice showed no signs of pain or distress following systemic peptide exposure, and they all recovered from anesthesia within approximately three minutes (Figure 1A). Higher peptide doses led to a respiratory and/or cardiac arrest within 30 minutes (Supplementary Videos 1 and 2). Higher doses were also associated with an abnormal erythrocyte morphology (Supplementary Figure S2).

K16ApoE facilitates a therapeutic window of minimum 30 minutes

DCE-MRI on healthy mice demonstrated a dose-dependent effect of the peptide. K16ApoE concentrations of 50 or 100 μg was insufficient for BBB permeabilization, i.e. allowing Omniscan to enter into the extravascular, extracellular space (EES) from the blood plasma, as seen by the K^{trans} values (Figure 1B). A major leakage of Omniscan contrast agent from blood into the brain tissue was observed when administered ten minutes after injection of 200 μg K16ApoE. This implicates that the peptide was able to successfully open the intact BBB (Figure 1C). Interestingly, our results also showed that the BBB was partially open for approximately one hour after K16ApoE injection, reflecting a putative time frame for effective drug administration (Figure 1C). Other DCE-MRI parameters besides K^{trans} are listed in Supplementary Table 1. Based on the preceding, the toxicity studies above and previous literature (34), we chose to use 200 μg per mouse for further *in vivo* experiments.

Endocytic pathways are involved in cellular uptake of K16ApoE

To acquire a mechanistic insight on how K16ApoE facilitates BBB permeability, we first conducted baseline studies for further *in vitro* experiments. We determined K16ApoE IC_{50} values for

five normal endothelial cell lines, and these were all within a relatively narrow range of 30.89–86.18 μg/mL (Supplementary Figure S3A–D). For H1_DL2 cells used in the intracardiac metastasis model, the IC_{50} was 25.75 μg/mL (Supplementary Figure S3E).

Live/Dead assays and scanning electron microscopy images of MDCK and RBE4 cells (Supplementary Figure S3F-H) showed a dose/time-dependent increase in the number of dead cells over 45 minutes (see also Supplementary Videos 3-6).

We then applied flow cytometry to assess endocytic activity in RBE4 cells treated with 20 μg/mL rhodamine–labelled K16ApoE. As shown in Figure 2A, high endocytic uptake of peptide was observed in the RBE4 cells (purple curve in Figure 2A). By adding chlorpromazine (green curve in Figure 2A) or dynasore (blue curve in Figure 2A), which are inhibitors of clathrin and dynamin mediated endocytosis, respectively, the peptide uptake was reduced with the strongest effect seen for chlorpromazine.

We then pre-treated RBE4 cells with AF647-labeled BSA and incubated with (yellow curve in Figure 2B) and without K16ApoE (blue curve in Figure 2B). When chlorpromazine was added as well, there was a reduction in BSA uptake (purple curve in Figure 2B). The lowest BSA uptake was seen in RBE4 cells incubated with chlorpromazine and no peptide (green curve in Figure 2B). Corresponding experiments were carried out on MDCK, hCMEC/D3, H1 and H2 cells studying BSA uptake after pre-treatment with endocytosis inhibitors (Supplementary Figure 4). The same pattern was seen across all cell lines: The highest BSA uptake was observed for cells pretreated with K16ApoE (purple curves), whereas endocytosis inhibitors reduced this increase (blue curves), chlorpromazine to a larger extent than dynasore. Dynamin-mediated endocytosis can be serum dependent. We therefore carried out the dynasore experiments with (Supplementary Figure S4) and without BSA (Figure 2). To summarize, both clathrin- and dynamin-mediated endocytosis are likely involved in K16ApoE uptake (below IC_{50}-doses).

In order to show that also other uptake mechanisms of K16ApoE likely are involved, we investigated the uptake of AF647-conjugated BSA in RBE4 cells with (blue curves in Fig 2C and

2D) and without (green curves in Fig 2C and 2D) pre-treatment with K16ApoE. When compared to 37 °C, the uptake of BSA was reduced in cells that were kept at 4° C (Figure 2D), i.e. at a temperature when endocytosis usually is abolished (Figure 2C). In conclusion, based on the above data, endocytic mechanisms are involved in peptide uptake, likely in combination with other mechanisms as described in the following.

K16ApoE has lytic properties at higher concentrations (above IC_{50})

We then studied changes in endothelial cell monolayer surfaces *in vitro* following K16ApoE exposure. Scanning electron microscopy images showed that MDCK II and RBE4 cells not exposed to the peptide formed uniform monolayers (Figure 3A and Supplementary Figure S3H, respectively) with occasional protruding cells with smooth surfaces. At increasing K16ApoE concentrations, the cell surface lost the uniform morphology, and punctures in the membranes could be observed, indicating dying cells (See inserts in Figure 3A). There was an association between increasing concentrations of the peptide and the number of punctured, protruding cells. This dose-dependent cell death was verified by the Live/Dead experiment (Figure 3B and Supplementary Figure S3F and G).

Taken together with data presented in Supplementary Figure S2 and S3, this indicates that cell lysis is likely involved especially at higher peptide concentrations, in addition to the endocytosis mechanisms indicated by flow cytometry (Figure 2).

BBB integrity is restored 15 h after treatment with the peptide

Cellular adhesion was measured prior to *in vitro* BBB modelling using crystal violet in 96-well plates after treatment with 0, 20, 40 or 80 µg/mL K16ApoE for 45 minutes. The strongest cellular adhesion was observed for untreated hCMEC/D3 cells. The adhesion potential was significantly reduced during peptide treatment in a dose-dependent manner (Supplementary Figure S5A and B). However, although not statistically significant, there was a tendency that the adhesion potential started to recover with increasing recovery times after 45 minutes of peptide exposure. Endothelial

cells exposed to 40 and 80 µg/mL showed a statistically significant increase in adhesion potential after 60 minutes (Supplementary Figure S5A).

In both human *in vitro* BBB models assessed, the cells were exposed to 0, 20, 40 or 80 µg/mL of the peptide for 45 minutes, before they were allowed to recover for as long as deemed necessary in a mono- and co-culture model. In the mono-culture model, the endothelial cell monolayers restored their integrity within three hours (Figure 3C), whereas in the co-culture model with endothelial cells and astrocytes, the integrity of both cell layers was restored after 15 hours (Figure 3D).

K16ApoE is eliminated from blood plasma within five minutes, through liver, kidney and spleen

The activity of ^{125}I-labeled K16ApoE in blood plasma was rapidly reduced over the total measured time of 30 minutes. The most prominent decline was observed within the first minute after the peptide was injected into the tail vein, whereas subsequent values quickly reached a baseline. The curve corresponds to a half-life of K16ApoE in blood of approximately one minute (Supplementary Figure S6B).

The biodistribution of ^{125}I-K16ApoE was analysed in numerous selected organs. The highest values of ^{125}I-K16ApoE accumulation were seen in the liver (164 570 cpm), kidney (160 107 cpm) and spleen (136 889 cpm), whereas the lowest counts were observed in colon (17 290 cpm), femur (14 720 cpm) and muscle tissue (13 608 cpm). Intermediate values were observed for ventricle (92 533 cpm), lungs (76 554 cpm), skin (38 835 cpm) and heart (28 482 cpm). The high activity seen in the kidneys, liver and spleen suggested that elimination occurred through all of these organs (Supplementary Figure S6C).

Since ^{125}I was labelled to the only histidine residue present in the peptide, the potency of the final ^{125}I-K16ApoE construct only allowed us to inject a concentration of 25 µg K16ApoE without exceeding the maximum volume possible to inject intravenously in a NOD/SCID mouse. Further, since the measurements were carried out more than 30 minutes after the peptide was injected, this is a time window that does not allow major remnants of the peptide to be detected in the brain. For these

reasons combined, we did not focus on the amount of peptide in the brain in this experiment, as both the concentration and time window likely is too small to see any significant uptake, as observed by DCE-MRI (Figure 1).

K16ApoE does not induce acute or long-term tissue damage

Histological analysis was carried out in two separate experiments (Supplementary Figure S1). In the first experiment, healthy NOD/SCID mice were subjected to a one-time exposure of 0, 200, 400, 600, 800 or 1 000 μg K16ApoE (Supplementary Figure S7A). In the second experiment, tumor-bearing animals were subjected to 200 μg K16ApoE twice a week over a period of six weeks (Supplementary Figure S7B). Representative H&E sections from brain, lungs, kidneys, liver, spleen, skin, muscle tissue, colon, stomach and heart did not reveal any pathological changes in animals from either treatment group, across both experiments (Supplementary Figures S7A and B).

K16ApoE improves the delivery of the BRAFi dabrafenib

We then studied whether a combined use of K16ApoE with dabrafenib (537.6 Da) could increase the therapeutic effects in a human brain metastasis animal model, compared to dabrafenib treatment alone.

A control experiment was carried out to evaluate whether the peptide had any effect on tumor burden. No such effects were observed (Supplementary Figure S8A–C).

The mean number of tumors as well as the mean total tumor volume in animals treated with a combination of K16ApoE and dabrafenib decreased at weeks four and six, compared to control animals (vehicle) or animals treated with dabrafenib only (Figure 4A–C). No statistically significant differences could be found in tumor numbers or tumor volumes between the dabrafenib group and the control group at week four and six, indicating that dabrafenib treatment alone was not effective.

Kaplan-Meier curves revealed no difference in survival between vehicle and dabrafenib treated animals whereas the combinatorial treatment group had a significant survival benefit (Figure 4D).

K16ApoE treatment causes an uptake of dabrafenib in the brain parenchyma

A pilot mass spectrometry imaging experiment revealed that dabrafenib was taken up in the brain in mice treated with a co-injection of peptide and dabrafenib, as shown in Supplementary Figure S9A. A negative control animal treated with vehicle is presented in Supplementary Figure S9B, where no uptake is detected. Dabrafenib was fragmented in two segments, namely at m/z 480.1 and 344.1 as seen in Supplementary Figure S9C.

K16ApoE facilitates blood-brain barrier penetration of large molecules

To test the potential of K16ApoE to carry even larger molecules than dabrafenib across the BBB, we injected 200 μg K16ApoE followed by ^{18}F-albumin (~67 kDa) or ^{18}F-IgG (~150 kDa) and performed subsequent dynamic PET/CT brain imaging. Over 30–60 minutes, we observed a significant increase in average standardized uptake values (SUV_{mean}) in peptide–injected mice as compared to vehicle–treated mice for both ^{18}F-albumin (Figure 5A) and ^{18}F-IgG (Figure 5B). This implies leakage of the radiolabeled molecules from the blood plasma and into the EEC. Thus, K16ApoE facilitates the delivery of compounds with a molecular weight of up to at least 150 kDa.

Discussion

The delivery of therapeutic drug concentrations across the BBB and into metastatic lesions remains a critical issue in the treatment of brain metastases. In the smallest lesions not detected by clinical MRI, the BBB is presumably intact. As the brain metastases progress, the barriers develop a heterogeneous permeability to different-sized molecules, still with many metastases showing minor or no permeability at all (15). Thus, efficient drug delivery to the brain lesions is often compromised, necessitating the need for strategies to increase the leakiness of the BBB (30). Here, we describe a treatment strategy using a BBB permeabilizing peptide and thereby improving the delivery of dabrafenib (537.6 Da), which previously has demonstrated profound effects towards extracranial melanomas with BRAF mutations. Although the anatomical distribution of dabrafenib is superior to several other BRAFis (9), the drug does not readily penetrate into the brain parenchyma if the BBB is intact. Here we show that our treatment strategy inhibits the progression of $BRAF^{V600E}$ mutated melanoma brain metastases, ascribed to an improved drug delivery across the BBB.

In a previous study with K16ApoE, Evans blue (M_W ~0.96 kDa) was injected ten minutes after administering the peptide, and the results indicated that a therapeutic window of approximately 60 minutes was facilitated (34). We used DCE-MRI which is a quantitative and highly sensitive MRI technique to validate these results. The observed increase in K^{trans} values demonstrates a genuine pharmacodynamic increase in BBB permeability and thus perfusion (35)–and this was directly attributable to peptide action.

However, although it has been shown by us and others that K16ApoE is able to permeabilize the BBB, the specific mechanisms responsible for this effect have not been firmly established (32,34,36). Meng and colleagues have previously seen that K16ApoE likely promotes endocytosis into endothelial cells (36). Our findings indicate that there are likely several mechanisms involved, including loss in cell membrane integrity and lytic properties–in addition to endocytosis, especially at higher peptide concentrations. We show that the cellular uptake of K16ApoE at lower doses (i.e. 20 μg/mL) was reduced by dynasore and chlorpromazine, inhibitors of dynamin-dependent and

clathrin-mediated endocytosis, respectively. Our data may suggest that clathrin-mediated endocytosis is the most active one of these two mechanisms, which is also in line with the literature (37). We found that peptide-mediated uptake of BSA was still present at low temperatures (4 °C) when endocytosis is significantly reduced, although at reduced levels. This adds to the hypothesis that also other cellular uptake-mechanisms may be involved. For instance, our scanning electron microscopy data indicated that the peptide exerted a dose-dependent, toxic effect on the cells, which has also been reported previously (36). At increasing concentrations, more cells with punctured cell membranes were observed (Figure 3A), suggesting also a lytic effect at higher concentrations. These findings were supported by our fluorescence time lapse study, which also indicated that the cells were relatively unaffected by the peptide during the first minute of exposure. In addition, the half-life of K16ApoE in the blood was approximately one minute, which taken together implies that relatively large doses of peptide (above the IC_{50} doses) may be injected safely into the bloodstream. This is also supported by the *in vivo* toxicity study summarized in Figure 1A.

The endothelial cell integrity after exposure to the peptide was studied using *in vitro* BBB models and by investigating peptide action on proteins important in the assembly and maintenance of tight junctions. The peptide reduced the endothelial barrier integrity as measured using both ECIS (Figure 3C) and cellZScope (Figure 3D). Within three hours, the endothelial monolayer was restored, whereas the co-culture system remodelled the barrier integrity after 15 hours. This time discrepancy may be explained based on the fact that the methods are not directly comparable to each other. In the ECIS system, the output values are normalized before the resistance values can be regarded as absolute, while the measured resistance in cellZscope is directly attributable to the cell layers. Also, in the ECIS measurements there was only one layer of cells while a co-culture was constructed for the cellZScope. Thus, both cell lines had to recover for the barrier to be intact. Nevertheless, the results from both systems indicate that the BBB is restored after being transiently exposed to K16ApoE. In addition to its added mechanistic information, these experiments also validate the peptide action in a 3D human system.

In the *in vivo* treatment study summarized in Figure 4, 200 μg K16ApoE was administered intravenously into each mouse, and with a blood volume of approximately 1.5 mL, this corresponds to a peptide concentration of around 133 μg/mL blood. No side effects were observed after these injections, presumably due to the quick clearance from the blood, which occurred mainly through the liver, spleen and kidneys. Meng and colleagues argued that there was a positive correlation between toxic effects of the peptide at higher concentrations and BBB permeabilization. They also indicated that interactions of the peptide with adjacent erythrocytes resulted in the formation of microthrombi, which could be the underlying mechanism of toxicity (36). Taken together with our findings of hemolysis after treatment with K16ApoE, the injection of 200 μg K16ApoE per mouse thus represents a compromise between a favorable BBB permeable effect of the peptide and potential unwanted toxic side effects.

Our drug delivery strategy involved intravenous administration of a drug that normally is given orally to patients, thus several potential effects on the drug from the gastrointestinal tract such as degrading enzymes, low pH or heterogenous blood perfusion were not taken into consideration. We also administered 10 mg/kg to the mice twice a week, while in the clinic, patients are commonly given 2 × 150 mg dabrafenib daily, which corresponds to 4 mg/kg for a 75 kg patient. Although the concentrations are not directly comparable, our findings clearly suggest that dabrafenib represents an effective treatment for melanoma brain metastases, provided successful entry through the BBB. The amount of injected drug that penetrated the BBB and accumulated within the mouse brains was not quantified. However, a pilot mass spectrometry experiment of brain tissue harvested from control mice and K16ApoE + dabrafenib treated mice was performed, showing the presence of dabrafenib within the brains after peptide administration. Dabrafenib was not found in brains from control mice. Further experiments should be carried out aiming to quantify the detected amount of drug when co-injected with K16ApoE.

The histopathological examination performed by an experienced neuropathologist showed that no changes in organ histology could be found after administering a single high-dose (1,000 μg)

of peptide to the mice, or at the end of the dabrafenib study, when the mice had been given 12 injections of 200 μg K16ApoE over six weeks.

As a final experiment, we used dynamic PET/CT to study whether the BBB was permeable, following K16ApoE exposure, to even larger molecules. We detected ^{18}F-labelled albumin (M_W ~67 kDa) and IgG (M_W ~150 kDa) in brain tissue. Although drug uptake across the BBB or BTB is not only limited to size, our results indicate that K16ApoE can facilitate the delivery of substances in the size range of immune checkpoint inhibitors to patients with brain metastases. Examples include ipilimumab (M_W ~148 kDa), which targets cytotoxic T-lymphocyte antigen 4 (CTLA4) or inhibitors of PD-1/PD-L1 such as for instance nivolumab (M_W ~143 kDa) and atezolizumab (M_W ~145 kDa), respectively. Thus, for future investigations, we aspire to carry out *in vivo* treatment experiments with immune checkpoint inhibitors on melanoma brain metastases.

In conclusion, the use of K16ApoE seems to be a promising strategy to improve drug delivery across the BBB. Potential toxicity issues preclude direct translation into the clinic as of today, warranting further studies with the peptide, which is also the case with several other methods of permeabilizing the BBB. Our strategy using K16ApoE serves as an easy, non-invasive and reliable tool to establish treatment effects *in vivo* with agents that otherwise do not penetrate the BBB.

Figure 1

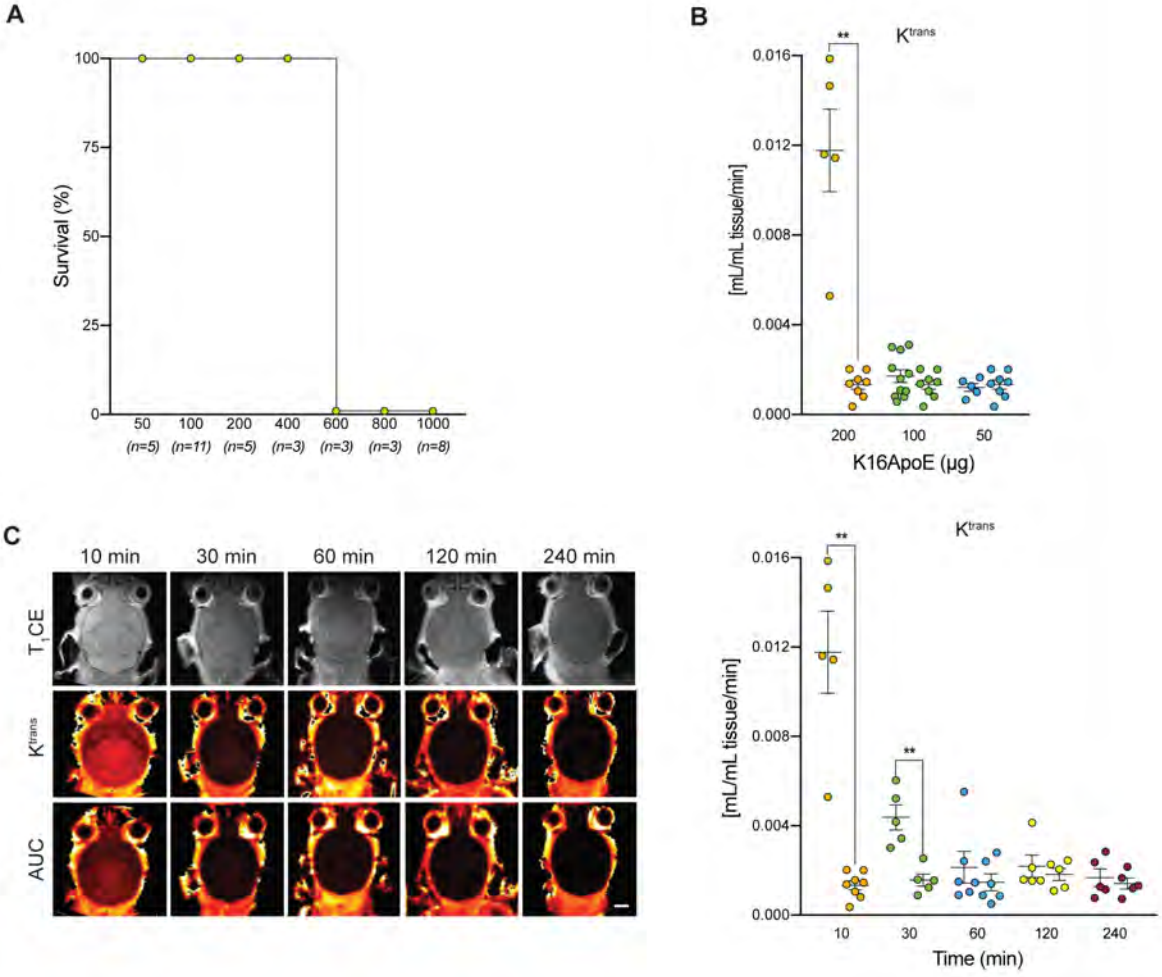

Figure 1

K16ApoE creates a time window for therapy for at least 30 minutes. **A,** Survival curves after K16ApoE dose escalation experiments. **B,** Scatter plots of the blood-to-tissue transfer constant (K^{trans}) demonstrate a dose-dependent reduction of contrast agent transfer from blood to tissue with decreasing peptide concentrations (n=5-10 mice). Mean ± SEM. **C,** Representative anatomical contrast enhanced T_1 weighted MR images (top row) and parametric MR images (K^{trans} and AUC maps; two bottom rows) of coronal brain sections of a control mouse are seen to the left. Scalebar = 2.5 mm. To the right, the quantified K^{trans} analysis demonstrates leakage of contrast agent from blood to tissue 10 and 30 minutes after injection of 200 µg of K16ApoE, compared to control animals (n=5-10 mice). Mean ± SEM. Abbreviations**:** K^{trans}: transfer constant, T_1CE: contrast enhanced T_1 weighted scan, AUC: area under curve, **: $p < 0.01$.

Figure 2

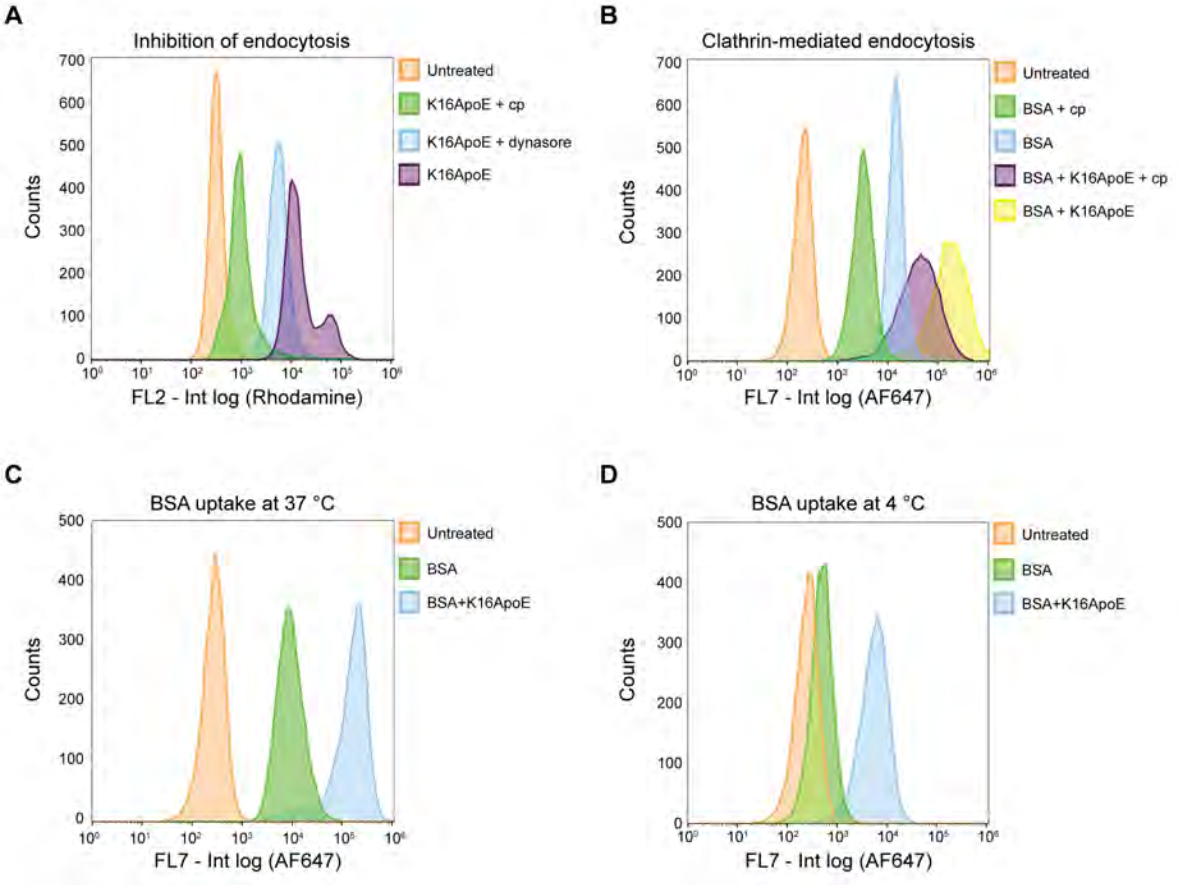

Figure 2

Mechanistic studies of the *in vitro* effects of K16ApoE. **A,** Flow cytometry data showing the effects of two endocytosis inhibitors, chlorpromazine and dynasore after 30 minutes of incubation, on K16ApoE uptake in RBE4 cells after 45 minutes of continued incubation. **B,** Flow cytometry data on uptake of BSA into cells while pre-treating RBE4 cells with chlorpromazine for 30 minutes, with and without using the peptide for 45 minutes. **C,** Flow cytometry data showing uptake of BSA at 37 °C and at **D,** 4 °C after incubating the cells for one hour. Abbreviations: RBE4: rat brain endothelial cells 4, BSA: bovine serum albumin, cp: chlorpromazine.

Figure 3

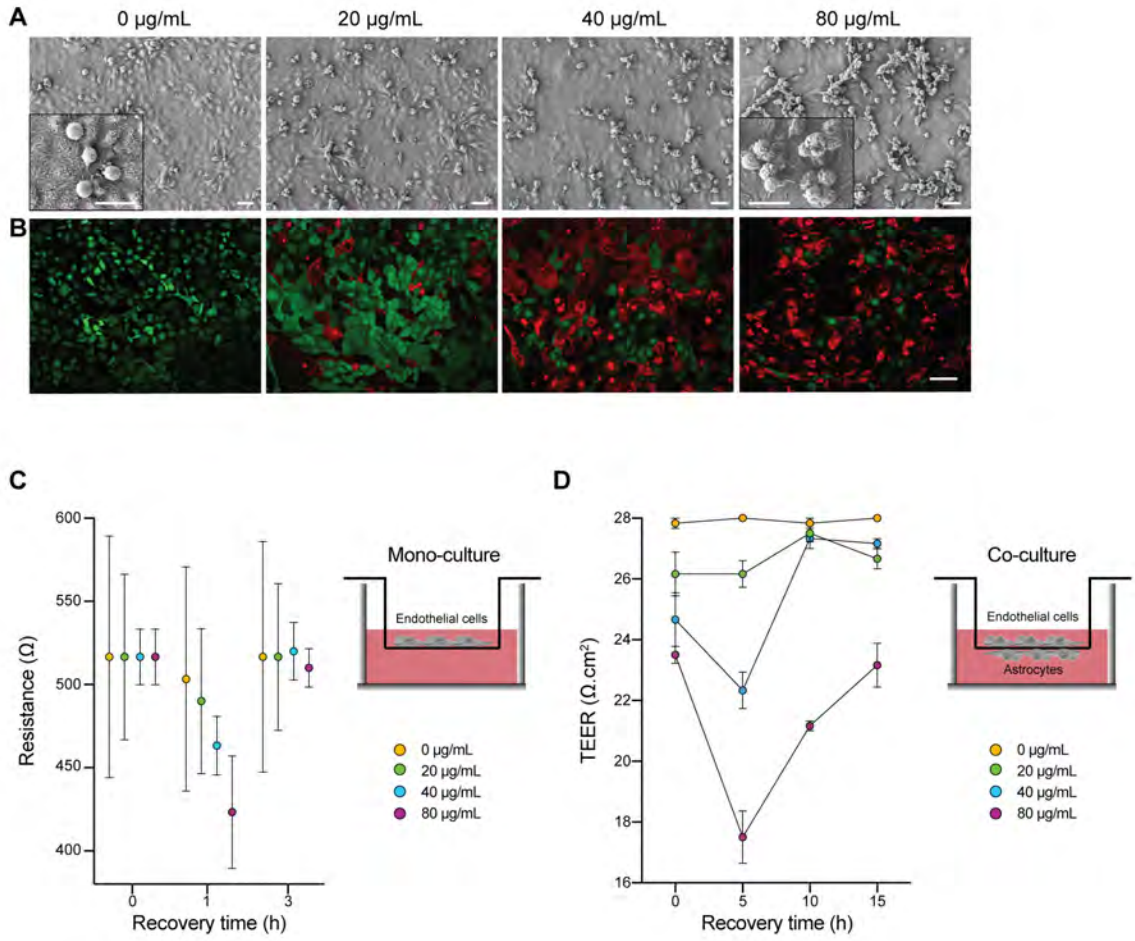

Figure 3

Integrity of an *in vitro* model of the blood-brain barrier after exposure to the peptide. **A,** Scanning electron microscopy images demonstrating nonspecific cell monolayer disruptions in preparations of MDCK II cells. Inserts in micrographs with cells exposed to 0 µg/mL K16ApoE demonstrate smooth cell membranes, whereas cells exposed to 80 µg/mL of the peptide have punctured cell membranes. All scalebars 20 µm. **B,** Cell death as a result of corresponding peptide concentrations as seen by Live/Dead staining of MDCK cells. Scalebar 50 µm. **C,** Recorded resistance values using the ECIS system in a monolayer of hCMEC/D3 endothelial cells. The resistance was restored 3 h after peptide exposure. **D,** Measured resistance (TEER) values using the CellZScope system in a co-culture consisting of astrocytes and hCMEC/D3 endothelial cells. Barrier integrity was restored 15 h after peptide exposure. Cell illustration from Somersault1824 (www.somersault1824.com).

Abbreviations: ECIS: Electric cell substrate impedance sensing, TEER: transendothelial/epithelial electrical resistance.

Figure 4

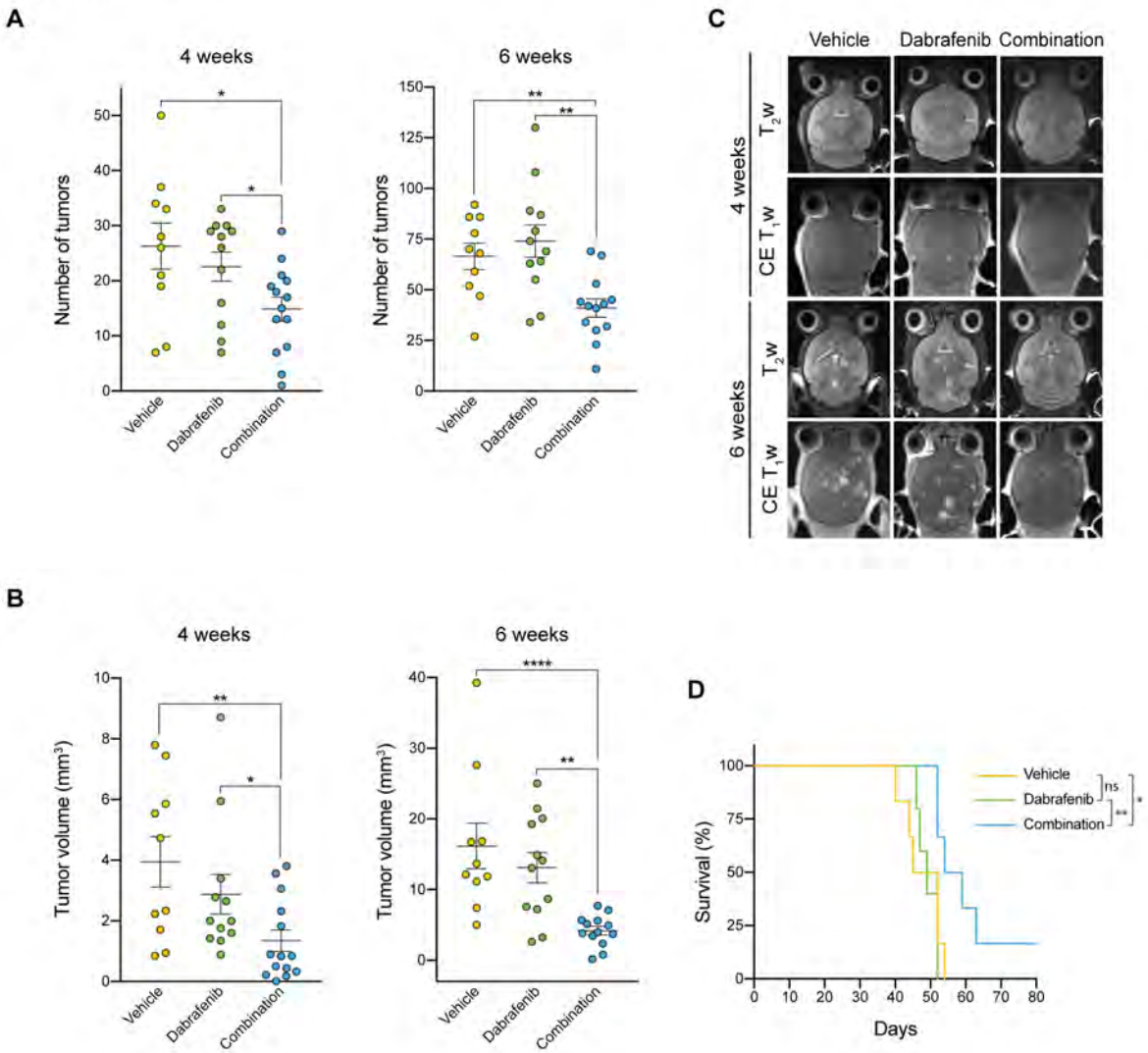

Figure 4

Combined treatment with K16ApoE and dabrafenib inhibits tumor development and increases animal survival in an animal model of melanoma brain metastasis. **A,** The mean, total number of tumors in the mouse brains four (left) and six (right) weeks after start of treatment. Mann-Whitney statistical test. Mean ± SEM. **B,** The mean, total tumor volumes in the mouse brains four (left) and six (right) weeks after start of treatment. Mean ± SEM. **C,** Representative CE T_1 weighted and T_2 weighted MR images from each treatment group at week four and six. Scalebar 2 mm. **D,** Survival curves for all animals in the treatment study. Abbreviations: *: $p<0.05$, **: $p<0.01$, ****: 0.0001, CE T_1: contrast enhanced T_1 weighted MR images obtained 5 minutes after injection of Omniscan, T_2: T_2 weighted MR images.

Figure 5

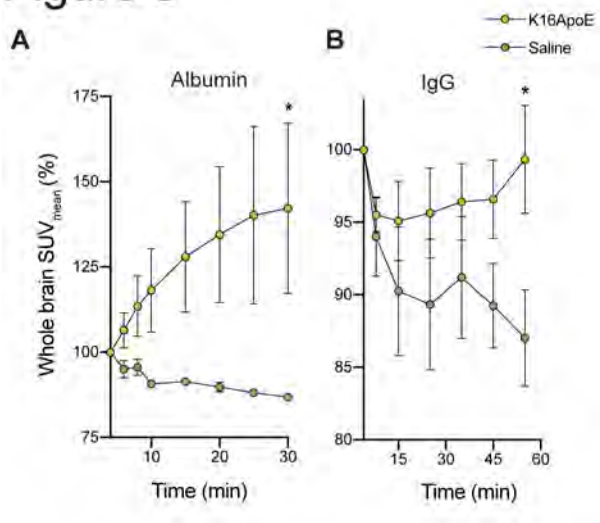

Figure 5

K16ApoE facilitates the delivery of large compounds across the BBB. **A,** Standardized uptake of ^{18}F-albumin into brain tissue, monitored by a 30 minutes dynamic PET/CT scan. Each mouse was scanned twice, with and without a prior injection of 200 µg K16ApoE, on separate days (n=3 mice). The mean standard uptake value (SUV_{mean}) was calculated within an ellipsoidal volume of interest, delineating the skull. Mean ± SEM. **B,** Standardized uptake of ^{18}F-IgG into brain tissue, monitored by a 60 minutes dynamic PET/CT scan. Each mouse was scanned twice, with and without a prior injection of 200 µg K16ApoE, on separate days (n=7 mice). The mean standard uptake value (SUV_{mean}) was calculated. Mean ± SEM. Abbreviations: SUV: standardized uptake values, ^{18}F: Fluorine-18, PET: positron emission tomography, IgG: immunoglobulin G, *: $p<0.05$.

Additional information

Ethics approval

We obtained written consent by the Regional Ethical Committee (#013.09) and the Norwegian Directorate of Health (#9634) before human tumor tissue was collected and stored. The National Animal Research Authority approved all animal procedures prior to all experiments (Application #8093, approved February 13th, 2016).

Availability of data and material

Raw data used in this paper is available from the corresponding author upon request.

Note

Supplementary data for this article is available at Molecular Cancer Therapeutics Online.

Authors contributions

Concept and design: S.N. Aasen, D.E. Olberg, G. Pilkington, G. Sarkar, R.B. Jenkins, T. Sundstrøm, R. Bjerkvig and F. Thorsen.

Development of methodology: S.N. Aasen, H. Espedal, O. Keunen, O. Tenstad, A.V. Eikeland, H. Baghirov, G. Pilkington, R. Bjerkvig and F. Thorsen

Acquisition of data: S.N. Aasen, H. Espedal, C.F. Holte, O. Keunen, T.V. Karlsen, Z. Maherally, T. Hoang, A.V. Eikeland, H. Baghirov and F. Thorsen

Analysis and interpretation of data: S.N. Aasen, H. Espedal, C.F. Holte, O. Keunen, Z. Maherally, H. Miletic, T. Hoang, A.V. Eikeland, H. Baghirov and F. Thorsen.

Writing, review and/or revision of the manuscript: S.N. Aasen, Z. Maherally, G. Pilkington, T. Sundstrøm, R. Bjerkvig and F. Thorsen.

Study supervision: R. Bjerkvig and F. Thorsen.

Acknowledgements

The authors thank Hege Avsnes Dale (Molecular Imaging Center, University of Bergen) for valuable assistance with confocal and light microscopy, Anne Karin Nyhaug (Molecular Imaging Center, University of Bergen) for help with tissue sample preparation before electron microscopy, Linda Sandven (Molecular Imaging Center, University of Bergen) for H&E staining, Miro Eigenmann (Institute of Biomedicine, University of Bergen) for input on the development of the biodistribution methodology, Mari-Ann Jørstad Davidsen (Department of Clinical Medicine, University of Bergen) for help with animal procedures, Brith Bergum (Department of Clinical Science, University of Bergen) for assistance with flow cytometry, Jubayer Hossain (The Department of Biomedicine, University of Bergen) for assistance with animal work, Marjo Yliperttula (University of Helsinki) for providing us MDCK II cells, Tilo Wolf Eichler (Department of Clinical Medicine, University of Bergen) for providing us MDCK cells, Michael Aschner (Vanderbilt University) for the RBE4 cells, Tom Christian Holm Adamsen (Department of Chemistry, University of Bergen) for valuable input on PET/CT methodology, Tina Pavlin (Molecular Imaging Center, University of Bergen) for help with the MRI.

The electron microscopy, confocal and small animal imaging was performed at the Molecular Imaging Center, Department of Biomedicine, University of Bergen.

References

1. Owonikoko TK, Arbiser J, Zelnak A, Shu HK, Shim H, Robin AM, *et al*. Current approaches to the treatment of metastatic brain tumours. Nat Rev Clin Oncol **2014**;11(4):203-22 doi 10.1038/nrclinonc.2014.25.

2. Sinik L, Minson KA, Tentler JJ, Carrico J, Bagby SM, Robinson WA, *et al*. Inhibition of MERTK Promotes Suppression of Tumor Growth in BRAF Mutant and BRAF Wild-Type Melanoma. Mol Cancer Ther **2019**;18(2):278-88 doi 10.1158/1535-7163.MCT-18-0456.

3. Grzywa TM, Paskal W, Wlodarski PK. Intratumor and Intertumor Heterogeneity in Melanoma. Transl Oncol **2017**;10(6):956-75 doi 10.1016/j.tranon.2017.09.007.

4. Villar-Prados A, Wu SY, Court KA, Ma S, LaFargue C, Chowdhury MA, *et al*. Predicting Novel Therapies and Targets: Regulation of Notch3 by the Bromodomain Protein BRD4. Mol Cancer Ther **2019**;18(2):421-36 doi 10.1158/1535-7163.MCT-18-0365.

5. Heller KN, Pavlick AC, Hodi FS, Thompson JA, Margolin KA, Lawrence DP, *et al*. Safety and survival analysis of ipilimumab therapy in patients with stable asymptomatic brain metastases. Journal of Clinical Oncology **2011**;29:8581– doi 10.1200/jco.2011.29.15_suppl.8581.

6. Kluger HM. Safety and activity of pembrolizumab in melanoma patients with untreated brain metastases. Journal of Clinical Oncology **2015**;33:9009 doi 10.1200/jco.2015.33.15_suppl.9009.

7. Long GV, Trefzer U, Davies MA, Kefford RF, Ascierto PA, Chapman PB, *et al*. Dabrafenib in patients with Val600Glu or Val600Lys BRAF-mutant melanoma metastatic to the brain (BREAK-MB): a multicentre, open-label, phase 2 trial. Lancet Oncol **2012**;13(11):1087-95 doi 10.1016/S1470-2045(12)70431-X.

8. Eichler AF, Chung E, Kodack DP, Loeffler JS, Fukumura D, Jain RK. The biology of brain metastases-translation to new therapies. Nat Rev Clin Oncol **2011**;8(6):344-56 doi 10.1038/nrclinonc.2011.58.

9. Mittapalli RK, Vaidhyanathan S, Dudek AZ, Elmquist WF. Mechanisms limiting distribution of the threonine-protein kinase B-RaF(V600E) inhibitor dabrafenib to the brain: implications for the treatment of melanoma brain metastases. J Pharmacol Exp Ther **2013**;344(3):655-64 doi 10.1124/jpet.112.201475.

10. Weidle UH, Niewohner J, Tiefenthaler G. The Blood-Brain Barrier Challenge for the Treatment of Brain Cancer, Secondary Brain Metastases, and Neurological Diseases. Cancer Genomics Proteomics **2015**;12(4):167-77.

11. Pardridge WM. The blood-brain barrier: bottleneck in brain drug development. NeuroRx **2005**;2(1):3-14 doi 10.1602/neurorx.2.1.3.

12. Palmieri D, Chambers AF, Felding-Habermann B, Huang S, Steeg PS. The biology of metastasis to a sanctuary site. Clin Cancer Res **2007**;13(6):1656-62 doi 10.1158/1078-0432.CCR-06-2659.

13. Lin X, DeAngelis LM. Treatment of Brain Metastases. J Clin Oncol **2015**;33(30):3475-84 doi 10.1200/JCO.2015.60.9503.

14. Terrell-Hall TB, Ammer AG, Griffith JI, Lockman PR. Permeability across a novel microfluidic blood-tumor barrier model. Fluids Barriers CNS **2017**;14(1):3 doi 10.1186/s12987-017-0050-9.

15. Thorsen F, Fite B, Mahakian LM, Seo JW, Qin S, Harrison V, *et al*. Multimodal imaging enables early detection and characterization of changes in tumor permeability of brain metastases. J Control Release **2013**;172(3):812-22 doi 10.1016/j.jconrel.2013.10.019.

16. Seoane J, De Mattos-Arruda L. Brain metastasis: new opportunities to tackle therapeutic resistance. Mol Oncol **2014**;8(6):1120-31 doi 10.1016/j.molonc.2014.05.009.

17. Samala R, Thorsheim HR, Goda S, Taskar K, Gril B, Steeg PS, *et al*. Vinorelbine Delivery and Efficacy in the MDA-MB-231BR Preclinical Model of Brain Metastases of Breast Cancer. Pharm Res **2016**;33(12):2904-19 doi 10.1007/s11095-016-2012-3.

18. Khuntia D, Brown P, Li J, Mehta MP. Whole-brain radiotherapy in the management of brain metastasis. J Clin Oncol **2006**;24(8):1295-304 doi 10.1200/JCO.2005.04.6185.

19. Hynynen K, McDannold N, Vykhodtseva N, Jolesz FA. Noninvasive MR imaging-guided focal opening of the blood-brain barrier in rabbits. Radiology **2001**;220(3):640-6 doi 10.1148/radiol.2202001804.

20. McDannold N, Arvanitis CD, Vykhodtseva N, Livingstone MS. Temporary disruption of the blood-brain barrier by use of ultrasound and microbubbles: safety and efficacy evaluation in rhesus macaques. Cancer Res **2012**;72(14):3652-63 doi 10.1158/0008-5472.CAN-12-0128.

21. Alkins R, Burgess A, Ganguly M, Francia G, Kerbel R, Wels WS, *et al*. Focused ultrasound delivers targeted immune cells to metastatic brain tumors. Cancer Res **2013**;73(6):1892-9 doi 10.1158/0008-5472.CAN-12-2609.

22. Rapoport SI, Hori M, Klatzo I. Testing of a hypothesis for osmotic opening of the blood-brain barrier. Am J Physiol **1972**;223(2):323-31 doi 10.1152/ajplegacy.1972.223.2.323.

23. Neuwelt EA, Barnett PA, Hellstrom I, Hellstrom KE, Beaumier P, McCormick CI, *et al*. Delivery of melanoma-associated immunoglobulin monoclonal antibody and Fab fragments to normal brain utilizing osmotic blood-brain barrier disruption. Cancer Res **1988**;48(17):4725-9.

24. Liu LB, Xue YX, Liu YH. Bradykinin increases the permeability of the blood-tumor barrier by the caveolae-mediated transcellular pathway. J Neurooncol **2010**;99(2):187-94 doi 10.1007/s11060-010-0124-x.

25. Cao Y, Tsien CI, Shen Z, Tatro DS, Ten Haken R, Kessler ML, *et al*. Use of magnetic resonance imaging to assess blood-brain/blood-glioma barrier opening during conformal radiotherapy. J Clin Oncol **2005**;23(18):4127-36 doi 10.1200/JCO.2005.07.144.

26. Bobo RH, Laske DW, Akbasak A, Morrison PF, Dedrick RL, Oldfield EH. Convection-enhanced delivery of macromolecules in the brain. Proc Natl Acad Sci U S A **1994**;91(6):2076-80.

27. Gupta B, Levchenko TS, Torchilin VP. TAT peptide-modified liposomes provide enhanced gene delivery to intracranial human brain tumor xenografts in nude mice. Oncol Res **2007**;16(8):351-9.

28. Saenz del Burgo L, Hernandez RM, Orive G, Pedraz JL. Nanotherapeutic approaches for brain cancer management. Nanomedicine **2014**;10(5):905-19 doi 10.1016/j.nano.2013.10.001.

29. Bregy A, Shah AH, Diaz MV, Pierce HE, Ames PL, Diaz D, *et al*. The role of Gliadel wafers in the treatment of high-grade gliomas. Expert Rev Anticancer Ther **2013**;13(12):1453-61 doi 10.1586/14737140.2013.840090.

30. Azad TD, Pan J, Connolly ID, Remington A, Wilson CM, Grant GA. Therapeutic strategies to improve drug delivery across the blood-brain barrier. Neurosurg Focus **2015**;38(3):E9 doi 10.3171/2014.12.FOCUS14758.

31. Shawkat H, Westwood M-M, Mortimer A. Mannitol: a review of its clinical uses. Continuing Education in Anaesthesia Critical Care & Pain **2012**;12(2):82-5 doi 10.1093/bjaceaccp/mkr063.

32. Sarkar G, Curran GL, Mahlum E, Decklever T, Wengenack TM, Blahnik A, *et al*. A carrier for non-covalent delivery of functional beta-galactosidase and antibodies against amyloid plaques and IgM to the brain. PLoS One **2011**;6(12):e28881 doi 10.1371/journal.pone.0028881.

33. Maherally Z, Fillmore HL, Tan SL, Tan SF, Jassam SA, Quack FI, *et al*. Real-time acquisition of transendothelial electrical resistance in an all-human, in vitro, 3-dimensional, blood-brain barrier model exemplifies tight-junction integrity. FASEB J **2018**;32(1):168-82 doi 10.1096/fj.201700162R.

34. Sarkar G, Curran GL, Sarkaria JN, Lowe VJ, Jenkins RB. Peptide carrier-mediated non-covalent delivery of unmodified cisplatin, methotrexate and other agents via intravenous route to the brain. PLoS One **2014**;9(5):e97655 doi 10.1371/journal.pone.0097655.

35. Barrett T, Brechbiel M, Bernardo M, Choyke PL. MRI of tumor angiogenesis. J Magn Reson Imaging **2007**;26(2):235-49 doi 10.1002/jmri.20991.

36. Meng Y, Wiseman JA, Nemtsova Y, Moore DF, Guevarra J, Reuhl K, *et al*. A Basic ApoE-Based Peptide Mediator to Deliver Proteins across the Blood-Brain Barrier: Long-Term Efficacy, Toxicity, and Mechanism. Mol Ther **2017**;25(7):1531-43 doi 10.1016/j.ymthe.2017.03.037.

37. García-Ruiz C, Ribas V, Baulies A, Fernández-Checa JC. Mitochondrial Cholesterol and the Paradox in Cell Death. In: Singh H, Sheu SS, editors. Pharmacology of Mitochondria Handbook of Experimental Pharmacology. Volume 240. Switzerland: Springer International Publishing; 2016.

Supplementary Materials

Materials and methods

Cell culture

The wild type Madin-Darby canine kidney epithelial cell line (MDCK) was a kind gift from Tilo Eichler (Department of Clinical Medicine, University of Bergen, Norway) and grown in Eagle's Minimum Essential Medium (ATCC, Manassas, VA, USA) supplemented with 10% fetal bovine serum (Thermo Fisher Scientific).

Madin-Darby canine kidney epithelial cells (MDCK II) were kindly donated by Professor Marjo Yliperttula (University of Helsinki, Finland). The cells were transduced with the red fluorescent protein mCherry (HIV-based lentiviralvector pGreenFire purchased from System Biosciences Paulo Alto, CA, USA) to also obtain the MDCK II mCherry cell line. The cells were grown in DMEM (Sigma-Aldrich), supplemented with 1% Penicillin/Streptomycin (BioWhittaker), 1% 200 mM L-Glutamine (BioWhittaker) and 5% fetal bovine serum (Thermo Fisher Scientific).

The rat brain endothelial 4 (RBE4) cell line was kindly gifted by Professor Michael Aschner (Vanderbilt University, Nashville, TN, USA). The cells were grown in 1:1 Hams F10 nutrient mix (Thermo Fisher Scientific) and Minimum Essential Mix (Thermo Fisher Scientific), supplemented with 2.5 μL/L human recombinant fibroblast growth factor (Sigma-Aldrich), 5% fetal bovine serum (Thermo Fisher Scientific) and 150 mg geneticin (Thermo Fisher Scientific).

Human cerebral microvascular endothelial cells (hCMEC/D3) were purchased from MerckMillipore (Burlington, MA, USA) and grown in endothelial basal media-2 (Lonza, Köln, Germany) supplemented with SingleQuots (Lonza) and 2% human serum (Sigma-Aldrich).

Human cerebral cortex-derived astrocytes SC-1800 were purchased from Caltag Medsystems (Buckingham, UK) and grown in astrocyte basal media (Lonza) supplemented with SingleQuots (Lonza) and 3% human serum (Sigma-Aldrich).

The H1 and H2 cell lines were established «in house» from biopsies from two different patients with brain metastases from melanoma as previously described (1). Written consent by the Regional Ethical Committee (#013.09) and the Norwegian Directorate of Health (#9634) was obtained before tumor tissue was collected and stored. The H1 cells were transduced with lentiviral vectors encoding the green fluorescent protein variant Dendra and Luciferase to obtain the H1_DL2 cells for *in vivo* experiments. The H1, H1_DL2 and H2 cell lines were grown in Dulbecco's Modified Eagle Medium (DMEM, Sigma-Aldrich Inc., St. Louis, MO, USA) supplemented with 10% heat-inactivated fetal calf serum (Thermo Fisher Scientific, Waltham, MA, USA), four times the prescribed concentration of non-essential amino acids (BioWhittaker, Verviers, Belgium), 2% L-glutamine (BioWhittaker), penicillin (100 IU/mL, BioWhittaker) and streptomycin (100 µL/mL, BioWhittaker).

All cells were kept in a standard tissue culture incubator at 37 °C with 100% humidity and 5% CO_2. Sub-culturing was done twice a week for the H1, H1_DL2, H2, hCMEC/D3 and SC-1800 cells, whereas this was done every second day for RBE4, MDCK and MDCK II cells. The endothelial cells were grown on collagen-coated dishes, prepared by diluting Collagen, Type I from rat tail (Sigma-Aldrich) in 1 x phosphate-buffered saline (PBS) and distributing this at 7.5 µg/cm^2 culture dish area. All cell lines were routinely tested for mycoplasma using the MycoAlert Mycoplasma Detection Kit (LT07-318, Lonza, Basel, Switzerland) according the manufacturers recommendations and authenticated using short tandem repeat profiling. Upon thawing, the cells were used in experiments for a maximum of ten passages.

K16ApoE peptide synthesis

The linear peptide KKKK-KKKK-KKKK-KKKK-LRVR-LASH-LRKL-RKRL-LRDA-(OH) necessary for this study was synthesized by the solid phase method using the CEM Liberty automatic microwave peptide synthesizer (CEM Corporation Inc., Matthews, NC), employing 9-fluorenylmethyloxycarbonyl (Fmoc) chemistry and commercially available amino acid (Merck

Millipore Novabiochem), single coupling (2× coupling for R). Peptides were cleaved from resin using trifluoroacetic acid (TFA) 95% (v/v); water, 2.5% (v/v); triisopropylsilane (TIS), 2.5% (v/v); two hours and precipitated by addition of ice-cold diethyl ether. The unprotected peptides were purified by preparative reverse-phase high performance liquid chromatography (RP-HPLC). Collected fractions containing purified peptide were pooled and lyophilized. The identity of the peptide was confirmed by high resolution mass spectrometry (HRMS).

Evaluation of the *in vivo* toxicity of K16ApoE

K16ApoE was injected as a bolus over 1 minute into the tail vein of 30 female and 8 male 16 weeks old NOD/SCID mice with an average bodyweight of 22.3 g, using peptide concentrations of 50 µg (n=5), 100 µg (n=11), 200 µg (n=5), 400 µg (n=3), 600 µg (n=3), 800 µg (n=3) or 1,000 µg (n=8). 9 mg/mL NaCl was used to adjust the total injection volume to 100 µL. The animals were then closely observed for the next two hours and immediately sacrificed if they showed any signs of acute toxic symptoms. Surviving animals were then observed over 48 hours to detect any signs of distress such as whisker alterations, cheek bulge, orbital tightening or changes in activity levels.

Eight 12-week-old NOD/SCID mice were injected with either 9 mg/mL NaCl or 1,000 µg K16ApoE in 9 mg/mL NaCl as a bolus over one minute. The cardiac response was monitored by ultrasound for the subsequent three minutes, which was the time it took before the animals in the peptide group died. Blood samples were collected from the left ventricle of the heart and blood smears were stained with eosin to evaluate the morphology. See Supplementary Figure S1A for details.

DCE-MRI

The T_2 weighted spin echo scans prior to DCE-MRI were acquired with a region of interest (ROI) over the mouse brain and neck musculature in coronal positioning (TR/TE: 4,000/48 ms, field of view (FOV): 2.00 cm, matrix size: 256 × 256, slice thickness: 1.00 mm, 7 slices and number of averages (NEX): 4, total scan time 6 minutes 13 seconds). The T_1 weighted scans were acquired with

the same geometry as the T_2 weighted scans (TR/TE 1,000/9 ms, and NEX: 4, total scan time of 3 minutes, 20 seconds). The perfusion scans were acquired in the middle position of the slice package. First, a series of FLASH sequences were acquired (TR/TE: 37.2/2.1 ms, FOV: 2.00 cm, matrix: 256 × 256, slice thickness, 1.00 mm and NEX: 1, total scan time of ~3 minutes), followed by the DCE-MRI sequence: This consisted of 900 repetitions of the FLASH protocol with the same geometry (TR/TE: 15 ms/2.1 ms, NEX: 1, FA: 17, temporal resolution: 1 second and total scan time of 16 minutes 12 seconds).

The perfusion scans were acquired by initiating a series of six fast low angle shot (FLASH) sequences with flip angles (FAs) 5, 10, 15, 20, 25 and 30 before the DCE-MRI scan sequence was acquired. 0.5 mmol/kg Omniscan (GE Healthcare, Little Chalfont, UK) was injected as a bolus through the tail vein using an injection pump (Harvard Apparatus, Holliston, MA, USA) 15 seconds after starting the DCE sequence.

The DCE-MRI data was analyzed using the Extended Tofts model implemented in nordicICE v2.3 (Nordic NeuroLab, Bergen, Norway) using local arterial input functions (AIFs) obtained from an adjacent neck muscle. AIFs were extracted by blind deconvolution (2), using custom developed routines implemented in Matlab 2015b (Mathworks, Natick, MA, USA). These routines are accessible through the online Perfusion Lab tool, available at http://perflab.cerit-sc.cz/. Maps of Area Under the Curve (AUC) and blood-to-tissue transfer constant (K^{trans}) were generated, and ROIs were drawn to cover the whole brain section including muscle tissue, white and grey matter. K^{trans} values were normalized to known values of the extravascular space (V_e) and vascular space (V_b) fractions in a reference muscle tissue, as previously described (3). Mean and standard deviation values were calculated for each ROI, time point and peptide dose, and statistically significant differences between K16ApoE receiving groups and corresponding 9 mg/mL NaCl receiving groups were established using the Mann-Whitney test function.

Flow cytometry

RBE4 cells were seeded in 6-well plates (Corning, New York, USA) at a density of 2.5×10^5 cells per well. After reaching the growth log-phase, the cells were incubated with 5 μg/mL AF647-BSA (Invitrogen Molecular Probes, Waltham, MA, USA) with or without 20 μg/mL rhodamine-conjugated K16ApoE for 45 minutes. For incubation in serum-free conditions, the cells were serum-starved for one hour before incubation in AF647-BSA with or without rhodamine-conjugated K16ApoE for 45 minutes. For endocytosis inhibition experiments, RBE4, MDCK, hCMEC/D3, H1 and H2 cells were seeded in 6-well plates at a density of 2.5×10^5 per well and pre-treated with 80 μM dynasore (a dynamin inhibitor) or 30 μM chlorpromazine (a clathrin inhibitor) for 30 minutes. The cells were then incubated with Alexa Fluor 647 (AF647)-conjugated BSA at a concentration of 5 μg/mL and 20 μg/mL K16ApoE in the continued presence of the endocytosis inhibitors for 45 minutes. For incubation at 4 °C, the RBE4 cells were pre-cooled on ice for 15 minutes, and then incubated with 5 μg/mL AF647-BSA with or without 20 μg/mL rhodamine-conjugated K16ApoE for 45 minutes. After incubation, the cells were washed with PBS, trypsinized and centrifuged twice before they were re-suspended in PBS and taken to the flow cytometer. Rhodamine-conjugated K16ApoE was excited by the blue laser line and detected using the FL2 detector, whereas AF647-BSA was excited by the red laser line and detected with the FL7 detector, using a Beckman Coulter flow cytometer (Beckman Coulter Inc., Brea, CA, USA) or a BD LSR Fortessa (BD Biosciences, San Jose, CA, USA).

***In vitro* cell viability**

5,000 MDCK, MDCK II, RBE4, hCMEC/D3 and H1 cells were seeded in each well in 96-well plates in 100 μL growth medium. After 24 hours of incubation, 100 μL of graded concentrations of K16ApoE (0.1, 1, 20, 40, 60, 80, 100 or 150 μg/mL) diluted in growth medium were added to each well (n = 6). 45 minutes later, the peptide was removed before each well was washed twice with PBS, and 100 μL/well of 0.1 mg/mL resazurin (Sigma-Aldrich) was added. The plates were measured after

four hours at 560 nm excitation and 590 nm emission using a VICTOR X3 multilabel plate reader (Perkin Elmer, Waltham, MA, USA) equipped with WorkOut 2.5 data analysis software. Wells containing 100 µL growth media without cells were used for background corrections. IC_{50} doses were defined as the drug concentration at which 50% of the cell growth was inhibited and was calculated using GraphPad Prism 7 for Mac OS X (GraphPad Software Inc., San Diego, CA, USA). The experiments were done in triplicate.

A Live/Dead assay (Thermo Fisher Scientific) was carried out using 5×10^4 MDCK cells seeded in µ-Slide 4-well glass bottom dishes (Ibidi GmbH, Munich, Germany). The cells were treated with 0, 20, 40 or 80 µg/mL K16ApoE. Immediately after treatment started, solutions of 4 mM Calcein-AM and 2 µM Ethidium Homodimer-1 solutions in the Live/Dead kit were mixed and distributed to the live cells according to the manufacturer's instructions. A time-lapse imaging sequence was obtained on a Leica TCS SP8 STED 3× confocal microscope (Leica, Wetzlar, Germany) using a 20× objective (HC PL APO CS2 20X/0.75 imm) capturing images every minute over a time period of 45 minutes. Calcein-AM was excited at 488 nm and emitted between 500-550 nm, and Ethidium Homodimer-1 was excited at 561 nm and emitted between 570-630 nm. The experiment was carried out once and the confocal images were analysed in FIJI (National Institutes of Health, Bethesda, MA, USA) by measuring the total signal from the red and green channels in all images acquired throughout the time–lapse.

Scanning electron microscopy

MDCK II or RBE4 cells were seeded on collagen coated 24-well plates (Nunc, Roskilde, Denmark) with 12 mm Ø coverslips at a density of 4,000 cells/500 µL growth medium and allowed to reach confluency prior to treatment with 0, 20, 40 or 80 µg/mL K16ApoE for 45 minutes. The cells were fixed using 2.7% glutamic acid aldehyde and then washed twice using 0.1 M sodium cacodylate buffer before post-fixation with 0.1 M OsO_4 in 0.1 M sodium cacodylate buffer and subsequent washing using 0.1 M sodium cacodylate buffer. The cells were then allowed to dry for 15 minutes in

graded concentrations of ethanol (30, 50, 70, 96 and 100%). Critical point drying was carried out on the coverslips before coating with 5 nm Cd-Au alloy, using a JEOL JFC-2300 HR High Resolution Fine Coater (JEOL Ltd., Tokyo, Japan). Microscopic analysis was performed using a Scanning Electron Microscope JEOL JSM-7400F (JEOL Ltd.).

Cell adhesion assay

hCMEC/D3 cells were seeded at 5,000 cells per well in 96-well plates (Greiner Bio-One, Kremsmünster, Austria) and incubated for 24 hours at 37 °C in a 5% CO_2 tissue incubator. K16ApoE at concentrations 0, 20, 40 or 80 µg/mL were added to the wells and incubated for 45 minutes. Subsequently, unattached cells were washed away with PBS and adherent cells were fixed with 4% formaldehyde at 0, 30 and 60 minutes after the peptide was replaced with fresh culture media. Adherent cells were then stained using 0.1% w/v crystal violet. Absorbance of stained nuclei was determined using a plate reader (POLARstar OPTIMA BMG Labtech, Ortenberg, Germany) at 570 nm.

***In vitro* BBB model**

For resistance monitoring using the Electric Cell Substrate Impedance Sensing (ECIS) system, ECIS arrays (8W10E+, 8 wells; Ibidi GmbH) were stabilized with L-cysteine (10nM; 10 minutes), washed in Hank's balanced salt solution (Thermo-Fisher, UK), coated with recombinant Human Endorepellin/Perlecan at 10 µg/mL (R&D systems, Minneapolis, MN, USA) and incubated at 37° C, 5% CO_2 for two hours. After seeding density optimization, 7,500 hCMEC/D3 cells were then seeded into each well and cell resistance monitored at 4,000 Hz using an ECIS Zθ (Applied Biophysics, USA) system for 70 hours at 37 °C with 5% CO_2. 0, 20, 40 or 80 µg/mL of K16ApoE peptide was then added to the system and resistance was further recorded until recovery of the barrier was observed. Resistance values were obtained in Ω. For each experiment, at least three replicates were measured.

For the cell automated sensing system, CellZscope®, 8 μm pore-size at 0.33 cm^2, polycarbonate membrane trans-well inserts (Corning, UK) were used. The transwell inserts were coated with 10 μg/mL human perlecan (R&D systems, Minneapolis, MN, USA) on the apical side of the filter membranes and with 5 μg/mL human fibronectin (Sigma-Aldrich) on the basal side of the filter. 2,500 of SC-1800 cells were seeded on the basal side of the porous filter membrane and left to adhere for two hours in the laminar flow hood before 7.5×10^4 hCMEC/D3 cells were seeded on the apical side of the filter. The cells were then incubated for 72 hours in the incubator at 37 °C and 5% CO_2. The resistance values were recorded using the CellZscope® automated cell monitoring system, CellZscope® (nanoAnalytics GmbH, Münster, Germany). Once the resistance plateaued, 0, 20, 40 and 80 μg/mL of K16ApoE was added and TEER values, expressed in $\Omega.cm^2$, were further recorded in real-time until recovery of the barrier was observed. High TEER values reflected tight junction formation. For each experiment, at least three replicates were measured.

In vivo biodistribution of ^{125}I–K16ApoE

The imidazole ring of histidine in K16ApoE was labelled with ^{125}I using 1,3,4,6-tetrachloro-3α,6α–diphenylglycouril (Iodo-Gen) at pH 9 (4,5). Briefly, 0.1 mg Iodo-Gen (T0656, Sigma-Aldrich) dissolved in 0.05 mL chloroform was dispersed in a 1.8 mL Nunc tube (Nunc). A film of the virtually water-insoluble Iodo-Gen was formed in the Nunc vial by allowing the chloroform to evaporate to dryness under nitrogen. Then, 1 mL 0.05 M phosphate buffer with pH 9.0, containing 2 mg K16ApoE and 2 MBq ^{125}I (Institute for Energy Technology, Kjeller, Norway) was added and the iodinating tube gently agitated for 10 minutes. The reaction was terminated by removing the solution from the Iodo-Gen tube. The stock solution was stored in the dark at 4 °C. Low molecular weight radioactivity accounted for about 40% of the total ^{125}I-activity, and was removed to undetectable levels before use by Pierce™ ^{18}C Spin Columns. ^{125}I-K16ApoE was validated by reversed phase and size exclusion chromatography and found to have the essentially similar elution pattern as unlabeled K16ApoE (Supplementary Figure S6A). Each bolus injection contained about 20 μg ^{125}I-K16ApoE.

Two 18 weeks old NOD/SCID mice were anaesthetized by intramuscular injection of 0.12 mg ketamin and 0.243 µg medetomidine per gram bodyweight dissolved in PBS. The core temperature was maintained at 37 °C with the aid of a heating lamp and a servo-controlled heating pad. A PE-50 catheter (AgnThos AB, Lidingö, Sweden) was inserted into the carotid artery of each mouse to allow blood sampling. 20 µg ^{125}I-K16ApoE diluted in 50 µL 9 mg/mL NaCl was injected into the tail vein of each mouse as a bolus over one minute. Arterial blood samples were then collected at 0.5, 1, 5, 10, 15, 20 and 30 minutes after the ^{125}I-K16ApoE administration was completed. The animals were then sacrificed by injecting saturated KCl into the carotid artery. Immediately after, brain, skin, heart, lung, liver, stomach, spleen, colon, kidneys, muscle tissue and femur were collected and counted for ^{125}I activity using a Wallac Wizard 1470 gamma counter (PerkinElmer, Waltham, MA, USA). The counts were corrected for background values before the peptide distribution was calculated as ^{125}I activity per gram organ or per 10 µL plasma.

***In vivo* treatment study**

Prior to intracardiac injections, the NOD/SCID mice were anesthetized and fixed in a supine position on a heating pad to maintain a core temperature at 37° C. 5×10^5 H1_DL2 cells resuspended in 0.1 mL PBS were injected during 30 seconds into the left cardiac ventricle of each mouse using a 30G insulin syringe (Omnican50, B. Brain Medical AS, Vestskogen, Norway), by ultrasound guidance (Vevo$^{(R)}$ 2100 Imaging System 230 V, Visual Sonics Inc., Toronto, Canada).

Contrast enhanced MRI was carried out four and six weeks after start of the treatment experiment to evaluate the brain metastatic burden. A 7 Tesla small-animal horizontal scanner (Bruker BioSpin GmbH) equipped with a 72 mm quadrature transmit coil and a four-channel mouse brain array receive coil was used. A T_2 weighted scan was performed in coronal orientation (TR/TE: 4,000/48 ms, FOV: 2.00 cm, matrix size: 256 × 256, slice thickness: 1.00 mm, number of slices: 7, NEX: 4, scan time: 6 minutes, 13 seconds) followed by T_1 scans using the same geometrical parameters (TR: 1,000 ms, TE: 9 ms, and NEX: 4, scan time: 3 minutes, 20 seconds) before and after

subcutaneous administration of 0.5 mmol/kg Omniscan (GE Healthcare). The MR images were analysed in OsiriX Lite v.9.5.2 (Pixmeo SARL, Bernex, Switzerland) to determine the tumor numbers and volumes ($4/3\ \pi\ r^3$) as a measure of metastatic burden.

Mass spectrometry

A pilot mass spectrometry experiment was performed by a company provider (ImaBiotech, Loos, France). Briefly, tumor bearing mice treated either with K16ApoE + dabrafenib or saline, were perfused with 4% formaldehyde, their brains were removed and immediately snap-frozen. Thereafter, the brains were embedded into paraffine according to standard protocols. 10 μm thick brain sections were mounted onto indium tin oxide conductive glass slides. 1 μL MALDI matrix (α-cyano-4-hydroxycinnamic acid) was added onto the sections, and the sections were dried under vacuum for 15 minutes. Direct analysis was performed with a 7T-MALDI-FTICR in Full Scan and Continuous Accumulation of Selected Ions positive mode. The data sets were analysed with DataAnalysis 4.1 (Bruker Daltonics, Bremen, Germany).

Labelling of albumin and IgG with ^{18}F

The *in vivo* BBB opening effect of K16ApoE was further evaluated by PET using ^{18}F-albumin from mouse serum (Sigma-Aldrich, cat no A3139) and ^{18}F-IgG from mouse serum (Sigma-Aldrich, cat no I5381). The labelling prosthetic group, [^{18}F]F-Py-TFP (6-[^{18}F]Fluoronicotinic acid 2,3,5,6-tetrafluorophenyl ester), and its precursor, (*N,N,N*-Trimethyl-5-((2,3,5,6-tetrafluorophenoxy)-carbonyl)pyridin-2-aminium trifluoromethanesulfonate) were made according to previously published methods (6). The crude reaction mixture of [^{18}F]F-Py-TFP (from 5 mg precursor) was diluted in 4 mL 20% acetic acid and passed through a preconditioned (5 mL MeCN + 5 mL water) SepPak Light tC18-cartridge. Unreacted precursor was removed with 5 mL 30% MeCN, and the cartridge washed with 5 mL water. [^{18}F]F-Py-TFP was eluted from the tC18-cartridge with 1 mL diethyl ether through a SepPak Dry-cartridge. The ether was removed by evaporation. The freshly

made [^{18}F]F-Py-TFP was used to label both albumin and IgG. The protein labelling was carried out by dissolving 1 mg of the protein in 200 µL 0.05 M phosphate buffer (pH ~ 9) and adding [^{18}F]F-Py-TFP dissolved in small amounts of MeCN. The solution was heated to 40 °C and stirred gently for 15 minutes. The product was purified by a PD MidiTrap G-10 size exclusion column, using 9 mg/mL NaCl solution as an eluent.

Dynamic positron emission tomography/computer tomography (PET/CT) imaging

PET/CT images were acquired on a small-animal nanoScanPC PET/CT scanner (Mediso Medical Imaging Systems, Budapest, Hungary). Healthy (non-tumor bearing) NOD/SCID mice were anesthetized using 3% sevoflurane (Abbott Laboratories Ltd.) mixed in oxygen for the duration of the scans, while monitored for breathing and temperature. CT scans (50 kvP, 300 ms) were performed for anatomical information and attenuation correction of PET images. ~2 MBq of tracer was injected into the tail vein and a dynamic acquisition scan (coincidence 1:5, normal count mode) was started immediately. PET and CT images were co-registered automatically. PET reconstruction was performed by Nucline software (Mediso) from list-mode using the following parameters: Reconstruction algorithm Tera-Tomo 3D (OSEM), energy window 400–600 keV, coincidence mode 1:5, voxel size 0.4 mm, four iterations and six subsets, corrections for random events, detector normalization, decay and dead time. Images were reconstructed to the following time frames: 5 × 2 minutes, 8 × 5 minutes (4 × 5 minutes for the 30 minutes scans). Data analysis was performed using InterView Fusion (version 3.01.004.0000, Mediso).

Four minutes before the PET/CT acquisition, the animals were injected with 200 µg K16ApoE dissolved in 9 mg/mL NaCl. 24 hours later, the same animals were injected with 9 mg/mL NaCl prior to repeating the PET/CT acquisition. Thus, each mouse served as their own negative control. For each animal, an ellipsoid volume of interest (VOI) delineating the skull was drawn to cover the whole brain of each mouse. The mean standard uptake value (SUV_{mean}) was calculated using the following

equation: $SUV_{mean} = C_{PET}(T)/(ID/BW)$, where $C_{PET}(T)$ is the mean measured activity in the VOI at time T, ID is injected dose measured in kBq, and BW is the animal weight in kg.

Supplementary Table 1: Mean V_e, K_{ep} and AUC after DCE-MRI.

Group	Minutes	n	V_e (%)	K_{ep} (min-1)	AUC (a.u.)
K16ApoE	10	5	58.98 ± 31.331	0.31 ± 0.203	17.73 ± 5.928
	30	5	43.08 ± 23.384	0.09 ± 0.039	5.78 ± 1.425
	60	6	10.82 ± 8.719	0.20 ± 0.069	2.65 ± 1.525
	120	5	10.42 ± 10.688	0.39 ± 0.343	2.62 ± 0.676
	240	5	2.126 ± 1.973	0.74 ± 0.453	1.68 ± 0.536
Saline	10	8	0.681 ± 0.411	0.59 ± 0.223	1.64 ± 0.809
	30	5	0.872 ± 0.347	0.69 ± 0.255	1.48 ± 0.460
	60	6	0.90 ± 0.819	0.69 ± 0.378	1.42 ± 0.760
	120	5	1.202 ± 0.528	0.69 ± 0.276	1.83 ± 0.534
	240	5	1.22 ± 0.947	0.74 ± 0.406	1.68 ± 0.432

All values are given as mean ± standard deviation. Abbreviations: Min: minutes, V_e: Fractional volume of extravascular extracellular space (EES), K_{ep}: Rate constant from compartment 2 to 1 (reversed K^{trans}), AUC: Area under curve, a.u.: arbitrary units.

Legends to Supplementary figures

Supplementary Figure S1

In vivo study design. **A,** An illustration of the study design used to evaluate K16ApoE toxicity on a total number of 38 NOD/SCID mice. **B,** An overview of the 45 NOD/SCID mice used in the *in vivo* treatment study shown in Figure 5 and Supplementary Figures S7 and S8.

Supplementary Figure S2

Blood smear from mice subjected to 1,000 µg K16ApoE. **A,** A representative phase contrast image of a blood smear sample from a NOD/SCID mouse subjected to 1 000 µg K16ApoE as a bolus injection over approximately one minute. **B,** A representative blood smear from a control NOD/SCID mouse injected with a bolus of 9 mg/mL NaCl. Scalebar 100 µm. **C,** Quantification of the number of erythrocytes with an abnormal morphology as a function of the total cell number per microscope image scaled to 100% (n = 3). Unpaired t-test. Mean ± SEM. Abbreviation: ****: $p<0.0001$.

Supplementary Figure S3

In vitro cell viability. **A,** IC_{50} curves for RBE4 **B,** MDCK **C,** MDCK II **D,** hCMEC/D3 and **E,** H1 cells after incubation with 0, 0.1, 20, 40, 80, 100 or 150 µg/mL K16ApoE for 45 minutes. **F,** Live/Dead staining of MDCK cells incubated with 0, 20, 40 or 80 µg/mL K16ApoE for 45 minutes. Scalebar 50 µm. **G** Quantification of live (green) and dead (red) cells in f. **H** SEM images of RBE4 cells treated with 80 µg/mL K16ApoE. Scalebar 20 µm.

Supplementary Figure S4

Mechanistic studies of the *in vitro* effects of K16ApoE **A**, Flow cytometry data showing the effects of two endocytosis inhibitors; chlorpromazine (left) and dynasore (right) after 30 minutes of incubation on H1, **B,** H2, **C,** hCMEC/D3 and **D,** MDCK cells measured as BSA uptake in the APC-A channel. Abbreviations: APC-A: allophycocyanin-A, BSA: bovine serum albumin, cp: chlorpromazine, dyn: dynasore, K16: K16ApoE.

Supplementary Figure S5

In vitro BBB model. **A,** Adhesion of hCMEC/D3 cells after incubation with 0, 20, 40 or 80 µg/mL of K16ApoE for 45 minutes as measured by crystal violet. 2way ANOVA statistical test. Mean ± SEM. **B,** Phase contrast images of hCMEC/D3 cells after corresponding incubation times and concentrations with the peptide. Scalebar 50 µm. Abbreviations: *: $p<0.05$, **: $p<0.01$.

Supplementary Figure S6

Biodistribution of ^{125}I-K16ApoE. **A,** Elution profiles demonstrating native K16ApoE and ^{125}I-K16ApoE. **B,** Temporal elimination of the ^{125}I-K16ApoE from blood plasma (n=3) during 30 minutes. Mean ± SEM. **C**, Accumulation of ^{125}I-K16ApoE within the specified tissues (n=3) after 30 minutes given in cpm/g. Mean ± SEM. Abbreviations: ^{125}I: iodide-125, cpm: counts per minute.

Supplementary Figure S7

Histopathological evaluation of tissue samples after long- and short-term treatment of NOD/SCID mice with the peptide. **A,** Tissue preparations from NOD/SCID mice treated once with the peptide. **B,** Tissue preparations from tumor-bearing NOD/SCID mice treated with the peptide twice a week over six weeks, drug only or vehicle. Scalebar 200 μm.

Supplementary Figure S8

In vivo treatment control experiment. **A,** Mean, total volume of brain metastases four (left) and six weeks (right) after commencing the control experiment, treating mice with saline or K16ApoE only. Mann-Whitney statistical test. Mean ± SEM **B,** Mean, total number of tumors four (left) and six weeks (right) after start of the control experiment. Mann-Whitney statistical test. Mean ± SEM. **C,** Representative contrast enhanced T_1 and T_2 weighted MRI images after four (left) and six (right) weeks. Abbreviations: CE: Contrast enhanced, T_1: T_1 MRI weighting, T_2: T_2 MRI weighting.

Supplementary Figure S9

Mass spectrometry of treated and untreated brain tissue. **A,** Dabrafenib (m/z 520.108) was fragmented and detected at m/z 480.1 and 344.1, as seen in the working standard. **B,** In the tissue sample originating from the brain of an untreated NOD/SCID mouse, none of these fragments were detected. **C,** In the tissue sample of a NOD/SCID mouse treated with a combination of K16ApoE and dabrafenib, the same fragments as in A were detected.

Legends to Supplementary Videos

Supplementary Video S1

Sonographic visualization of the axial position of the heart of a NOD/SCID mouse injected with 9 mg/mL NaCl intravenously.

Supplementary Video S2

Sonographic visualization of the axial position of the heart of a NOD/SCID mouse injected with 1 000 µg K16ApoE intravenously.

Supplementary Video S3

A time-lapse series recorded on a Leica TCS SP8 STED confocal microscope, showing a control sample of MDCK cells labeled with Calcein-AM (green), which indicates live cells and Ethidium homodimer-1 (red), indicating dead cells.

Supplementary Video S4

A time-lapse series recorded on a Leica TCS SP8 STED confocal microscope, showing MDCK cells treated with 20 µg of K16ApoE immediately after labelling with calcein-AM, indicating live cells (green) and ethidium homodimer-1, indicating dead cells (red).

Supplementary Video S5

A time-lapse series recorded on a Leica TCS SP8 STED confocal microscope, showing MDCK cells treated with 40 µg of K16ApoE immediately after labelling with calcein-AM, indicating live cells (green) and ethidium homodimer-1, indicating dead cells (red).

Supplementary Video S6

A time-lapse series recorded on a Leica TCS SP8 STED confocal microscope, showing MDCK cells treated with 80 µg of K16ApoE immediately after labelling with calcein-AM, indicating live cells (green) and ethidium homodimer-1, indicating dead cells (red).

Bibliography

1. Wang J, Daphu I, Pedersen PH, Miletic H, Hovland R, Mork S*, et al.* A novel brain metastases model developed in immunodeficient rats closely mimics the growth of metastatic brain tumours in patients. Neuropathol Appl Neurobiol **2011**;37(2):189-205 doi 10.1111/j.1365-2990.2010.01119.x.

2. Kratochvila J, Jirik R, Bartos M, Standara M, Starcuk Z, Jr., Taxt T. Distributed capillary adiabatic tissue homogeneity model in parametric multi-channel blind AIF estimation using DCE-MRI. Magn Reson Med **2016**;75(3):1355-65 doi 10.1002/mrm.25619.

3. Keunen O, Johansson M, Oudin A, Sanzey M, Rahim SA, Fack F*, et al.* Anti-VEGF treatment reduces blood supply and increases tumor cell invasion in glioblastoma. Proc Natl Acad Sci U S A **2011**;108(9):3749-54 doi 10.1073/pnas.1014480108.

4. Fraker PJ, Speck JC, Jr. Protein and cell membrane iodinations with a sparingly soluble chloroamide, 1,3,4,6-tetrachloro-3a,6a-diphrenylglycoluril. Biochem Biophys Res Commun **1978**;80(4):849-57.

5. Salacinski PR, McLean C, Sykes JE, Clement-Jones VV, Lowry PJ. Iodination of proteins, glycoproteins, and peptides using a solid-phase oxidizing agent, 1,3,4,6-tetrachloro-3 alpha,6 alpha-diphenyl glycoluril (Iodogen). Anal Biochem **1981**;117(1):136-46.

6. Olberg DE, Arukwe JM, Grace D, Hjelstuen OK, Solbakken M, Kindberg GM*, et al.* One step radiosynthesis of 6-[(18)F]fluoronicotinic acid 2,3,5,6-tetrafluorophenyl ester ([(18)F]F-Py-TFP): a new prosthetic group for efficient labeling of biomolecules with fluorine-18. J Med Chem **2010**;53(4):1732-40 doi 10.1021/jm9015813.

Supplementary Figure S1

A

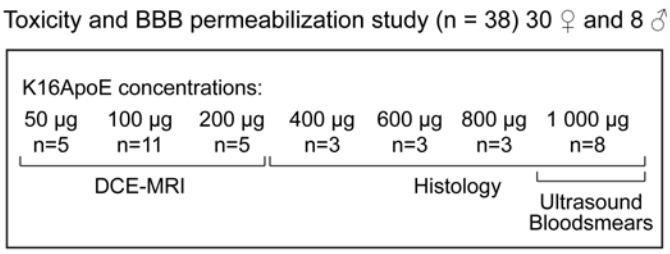

B

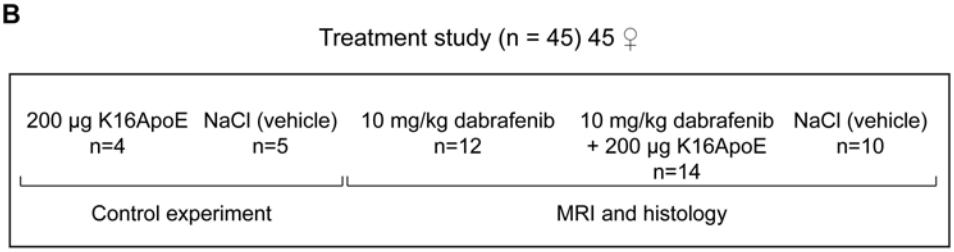

Supplementary Figure S2

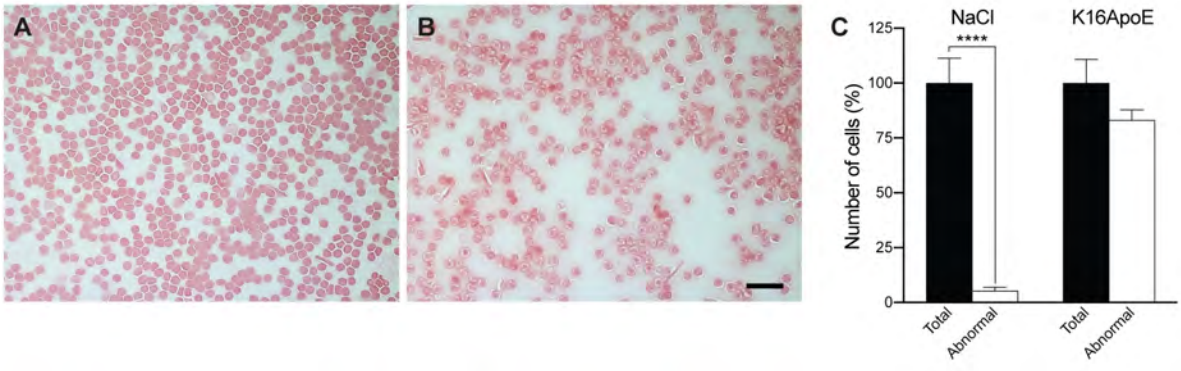

Supplementary Figure S3

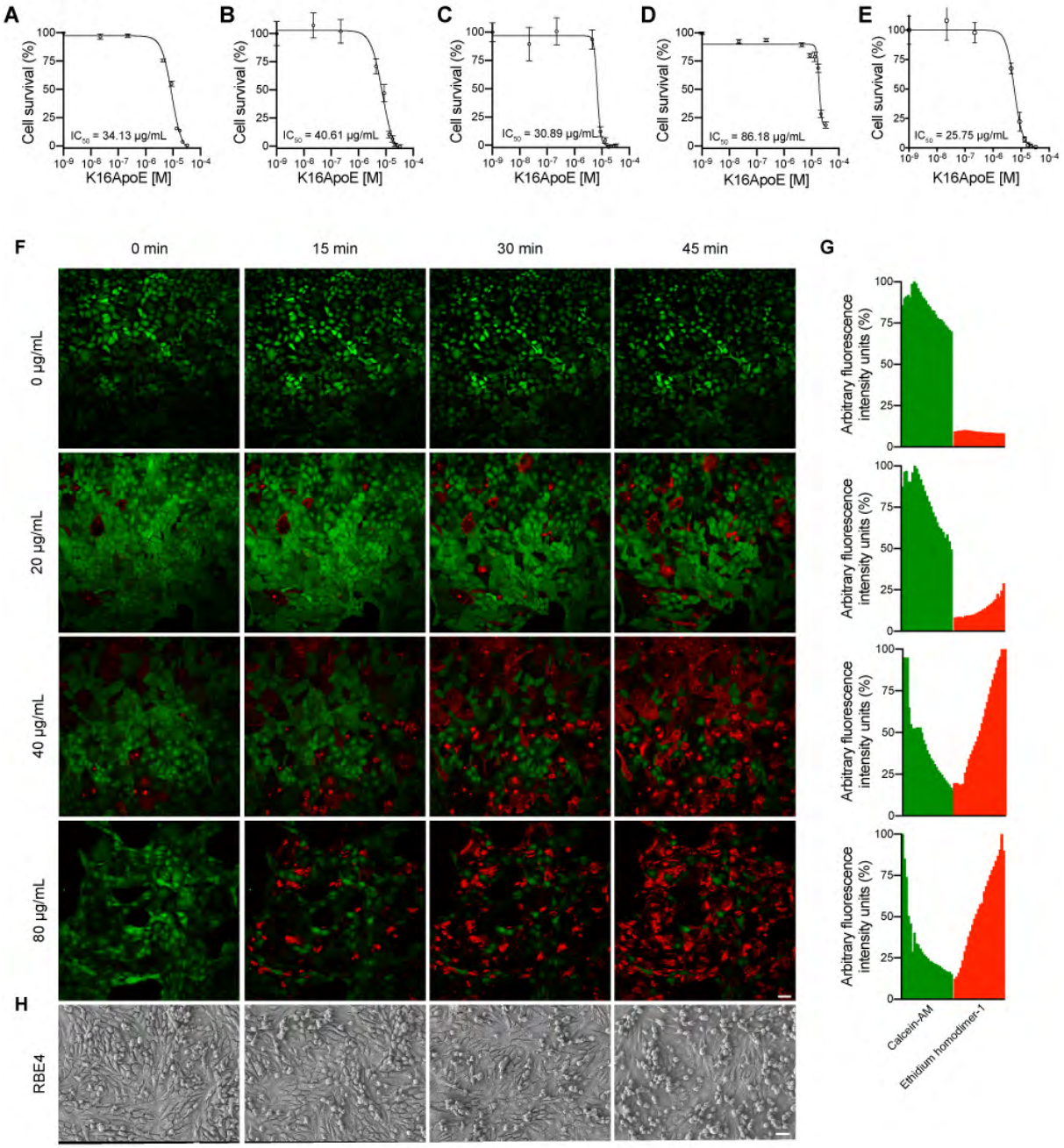

Supplementary Figure S4

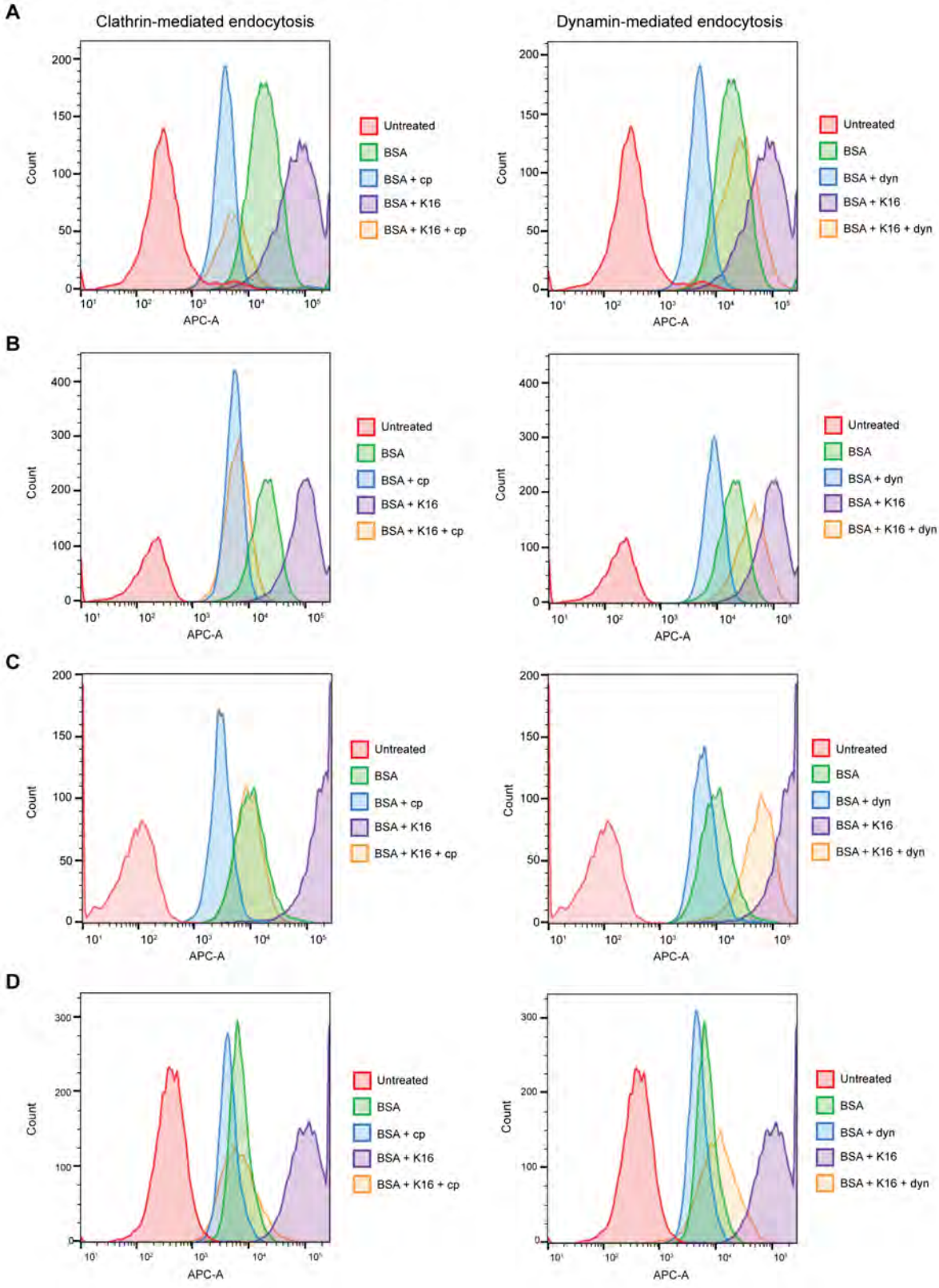

Supplementary Figure S5

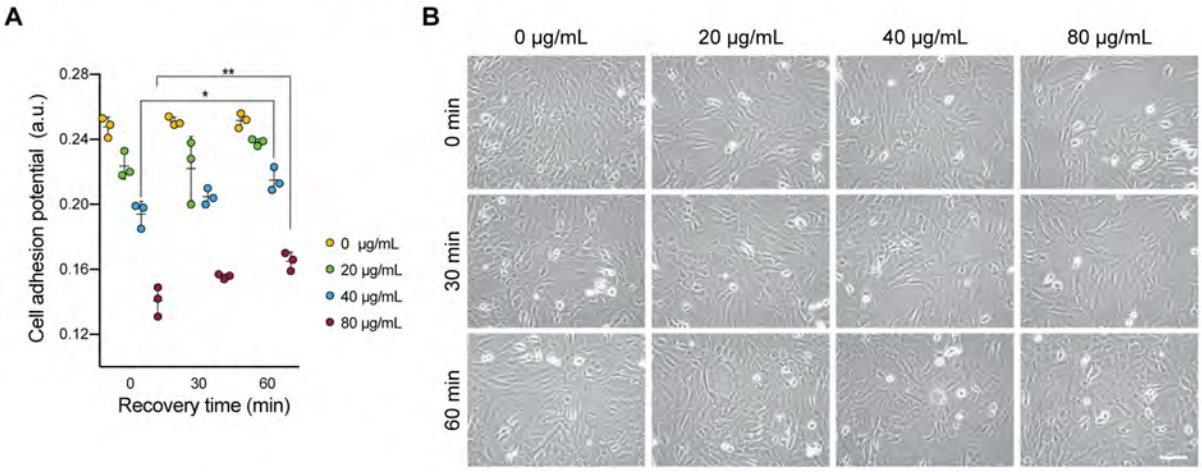

Supplementary Figure S6

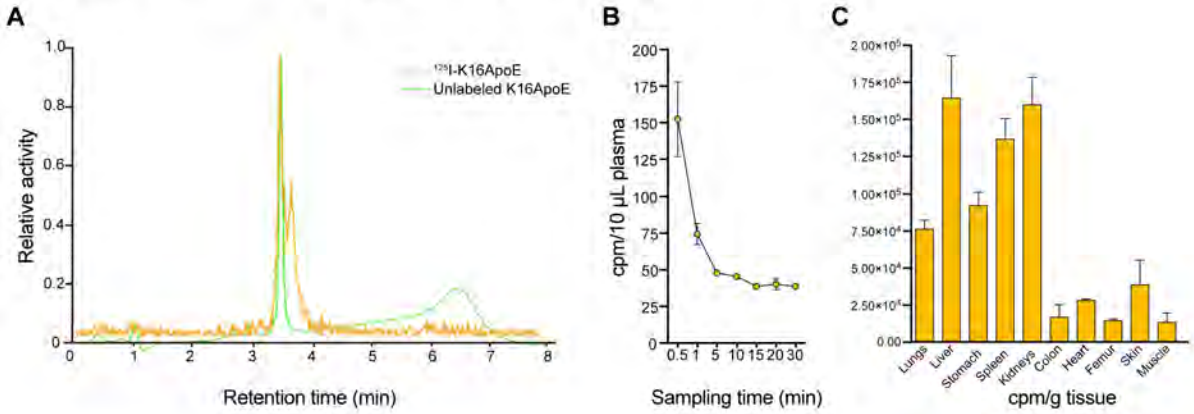

Supplementary Figure S7

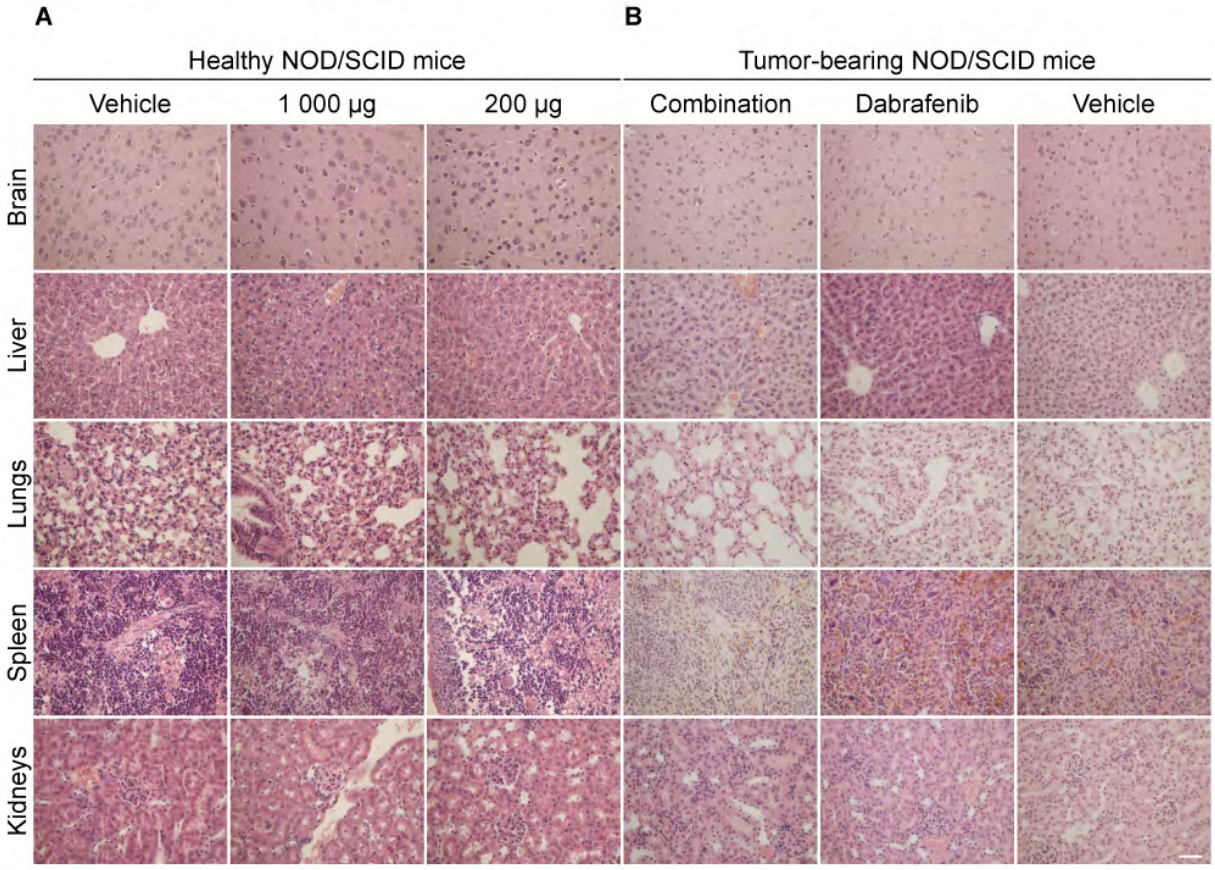

Supplementary Figure S8

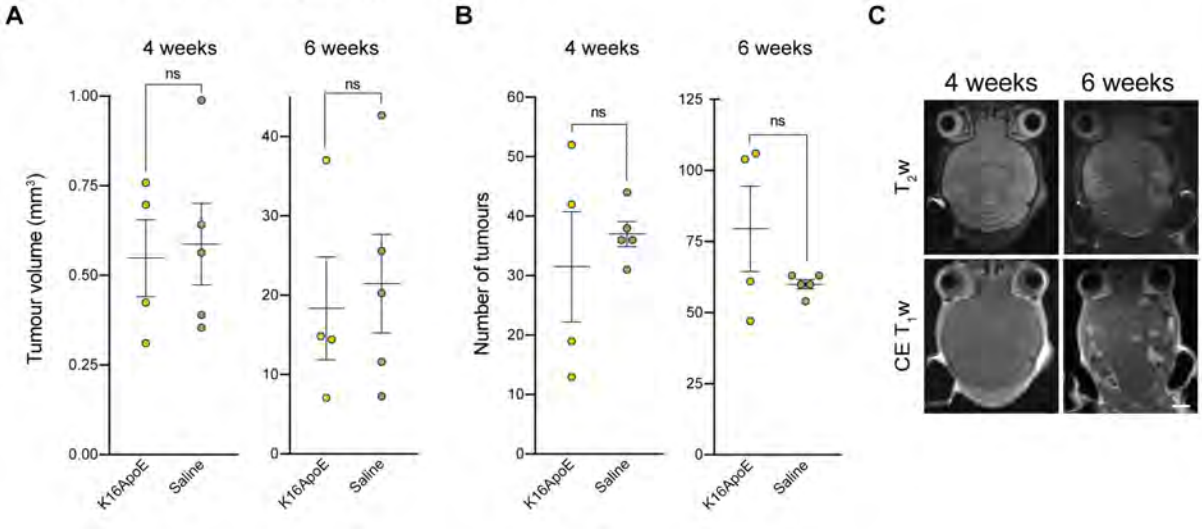

Supplementary Figure S9

A Working standard

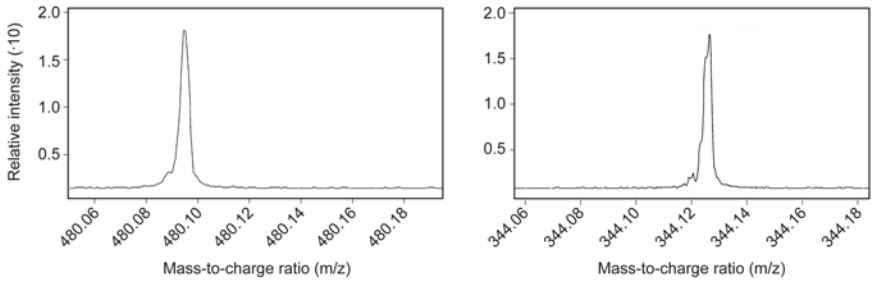

B Negative control mouse

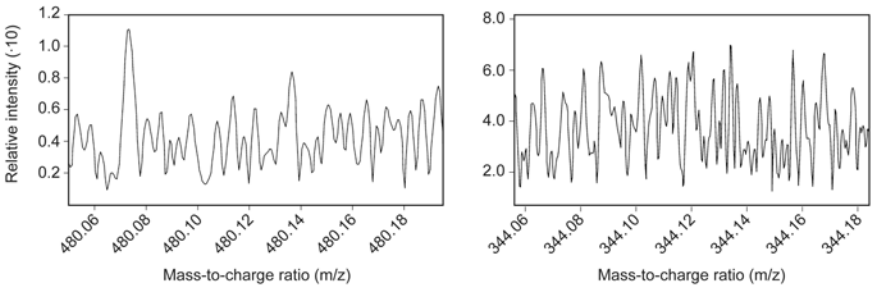

C K16ApoE + dabrafenib treated mouse

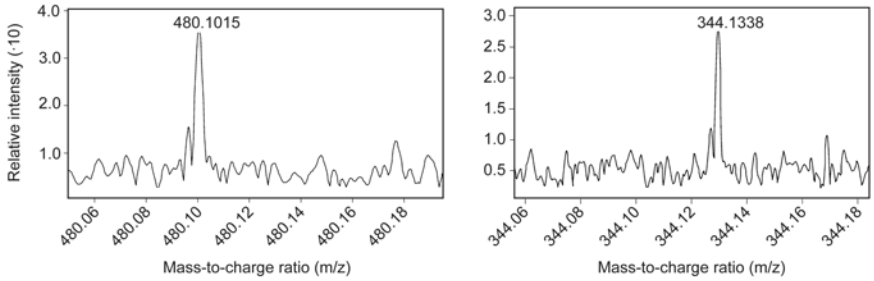

Acta Neuropathologica Communications

RESEARCH Open Access

Inhibition of mitochondrial respiration prevents *BRAF*-mutant melanoma brain metastasis

Terje Sundstrøm[1,2,3], Lars Prestegarden[1,2,4], Francisco Azuaje[5,6], Synnøve Nymark Aasen[1,7], Gro Vatne Røsland[8], Jobin K. Varughese[1], Marzieh Bahador[1], Simon Bernatz[9], Yannick Braun[9], Patrick N. Harter[9], Kai Ove Skaftnesmo[10], Elizabeth S. Ingham[11], Lisa M. Mahakian[11], Sarah Tam[11], Clifford G. Tepper[12], Kjell Petersen[13], Katherine W. Ferrara[11], Karl Johan Tronstad[8], Morten Lund-Johansen[2,3], Rudi Beschorner[14], Rolf Bjerkvig[1,5†] and Frits Thorsen[1,15*†]

Abstract

Melanoma patients carry a high risk of developing brain metastases, and improvements in survival are still measured in weeks or months. Durable disease control within the brain is impeded by poor drug penetration across the blood-brain barrier, as well as intrinsic and acquired drug resistance. Augmented mitochondrial respiration is a key resistance mechanism in *BRAF*-mutant melanomas but, as we show in this study, this dependence on mitochondrial respiration may also be exploited therapeutically. We first used high-throughput pharmacogenomic profiling to identify potentially repurposable compounds against *BRAF*-mutant melanoma brain metastases. One of the compounds identified was β-sitosterol, a well-tolerated and brain-penetrable phytosterol. Here we show that β-sitosterol attenuates melanoma cell growth in vitro and also inhibits brain metastasis formation in vivo. Functional analyses indicated that the therapeutic potential of β-sitosterol was linked to mitochondrial interference. Mechanistically, β-sitosterol effectively reduced mitochondrial respiratory capacity, mediated by an inhibition of mitochondrial complex I. The net result of this action was increased oxidative stress that led to apoptosis. This effect was only seen in tumor cells, and not in normal cells. Large-scale analyses of human melanoma brain metastases indicated a significant role of mitochondrial complex I compared to brain metastases from other cancers. Finally, we observed completely abrogated BRAF inhibitor resistance when vemurafenib was combined with either β-sitosterol or a functional knockdown of mitochondrial complex I. In conclusion, based on its favorable tolerability, excellent brain bioavailability, and capacity to inhibit mitochondrial respiration, β-sitosterol represents a promising adjuvant to BRAF inhibitor therapy in patients with, or at risk for, melanoma brain metastases.

Keywords: Cancer, Melanoma, Brain metastasis, BRAF V600E, β-Sitosterol, Treatment

Introduction

Melanoma incidence rates are increasing, and brain metastases represent a leading cause of melanoma-associated deaths [10, 14, 17, 48]. Even though phase II clinical trials have shown promising therapeutic effects by the use of BRAF inhibitors (BRAFi) + MEK inhibitors (MEKi), resistance still develops [18, 32]. Also, in experimental studies it has been shown that immunotherapy combining anti-PD1 plus CTLA4 may have a therapeutic effect [59]. However, a major problem is the presence of the blood-brain barrier (BBB), which is intact during early stages of brain metastasis development [51]. Although the presence of metastases can compromise the structure and integrity of the BBB, it is still a significant obstacle for efficient drug delivery [22, 31, 37, 66]. Moreover, cancer cells that have extravasated to the brain parenchyma may find protection within the brain

* Correspondence: frits.thorsen@uib.no
†Rolf Bjerkvig and Frits Thorsen contributed equally to this work.
[1]Kristian Gerhard Jebsen Brain Tumour Research Centre, Department of Biomedicine, University of Bergen, Jonas Lies vei 91, 5009 Bergen, Norway
[15]The Molecular Imaging Center, Department of Biomedicine, University of Bergen, Jonas Lies vei 91, 5009 Bergen, Norway
Full list of author information is available at the end of the article

microenvironment, and be more prone to develop resistance due to sub-therapeutic drug concentrations [46, 52]. There are also significant concerns associated with drug-related adverse effects, patient selection, and costs versus benefits [56, 67]. Thus, there is a prevailing need to find new therapeutic and preventive approaches that offer improved and sustained responses against brain metastases [3, 52].

Recently, it has been shown that molecular drivers of cellular metabolic reprogramming events may be critical in tumor development, metastasis formation and drug resistance [1]. For instance, subsets of melanomas that show primary resistance to targeted therapies seem to rely more on mitochondrial respiration than glycolysis [45, 63]. Furthermore, when *BRAF*-mutant melanomas are treated with vemurafenib (a BRAFi), the MITF-PGC1α axis is up-regulated, which leads to increased mitochondrial respiration and scavenging of reactive oxygen species (ROS) [24]. These intrinsic and acquired resistance mechanisms provide obvious survival advantages, but the dependence on mitochondrial respiration may also be exploited therapeutically [24, 45, 49, 63, 69].

The metabolic alterations that occur in melanoma brain metastases are largely unknown, but cell lines derived from metastatic melanomas and melanoma metastases (non-brain) have shown elevated levels of mitochondrial respiration when compared to primary melanomas [7, 26]. In the brain, metastatic breast cancer cells have been shown to be less dependent on glucose, and instead utilize mitochondrial respiration for energy production and antioxidant defense [15, 16]. Moreover, metastatic breast cancer cells have been shown to display neuron-like characteristics in the brain microenvironment [39, 41]. Whether these changes reflect intrinsic or adaptive capabilities of tumor cells to thrive in the neural niche remains to be determined. Nevertheless, to survive and grow, extravasated cancer cells can adjust to the lower glucose levels in the brain interstitium [16]. Notably, when cancer cells are deprived of glucose they switch from glycolysis to mitochondrial respiration and become sensitive to low doses of mitochondrial complex I (CI) inhibitors that do not affect normal (non-cancerous) cells [40].

In this study (scientific flowchart outlined in Additional file 1: Figure S1), using a well-established patient derived metastatic xenograft model, we identified a melanoma brain metastasis gene signature by RNA-sequencing (RNA-seq). We then utilized the Connectivity Map drug discovery tool (cMap; Broad Institute) to search for putative therapeutic compounds with the potential to invert the signature. The lead compounds identified were then tested in predictive xenograft models of *BRAF*-mutant melanoma brain metastases. Here, we show that β-sitosterol, a well-tolerated and brain-penetrable phytosterol, effectively prevented the emergence of brain metastases leading to a significant survival benefit. Mechanistically, we show that β-sitosterol targets mitochondrial CI that leads to an inhibition of mitochondrial respiration. We also show that β-sitosterol abrogates potential resistance to BRAFi, inferring a clear therapeutic rationale for using β-sitosterol as a therapeutic agent towards melanoma metastases.

Materials and methods

Cell lines

The H1 cell line was generated from a human melanoma brain metastasis and transduced with lentiviral vectors expressing the genes for GFP and luciferase (H1_DL2) as previously described [60], or shRNAs targeting NDUFA8 (H1_shNDUFA8; TAGAAGACGCACCGGCGGTGTTTA GGGGAAGGTAAAGTTAATATTCATAGCTTTGCCTT CCTCTAAACACCGTTTTTTGGCAAGCAAAAGACGG CATACGAGATATGTACCAGTCAGTACCAGTTTCGC CGTCTTCGT). The Melmet 1 and Melmet 5 melanoma cell lines were developed from a skin and a lymph node metastasis, respectively, and were kindly provided by Ø. Fodstad (University of Oslo, Oslo, Norway). The A375 cell line was purchased from the American Type Culture Collection (ATCC). A human lung fibroblast cell line, SV-80, was purchased from CLS Cell Lines Service GmbH. The PC14-PE6 cell line was kindly provided by F. Winkler (University Hospital Heidelberg & German Cancer Research Center, Heidelberg, Germany), and a brain seeking subline PC14_PE6_Br2 was generated in our laboratory as described earlier [27]. The Melmet 1 and Melmet 5 cell lines were transduced with a lentiviral pGF1-CMV reporter vector that co-expresses copGFP and firefly luciferase linked by the self-cleaving peptide T2A (System Biosciences). The immortalized human melanocytes-hTERT (cat. no. T0463) and astrocytes (cat.no. T0281) were both purchased from Applied Biological Materials (Richmond, BC, Canada). The primary epidermal melanocytes HEMa (cat.no. PCS-200-013) were purchased from ATCC. The H1, Melmet 1, Melmet 5 and A375 cell lines have the $BRAF^{V600E}$ mutation. The transduced cell lines were used in all experiments, authenticated within the last six months using short tandem repeat (STR) profiling, and maintained as previously described [57].

In vivo generation of samples for RNA sequencing

Eight weeks old female NOD.CB17-$Prkdc^{scid}$/NcrCrl mice were purchased from Charles River Laboratories International. Anesthesia was induced with 3% and maintained with 1.5% isofluorane in oxygen. We performed intracardiac injections in seven mice (5×10^5 H1_DL2 cells suspended in 0.1 mL PBS) as previously described [60]. Whole-body bioluminescence imaging (BLI) was used to evaluate injection failure 10 min post-injection and weekly over seven weeks to monitor

metastasis formation (Additional file 2: Figure S2a) using a Xenogen Ivis 100 Small Animal Molecular Imager (Xenogen Corporation) as previously described [60]. At seven weeks, we injected 150 mg/kg D-luciferin Firefly (Gold Biotechnology), sacrificed the mice ten min later, and performed ex vivo BLI to evaluate organ involvement in detail. All animals invariably developed metastases in their brain, adrenals, ovaries, and femurs, and these organs from five animals showing the highest tumor burden on BLI, were dissociated using tailored protocols based on the Liberase TM Research Grade enzyme reagent (Roche Applied Science; Additional file 3 Table S1). Sample yields of GFP positive tumor cells were checked by fluorescence microscopy prior to cell sorting (Additional file 2: Figure S2b) using the BD Influx high-speed cell sorter (BD Biosciences). We aimed for a minimum of 150,000 cells in each sample, and picked the three tumor cell samples from each organ with the most cells for subsequent RNA sequencing: 1) brain (151,023, 150,835 and 154,797 cells); 2) adrenals (151,968, 184,506 and 276,146 cells); 3) ovaries (159,736, 171,814 and 433,703 cells); and 4) femurs (120,530, 91,055 and 73,942 cells). These 12 samples (3 samples × 4 organs) of metastatic melanoma cells were kept in 1% FBS medium, pelleted by centrifugation, transported on dry ice and stored in a − 80 °C freezer.

RNA isolation

Total cellular RNA was isolated from the cell pellets using the TRIzol reagent (Life Technologies) and a modified protocol that incorporates an additional extraction with phenol/chloroform/isoamyl alcohol (25:24:1, pH 4.3). RNA quantity and quality were assessed on a NanoDrop spectrophotometer (Thermo Scientific) and the Agilent 2100 Bioanalyzer (Agilent Technologies), respectively.

Library preparation for RNA sequencing

RNA sequencing (RNA-Seq) libraries were prepared from 1.0 μg total RNA using the TruSeq RNA Sample Preparation Kit (Illumina) according to the manufacturer's protocol. Briefly, poly-adenylated mRNA was purified from total RNA and ribosomal RNA removed by two rounds of binding to magnetic poly-dT beads. This was followed by RNA fragmentation by incubation in the presence of divalent cations at 94 °C for 5 min. Double-stranded cDNA was then generated by random-primed first-strand synthesis with SuperScript II reverse transcriptase and subsequent second strand synthesis with RNase H and DNA Polymerase I. The cDNA was then blunt-ended with T4 and Klenow DNA polymerases to remove the 3′-overhangs and fill in 5′-overhangs, phosphorylated with T4 PNK, and then 3′-A tailed by incubation with Klenow Fragment (3′ → 5′ exo−) and dATP. Illumina paired-end (PE) adapters were then ligated, followed by purification with AMPure XP beads. The library was then enriched by high-fidelity PCR amplification (15 cycles) with Phusion DNA Polymerase (Finnzymes Oy) and adapter-specific primers. The molar concentration of the libraries was determined by measuring concentration with a Qubit fluorometer (Invitrogen), determining the insert length with an Agilent 2100 Bioanalyzer, and then qPCR-based quantification (KAPA Library Quantification Kit).

RNA sequencing

Indexed libraries were pooled, loaded on TruSeq paired-end flow cells, and paired-end sequencing (2 × 100 bp, paired-end; 4 libraries/lane) was performed with an Illumina HiSeq 2000 sequencing system (BGI@UC Davis Joint Genome Center) using standard Illumina kitted reagents (TruSeq SBS Kit v3-HS). Image processing, base calling, quality scoring (Phred), and sample demultiplexing were executed by HiSeq Control Software with Real Time Analysis (HCS 1.5/RTA 1.13) and CASAVA 1.8 software (Illumina). The Tuxedo protocol (http://compbio.mit.edu/cummeRbund) was followed using the alternate protocol of quantification of reference annotation only. We used Ensembl's human genome build 19, and supplied TopHat with a set of known transcripts from Ensembl. The three BAM files from each individual organ were merged using Picard 1.91 (http://broadinstitute.github.io/picard), and these merged files were subsequently visualized using Integrative Genomics Viewer 2.3 (http://www.broadinstitute.org/igv). The cummeRbund package (http://compbio.mit.edu/cummeRbund) and Partek Genomics Suite 6.12 (Partek Inc.) were used to produce visualizations (Additional file 2: Figure S2c).

Gene expression analysis and brain metastasis gene signature

We developed an integrated workflow of several independent analyses to build a brain metastasis gene expression profile (Fig. 1b and Additional file 2: Figure S2d). First, there were 134 genes differentially expressed in brain metastases and metastases to any of the other organs; 122 genes were upregulated and 54 were downregulated in brain (some genes appeared in multiple lists). Second, we used Prediction Analysis for Microarrays (PAM; http://statweb.stanford.edu/~tibs/PAM) to identify which of the 134 genes consistently distinguished brain metastases from other organ metastases. We found ten upregulated genes specific to brain metastases. Third, we validated eight of these ten genes using a combination of other computational analyses: A supervised rank product analysis (RankProd; http://www.bioconductor.org/packages/release/bioc/html/RankProd.html) of brain metastases compared with all the other organs pooled together

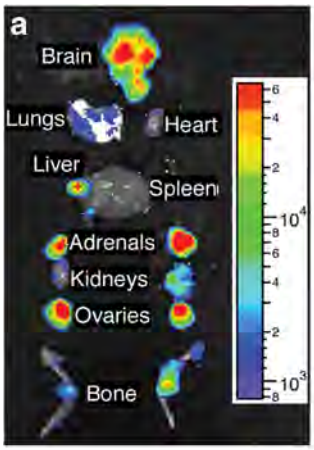

c

Compounds with potential to invert the brain metastasis gene signature

Name	CAS	Dose (μM)	cMap score	MW (g/mol)
Meticrane	1084-65-7	15	-1	275.34
Tolazamide	1156-19-0	13	-0.989	311.4
β-sitosterol	83-46-5	10	-0.984	414.7
Memantine	41100-52-1	19	-0.971	215.77
Niridazole	61-57-4	19	-0.967	214.22
Valproic acid	1069-66-5	200	-0.966	166.2
Letrozole	112809-51-5	14	-0.965	285.31
Todralazine	3778-76-5	15	-0.96	268.7
Thiostrepton	1393-48-2	2	-0.932	1664.8
Levocabastine	79547-78-7	9	-0.927	456.98

Fig. 1 Prediction of candidate compounds from inverse gene profiling. **a** Detailed mapping of organ involvement by ex vivo BLI of a representative NOD.CB17-*Prkdc*^{scid}/NcrCrl mouse seven weeks after intracardial injection of 5×10^5 H1_DL2 cells ($n = 7$). **b** Dendrogram of all replicates ($n = 3$ per organ) based upon cluster analysis of gene expression profiles. Numbers 1, 2 and 3 indicate sample ID. **c** Top ten compounds from the Connectivity Map (cMap) analysis with the potential to induce the opposite transcriptional response to the brain metastasis signature («anti-brain metastasis signature»). Chemical abstracts service (CAS) registry numbers, reported dose tested, cMap score and molecular weight (M_W) are provided. A cMap score of − 1 indicates complete reversal of the signature (negative correlation)

(pfp < 0.01); a meta-analysis of rank product analyses (RankProd) of brain metastases versus each of the other organs (pfp < 0.01); and significance analysis of microarrays (http://statweb.stanford.edu/~tibs/SAM) with a q-value cutoff of 0.05. Fourth, we performed hierarchical clustering using J-Express 2012 (http://jexpress.bioinfo.no/site) and identified 46 genes that clustered together with the cross-validated eight-gene list; these 54 up-regulated genes were used to build a brain metastasis gene signature. Fifth, to enable analysis with the Connectivity Map (cMap) database, we appended the 54 most downregulated genes from the supervised rank product analysis (RankProd) of brain metastases when compared with all the other organs pooled together; all of these 54 downregulated genes were also featured in the 134-gene list of differentially expressed genes, as described above. Thus, the 108-gene brain metastasis signature was comprised of 54 upregulated and 54 downregulated genes (Additional file 2: Figure S2d).

Computational prediction of candidate compounds

We queried the cMap build 2 database (http://www.broadinstitute.org/cmap) using our 108-gene signature for candidate drugs. cMap is an initiative by the Broad Institute of MIT and Harvard, where the effects of 1309 small molecules on a number of cultured human cells were examined systematically, resulting in a collection of more than 7000 expression profiles that can be freely queried using their web interface. This resource can be used to select for drugs that produce a disease-negating gene signature. In this study, cMap was hypothesized to predict drugs with the potential to induce opposite expression profiles to those observed in our brain metastasis gene signature (Additional file 2: Figure S2e). Before cMap analysis, gene symbols were mapped to HG-U133A probe IDs (microarray used in cMap). The HG-U133A probe file (Platform GPL96) was downloaded and mapping was done with a code written in our laboratory. Of the 54 upregulated genes, 37 genes

had at least one matching probe and 55 probes were retrieved in total. Of the 54 downregulated genes, 29 genes had at least one matching probe, and 40 probes were retrieved in total. Mappings were subsequently verified with the GeneAnnot (http://genecards.weizmann.ac.il/geneannot/index.shtml) and GeneCards (http://www.genecards.org) databases.

Candidate drugs

Nine drugs were purchased from Santa Cruz Biotechnology, Inc.: Meticrane, tolazamide, β-sitosterol, memantine hydrochloride (herein referred to as memantine), valproic acid, letrozole, todralazine, thiostrepton, and levocabastine. Niridazole was not available. For in vitro screening, all compounds were dissolved in 100% dimethyl sulfoxide (DMSO) to a stock concentration of 250 mM. All stock solutions were subsequently diluted in complete DMEM to nine working solutions ranging from 0.2 to 1312.3 μM. This dose spectrum covered well below and above the reported dose levels for all drugs described in cMap. PLX4720 (ChemieTek) was solubilized and diluted in a similar manner to nine working solutions ranging from 0.01 to 1562.5 μM. Prior to in vitro testing, we pre-warmed (37 °C) and sonicated all working solutions.

Proliferation assays

Cells from four BRAF mutated cell lines (H1_DL2, Melmet 1, Melmet 5, A375) and three normal cell lines (SV80; fibroblasts, hTERT melanocytes and human astrocytes) were quantified using a hemocytometer and seeded into 96-well plates (5000 cells per well) in 100 μL complete DMEM. After 24 h incubation, we added 100 μL of the nine graded candidate drug dilutions, PLX4720, or 100 μL 0.1% or 1.0% DMSO in complete DMEM to each well ($n = 18$ per cell line per drug per drug concentration). Three days later, we added 20 μL of resazurin 0.1 mg/mL (Sigma-Aldrich Co.) per well and read the plates 4 h later (Fig. 2a and Additional file 4: Figure S3a-f) using a VICTOR X3 multilabel plate reader (PerkinElmer) with Workout 2.5 data analysis software (560 nm excitation and 590 nm emission). Wells with 200 μL complete DMEM and no cells were used for background correction ($n = 60$). IC_{50} values were calculated (Fig. 2c, and Additional file 4: Figure S3) using GraphPad Prism 6 for Mac OS X (GraphPad Software Inc.).

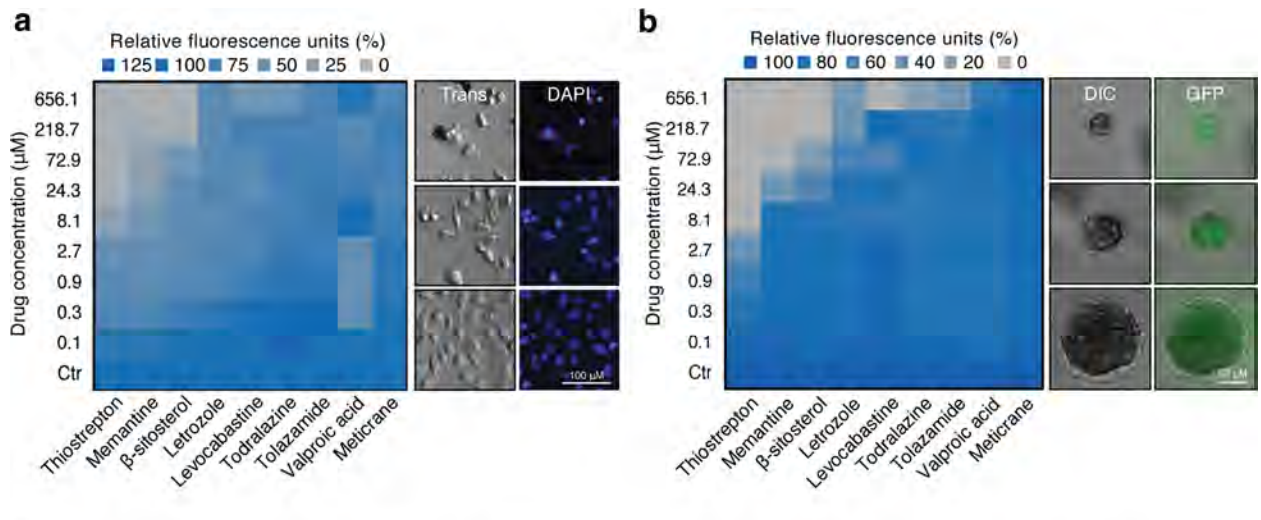

Fig. 2 In vitro drug screening. **a** Heatmap of three days H1_DL2 monolayer proliferation assays (left panel) and representative transmission (Trans) and 4′,6-Diamidino-2-Phenylindole (DAPI) images (right panel). **b** Heatmap of ten days H1_DL2 tumorsphere assays (left panel) and representative differential interference contrast (DIC) and green fluorescent protein (GFP) fluorescence microscopy images (right panel). **a-b** Right image panels show examples of β-sitosterol 218.7 μM (top), β-sitosterol 2.7 μM (middle) and control (bottom). **c** Half maximal inhibitory concentration (IC_{50}) values for the three most potent compounds across different cell lines and assays. (a–c) Mean; $n = 6$ per cell line per drug per drug concentration. See Additional file 4: Figure S3a–c for more details on this experiment

Cells were fixed by adding 50 μL 8% paraformaldehyde (PFA) per well for 24 h after which time the liquid contents of all wells were replaced with 50 μL PBS. Differential interference contrast (DIC) and 4′,6-diamidino-2-phenylindole (DAPI) image stacks were acquired (Fig. 2a) with 10× magnification using a Nikon Eclipse TE2000 inverted microscope (Nikon Instruments Inc.).

Tumorsphere assay

A standardized 3D tumor spheroid growth assay was carried out as reported previously [58]. Briefly, 100 μL of the graded drug dilutions and DMSO controls were added to 96-well plates with 4000 cells in soft agar per well (n = 6 per cell line per drug concentration). After a ten-day incubation period, a resazurin assay was performed, and cells were fixed as described above. DIC and GFP z-stack images were acquired with 10× magnification using a BD Pathway 855 High-Content Imager (Becton, Dickinson and Company).

Tumor cell injections, quantification of tumor cell load in the brain and multimodal imaging of metastasis formation

Six to eight weeks old female NOD/SCID mice were purchased from the University of Bergen animal facility. Anesthesia was induced with 3% and maintained with 1.5% isoflurane in oxygen. Mice were monitored daily and sacrificed upon signs of illness. Intracardiac injections were performed using ultrasound-guidance (5×10^5 cells per 0.1 mL PBS per mouse) as reported previously [58]. H1_DL2 cells were pre-labeled with superparamagnetic iron oxide nanoparticles and MRI was carried out 24 h after injections [57]; T2*-weighted images for automated quantification of tumor cell load in the mouse brains and T2-weighted images to assess the presence of focal brain lesions. MRI equipment and sequence details have previously been described [58]. For T2*-weighted quantification we developed a cell-line specific training set for the integrated neural network analysis. Only mice with comparable tumor cell load in their brains and without ischemic lesions were included in further studies. We omitted five mice in the candidate drug study and six mice in the β-sitosterol study, based on an uneven tumor load to the brain.

We performed brain MRI to evaluate the brain metastatic burden with T2-weighted sequences and pre −/post-contrast T1-weighted sequences as previously described [58]. Images were obtained at pre-defined week numbers (Figs. 3a, b and 4a, b). The number of tumors, contrast enhancement and volume ($4/3 \times \pi \times r^3$) were assessed using OsiriX 5.8.1 32-bit (Pixmeo SARL).

In parallel with the MRI, we did BLI to evaluate brain metastatic burden. Mice were imaged 10 min after i.p. injection of 150 mg/kg D-luciferin Firefly (Gold Biotechnology). To reduce distress, they were not depilated. Images were acquired using an Optix MX3 Small Animal Molecular Imager (ART Inc.) and analyzed with Optix OptiView 3.02 (ART Inc.). Total photon counts (ventral + dorsal) were registered from identically sized regions of interest (ROIs) placed over the head.

In vivo treatment protocols

In the drug screening study on H1_DL2 brain metastases, treatment started one week post-injection and stopped at the end of week seven (Fig. 3a and Additional file 5: Figure S4). Test groups received 0.2 mL i.p. injections of 40 mg/kg thiostrepton every second day ($n = 5$), 10 mg/kg memantine daily (n = 5), 5 mg/kg β-sitosterol daily ($n = 4$), or 0.5% DMSO (n = 5) daily. Stock solutions of the respective drugs, as described above, were diluted with saline solution, pre-warmed (37 °C) and sonicated prior to i.p. injections (the partly miscible thiostrepton solution was homogenized before administration). Fresh solutions were made every second week and stored at 4 °C.

In the validation study with β-sitosterol treatment on H1_DL2 cells and PC14_PE6_Br2 brain metastases, treatment started one week prior to intracardiac injections and was continued until sacrifice for the vehicle groups ($n = 10$) and for ten weeks for the β-sitosterol groups ($n = 9$). Test groups received daily i.p. injections of 0.1 mL olive oil or 5 mg/kg β-sitosterol in 0.1 mL olive oil. β-sitosterol was mixed with olive oil (Santa Cruz Biotechnology Inc) and solubilized over 4 h with a heated magnetic stirrer (50 °C). Fresh solutions were made every second week and stored at room temperature.

In the subcutaneous tumor model, we used the Melmet 5 melanoma cell line. We injected 1×10^6 cells in 0.1 mL PBS in the cervical skin fold of 32 mice. After two weeks, when the average tumor volume was approximately 30 mm^3, the mice were randomized to daily i.p. injections of 0.1 mL vehicle (olive oil), 20 mg/kg β-sitosterol in olive oil, 25 mg/kg PLX4720 in 0.05% DMSO, or a combination of the two latter ($n = 8$ in each group). Caliper measurements were carried out every sixth day to evaluate tumor growth. Tumor volume was calculated using the formula $(\text{width}^2 \times \text{length})/2$.

Functional classification of the brain metastasis gene signature

We performed a functional classification of human biological processes and signaling pathways associated with the 108-gene signature using the Protein Analysis Through Evolutionary Relationships (PANTHER) classification system (http://www.pantherdb.org/).

Protein interactions of β-sitosterol

We examined known and predicted protein interactions of β-sitosterol using the Search Tool for Interactions of

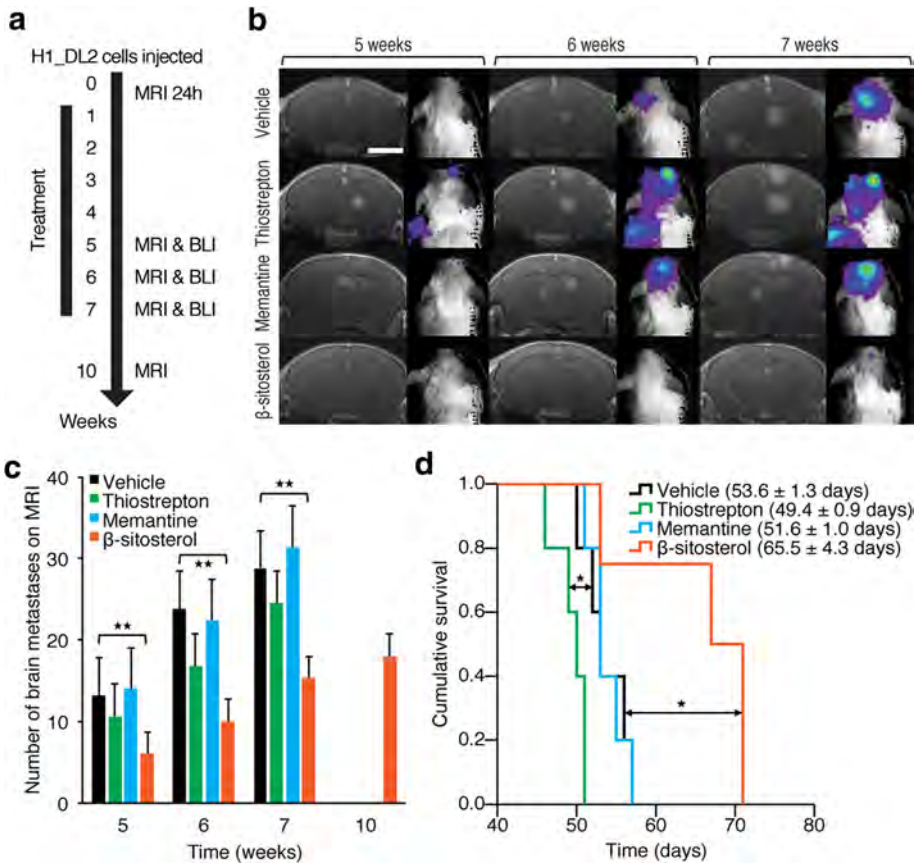

Fig. 3 In vivo drug screening. **a** Experimental overview: Intracardiac injections of 5×10^5 H1_DL2 cells in NOD/SCID mice were followed by MRI-based quantification of nanoparticle-labeled melanoma cells in the mouse brains after 24 h for group homogenization (Additional file 5: Figure S4a). Treatment started after one week, and test groups received 0.2 mL i.p. injections of 40 mg/kg thiostrepton every second day ($n = 5$), 10 mg/kg memantine daily (n = 5), 5 mg/kg β-sitosterol daily ($n = 4$) or vehicle (0.5% DMSO; n = 5). See Additional file 5: Figure S4 for more details. **b** Development of brain metastases visualized by MRI (T1-weighted images with contrast) and BLI at five, six and seven weeks. Scale bar MRIs, 0.25 cm. **c** Number of brain metastases at T1-weighted MRI with contrast (Student's *t*-test). **d** Kaplan-Meier survival plot (Mantel-Cox log-rank test). There was no significant difference between vehicle- and memantine-treated mice. * $P < 0.05$; ** $P < 0.01$. All values are given as the mean ± s.e.m

Chemicals (STITCH 4.0; http://www.stitch.embl.de). We applied a high confidence level cut-off (0.700) and a maximal number of interactions ($n = 50$). We next investigated with which cellular processes these protein targets were associated using the Human Experimental/Functional Mapper (HEFalMp).

Protein phosphorylation assay

For the determination of the relative levels of protein phosphorylation of 43 kinases and 2 related total proteins (HSP60 and β-Catenin), we used the Human Phospho-Kinase Array (R&D Systems, Inc.) as specified by the manufacturer. H1_DL2 cells were treated with vehicle (0.05% DMSO) or β-sitosterol (50 μM) for 24 h.

Linkage analyses to mitochondrial metabolism

We obtained the mitochondrial metabolism genes from the Gene Ontology (GO) database using AmiGO (http://amigo.geneontology.org/amigo) and the search term «oxidative phosphorylation» (filter: *Homo sapiens*). This resulted in 121 unique gene symbols among a total of 209 gene-term associations. β-sitosterol targets were extracted from ChEMBL (Chemical Database of the European Molecular Biology Laboratory; https://www.ebi.ac.uk/chembl): 16 targets reported in humans. CHEMBL_IDs were converted to gene symbols with UnitProtKB (Universal Protein Resource Knowledgebase; http://www.uniprot.org). Network generation and visualization were implemented in Cytoscape 3.3.0 (http://www.cytoscape.org). Interactions between query and mitochondrial metabolism gene sets were extracted with ANAT (Advanced Network Analysis Tool; http://www.cs.tau.ac.il/~bnet/ANAT). β-sitosterol targets and signature genes were defined as network anchors, and the oxidative phosphorylation genes as network terminals. Anchored network analysis was applied with focus on: human interactions,

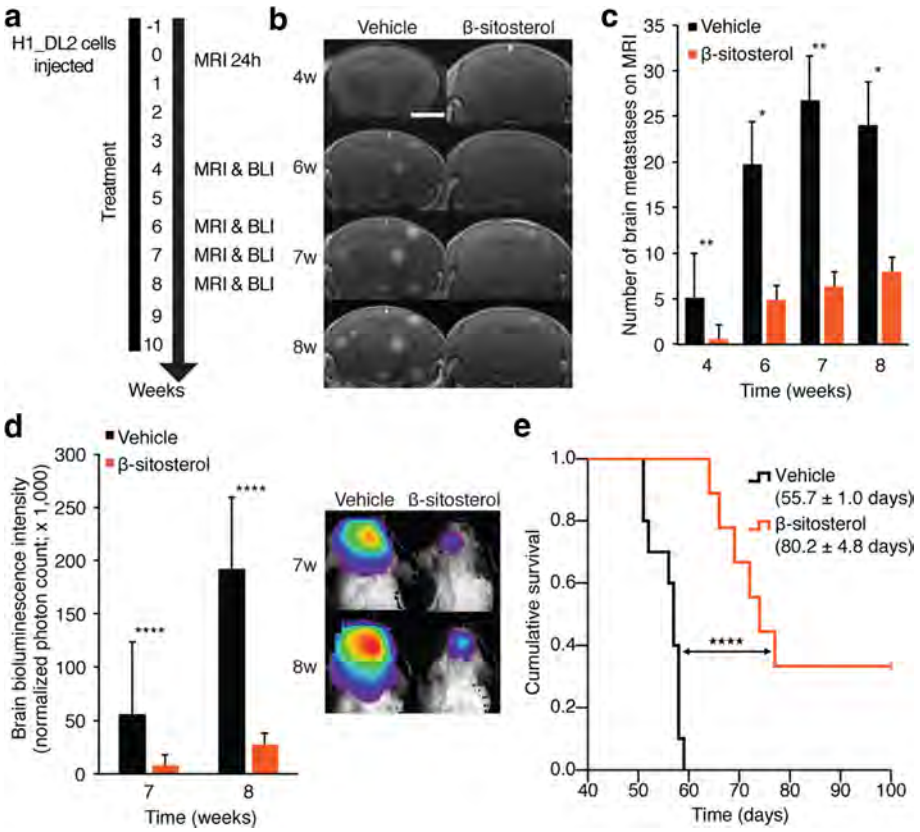

Fig. 4 In vivo validation of β-sitosterol pre-treatment. **a** Experimental overview: Treatment started one week prior to intracardiac injections of 5×10^5 H1_DL2 cells in NOD/SCID mice. Quantification of tumor cell exposure in the mouse brains was carried out 24 h after injections for group homogenization (Additional file 6: Figure S5a). Test groups received daily i.p. injections of 0.1 mL vehicle (olive oil; $n = 10$) or β-sitosterol diluted in olive oil (5 mg/kg; $n = 9$). Vehicle treatment was continued until euthanization and β-sitosterol was given for ten weeks. See Additional file 6: Figure S5 for more details on this experiment. **b** Development of brain metastases assessed by MRI at four, six, seven and eight weeks. Scale bar MRIs (T1-weighted images with contrast), = 0.25 cm. **c** Number of brain metastases assessed by T1-weighted MRI with contrast (Student's *t*-test). The mean number of brain metastases in the vehicle group decreased slightly from seven to eight weeks as four mice with the greatest number of brain metastases were sacrificed between these observation points. **d** Brain BLI at seven and eight weeks (total photon count = dorsal + ventral region of interest (ROI); Student's *t*-test). **e** Kaplan-Meier survival plot (Mantel-Cox log-rank test). The experiment was terminated at 100 days, and three mice in the β-sitosterol group were still alive and healthy. * $P < 0.05$; ** $P < 0.01$; **** $P < 0.0001$. All values are given as the mean ± s.e.m

protein-protein and protein-DNA interactions and default search parameters. Interaction directionality from anchors to terminals was specified.

Extracellular flux analysis

Extracellular flux analysis with concurrent detection of oxygen (mitochondrial respiration) and pH (lactate production indicating glycolysis) was employed. The measurements were performed in 96-well H1_DL2 and HEMa cell cultures using the Seahorse XF96 Analyzer system (Seahorse Bioscience), according to manufacturer's protocol. The assay conditions were optimized with regard to cell number and concentrations of carbonyl cyanide 3-chlorophenylhydrazone (CCCP) or carbonyl cyanide-4 (trifluoromethoxy) phenylhydrazone (FCCP) and oligomycin. Cells were seeded in quadruplicate wells (2×10^4 cells per well), and exposed to 50 μM β-sitosterol for 24 h before the analysis. Control cells received 0.05% DMSO. Following this treatment, the growth medium was replaced with assay medium consisting of phenol-free DMEM supplemented with 2 mM L-glutamine and 2 mM sodium pyruvate. 10 mM glucose was added to the medium for measurement of mitochondrial respiration. The assay medium was adjusted to a pH of 7.4. The cells were incubated at 37 °C in a CO_2-free incubator (Seahorse XF Prep station) for 1 h before they were transferred to the analyzer. To investigate mitochondrial respiratory function, assessment of the initial oxygen consumption rate (OCR), indicating the basal rate, was followed by sequential additions of several modulators: 1) the ATP synthase inhibitor oligomycin (3 μM for H1_DL2 and 2 μM for HEMa cells) was used to measure phosphorylation independent respiration (Leak); 2) the uncoupler CCCP or FCCP (1.5 or 2 μM for H1_DL2 and HEMa cells,

respectively) to measure the capacity of the electron transport system (respiratory capacity); 3) the Complex I (CI) inhibitor rotenone (1 μM) to determine CI independent respiration; and 4) the CIII inhibitor antimycin A (1 μM) to assess residual background OCR not related to mitochondrial respiration; this was subtracted as background from the other measurements in the statistical analysis. To analyze the glycolytic function, the extracellular acidification rate (ECAR) was measured after sequential additions of glucose (10 mM) to determine basal glycolysis and oligomycin (3 μM) to obtain glycolytic capacity. CCCP (1.5 μM) was injected to address the possible influence of uncoupling, and 2-deoxyglucose (2-DG; 100 mM) was used to obtain the non-glycolytic background. In statistical analysis, the residual ECAR was subtracted as background from the other measurements. All experiments were performed three times.

High-resolution respirometry

Oxygen consumption was analyzed using the Oxygraph O2K instrument and DatLab software (Oroboros Instruments). The H1_DL2 cells were harvested and washed in PBS before they were suspended in the assay medium (20 mM K-hepes, 83 mM KCl, 4 mM KH2PO4, 1 mM EGTA and 1 mM MgCl2) and transferred to the assay chamber (37 °C) at 1.25×10^6 cells per 2 mL assay medium. Digitonin (8.1 μM) was added to permabilize the cell membrane. The combined CI + CII-driven respiration was obtained in the presence of malate (2 mM), pyruvate (1 mM), succinate (10 mM), and FCCP (titrated to 0.18 μM). Following injection of β-sitosterol (50 μM) or DMSO (0.05%) and assessment of the resulting OCRs, rotenone (0.5 μM) was injected to determine if the effect was linked to CI and/or CII. Antimycin A (2.3 μM) was added to provide the non-mitochondrial background activity, which was subtracted during data analysis. This experiment was performed three times.

Measurement of reactive oxygen species and apoptosis assay

H1_DL2 cells were treated with 0.05% DMSO or 50 μM β-sitosterol for 24 h, and apoptosis was detected and quantified using the disodium salt of 3, 4, 5, 6,-tetrachloro-2′, 4′, 5′, 7′-tetraiodofluorescein (TCTF) as previously described ($n = 3$) [34]. The cellular content of reactive oxygen species (ROS) was measured using the CM-H_2DCFDA probe according to the manufacturer's instructions (Life Technologies). Briefly, naïve H1 cells were treated with 0.05% DMSO or 50 μM β-sitosterol for 2 h before exposure to 5 μM CM-H_2DCFDA for 15 min (two experiments with triplicate measurements). Data were analyzed using a BD Accuri C6 flow cytometer (BD Biosciences).

Western blot

Protein extraction and western blotting was carried out as described previously [58]. Antibodies were diluted in blocking buffer and the following antibodies were used: Caspase-3 (1:500) and PGC1α (1:500) (Cell Signaling Technology); and NDUFA8 (ab74126; 1:500), GAPDH (1:20,000) and β-actin (1:20,000) (Abcam).

MitoTracker red fluorescence

MitoTracker Red (Invitrogen) mean fluorescence intensity was measured in H1 cells treated with DMSO (0.05%) or PLX4720 (1.5 μM) for 72 h (n = 3). Data were analyzed using a BD Accuri C6 flow cytometer (BD Biosciences).

Colony formation assay

5×10^3 H1 cells were cultured in 6-well plates and treated with DMSO (0.05%), PLX4720 (1.5 μM), β-sitosterol (50 μM), or a combination of the latter two for one (controls) or three weeks (treatment groups) (n = 3). The same protocol was used for H1_shNDUFA8 cells, but these were not treated with β-sitosterol.

Immunohistochemistry of human brain metastases

We stained 197 formalin-fixed and paraffin-embedded human brain metastases using NDUFB8 (ab110242; Abcam). Samples were derived from melanoma ($n = 78$), non-small cell lung cancer ($n = 52$), breast cancer ($n = 25$), renal cell cancer ($n = 9$), colon cancer (n = 9), small cell lung cancer (n = 7), carcinomas not otherwise specified (n = 9) and other rare cases like ovarian and esophageal cancer ($n = 8$). All staining procedures were performed using an automated immunostainer (Leica Bond III) and analyzed by ≥ two observers using a semi-quantitative score (H-Score) ranging from 0 to 300. H-Score is defined by the staining intensity (1 = weak, 2 = moderate, 3 = strong) multiplied with the frequency of positive cells (%).

Statistics

Statistical analyses were conducted with SPSS 21 for Mac (SPSS Inc.) and Prism 7 for Mac, Version 7.0b (La Jolla, CA, USA). An independent samples Student's *t*-test was used to compare two normally distributed groups. The Kruskal-Wallis test was used to analyze nonparametric data and Dunn's or Sidak's test was used to correct for multiple testing. Levene's test was used to assess the variance. Kaplan-Meier survival analysis and Mantel-Cox log-rank test were used to assess survival differences between groups. Values are presented as means ± standard error of the mean (s.e.m.) unless otherwise specified. A two-tailed $P \leq 0.05$ was considered significant.

Study approval

We obtained written informed consent before human tumor material was collected. The Regional Ethical Committee and the Norwegian Directorate of Health approved the collection and storage of human tissue. The Institutional Animal Care and Use Committee at the University of California Davis and at the University of Bergen approved the mouse experiments. At both institutions, mice were maintained in animal facilities certified by the Association for Assessment and Accreditation of Laboratory Animal Care International. The local ethical committee at the University Cancer Center Frankfurt approved the immunohistochemical analyses of human brain metastases.

Results

Predicting therapeutic compounds using inverse gene expression profiling

Using a highly characterized metastatic *BRAF*-mutant human melanoma xenograft model [57], we isolated and sorted tumor cells from brain, bone, adrenals and ovaries by flow cytometry (Fig. 1a, Additional file 2: Figure S2a, b). By comparing RNA-seq data from the different metastases, we identified a 108-gene brain metastasis signature using a comparative workflow of independent analyses of gene expression profiles from brain versus the other organ metastases (Fig. 1b, and Additional file 2: Figure S2c, d). The signature consisted of 54 upregulated and 54 downregulated genes (Additional file 2: Figure S2d). To identify therapeutic compounds with the potential to revert the gene signature, we queried cMap with the 108-gene brain metastasis signature. cMap revealed 1313 expression profiles, with a cMap score < 0, which represent compounds with the potential to induce the opposite transcriptional response when compared with the signature (Additional file 2: Figure S2e). For further studies, we focused on the top 10 candidate compounds (all with cMap scores < − 0.90) as shown in Fig. 1c.

In vitro and in vivo drug screening reveals β-sitosterol as a potential therapeutic agent

The therapeutic efficacy of the compounds was assessed on four metastatic melanoma cell lines using monolayer viability and tumorsphere assays (Fig. 2a-c and Additional file 4: Figure S3). IC_{50} values were generally lower in tumorspheres than in monolayers. The most potent compounds for reducing viability were thiostrepton, memantine, and β-sitosterol (Fig. 2a, b). The IC_{50} values for normal human fibroblasts and astrocytes were 128.3 μM and 1200.5 μM respectively, whereas normal human melanocytes were not sensitive to β-sitosterol within the dose range studied (Additional file 4: Figure S3).

We next assessed the therapeutic efficacy of thiostrepton, memantine, and β-sitosterol using a highly standardized human-to-mouse brain metastasis model [57] (Fig. 3a). Quantitative analysis of baseline H1_DL2 melanoma cells (i.e. accumulation of tumor cells within the brain 24 h after injection) showed no significant differences between the treatment and vehicle (control) groups (Additional file 5: Figure S4a). Drug treatment was commenced one week after tumor cell injections. High-resolution magnetic resonance imaging (MRI) over the next 5–10 weeks revealed a significant reduction in the number and volume of brain metastases in the β-sitosterol-treated mice when compared with vehicle-treated mice (Fig. 3b, c and Additional file 5: Figure S4b). There were no differences in brain metastasis frequency or size between the vehicle and the thiostrepton or memantine groups (Student's *t*-test, $P \geq 0.05$ for all comparisons). BLI intensity was significantly lower for the β-sitosterol group when compared to the vehicle group at all time points, with the exception of brain BLI intensity at five weeks (Student's *t*-test, $P \geq 0.05$; Additional file 5: Figure S4c). Importantly, β-sitosterol-treated mice survived significantly longer than vehicle-treated mice, whereas thiostrepton-treated mice had a significantly shorter lifespan. Also, memantine treatment did not affect survival (Fig. 3d).

β-Sitosterol pre-treatment inhibits the formation of brain metastasis and increases animal survival

To further validate the β-sitosterol treatment effect, we performed a new and more extensive in vivo study where β-sitosterol treatment started 1 week before tumor cell injection (Fig. 4a). MRI-based quantification of baseline H1_DL2 melanoma cells in mouse brains again showed an equal tumor cell exposure in the β-sitosterol and vehicle groups (Additional file 6: Figure S5a). Vehicle-treated mice progressively lost weight from four weeks and onwards, whereas β-sitosterol-treated mice maintained a stable body weight (Additional file 6: Figure S5b). There were significantly fewer and smaller brain metastases in the β-sitosterol group than in the vehicle group (Fig. 4b, c and Additional file 6: Figure S5c). Brain BLI intensity was significantly lower in the β-sitosterol treatment group compared to the vehicle group at comparable time points (Fig. 4d). β-sitosterol treatment provided a significant survival benefit when compared with vehicle treatment (Fig. 4e). When the study was terminated at 100 days, three out of nine mice treated with β-sitosterol were healthy and tumor-free as evaluated by brain MRI and histology. To confirm that the effects observed were not associated with the model used, we performed the same study using another highly aggressive brain tropic cell line (PC14_PE6_Br2). Also here, a significant

reduction in brain metastatic burden was seen leading to a significant improved survival (Additional file 7: Figure S6).

β-Sitosterol targets mitochondrial respiration through complex I inhibition

To obtain mechanistic insight into the therapeutic action of β-sitosterol, we first examined the biological processes and signaling pathways associated with our brain metastasis signature. Functional classification of the signature genes showed an association with human metabolic processes and a number of cancer-related signaling pathways (Additional file 8: Figure S7a, b). We next examined known and predicted protein interactions of β-sitosterol and found direct interactions with 12 proteins within two distinct clusters related to apoptosis and cholesterol homeostasis (Additional file 8: Figure S7c). These 12 proteins acted in conjunction and were significantly associated with several biological processes, particularly metabolism and cell division (Additional file 8: Figure S7d). In order to explore whether specific signal transduction pathways were affected through the treatment with β-sitosterol, we performed a phosphorylation screen in vitro, and found reduced phosphorylation levels of a large number of oncogenic kinases following β-sitosterol treatment (Additional file 9: Figure S8). These data connected major regulators of cell homeostasis to the therapeutic potential of β-sitosterol and suggested that β-sitosterol may interfere with basic cellular functions such as energy metabolism and apoptosis.

Previous studies have shown that metastatic cells adapt their energy production in order to thrive in the brain microenvironment by increasing their mitochondrial respiration. This process has been shown to be a key mediator of resistance to BRAFi [15, 16, 24, 63]. We therefore investigated, by bioinformatics analyses, protein-protein and protein-DNA interactions between the 121 Gene Ontology-annotated genes implicated in oxidative phosphorylation and (a) our brain metastasis signature or (b) known β-sitosterol targets. These analyses revealed large interaction networks with centrally located signature genes (Additional file 10: Figure S9) and β-sitosterol targets (Additional file 11: Figure S10). These data indicate that the therapeutic effect of β-sitosterol is linked to mitochondrial interference. Thus, we measured mitochondrial respiration and glycolysis by extracellular flux analysis in H1_DL2 melanoma cells following β-sitosterol treatment. As shown in Fig. 5a, β-sitosterol strongly reduces basal mitochondrial respiration and respiratory capacity. The extracellular flux analysis further shows that inhibition of ATP synthase (with oligomycin) is similar in vehicle- and β-sitosterol-treated cells (Fig. 5a), indicating that β-sitosterol does not disrupt the integrity of the mitochondrial inner membrane. Inhibition of respiratory CI revealed that most of the respiratory activity is linked to this complex (Fig. 5a) and importantly, suggested that CI was a likely β-sitosterol target. Basal glycolysis and glycolytic capacity were, however, unaffected by β-sitosterol (Fig. 5b). Interestingly, melanoma cells showed minimal glycolytic reserve (glycolytic capacity minus basal glycolysis) if mitochondrial ATP production should cease (Fig. 5b). Thus, the cells could be particularly sensitive to inhibitors of mitochondrial respiration such as β-sitosterol. For comparison, we also measured the respiratory capacity of normal melanocytes following β-sitosterol treatment. Compared to the tumor cells, no changes in respiratory capacity was observed (Additional file 12: Figure S11).

To determine if the inhibitory effect of β-sitosterol on mitochondrial respiration was directly linked to the activity of CI or CII, we analyzed oxygen consumption rates in permeabilized cells by high-resolution respirometry. The CI + CII-driven respiratory activity was inhibited immediately following β-sitosterol exposure (Fig. 5c). Addition of the CI inhibitor, rotenone, did not provide further inhibition, and the remaining CII-driven rate was similar in the presence of β-sitosterol or rotenone (Fig. 5c). In summary, β-sitosterol inhibits mitochondrial respiration in tumor cells by acting as a CI inhibitor. Such an inhibition was not seen in normal melanocytes.

β-Sitosterol increases oxidative stress and induces apoptosis

Beyond their function in ATP synthesis, mitochondria are major producers of ROS. CI respiratory capacity is of particular importance in this respect, –and inhibition of its activity often results in increased ROS production [36]. Consistent with previous studies [4, 50], we observed a significant increase in cellular ROS content following β-sitosterol treatment (Fig. 6a). Interestingly, recent observations have shown that oxidative stress inhibits metastatic melanoma cells in the blood and visceral organs in vivo [42]. Since increased ROS levels have been linked to apoptosis induction, we next performed apoptosis analyses. As shown in Fig. 6b, a significant induction of apoptosis was observed following β-sitosterol treatment. This is in line with previous studies showing that β-sitosterol can induce both mitochondrial- and death receptor-mediated apoptosis in cancer cells [4, 8, 23, 50, 64, 65, 70]. Additionally, immunoblots for apoptotic markers (Fig. 6c) confirmed our protein interaction analysis (Additional file 8: Figure S7c). In summary, respiratory capacity is inhibited following β-sitosterol treatment which leads to an induction of apoptosis. In this context, it should also be emphasized that apoptosis is a hallmark of MAPK-targeted therapies as well as mitochondrial inhibitors, including known inhibitors of CI-mediated respiration [24, 36, 68].

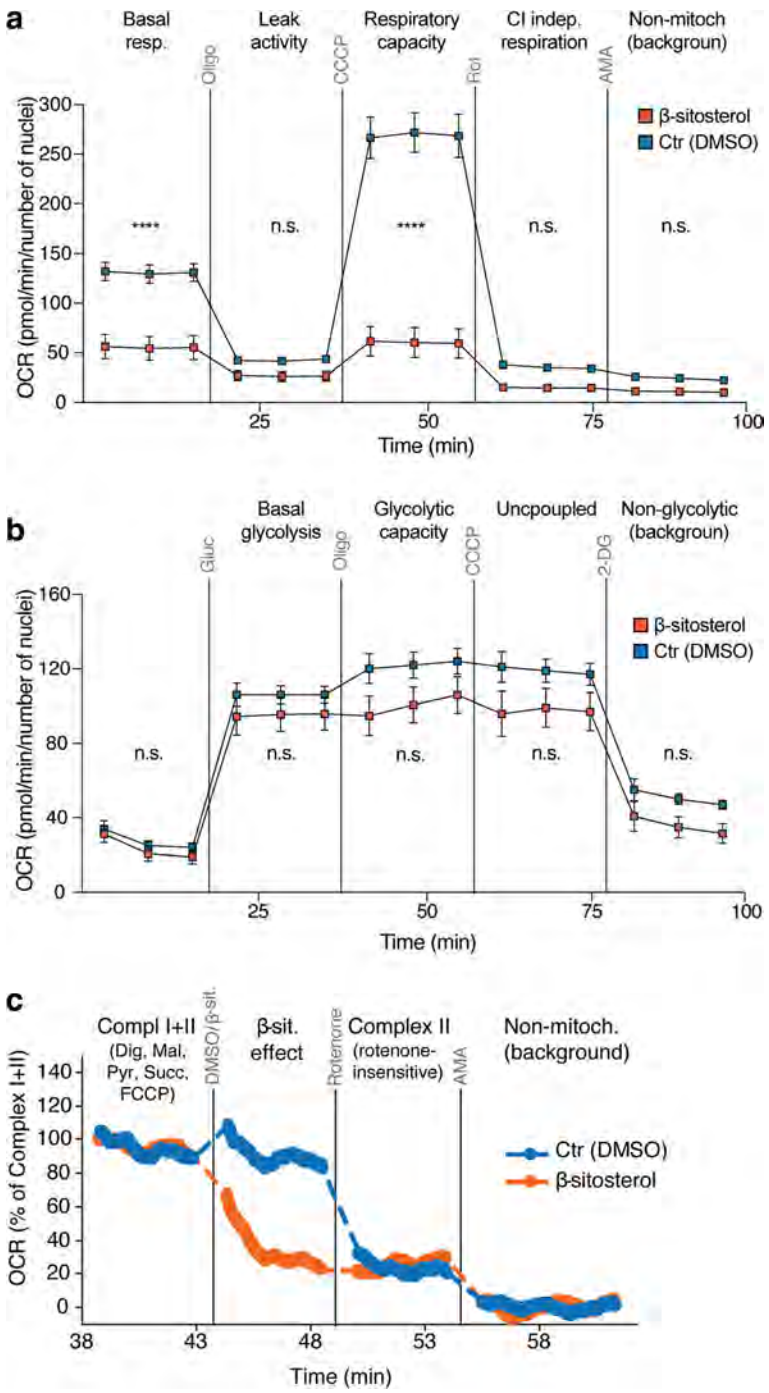

Fig. 5 (See legend on next page.)

β-Sitosterol abrogates potential resistance to BRAF inhibition

Consistent with our previous observations that β-sitosterol inhibits mitochondrial respiration (Fig. 5a) and increases oxidative stress (Fig. 6a), we found a compensatory increase in PGC1α expression with increasing concentrations of β-sitosterol (Fig. 7a). The MITF-PGC1α axis is a master regulator of mitochondrial function in melanomas [24, 63]. PGC1α promotes mitochondrial respiration and protects against oxidative stress. A subset of melanomas overexpresses PGC1α, and treatment of *BRAF*-mutant melanomas with the BRAFi PLX4720 (a vemurafenib analogue) has been shown to upregulate PGC1α [24, 63]. In agreement with these data, we

(See figure on previous page.)
Fig. 5 β-sitosterol reduces mitochondrial respiration through complex I inhibition. **a-b** Oxygen consumption rate (OCR) and extracellular acidification rate (ECAR) were measured to assess rates of mitochondrial respiration and glycolysis, respectively, in H1_DL2 cells treated with 50 μM β-sitosterol or 0.05% DMSO for 24 h (both: n = 4). **a** Basal respiration was determined, followed by sequential additions of oligomycin (3 μM) to assess respiration due to proton leak, carbonyl cyanide 3-chlorophenylhydrazone (CCCP; 1.5 μM) to measure respiratory capacity, rotenone (1 μM) to assess Complex I (CI) independent respiration and antimycin A (AMA; 1 μM) to determine background OCR. **b** Glucose (10 mM) was provided to determine basal glycolysis, followed by sequential additions of oligomycin (3 mM) to obtain glycolytic capacity, CCCP (1.5 μM) to evaluate the influence of uncoupling and 2-deoxyglucose (2-DG; 100 mM) to measure the non-glycolytic background. **c** High-resolution respirometry in H1_DL2 cells to detect direct effects of β-sitosterol. First, the maximal CI + CII driven respiratory capacity was measured in the presence of digitonin (8.1 μM), malate (2 mM), pyruvate (1 mM), succinate (10 mM) and carbonylcyanide-4-(trifluoromethoxy)-phenylhydraqone (FCCP, 0.18 μM). The respiratory rate was then measured after adding β-sitosterol (50 μM) or DMSO (0.05%), followed by rotenone (0.5 μM) to inhibit CI, and AMA (2.3 μM) to determine residual oxygen consumption. The experiment was repeated 3 times. **a-c** Student's *t*-test: n.s. = not significant, $P \geq 0.05$, **** $P < 0.0001$. Values are given as the mean ± s.d

found that PLX4720 induced MitoTracker Red fluorescence, a measure of mitochondrial activity and mass (Fig. 7b). Importantly, these intrinsic and acquired survival advantages render melanoma cells resistant to BRAFi, and combined approaches that exploit the resultant dependence on mitochondrial respiration are highly sought [24, 45, 49, 63, 69].

We therefore investigated the possible therapeutic benefits of combining BRAFi and mitochondrial CI inhibitors in colony formation assays. Both PLX4720 and β-sitosterol were effective as monotherapies, but regrowth of resistant clones appeared after long-term incubation (Fig. 7c). Combination treatment with PLX4720 and β-sitosterol, however, completely inhibited cell growth (Fig. 7c). To further substantiate the therapeutic potential of targeting mitochondrial CI (Fig. 5a, c), we constructed a stable NDUFA8 knockdown in the H1 melanoma cell line (H1_shNDUFA8) (Fig. 7d). NDUFA8 is an accessory subunit of mitochondrial CI, in which knockdown results in failure of a functional complex and severe respiratory deficiency [55]. Long-term colony formation assays with PLX4720 alone or H1_shNDUFA8 alone displayed attenuated growth, whereas the combination totally eliminated cell growth (Fig. 7e). Next, we examined whether or not the combined effect was cell line specific. We performed monolayer viability assays in three other melanoma cell lines. Combination treatment with β-sitosterol and PLX4720 substantially reduced the IC_{50} values for all cell lines (Fig. 7f). As BRAFis in general have limited penetrability through an intact BBB [37] and the BBB is commonly not degraded in animal models until late in metastatic development [60], we carried out a proof of concept study in a subcutaneous Melmet 5 melanoma model. Both PLX4720 and β-sitosterol were effective as monotherapies, but combination treatment significantly reduced tumor growth (Fig. 7g).

To evaluate CI activity and the potential clinical relevance of our findings, we performed immunohistochemical staining of NDUFB8 (accessory subunit of CI) in 197 human brain metastases from various cancers.

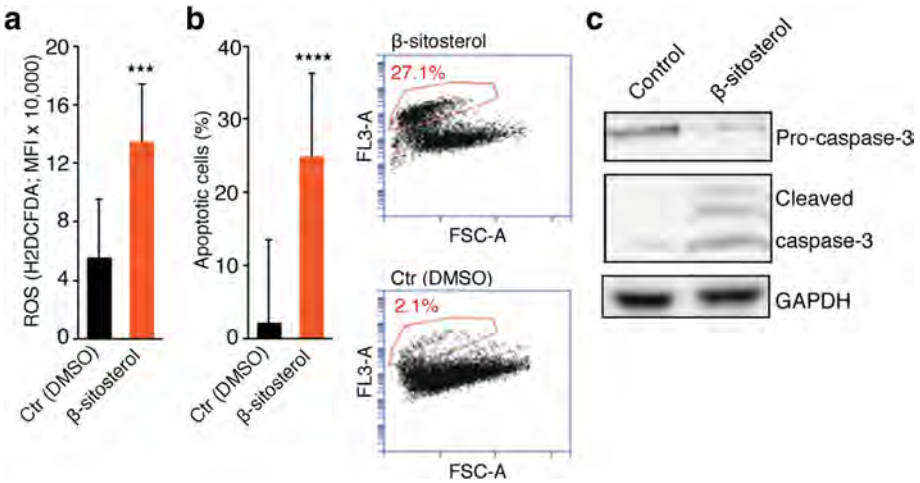

Fig. 6 β-sitosterol increases ROS production and apoptosis. **a** ROS content (CM-H_2DCFDA probe; mean fluorescence intensity (MFI); $n = 2$ with triplicates). **b** Flow cytometric apoptosis assay (n = 3) showing a strong induction of apoptosis following ß-sitosterol treatment. **c** Western blot of pro-caspase-3, cleaved caspase-3 and GAPDH in H1_DL2 cells exposed to DMSO (0.05%) or β-sitosterol (50 μM) for 2, 24 or 24 h, respectively. Student's *t*-test: *** $P < 0.001$, **** $P < 0.0001$. Values are given as the mean ± s.e.m

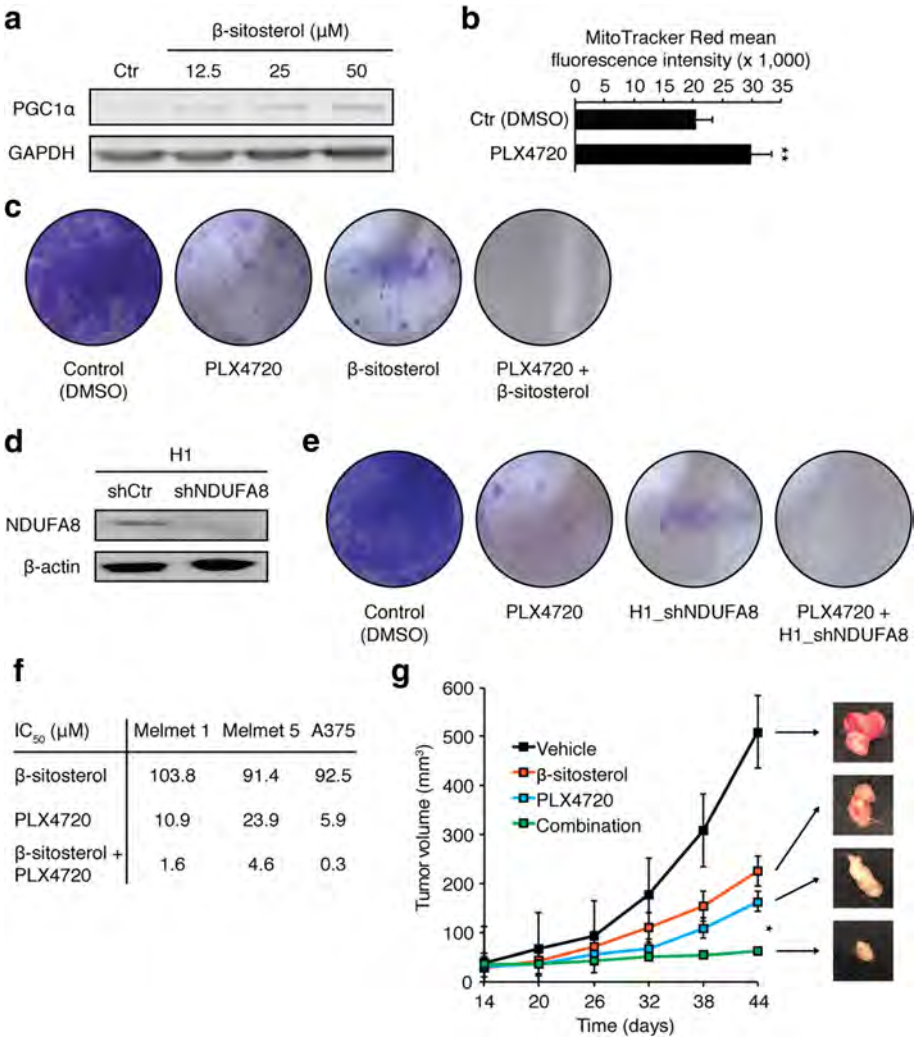

Fig. 7 Mitochondrial complex I inhibition prevents BRAFi resistance. **a**. Western blot of PGC1α and GAPDH in H1 cells treated with DMSO (0.05%) or β-sitosterol (12.5, 25 or 50 μM) for 24 h (n = 3). **b**. MitoTracker Red mean fluorescence intensity in H1 cells treated with DMSO (0.05%) or vemurafenib (1.5 μM) for 72 h (n = 3). **c** Colony formation assay (crystal violet staining) of H1 cells treated with DMSO (0.05%) for 1 week, or vemurafenib (1.5 μM), β-sitosterol (50 μM), or vemurafenib + β-sitosterol for 3 weeks (n = 3). **d** Western blot of NDUFA8 and β-actin in H1_shCtr and H1_shNDUFA8 cells (NDUFA8 is required for assembly of a functional complex I). **e** Colony formation assay of H1 cells treated with DMSO (0.05%) for one week or vemurafenib (1.5 μM) for three weeks, and H1_shNDUFA8 cells alone or treated with vemurafenib (1.5 μM) for three weeks (n = 3). **f** Half maximal inhibitory concentration (IC_{50}) values for β-sitosterol, PLX4720 and the combination thereof in Melmet 1, Melmet 5 and A375 cell lines (n = 3). **g** Subcutaneous tumor volume (width^2 × length)/2) in mice injected with 1×10^6 Melmet 5 cells. Mice were from two weeks onwards given daily i.p. injections of 0.1 mL vehicle (olive oil), 20 mg/kg β-sitosterol in olive oil, 25 mg/kg PLX4720 in 0.05% DMSO, or a combination of the two latter ($n = 8$ in each group). Representative images of tumors at 44 days are shown in the right panel. Student's *t*-test: * $P < 0.05$. Values are given as the mean ± s.e.m

Intriguingly, we found the highest expression levels for melanoma brain metastases (Additional file 13: Figure S12a, b). There was no difference in NDUFB8 expression between BRAF mutated and BRAF wild type melanoma brain metastases (Additional file 13: Figure S12c). Taken together, our data suggest that β-sitosterol prevents a key resistance mechanism to BRAFi therapy and may therefore be a beneficial therapeutic adjuvant in the treatment of melanoma brain metastasis.

Discussion

In this study, we used computational predictions based on gene expression analyses to identify potential drugs against *BRAF*-mutant melanoma brain metastases. The cholesterol analogue β-sitosterol was well tolerated, effectively reduced the number and volume of brain metastases, and improved survival in reproducible and predictive human-to-mouse brain metastasis models. As shown in Additional file 9: Figure S8, β-sitosterol may assert its function on many biological processes. From a

therapeutic viewpoint, targeted therapies may have a limited effect, based on their complexity (heterogeneity and numerous cell signaling events occurring in melanomas). In the current work, we have shown that β-sitosterol has a particular effect on BRAF-driven tumors, but this does not exclude an action of β-sitosterol on other biological processes in tumor cells. For instance, the PC14_PE6_Br2 lung adenocarcinoma cell line, which is BRAF wild type, was also sensitive to β-sitosterol treatment, but to a lesser extent. We found in particular that the compound inhibited mitochondrial respiration through targeting of mitochondrial CI, which is a major facilitator of intrinsic and acquired resistance to MAPK-targeted therapies [24, 63]. Importantly, we also found that the combination of β-sitosterol and a BRAFi exhibited a strong therapeutic effect, compared to monotherapies.

Regarding a potential translational value of the presented findings, the preventive effect of β-sitosterol on the establishment of brain metastasis should be highlighted (Fig. 4). Since patients with melanomas and lung cancer show a significant propensity to develop brain metastasis during disease progression, β-sitosterol may, in a preventive setting, inhibit brain metastasis from the primary tumor.

To our knowledge, this is the first example of successful preclinical repurposing of a drug to treat melanoma-associated brain metastases. Repurposing of approved, non-anticancer drugs is an attractive drug discovery strategy in cancer with substantial advantages of cheaper, faster, and safer preclinical and clinical validation [11]. It should also be emphasized that high doses (3–4 g) of β-sitosterol can be given daily to patients without side effects [30].

The phytosterol β-sitosterol is known as a competitive inhibitor of intestinal cholesterol uptake [30]. Phytosterols are generally classified as safe by the United States Food and Drug Administration, and the European Foods Safety Authority has concluded that a daily phytosterol and/or phytostanol intake of 1.5–2.4 g can reduce blood cholesterol by 7–10.5% and sustain this effect for up to 85 weeks [13]. Notably, we used a daily dose of 5 mg/kg in our experimental studies, which translates into 375 mg for a person weighing 75 kg. Randomized controlled trials (RCTs) in humans have found beneficial effects of β-sitosterol (and its ester) on hypercholesterolemia, but also on benign prostatic hyperplasia, androgenic alopecia, and as an adjuvant in the treatment of tuberculosis, and anogenital warts [9, 20, 35, 43, 53]. No clinical trials have examined the effects of β-sitosterol on cancer. However, epidemiological studies have suggested that increased consumption of phytosterols can reduce the risk of different cancers [19, 33, 38, 61]. Data from cancer cell lines have shown that β-sitosterol can reduce cell proliferation and induce apoptosis in addition to inhibiting adhesion, invasion, and migration [2, 4–6, 8, 50, 64, 65, 70]. β-sitosterol has also been shown to inhibit the growth of tumor xenografts, reduce progression of carcinogen-induced tumors, and prevent metastatic lung and lymph node colonization [5, 8, 28, 29, 54]. The anticancer effects of β-sitosterol remain somewhat elusive, but a number of underlying mechanisms have been proposed [23]. As a potential therapeutic agent against brain metastases, it is particularly interesting that β-sitosterol has been shown to cross the BBB and accumulate in the brain [25, 62]. With respect to our findings, it has previously been shown that β-sitosterol can incorporate into the inner mitochondrial membrane where it increases membrane fluidity [47]. It is also known that cancer cells may have an altered cholesterol loading, that may impair mitochondrial function leading to apoptosis protection [44]. Further studies on how β-sitosterol causes metabolic alterations in cancer cells are therefore warranted.

We found that, β-sitosterol displays broad-spectrum effects at both the genomic, proteomic, and metabolomic levels. Although extensive suppression of the MAPK pathway appears to be particularly important for metastatic melanoma, we also delineated a highly relevant mechanism of β-sitosterol, namely the reduction of mitochondrial respiration through CI inhibition with concurrent induction of ROS leading to apoptosis. This mitochondrial inhibition may have important ramifications for patients with metastatic melanoma, as increased mitochondrial oxidative capacity has been shown to mediate resistance to MAPK-targeted therapeutics and provide protection against oxidative damage and apoptosis [24, 63, 68]. Previous studies have indicated a therapeutic potential of various mitochondrial inhibitors and CI inhibitors in melanoma [21, 24, 36, 45, 49, 63, 68, 69]. In *BRAF*-mutant melanoma brain metastasis, we show that β-sitosterol efficiently prevented resistance to BRAFi therapy in vivo. Furthermore, large-scale analyses of human brain metastases indicated a significant role of mitochondrial CI, which warrants further investigation. Intriguingly, emerging evidence suggests that mitochondrial respiration may be a particularly important survival mechanism and growth facilitator for metastatic cells in the brain microenvironment [7, 15, 16, 26].

Conclusions

In conclusion, we here leveraged robust in vivo model systems of brain metastasis to demonstrate the effects of β-sitosterol on *BRAF*-mutant melanoma [57]. Our study also indicates a therapeutic potential beyond brain metastasis that warrants further exploration in site-specific model systems. Importantly, to accomplish translational

advances in brain metastasis research, there is a strong need for more preventive trials in selected high-risk patients or in patients with limited brain involvement [12]. Many metabolic modulators, including natural compounds and drugs used for conditions other than cancer, have favorable cost and toxicity profiles and might offer additional therapeutic benefit in metastatic melanoma. β-sitosterol can readily penetrate the BBB and has been studied in several randomized clinical trials of non-cancerous diseases [9, 20, 25, 35, 43, 53, 62]. Thus, our findings strongly encourage further assessment of β-sitosterol as an adjuvant to established MAPK-targeted therapies for patients with melanoma brain metastases or patients at risk of developing such metastases.

Additional files

Additional file 1: Figure S1. The diagram illustrates the step-by-step workflow and analysis strategy used in the current study. (TIF 1390 kb)

Additional file 2: Figure S2. Generation of organ samples for RNA sequencing, brain metastasis gene signature and Connectivity Map analysis. a BLI five weeks after intracardiac injection of 5×10^5 H1_DL2 cells in NOD.CB17-*Prkdc*^{scid}/NcrCrl mice ($n = 7$). M1-M7, indicate mouse 1 to 7. b Fluorescence-activated cell sorting (FACS) of GFP-positive tumor cells from the metastatic lesions. The sorted cells were analyzed by RNA-seq (n = 7). c Heatmap of the 108-gene brain metastasis signature with organ samples in rows and genes in columns. d The brain metastasis gene signature with the left two panels showing 54 upregulated genes in brain metastases and the right two panels showing 54 downregulated genes. e Query results from the Connectivity Map (cMap) database using the 108-gene signature. A score of < 0 to − 1 means net reversal of the signature (negative correlation) and a score of > 0 to + 1 means net induction of the signature (positive correlation). (TIF 2033 kb)

Additional file 3: Table S1. Tissue Digestion Protocols. Preparation of Liberase TM Research Grade (Roche Applied Science) working solution and organ-tailored protocols for tissue digestion (brain, adrenals, ovaries and bone). (DOCX 18 kb)

Additional file 4: Figure S3. Cell viability in vitro by increasing β-sitosterol concentrations. Human melanoma cell lines: a Melmet 1, b Melmet 5, and c A375 ($n = 18$ per cell line per drug per drug concentration). Normal cells: d SV-80 human lung fibroblasts (n = 18 per drug concentration), e hTERT immortalized melanocytes and f Human astrocytes. All values are given as the mean ± s.e.m. (TIF 943 kb)

Additional file 5: Figure S4. In vivo efficacy of candidate compounds on H1_DL2 brain metastases. a Left panel: Tumor cell load into the brain was quantified by MRI-based automated quantification of nanoparticle-labeled cells in NOD/SCID mouse brains 24 h after intracardiac injection of 5×10^5 H1_DL2 cells. Right panel: Images show typical MRI T2*-weighted images of mouse brains (scale bar, 0.25 cm) with an overlay of detected signals (blue). Study groups received 0.2 mL i.p. injections of 40 mg/kg thiostrepton every second day ($n = 5$), 10 mg/kg memantine daily (n = 5), 5 mg/kg β-sitosterol daily ($n = 4$) or vehicle (0.5% DMSO; n = 5) from one week post-injection. See Fig. 3 for more details on this experiment. b Volume of brain metastases determined by MRI (T1-weighted with contrast). Total volume of brain metastases per animal was compared at group level. c Brain BLI (total photon count = dorsal + ventral region of interest (ROI). a-c Student's *t*-test: n.s. $P \geq 0.05$, * $P < 0.05$, ** $P < 0.01$, *** $P < 0.001$. All values are given as the mean ± s.e.m. (TIF 3422 kb)

Additional file 6: Figure S5. In vivo validation of β-sitosterol on H1_DL2 brain metastasis. a Initial tumor cell load into the brain assessed by MRI-based automated quantification of nanoparticle-labeled cells 24 h after intracardiac injection of 5×10^5 H1_DL2 cells. Images show typical MRI T2*-weighted images of mouse brains (scale bar, 0.25 cm) with an overlay of detected signals (blue). The study groups received daily i.p. injections of 0.1 mL vehicle (olive oil; $n = 10$) or β-sitosterol 5 mg/kg diluted in olive oil ($n = 9$) starting one week before tumor cell injections. See Fig. 4 for more details on this experiment. b Body weight from week zero to eight. At 100 days, the three remaining β-sitosterol mice had an average body weight of 26.7 ± 0.6 g. c Volume of brain metastases assessed by MRI (T1-weighted with contrast). Total volumes of brain metastases per animal were compared at group level. a-c Student's *t*-test: n.s. $P \geq 0.05$, * $P < 0.05$, ** $P < 0.01$, *** $P < 0.001$, **** $P < 0.0001$. All values are given as the mean ± s.e.m. (TIF 726 kb)

Additional file 7: Figure S6. β-sitosterol treatment effect is not model specific. a Experiment overview. Mice were injected intracardially with 5×10^5 PC14_PE6_Br2 cells. Test groups received daily i.p. injections of 0.1 mL vehicle (olive oil; n = 4) or β-sitosterol 5 mg/kg ($n = 6$). Treatment started one week prior to tumor cell injections and was continued until euthanization. b Body weight from week zero to four for vehicle and β-sitosterol-treated mice. c Number and d volume of brain metastases at MRI at three weeks (T1-weighted with contrast). Total volume of brain metastases per animal compared at group level. e Brain BLI at three weeks (total photon count = dorsal + ventral region of interest). b-e Student's *t*-test: n.s. $P \geq 0.05$, * $P < 0.05$, ** $P < 0.01$, *** $P < 0.001$. f Kaplan-Meier survival plot (Mantel-Cox log-rank test: *** $P < 0.001$). All values are given as the mean ± s.e.m. (TIFF 2165 kb)

Additional file 8: Figure S7. a Functional classification of the brain metastasis gene signature. Human biological processes (metabolic processes are highlighted in red), and b signaling pathways associated with the 108-gene brain metastasis signature using the Protein Analysis Through Evolutionary Relationships (PANTHER) classification system. c Known and predicted protein interactions of β-sitosterol from the Search Tool for Interactions of Chemicals (STITCH 4.0). Green lines represent direct interactions with β-sitosterol whereas blue lines represent protein-protein interactions. Direct activation (green arrows) or inhibition (red lines) is indicated. d Significant statistical associations of β-sitosterol targets with cellular processes predicted with the Human Experimental/Functional Mapper (HEFalMp). *P*-values represent approximate multiple hypothesis corrected values. (TIF 1333 kb)

Additional file 9: Figure S8. Protein phosphorylation screening following β-sitosterol treatment. Parallel determination of protein phosphorylation levels (43 oncogenic kinases and two total proteins) in H1_DL2 cells after 24 h treatment with vehicle (0.05% DMSO) or β-sitosterol (50 μM). (TIF 418 kb)

Additional file 10: Figure S9. Interaction network of signature genes and oxidative phosphorylation. The 121 Gene Ontology (GO)-annotated genes implicated in oxidative phosphorylation (red nodes) have 163 experimentally validated protein-protein and protein-DNA interactions involving 143 genes/proteins, including eight signature genes (green nodes). Purple nodes: Other genes that mediate interactions between signature and oxidative phosphorylation genes. Interaction directionality is represented with arrows. (TIF 1057 kb)

Additional file 11: Figure S10. Interaction network of β-sitosterol targets and oxidative phosphorylation. The 121 Gene Ontology (GO)-annotated genes implicated in oxidative phosphorylation (red nodes) have 155 experimentally validated protein-protein and protein-DNA interactions involving 141 genes/proteins, including four β-sitosterol targets (green nodes). Purple nodes: Other genes that mediate interactions between β-sitosterol targets and oxidative phosphorylation genes. Interaction directionality is represented with arrows. (TIF 1056 kb)

Additional file 12: Figure S11. The respiratory capacity (OCR) in normal melanocytes following β-sitosterol treatment as measured by the Seahorse system. Compared to the tumor cells (Fig. 5a) no changes in respiratory capacity was observed. (TIF 263 kb)

Additional file 13: Figure S12. Mitochondrial complex I activity in human brain metastases. a Expression levels of complex I subunit NDUFB8 in 197 human brain metastases from different cancers: Carcinoma not otherwise specified (NOS; n = 9), colon cancer (n = 9), breast cancer ($n = 25$), renal cell cancer (RCC; n = 9), non-small cell lung

cancer (NSCLC; $n = 52$), small cell lung cancer (SCLC; $n = 7$), melanoma ($n = 78$) and others ($n = 8$). H-Score = [staining intensity (1 = weak, 2 = moderate, 3 = strong)] x [frequency of positive cells (%)]. Kruskal-Wallis test with Dunn's multiple comparisons test: * $P < 0.05$, ** $P < 0.01$, **** $P < 0.0001$ and for comparisons not indicated $P \geq 0.05$. b Immunohistochemistry of NDUFB8 in a human melanoma brain metastasis. c Expression levels of complex I subunit NDUFB8 in BRAF mutated melanoma (BRAFV600E; $n = 24$) and BRAF wild type melanoma (no BRAFV600E; $n = 23$). Kruskal-Wallis test with Dunn's multiple comparisons test: n.s.: not significant. (TIFF 12141 kb)

Acknowledgments
We thank Bridget McLaughlin (University of California Davis) for assistance with fluorescence-activated cell sorting. We thank Stephenie Y. Liu and Ryan R. Davis (UC Davis Comprehensive Cancer Center) for technical assistance with the RNA-Seq analysis. We thank Øystein Fodstad (University of Oslo) and Frank Winkler (University Hospital Heidelberg & German Cancer Research Center, Heidelberg, Germany) for providing cell lines. We thank Petr Nazarov and Arnaud Muller (Luxembourg Institute of Health) and the BioStars community for helpful discussions on the bioinformatics. Imaging was performed at the Molecular Imaging Center (MIC), Department of Biomedicine, University of Bergen. We thank Hege A. Dale (MIC) for microscopy assistance, Tina Pavlin (MIC) for MRI technical assistance and Heidi Espedal (MIC) for valuable input on the cellular metabolism experiments. We thank Erlend Hodneland (University of Bergen) for quantifications of labeled tumor cells. We thank Knut Wester (University of Bergen) for manuscript proofreading. This work was supported by the Western Norway Regional Health Authority (911645, 911558 and 911990), Stiftelsen Kristian Gerhard Jebsen (2014-03), the University of Bergen (236608 and 710028), the Norwegian Cancer Society (182716), the Norwegian Research Council (214187 and 214381), the National Cancer Institute Cancer Center Support Grant P30 (P30 CA093373), the United States National Institutes of Health (R01HL124879 and R01CA134659) and the UC Davis RISE program.

Availability of data and materials
The raw sequence and processed expression data files are publicly available through NCBI GEO (http://www.ncbi.nlm.nih.gov/geo/) with accession number GSE100066.

Authors' contributions
TS, LP, FA, KP, KWF, KJT, ML-L, RB, and FT designed the study. TS, LP, FA, GVR, JKV, SNA, MB, SB, YB, KOS, ESI, LMM, ST, RUB, CGT, and FT conducted the experiments. TS, LP, FA, GVR, MB, JKV, PH, KOS, CT, KP, KJT, RB, and FT analyzed the data. TS, RB, and FT wrote the manuscript. All authors contributed to and approved the final manuscript.

Competing interests
The authors declare that they have no competing interests.

Publisher's Note

Author details
[1]Kristian Gerhard Jebsen Brain Tumour Research Centre, Department of Biomedicine, University of Bergen, Jonas Lies vei 91, 5009 Bergen, Norway. [2]Department of Clinical Medicine, University of Bergen, Haukelandsveien 22, 5021 Bergen, Norway. [3]Department of Neurosurgery, Haukeland University Hospital, Haukelandsveien 22, 5021 Bergen, Norway. [4]Department of Dermatology, Haukeland University Hospital, Haukelandsveien 22, 5021 Bergen, Norway. [5]NorLux Neuro-Oncology Laboratory, Department of Oncology, Luxembourg Institute of Health, 84 Val Fleuri, 1526 Luxembourg, Luxembourg. [6]Present address: Proteome and Genome Research Unit, Department of Oncology, Luxembourg Institute of Health, 1A-B, rue Thomas Edison, L-1445 Strassen, Luxembourg, Luxembourg. [7]Department of Oncology and Medical Physics, Haukeland University Hospital, Haukelandsveien 22, 5021 Bergen, Norway. [8]Department of Biomedicine, University of Bergen, Jonas Lies vei 91, 5009 Bergen, Norway. [9]Edinger-Institute (Neurological Institute), Goethe-University Medical School, Heinrich-Hoffmann-Strasse 7, 60528 Frankfurt am Main, Germany. [10]Institute of Marine Research, Nordnesgaten 50, 5005 Bergen, Norway. [11]Department of Biomedical Engineering, University of California Davis, 451 East Health Sciences Drive, Davis, CA 95616, USA. [12]Department of Biochemistry and Molecular Medicine, UC Davis Comprehensive Cancer Center, 4645 Second Avenue, Sacramento, CA 95817, USA. [13]Computational Biology Unit, Department of Informatics, University of Bergen, Thormøhlensgate 55, 5008 Bergen, Norway. [14]Institute of Pathology and Neuropathology, Department of Neuropathology, University of Tuebingen, Tuebingen, Germany. [15]The Molecular Imaging Center, Department of Biomedicine, University of Bergen, Jonas Lies vei 91, 5009 Bergen, Norway.

Received: 7 March 2019 Accepted: 27 March 2019
Published online: 10 April 2019

References
1. Abildgaard C, Guldberg P (2015) Molecular drivers of cellular metabolic reprogramming in melanoma. Trends Mol Med 21:164–171. https://doi.org/10.1016/j.molmed.2014.12.007
2. Alvarez-Sala A, Attanzio A, Tesoriere L, Garcia-Llatas G, Barbera R, Cilla A (2018) Apoptotic effect of a phytosterol-ingredient and its main phytosterol (beta-sitosterol) in human cancer cell lines. Int J Food Sci Nutr:1–12. https://doi.org/10.1080/09637486.2018.1511689
3. Arvold ND, Lee EQ, Mehta MP, Margolin K, Alexander BM, Lin NU et al (2016) Updates in the management of brain metastases. Neuro-Oncology 18:1043–1065. https://doi.org/10.1093/neuonc/now127
4. Awad AB, Burr AT, Fink CS (2005) Effect of resveratrol and beta-sitosterol in combination on reactive oxygen species and prostaglandin release by PC-3 cells. Prostaglandins Leukot Essent Fatty Acids 72:219–226. https://doi.org/10.1016/j.plefa.2004.11.005
5. Awad AB, Fink CS, Williams H, Kim U (2001) In vitro and in vivo (SCID mice) effects of phytosterols on the growth and dissemination of human prostate cancer PC-3 cells. Eur J Cancer Prev 10:507–513
6. Awad AB, Williams H, Fink CS (2001) Phytosterols reduce in vitro metastatic ability of MDA-MB-231 human breast cancer cells. Nutr Cancer 40:157–164. https://doi.org/10.1207/S15327914NC402_12
7. Barbi de Moura M, Vincent G, Fayewicz SL, Bateman NW, Hood BL, Sun Met al (2012) Mitochondrial respiration--an important therapeutic target in melanoma. PLoS One 7: e40690 https://doi.org/10.1371/journal.pone.0040690
8. Baskar AA, Ignacimuthu S, Paulraj GM, Al Numair KS (2010) Chemopreventive potential of beta-Sitosterol in experimental colon cancer model--an in vitro and in vivo study. BMC Complement Altern Med 10:24. https://doi.org/10.1186/1472-6882-10-24
9. Berges RR, Windeler J, Trampisch HJ, Senge T (1995) Randomised, placebo-controlled, double-blind clinical trial of beta-sitosterol in patients with benign prostatic hyperplasia. Beta-sitosterol Study Group. Lancet 345:1529–1532
10. Berghoff AS, Preusser M (2018) New developments in brain metastases. Ther Adv Neurol Disord 11:1–14. https://doi.org/10.1177/1756286418785502
11. Bertolini F, Sukhatme VP, Bouche G (2015) Drug repurposing in oncology--patient and health systems opportunities. Nat Rev Clin Oncol 12:732–742. https://doi.org/10.1038/nrclinonc.2015.169
12. Brabletz T, Lyden D, Steeg PS, Werb Z (2013) Roadblocks to translational advances on metastasis research. Nat Med 19:1104–1109. https://doi.org/10.1038/nm.3327
13. Bresson J-L, Flynn A, Heinonen M, Hulshof K, Korhonen H, Lagiou P et al (2008) Plant Sterols and Blood Cholesterol - Scientific substantiation of a health claim related to plant sterols and lower/reduced blood cholesterol and reduced risk of (coronary) heart disease pursuant to Article 14 of Regulation (EC) No 1924/2006. The EFSA Journal 781:1–12. https://doi.org/10.2903/j.efsa.2008.781
14. Capper D, Berghoff AS, Magerle M, Ilhan A, Wohrer A, Hackl M et al (2012) Immunohistochemical testing of BRAF V600E status in 1,120 tumor tissue samples of patients with brain metastases. Acta Neuropathol 123:223–233. https://doi.org/10.1007/s00401-011-0887-y
15. Chen EI, Hewel J, Krueger JS, Tiraby C, Weber MR, Kralli A et al (2007) Adaptation of energy metabolism in breast cancer brain metastases. Cancer Res 67:1472–1486. https://doi.org/10.1158/0008-5472.CAN-06-3137
16. Chen J, Lee HJ, Wu X, Huo L, Kim SJ, Xu L et al (2015) Gain of glucose-independent growth upon metastasis of breast cancer cells to the brain. Cancer Res 75:554–565. https://doi.org/10.1158/0008-5472.CAN-14-2268

17. Cohen JV, Tawbi H, Margolin KA, Amravadi R, Bosenberg M, Brastianos PK et al (2016) Melanoma central nervous system metastases: current approaches, challenges, and opportunities. Pigment Cell Melanoma Res 29:627–642. https://doi.org/10.1111/pcmr.12538
18. Davies MA, Saiag P, Robert C, Grob JJ, Flaherty KT, Arance A et al (2017) Dabrafenib plus trametinib in patients with BRAF(V600)-mutant melanoma brain metastases (COMBI-MB): a multicentre, multicohort, open-label, phase 2 trial. Lancet Oncol 18:863–873. https://doi.org/10.1016/S1470-2045(17)30429-1
19. De Stefani E, Boffetta P, Ronco AL, Brennan P, Deneo-Pellegrini H, Carzoglio JC et al (2000) Plant sterols and risk of stomach cancer: a case-control study in Uruguay. Nutr Cancer 37: 140–144 https://doi.org/10.1207/S15327914NC372_4
20. Donald PR, Lamprecht JH, Freestone M, Albrecht CF, Bouic PJ, Kotze D et al (1997) A randomised placebo-controlled trial of the efficacy of beta-sitosterol and its glucoside as adjuvants in the treatment of pulmonary tuberculosis. Int J Tuberc Lung Dis 1:518–522
21. Fischer GM, Jalali A, Kircher DA, Lee WC, McQuade JL, Haydu LE et al (2019) Molecular profiling reveals unique immune and metabolic features of melanoma brain metastases. Cancer Discov. https://doi.org/10.1158/2159-8290.CD-18-1489
22. Gerstner ER, Fine RL (2007) Increased permeability of the blood-brain barrier to chemotherapy in metastatic brain tumors: establishing a treatment paradigm. J Clin Oncol 25:2306–2312. https://doi.org/10.1200/JCO.2006.10.0677
23. Grattan BJ Jr (2013) Plant sterols as anticancer nutrients: evidence for their role in breast cancer. Nutrients 5:359–387. https://doi.org/10.3390/nu5020359
24. Haq R, Shoag J, Andreu-Perez P, Yokoyama S, Edelman H, Rowe GC et al (2013) Oncogenic BRAF regulates oxidative metabolism via PGC1alpha and MITF. Cancer Cell 23:302–315. https://doi.org/10.1016/j.ccr.2013.02.003
25. Heverin M, Bogdanovic N, Lutjohann D, Bayer T, Pikuleva I, Bretillon L et al (2004) Changes in the levels of cerebral and extracerebral sterols in the brain of patients with Alzheimer's disease. J Lipid Res 45:186–193. https://doi.org/10.1194/jlr.M300320-JLR200
26. Ho J, de Moura MB, Lin Y, Vincent G, Thorne S, Duncan LM et al (2012) Importance of glycolysis and oxidative phosphorylation in advanced melanoma. Mol Cancer 11:76. https://doi.org/10.1186/1476-4598-11-76
27. Ilhan-Mutlu A, Osswald M, Liao Y, Gommel M, Reck M, Miles D et al (2016) Bevacizumab prevents brain metastases formation in lung adenocarcinoma. Mol Cancer Ther 15:702–710. https://doi.org/10.1158/1535-7163.MCT-15-0582
28. Imanaka H, Koide H, Shimizu K, Asai T, Kinouchi Shimizu N, Ishikado A et al (2008) Chemoprevention of tumor metastasis by liposomal beta-sitosterol intake. Biol Pharm Bull 31:400–404
29. Ju YH, Clausen LM, Allred KF, Almada AL, Helferich WG (2004) Beta-Sitosterol, beta-Sitosterol glucoside, and a mixture of beta-Sitosterol and beta-Sitosterol glucoside modulate the growth of estrogen-responsive breast Cancer cells in vitro and in Ovariectomized Athymic mice. J Nutr 134: 1145–1151. https://doi.org/10.1093/jn/134.5.1145
30. Law M (2000) Plant sterol and stanol margarines and health. BMJ 320:861–864
31. Lockman PR, Mittapalli RK, Taskar KS, Rudraraju V, Gril B, Bohn KA et al (2010) Heterogeneous blood-tumor barrier permeability determines drug efficacy in experimental brain metastases of breast cancer. Clin Cancer Res 16:5664–5678. https://doi.org/10.1158/1078-0432.CCR-10-1564
32. Long GV, Trefzer U, Davies MA, Kefford RF, Ascierto PA, Chapman PB et al (2012) Dabrafenib in patients with Val600Glu or Val600Lys BRAF-mutant melanoma metastatic to the brain (BREAK-MB): a multicentre, open-label, phase 2 trial. Lancet Oncol 13:1087–1095. https://doi.org/10.1016/S1470-2045(12)70431-X
33. Mendilaharsu M, De Stefani E, Deneo-Pellegrini H, Carzoglio J, Ronco A (1998) Phytosterols and risk of lung cancer: a case-control study in Uruguay. Lung Cancer 21:37–45
34. Meyer M, Essack M, Kanyanda S, Rees J (2008) A low-cost flow cytometric assay for the detection and quantification of apoptosis using an anionic halogenated fluorescein dye. Biotechniques 45:317–320. https://doi.org/10.2144/000112908
35. Miettinen TA, Puska P, Gylling H, Vanhanen H, Vartiainen E (1995) Reduction of serum cholesterol with sitostanol-ester margarine in a mildly hypercholesterolemic population. N Engl J Med 333:1308–1312. https://doi.org/10.1056/NEJM199511163332002
36. Miskimins WK, Ahn HJ, Kim JY, Ryu S, Jung YS, Choi JY (2014) Synergistic anti-cancer effect of phenformin and oxamate. PLoS One 9:e85576. https://doi.org/10.1371/journal.pone.0085576
37. Mittapalli RK, Vaidhyanathan S, Dudek AZ, Elmquist WF (2013) Mechanisms limiting distribution of the threonine-protein kinase B-RaF(V600E) inhibitor dabrafenib to the brain: implications for the treatment of melanoma brain metastases. J Pharmacol Exp Ther 344:655–664. https://doi.org/10.1124/jpet.112.201475
38. Nair PP, Turjman N, Kessie G, Calkins B, Goodman GT, Davidovitz H et al (1984) Diet, nutrition intake, and metabolism in populations at high and low risk for colon cancer. Dietary cholesterol, beta-sitosterol, and stigmasterol. Am J Clin Nutr 40:927–930. https://doi.org/10.1093/ajcn/40.4.927
39. Neman J, Termini J, Wilczynski S, Vaidehi N, Choy C, Kowolik CM et al (2014) Human breast cancer metastases to the brain display GABAergic properties in the neural niche. Proc Natl Acad Sci U S A 111:984–989. https://doi.org/10.1073/pnas.1322098111
40. Palorini R, Simonetto T, Cirulli C, Chiaradonna F (2013) Mitochondrial complex I inhibitors and forced oxidative phosphorylation synergize in inducing cancer cell death. Int J Cell Biol 2013:243876. https://doi.org/10.1155/2013/243876
41. Park ES, Kim SJ, Kim SW, Yoon SL, Leem SH, Kim SB et al (2011) Cross-species hybridization of microarrays for studying tumor transcriptome of brain metastasis. Proc Natl Acad Sci U S A 108:17456–17461. https://doi.org/10.1073/pnas.1114210108
42. Piskounova E, Agathocleous M, Murphy MM, Hu Z, Huddlestun SE, Zhao Z et al (2015) Oxidative stress inhibits distant metastasis by human melanoma cells. Nature 527:186–191. https://doi.org/10.1038/nature15726
43. Prager N, Bickett K, French N, Marcovici G (2002) A randomized, double-blind, placebo-controlled trial to determine the effectiveness of botanically derived inhibitors of 5-alpha-reductase in the treatment of androgenetic alopecia. J Altern Complement Med 8:143–152. https://doi.org/10.1089/acm.2002.8.143
44. Ribas V, Garcia-Ruiz C, Fernandez-Checa JC (2016) Mitochondria, cholesterol and cancer cell metabolism. Clin Transl Med 5:22. https://doi.org/10.1186/s40169-016-0106-5
45. Roesch A, Vultur A, Bogeski I, Wang H, Zimmermann KM, Speicher D et al (2013) Overcoming intrinsic multidrug resistance in melanoma by blocking the mitochondrial respiratory chain of slow-cycling JARID1B(high) cells. Cancer Cell 23:811–825. https://doi.org/10.1016/j.ccr.2013.05.003
46. Seifert H, Hirata E, Gore M, Khabra K, Messiou C, Larkin J et al (2016) Extrinsic factors can mediate resistance to BRAF inhibition in central nervous system melanoma metastases. Pigment Cell Melanoma Res 29:92–100. https://doi.org/10.1111/pcmr.12424
47. Shi C, Wu F, Xu J (2013) Incorporation of beta-sitosterol into mitochondrial membrane enhances mitochondrial function by promoting inner mitochondrial membrane fluidity. J Bioenerg Biomembr 45:301–305. https://doi.org/10.1007/s10863-012-9495-3
48. Singh M, Venugopal C, Tokar T, Brown KR, McFarlane N, Bakhshinyan D et al (2017) RNAi screen identifies essential regulators of human brain metastasis-initiating cells. Acta Neuropathol 134:923–940. https://doi.org/10.1007/s00401-017-1757-z
49. Smith MP, Brunton H, Rowling EJ, Ferguson J, Arozarena I, Miskolczi Z et al (2016) Inhibiting drivers of non-mutational drug tolerance is a salvage strategy for targeted melanoma therapy. Cancer Cell 29:270–284. https://doi.org/10.1016/j.ccell.2016.02.003
50. Sook SH, Lee HJ, Kim JH, Sohn EJ, Jung JH, Kim B et al (2014) Reactive oxygen species-mediated activation of AMP-activated protein kinase and c-Jun N-terminal kinase plays a critical role in beta-sitosterol-induced apoptosis in multiple myeloma U266 cells. Phytother Res 28:387–394. https://doi.org/10.1002/ptr.4999
51. Spagnolo F, Picasso V, Lambertini M, Ottaviano V, Dozin B, Queirolo P (2016) Survival of patients with metastatic melanoma and brain metastases in the era of MAP-kinase inhibitors and immunologic checkpoint blockade antibodies: a systematic review. Cancer Treat Rev 45:38–45. https://doi.org/10.1016/j.ctrv.2016.03.003
52. Steeg PS, Camphausen KA, Smith QR (2011) Brain metastases as preventive and therapeutic targets. Nat Rev Cancer 11:352–363. https://doi.org/10.1038/nrc3053
53. Stefanaki C, Fasoulaki X, Kouris A, Caroni C, Papagianaki K, Mavrogianni P et al (2015) A randomized trial of efficacy of beta-sitosterol and its

glucoside as adjuvant to cryotherapy in the treatment of anogenital warts. J Dermatolog Treat 26:139–142. https://doi.org/10.3109/09546634.2014.925535
54. Stoner GD, Chen T, Kresty LA, Aziz RM, Reinemann T, Nines R (2006) Protection against esophageal cancer in rodents with lyophilized berries: potential mechanisms. Nutr Cancer 54:33–46. https://doi.org/10.1207/s15327914nc5401_5
55. Stroud DA, Surgenor EE, Formosa LE, Reljic B, Frazier AE, Dibley MG et al (2016) Accessory subunits are integral for assembly and function of human mitochondrial complex I. Nature 538:123–126. https://doi.org/10.1038/nature19754
56. Sullivan RJ, Flaherty KT (2015) New strategies in melanoma: entering the era of combinatorial therapy. Clin Cancer Res 21:2424–2435. https://doi.org/10.1158/1078-0432.CCR-14-1650
57. Sundstrom T, Daphu I, Wendelbo I, Hodneland E, Lundervold A, Immervoll H et al (2013) Automated tracking of nanoparticle-labeled melanoma cells improves the predictive power of a brain metastasis model. Cancer Res 73:2445–2456. https://doi.org/10.1158/0008-5472.CAN-12-3514
58. Sundstrom T, Espedal H, Harter PN, Fasmer KE, Skaftnesmo KO, Horn S et al (2015) Melanoma brain metastasis is independent of lactate dehydrogenase a expression. Neuro-Oncology 17:1374–1385. https://doi.org/10.1093/neuonc/nov040
59. Taggart D, Andreou T, Scott KJ, Williams J, Rippaus N, Brownlie RJ et al (2018) Anti-PD-1/anti-CTLA-4 efficacy in melanoma brain metastases depends on extracranial disease and augmentation of CD8(+) T cell trafficking. Proc Natl Acad Sci U S A 115:E1540–E1549. https://doi.org/10.1073/pnas.1714089115
60. Thorsen F, Fite B, Mahakian LM, Seo JW, Qin S, Harrison V et al (2013) Multimodal imaging enables early detection and characterization of changes in tumor permeability of brain metastases. J Control Release 172:812–822. https://doi.org/10.1016/j.jconrel.2013.10.019
61. Torres-Sanchez L, Galvan-Portillo M, Wolff MS, Lopez-Carrillo L (2009) Dietary consumption of phytochemicals and breast cancer risk in Mexican women. Public Health Nutr 12:825–831. https://doi.org/10.1017/S136898000800325X
62. Vanmierlo T, Weingartner O, van der Pol S, Husche C, Kerksiek A, Friedrichs S et al (2012) Dietary intake of plant sterols stably increases plant sterol levels in the murine brain. J Lipid Res 53:726–735. https://doi.org/10.1194/jlr.M017244
63. Vazquez F, Lim JH, Chim H, Bhalla K, Girnun G, Pierce K et al (2013) PGC1alpha expression defines a subset of human melanoma tumors with increased mitochondrial capacity and resistance to oxidative stress. Cancer Cell 23:287–301. https://doi.org/10.1016/j.ccr.2012.11.020
64. von Holtz RL, Fink CS, Awad AB (1998) Beta-Sitosterol activates the sphingomyelin cycle and induces apoptosis in LNCaP human prostate cancer cells. Nutr Cancer 32:8–12. https://doi.org/10.1080/01635589809514709
65. Vundru SS, Kale RK, Singh RP (2013) Beta-Sitosterol induces G1 arrest and causes depolarization of mitochondrial membrane potential in breast carcinoma MDA-MB-231 cells. BMC complement Altern med 13: 280. https://doi.org/10.1186/1472-6882-13-280
66. Wager TT, Villalobos A, Verhoest PR, Hou X, Shaffer CL (2011) Strategies to optimize the brain availability of central nervous system drug candidates. Expert Opin Drug Discov 6:371–381. https://doi.org/10.1517/17460441.2011.564158
67. Webster RM, Mentzer SE (2014) The malignant melanoma landscape. Nat Rev Drug Discov 13:491–492. https://doi.org/10.1038/nrd4326
68. Wheaton WW, Weinberg SE, Hamanaka RB, Soberanes S, Sullivan LB, Anso E et al (2014) Metformin inhibits mitochondrial complex I of cancer cells to reduce tumorigenesis. Elife 3:e02242. https://doi.org/10.7554/eLife.02242
69. Zhang G, Frederick DT, Wu L, Wei Z, Krepler C, Srinivasan S et al (2016) Targeting mitochondrial biogenesis to overcome drug resistance to MAPK inhibitors. J Clin Invest 126:1834–1856. https://doi.org/10.1172/JCI82661
70. Zhao Y, Chang SK, Qu G, Li T, Cui H (2009) Beta-sitosterol inhibits cell growth and induces apoptosis in SGC-7901 human stomach cancer cells. J Agric Food Chem 57:5211–5218. https://doi.org/10.1021/jf803878n

Dual targeting of the MAPK and PI3K signalling pathways in the treatment of metastatic melanoma

Synnøve Nymark Aasen[1,2†], Himalaya Parajuli[1†], Tuyen Hoang[1], Zichao Feng[1,3], Krister Stokke[1], Jiwei Wang[1,3], Kislay Roy[1], Rolf Bjerkvig[1,4], Stian Knappskog[2,5] and Frits Thorsen[1,4,6*]

[1]Kristian Gerhard Jebsen Brain Tumour Research Centre, Department of Biomedicine, University of Bergen, Jonas Lies vei 91, 5009 Bergen, Norway.

[2]Department of Oncology and Medical Physics, Haukeland University Hospital, Jonas Lies vei 65, 5021 Bergen, Norway.

[3]Department of Neurosurgery, Qilu Hospital of Shandong University and Brain Science Research Institute, Shandong University, Key Laboratory of Brain Functional Remodeling, Shandong, 107# Wenhua Xi Road, Jinan, 250012, P.R. China.

[4]NorLux Neuro-Oncology Laboratory, Department of Oncology, Luxembourg Institute of Health, 84 Val Fleuri, 1526 Luxembourg, Luxembourg.

[5]Section of Oncology, Department of Clinical Science, University of Bergen, 5020, Bergen, Norway.

[6]The Molecular Imaging Center, Department of Biomedicine, University of Bergen, Jonas Lies vei 91, 5009 Bergen, Norway.

[†]Shared first authorship

***Correspondence**: Prof. Frits Thorsen, Jonas Lies vei 91, N-5021 Bergen, Tel: +47 55586272, Fax: +47 55586360, Email: frits.thorsen@uib.no

Running title: MAPK and PI3K inhibition in melanoma

Abstract

Malignant melanoma is the most aggressive type of skin cancer where around 50% of the patients develop brain metastases. Despite aggressive treatment, patient survival has traditionally been measured in months, emphasizing the need for new and improved therapies. The mitogen activated protein kinase (MAPK) and the phosphoinositide 3-kinase (PI3K) signalling pathways are commonly altered in melanoma, and inhibition of one pathway often upregulates the other, leading to treatment resistance. Thus, combined treatment targeting both pathways was hypothesized as a potential strategy to overcome resistance. Here, we studied the *in vitro* and *in vivo* the effects of the PI3K inhibitor buparlisib and the MEK1/2 inhibitor trametinib, used either as targeted monotherapies or in combination. Scratch wound and trans-well assays were carried out to assess the migratory capacity of human melanoma cells following drug treatment, whereas flow cytometry, apoptosis array and western blots were used to study apoptosis. Finally, an *in vivo* treatment experiment was carried out on subcutaneous tumours in NOD/SCID mice. We show that combination treatment was more effective than single drug treatment, inhibiting cell viability, cell proliferation, cell migration and colony formation. Combined treatment also more effectively increased apoptosis, and inhibited subcutaneous tumour growth *in vivo*. Our results show the potential of combined treatment to overcome treatment resistance that may develop after single drug treatment, and should be evaluated further as a novel treatment approach to melanoma patients with metastatic spread to the brain.

Key words: Melanoma, brain metastasis, BRAF, MAPK, PI3K, combined treatment, apoptosis

Introduction

Melanoma is the most lethal and aggressive skin cancer, representing around 5% of all skin cancer cases[1]. Together with non-small cell lung cancer (NSCLC) and breast cancer, melanoma show the highest propensity of all cancers to metastasize to the brain. Around 50% of melanoma patients exhibit cancer spread to the brain, a number that rises to more than 70% at autopsy[2]. The incidence is increasing[3], and despite the use of standard as well as novel therapies, metastatic melanoma is associated with divergent prognoses[2,4,5]. Thus, there is still an urgent need for developing new and improved treatment strategies for melanoma patients.

Comprehensive surveys of the genetic landscape of malignancies have shown that melanomas have the highest mutation frequency of all cancers analysed[6]. In particular, the mitogen activated protein kinase (MAPK) and the phosphoinositide 3-kinase (PI3K) signalling pathways are commonly altered in melanoma[7]. Up to 90% of melanomas display an aberrant activation of the MAPK pathway, leading to cell cycle deregulation and inhibition of apoptosis[8]. The most common somatic mutations are point mutations in the v-Raf murine sarcoma viral oncogene homolog (BRAF; 35–50% of melanomas) and neuroblastoma RAS viral oncogene homolog (NRAS; 10–25%), and loss-of-function mutations affecting neurofibromin 1 (NF1; ~15%)[9]. The substitution of valine for glutamic acid (V600E) is found in approximately 90% of all BRAF mutations ($BRAF^{V600E}$)[10]. Activated BRAF leads to the down-stream activation of protein mitogen-activated protein kinase kinase (MEK) by inducing phosphorylation of the serine residues. Activated MEK triggers the serine/threonine kinase ERK by phosphorylation of the Thr-Glu-Tyr motif. The phosphorylated ERK translocates into the nucleus and regulates gene expression of over 50 substrates leading to cancer progression[11].

The PI3K signalling pathway is also frequently activated in melanoma, often as a consequence of mutations or loss of phosphatase and tensin homolog (PTEN); an inhibitor of protein kinase B (Akt), and further dysregulation of Akt expression[12]. This pathway plays a key

role in inducing drug resistance after treatment of melanoma patients with BRAF/MEK inhibitors, and therefore represent a decisive target for melanoma therapy[13]. It has been shown that PI3K signalling may result in therapeutic resistance in $BRAF^{V600E}$ mutated melanoma cells, by modulating MAPK signalling and altering MEK activity[14,15]. Inhibition of one of the pathways often upregulates the other, thereby inducing therapy resistance[16,17].

Mutations in MEK can induce resistance to BRAF inhibition, however, combining a MEK inhibitor with a PI3K inhibitor has been found to overcome this resistance[18]. Thus, a combined PI3K and MEK inhibition can ensure suppression of downstream proliferation, inhibition of growth, and survival signals in tumours. The combination of two inhibitors can, therefore enhance toxicity. Trametinib is one of the most effective allosteric inhibitors of MEK1/MEK2 activation and kinase activity[19]. The U.S. Food and Drug Administration (FDA) approved trametinib (GSK1120212) for treatment of BRAF-mutant metastatic melanoma[20], and a phase III clinical trial using trametinib in melanomas with $BRAF^{V600E}$ or $BRAF^{V600K}$ mutations showed promising responses[21]. Furthermore, more than 30 small molecule PI3K inhibitors have entered clinical trials[22]. A common disadvantage is that they may not effectively downregulate all isoforms of PI3K[23]. Buparlisib (BKM120) is an oral pan-class I PI3K inhibitor targeting all isoforms of PI3K [24]. The anti-proliferative, pro-apoptotic, and antitumor activity of buparlisib has been demonstrated *in vitro*[24], *in vivo*[25] and in clinical trials[26]. The drug combination has even been described as an emerging treatment strategy suitable for clinical investigation[27].

In the present study, we investigated the *in vitro* and *in vivo* effects of buparlisib and trametinib, used either as targeted monotherapies or in combination, on patient-derived melanoma cell lines (H1, H2, H3 and H10) of brain metastatic origin. We show that combined treatment using trametinib and buparlisib was more effective than single drug treatment, to increase tumour cell death overcoming drug resistance.

Results

Combining trametinib and buparlisib of is more effective than monotherapy

Buparlisib reduced cell viability to a greater extent than trametinib in both H1 and H2 cells (**Figs. 1a, b**). Combined treatment was more effective than either monotherapy in H1 cells, whereas combined treatment did not further increase cell death in H2 cells (**Fig. 1b**). The H10 cells were more sensitive to trametinib than buparlisib, and combined treatment was more effective than either of the monotherapies (**Fig. 1b).** The $BRAF^{L577F}$ mutated H3 cells were more resistant to single drug treatment than the other, $BRAF^{V600E}$ mutated cell lines. Nevertheless, combined treatment was more effective than the single drug treatments (**Fig. 1b**). See **Supplementary Figure S1** for IC_{50} curves of H2, H3 and H10 cells. The results were used as a baseline for further *in vitro* experiments.

Melanoma cell morphology is altered upon combination treatment

The morphology of the brain metastatic melanoma cells was altered following drug treatment. For all four cell lines, an elongated morphology was observed after treatment with trametinib, whereas buparlisib or combination treatment resulted in a circular cell shape (**Supplementary Figure S2**). Treated cells also appeared more apoptotic with membrane blebbing, fragmentation and development of apoptotic bodies.

The therapeutic inhibition of the PI3K and MAPK pathways is verified by western blot

Untreated H1, H2, H3 and H10 cells expressed PI3K and MEK1/2, as shown by western blots (**Supplementary Figure S3**). The expression of phosphorylated PI3K and phosphorylated MEK1/2 decreased after single drug treatments, however combined treatment most effectively down-regulated the expression.

Combined treatment inhibits 2D and 3D colony formation more effectively than single drug treatment

Only H1 and H2 cells grew as colonies in 2D. The number of colonies of untreated H1 cells were counted and scaled to 100%. Cells pre-treated with buparlisib developed 43.7% colonies compared to untreated cells, and H1 cells pre-treated with trametinib developed 30% colonies (for both, $P < 0.01$; **Fig. 2a**). Combination treatment was most effective, as only 17.5% colonies developed, compared to untreated cells ($P < 0.05$ compared to trametinib treatment; **Fig. 2a**). For H2 cells, single drug treatment with buparlisib was more effective than trametinib, whereas combinatorial treatment again was more efficient than single drug treatments ($P < 0.0001$ compared to untreated cells, **Supplementary Figure S4**).

Only H1 cells grew as colonies in 3D. The growth area covered by untreated H1 cells grown in an anchorage-independent environment after 21 days was scaled to 100% (**Fig. 2b**). H1 cells pre-treated with trametinib and grown in the same conditions covered in comparison around 91.0% of the field of view. Cells treated with buparlisib covered around 78.4% of the total area ($P < 0.01$, compared to untreated cells), while the area covered after combined treatment was around 22.1% ($P < 0.0001$, compared to untreated cells; **Fig. 2b**).

Tumour cell migration is hampered by combinatorial treatment

During the scratch wound assay, the cells were under constant exposure to the respective drugs. The wound confluence measured during the experiments was scaled to percentage. Across all cell lines, the most efficient treatment was a combination of buparlisib and trametinib, followed by buparlisib and then trametinib (**Fig. 3, Supplementary Figure S5**). After approximately 50 h, the wound was completely closed for untreated H1 cells (**Figs. 3a, b**). After 90 h, none of the other treatment groups had managed to regrow the wound completely. The lowest percentage of confluence was observed after combined treatment of the

H1 cells (**Figs. 3a, b**). Among the other cell lines used, H3 was the only one that was completely regrown into the wound upon completion of the experiment at 90 h (**Supplementary Figure S5b**). H10 cells were the most sensitive to all treatments (**Supplementary Figure S5c**).

Combined pre-treatment inhibits directional cell migration towards a chemo-attractant

In the trans-well assay, the evaluation of cell migration was carried out after pre-treating the cells with the respective drugs for 24 h. In contrast to the scratch-wound assay, the trans-well assay revealed that trametinib was a more effective monotherapy than buparlisib in inhibiting migratory properties of cells across all cell lines. Also here, the combination treatment was more effective than either of the monotherapies (**Figs. 3c, d** and **Supplementary Figure S6**).

Combined treatment induces more apoptosis than single drug treatment

Apoptosis was first studied by flow cytometry using a PI and annexin V assay (**Fig. 4**). There was an overall tendency that combination treatment reduced the amount of viable cells. For untreated H1 cells, around 94% of the cells were viable (**Figs. 4a, b**). Single drug treatment decreased the viability to around 55%, while combined treatment showed a higher efficacy and decreased the number of viable cells to around 40%. Approximately 10% of the H2 cells survived after trametinib treatment, and almost 30% of the cells were healthy after being exposed to buparlisib. Combined treatment resulted in only 7% cell survival (**Fig. 4b**). For the H3 cell line, cell survival after exposure to single drug treatment was around 58% (trametinib) and 37% (buparlisib). Again, the combined treatment effectively reduced cell survival, compared to monotherapies to around 25% (**Fig. 4b**). Between 40-50% of H10 cells treated with single drugs survived the treatment, whereas combined treatment showed a higher efficacy and reduced the number of healthy cells to approximately 6% (**Fig. 4b**). For H1, H2 and H10,

trametinib was the most effective among the monotherapies, which was statistically tested against the combination group as indicated in the graphs. For H3 cells, buparlisib was the most effective monotherapy.

Apoptosis was further studied using an apoptosis array (**Figs. 5a, b**). Both monotherapy and combination treatment resulted in statistical increases in apoptotic protein expression (Bad, cleaved caspase-3, p27/kip1 and TNFR1). There were also tendencies of increased expression of cytochrome-C, TRAIL R2 and Fas in the monotherapies (**Fig. 5A**). Expressions of key inhibitors of apoptosis such as Bcl-2, cIAP-1, claspin, HIF-1α, HSP70, survivin and XIAP were found to be significantly downregulated following monotherapy and combination treatment. Tendencies of decreased expression after monotherapies was also seen for HSP27 (**Fig. 5b**).

A selection of key apoptotic and anti-apoptotic proteins from **Figs. 5a and b** was then verified by western blot (**Fig. 5c**) and quantified (**Fig. 5d**). Statistically significant increases in protein expression of cleaved caspase-3 was found in lysates from H1 cells treated with trametinib ($P < 0.01$). Increased expression of p27/kip1 was seen for cells treated with trametinib and combination therapy (both $P < 0.0001$). Statistically significant decreases were also detected for Bcl-2 in the combination group ($P < 0.05$) and for HIF-1α across buparlisib, trametinib and the combination group ($P < 0.001$, 0.0001 and 0.0001, respectively). PARP was downregulated in the combination group ($P < 0.05$; **Figs. 5c and d**).

The combinatorial approach is more efficacious than single treatments *in vivo*

The finding that combined treatment with buparlisib and trametinib *in vitro* was more efficient than single treatments, was verified *in vivo* in NOD/SCID mice with subcutaneous H1_DL2 derived tumours. At the endpoint of the experiment (after 30 days), the average tumour volume in the combination group was 37.7 mm^3, in the trametinib group 89.7 mm^3, in the buparlisib 186.3 mm^3 and the tumours in the vehicle group 746.7 mm^3 (**Fig. 6a**). Compared

to vehicle treated tumours, buparlisib, trametinib and combination treated mice showed a statistically significant reduction in total tumour volumes (all $P < 0.0001$). When the combination treatment group was compared to the trametinib group, there was also a statistically significant difference ($P < 0.01$; **Fig. 6a**). The number of Ki67 positive cells was quantified from histological sections from tumour tissue across all treatment groups. There were statistically significant differences between vehicle treated tumours and all treatment groups (all $P < 0.0001$; **Figs. 6b and c**).

Discussion

In view of previous research showing a synergetic effect of combining MEK1/2 with PI3K inhibitors[28], we evaluated the therapeutic activity of the combinatorial approach in $BRAF^{V600E}$ and $BRAF^{L577F}$ mutated melanoma cells of brain metastatic origin.

Trametinib has previously been used to inhibit cell proliferation in $BRAF^{V600E}$ mutated melanoma[29]. However, inhibiting the MAPK pathway has been associated with acquired treatment resistance[20,30]. The PI3K pathway represents a second essential signalling pathway in melanoma progression[13]. As an example, it has previously been shown that its activation can mediate resistance to MEK inhibitors in certain cancers[31]. It has also been reported that inhibiting the PI3K pathway can sensitize melanoma cells towards chemotherapies[32]. PI3K inhibition using buparlisib has previously been demonstrated as a promising treatment strategy in BRAF mutated brain metastases in nude mice[4].

The efficacy of therapeutic inhibition of MAPK and PI3K signaling combined has previously been evaluated in a preclinical glioblastoma model. The PI3K pathway was suppressed *in vitro* in a time and concentration-dependent manner, glioblastoma growth was impeded by induction of apoptosis and animal survival was improved[33]. Also, the combination of PI3K and MEK inhibition induced tumour regression in an animal model with colorectal cancer by inducing cell cycle arrest (G_1 phase), activating apoptotic pathways and inhibiting anti-apoptotic pathways[34]. In 2015, the results from a phase Ib clinical trial with 113 patients treated with buparlisib and trametinib were published. Nine of the enrolled patients had cutaneous melanoma[35]. The treatment was well-tolerated short-term; however, the long-term effects were hard to elucidate due to frequent treatment interruptions. Also, the melanoma patients were only evaluated for a maximum tolerated dose (dose escalation phase) and not assessed further for recommended dose in a phase II trial (dose expansion phase) illustrating the limited clinical knowledge about the drug combination.

As seen in **Supplementary Figure S3**, trametinib downregulated the expression of MEK1/2 in all $BRAF^{V600E}$ cell lines. In the H3 $BRAF^{L577F}$ mutated cell line, there was no reduction in protein expression, which may indicate resistance against trametinib. Upon treatment with buparlisib, however, PI3K was downregulated in all cell lines, and the combinatorial approach reduced the protein expression in all cell lines, regardless of BRAF status. Our results suggest that cell lines not harbouring the $BRAF^{V600E}$ mutation are more susceptible to PI3K inhibition. This is in line with previous research, where a decrease in Akt phosphorylation and hence buparlisib activity in both $BRAF^{WT}$ and $BRAF^{V600E}$ mutated melanoma cells was demonstrated[4]. Our results also indicate a higher degree of resistance towards MEK inhibition and that combining it with PI3K inhibitors has the potential to abrogate trametinib resistance. We emphasize that the mutation found in the H3 cells has not been reported in the literature to date, so the oncogenic potential of this mutation is not clear.

The flow cytometric apoptosis study (**Fig. 4)** showed that for all $BRAF^{V600E}$ mutated cell lines (H1, H2 and H10), trametinib induced more apoptosis than buparlisib, and combination treatment further enhanced the effect. Also here, and in line with the literature, H3 was more resistant to trametinib and more susceptive to PI3K inhibition.

It has formerly been reported that buparlisib can alter the cellular morphology by means of reduced focal adhesion and changes in the microtubule dynamics[36]. In our study, all cell lines exhibited traits consistent with the onset of apoptosis after buparlisib treatment, which was also seen after combined treatment (**Supplementary Figure 2**). We also observed a different morphology in cells treated with trametinib, however, this change resembled an EMT, which is associated with loss of apicobasal polarity and stable cell-cell adhesion. This has also been reported previously after treatment with MAPK inhibitors of melanoma cells[37] and NSCLC cells[38].

Of the cell lines used in this study, only H1 and H2 cells were able to grow as monolayer colonies when pre-treated and thereafter seeded in 6-well plates. For both cell lines, there was a statistically significant difference in growth between untreated and combination treated cells (both $P < 0.0001$). For the H1 cells, the most efficient drug was trametinib, whereas buparlisib inhibited cell growth more in H2 cells (**Fig. 2a, Supplementary Figure S4**). When growing the H1 cells in an anchorage-independent environment, the effects of the monotherapies were greatly reduced, as compared to the monolayer experiments. This is likely due to reduced penetration of the individual drugs into a 3D tumour structure (**Fig. 2b**).

Combined treatment upregulated the expression of the four apoptotic markers bad, cleaved caspase 3, p27/kip1 and TNFR1 (**Fig. 5a**). The results for cleaved caspase 3 and p27/kip1 were also verified by western blots (**Figs. 5c, 5d**). Bad is a member of the Bcl-2 family, a substrate of Akt and represents a converging link between inhibition and promotion of apoptosis[15]. It has been found that in addition to the pro-apoptotic activity, bad can also create heterodimers with Bcl-2 and Bcl-$_{XL}$ and hamper anti-apoptotic activity[39]. Caspase 3 is known as the master regulator of apoptosis by regulating the repopulation of tumours following treatment[40]. Across all groups, we found a substantial increase in the levels of the cyclin-dependent kinase inhibitor p27/kip1, which inhibition is a characteristic of malignant growth. PI3K inhibition is linked to p27/kip1 inactivation[41]. The tumour necrosis factor receptor (TNFR) is activated by cytokines belonging to the TNF protein family. Upon receptor mediated activation, apoptosis might be induced. Therapeutic MAPK inhibition is associated with acquired drug resistance[42], which may be mediated through increased PI3K signalling[13]. The PI3K signalling pathway regulates the expression of anti-apoptotic proteins such as Bcl-2[43], cIAP-1[44], claspin[45], HIF-1α[46], Hsp27[47], Hsp70[48], XIAP[49] and survivin[50].

In general, we also found reduced expression levels in the anti-apoptotic proteins after treatment (**Fig. 5b**). Expression levels of Bcl-2, cIAP-1 and HIF-1α were verified by western

blots. For all three markers, combinatorial treatment resulted in significant reductions in protein levels (**Figs. 5c and d**). These results are in line with prior reports showing reduced levels of Bcl-2 following trametinib and combination treatment [51]. This effect was not seen after buparlisib treatment. Furthermore, high HIF-1α tumour levels has been associated with apoptosis and higher survival rates[52]. HIF-1α is also known to mediate the expression of vascular endothelial growth factor (VEGF), thereby promoting aggressive tumour growth[53]. Constitutive activity in the PI3K signalling pathway has been shown to enhance the activation of HIF-1α and contribute to HIF-1α-mediated apoptosis in sarcoma cells[46]. cIAP-1, XIAP and survivin are all members of the inhibitor of apoptosis (IAP) protein family[54]. Survivin expression is linked to several aberrant activations associated with cancer growth, such as for instance the PI3K and MAPK signalling pathways[55]. Finally, PARP cleavage is also a well-known hallmark of apoptosis[56]. Our western blot results indicated cleaved PARP in all groups, however, the difference was only statistically significant in buparlisib treated cells (**Fig. 5d**).

As mentioned initially, melanoma has a strong tendency to metastasize to the brain. It is acknowledged in the literature that metastasis is a dynamic process that depends on the ability of tumour cells to migrate within the microenvironment[57]. Scratch wound assays evaluate the ability of cells to migrate and close an induced wound when grown as a monolayers, whereas trans-well assays give information on the propensity of cells to detect and subsequently migrate towards a chemo-attractant through a physical barrier[58]. During constant exposure to the drugs in the scratch wound assay, buparlisib inhibited cell migration more than trametinib (**Fig. 3a** and **Supplementary Figure S5**). Interestingly, it has previously been shown that a MEK inhibitor was able to promote cell migration, despite drug-induced cell death in a dose-dependent manner[59]. Concerning the trans-well assay, pre-treating cells with trametinib seemed to inhibit cell migration more than buparlisib (**Fig. 3c** and **Supplementary Figure S6**). This may indicate that trametinib exhibits a longer lasting anti-tumour effect compared to buparlisib

in vitro. Another explanation may be that melanoma cells are less likely drawn towards a chemoattractant after inhibition of the MAPK compared to the PI3K signalling pathway. In both experimental layouts, however, combined treatment was the most effective across all cell lines.

In the present work, subcutaneous melanoma tumours derived from brain metastases in NOD/SCID mice were effectively treated with buparlisib combined with trametinib (**Fig. 6**). In general, MEK1/2 inhibitors are well tolerated in preclinical doses up to 10-30 mg/kg [60]. Itamura et al administered 0.1 and 0.3 mg/kg trametinib orally to mice[61], and doses around 1 mg/kg have frequently been used[62-65]. In our *in vivo* experiments, we used 1 mg/kg, which significantly reduced the tumour burden in the monotherapy group receiving trametinib. Further, buparlisib has been administered daily from 2 to 50 mg/kg preclinically[36,66]. Based on previous reports, we chose to use 50 mg/kg in the single drug group, which was well-tolerated *in vivo*. Drawn from our animal experiments, monotherapy with trametinib seemed to be more efficient than buparlisib on H1_DL2 tumours. This is in contrast to some of the *in vitro* experiments with H1 cells, however, some of these exhibited a constant drug exposure to the tumour cells, while in the preclinical study, the drugs were administered once per day, enabling time for drug clearance between treatments[67]. Thus, the results suggest that a constant exposure to trametinib is needed for optimal efficacy.

Despite using a subcutaneous tumour model, our results can serve as a proof-of-principle for brain metastatic melanoma as well. In case of a brain metastasis model, buparlisib is expected to cross an intact BBB[36]. However, a technique for delivering trametinib across the BBB would have to be employed, as the relatively large molecular weight (615.39 Da) and the presence of efflux pumps within the BBB prevents its ability to enter the brain[68]. Thus, we used a subcutaneous model as proof-of-principle to ensure combined drug uptake upon oral administration. It should, however, be noted that in a clinical setting, the BBB is normally

disrupted in brain metastases larger than 2-3 mm[69], which should facilitate penetrance of trametinib into the brain metastatic lesions.

In conclusion, we show that combined treatment with buparlisib and trametinib was superior to single drug treatment *in vitro*, inhibiting growth and migration of human melanoma brain metastasis cells. In a proof-of-principle *in vivo* study, the combined treatment was also more effective than monotherapies. Thus, buparlisib and trametinib should be further evaluated as a novel combinatorial treatment approach on melanoma patients with metastatic spread to the brain.

Methods

Cell lines and cell culture

The H1, H2, H3 and H10 cell lines were established in our laboratory from patient biopsies of human melanoma brain metastases. The H1, H2 and H10 cell lines are V600E mutated, while the H3 cells are L577F mutated. See Supplementary Materials for cell culturing details.

Drugs

Buparlisib (BKM-120) and trametinib (GSK1120212) were purchased from ChemieTek (Indianapolis, NI, USA). Both drugs were dissolved in dimethylsulfoxide (DMSO) and stock concentrations of 250 mM buparlisib and 50 mM trametinib were stored at −20 °C in aliquots until further use.

Cell viability assay

Cell proliferation upon treatment with buparlisib and/or trametinib was studied using a resazurin assay, as previously described[7] and is elaborated in Supplementary Materials.

Clonogenic assay

In order to measure the potential loss of reproductive integrity of cancer cells, a clonogenic assay was performed. Briefly, H1, H2, H3 and H10 cells were pre-treated with buparlisib, trametinib or a combination for 72 h prior to seeding the cells in low numbers in 6-well plates. The cells were scored for colony growth after 21 days. See Supplementary Materials for protocol details.

3D colony formation assay

The cells were grown in an anchorage-independent environment, using a 3D colony formation assay. Pre-treated H1, H2, H3 and H10 cells were seeded in low melting point agarose after pre-treatment with buparlisib, trametinib or combination therapy for 72 h and scored for colony formation 21 days later as described in Supplementary Materials.

Cell migration

To study the effects of treatment on cell motility, two cell migration experiments were carried out. First, a cell migration assay was performed in trans-well layout with pre-treated cells migrating towards a chemoattractant. H1, H2, H3 and H10 cells were pre-treated and seeded in Thinsert^{TM} cell culture inserts (Greiner Bio-One GmbH, Frickenhausen, Germany) in 24 well plates (Nunc) and allowed to migrate towards 30% serum in the lower chambers for 48 h, as described in Supplementary Materials.

In the second experiment, the migratory capacity of cells was studied under constant exposure to drugs for 72 h. H1, H2, H3 and H10 cells were seeded in Essen BioScience ImageLock 96-well plates (cat. no. 4379, Essen BioScience Ltd., Hertfordshire, UK). After 24 h, a wound-maker tool was employed to simultaneously create a consistent wound with a uniform width across all wells, before drug was added to all wells. Imaging was carried out every 2 h using a 10× objective in the IncuCyte® Live Cell Imaging System (Essen BioScience Ltd.) and analysed to find the wound width in μm using the IncuCyte® Scratch Wound Cell Migration Software Module (cat. no. 9600-0012, Essen BioScience Ltd.). See Supplementary Materials.

Apoptosis assay

An Annexin-V flow cytometry assay was performed to assess the effects of combination treatment on apoptosis. The H1, H2, H3 and H10 lines were seeded in 6-well plates (Nunc) and allowed to reach 75% confluency before treatment was added. The cells were treated for 72 h and prepared for flow cytometry by staining with Annexin V and propidium iodide (PI; AlexaFluor®488 Annexin v/dead cell apoptosis kit; Molecular Probes, Life Technologies) according to the manufacturer's instructions. Fluorescence in the FITC-A and PE-A channels were gated to a two-parameter histogram, and analysed using FloJo software (Tree Star Inc., Ashland, OR, USA). See Supplementary Materials for details.

Apoptosis array

A human apoptosis antibody array kit (R&D Systems, Inc., Minneapolis, MN, USA) was used to study the effects of treatment on 35 apoptosis-related proteins on H1 cells after 72 h. The experiment was performed once, each of the 35 proteins were spotted twice on the membrane. See Supplementary Materials.

Western blot analysis

Cell lysates from H1, H2, H3 and H10 cells treated with buparlisib and/or trametinib for 72 hours were prepared for western blot analysis as described in Supplementary Materials. Relative protein levels were first normalised against the loading control (beta actin) and then calculated and presented as a ratio of the untreated control.

***In vivo* experiments**

1×10^6 H1_DL2 cells in 0.1 ml PBS was injected subcutaneously in the neck region of 48 female NOD/SCID mice. After two weeks, the average tumour volume was measured to

approximately 70 mm^3. The mice were then randomized to daily gavage treatments of 0.1 ml vehicle (0.5% methyl cellulose with 0.2% Tween20), 50 mg/kg buparlisib, 1 mg/kg trametinib, or a combination of the two latter (25 mg/kg buparlisib + 0.5 mg/kg trametinib; n = 8 mice in each group). The mice were monitored daily, and calliper tumour measurements were carried out every third day. Tumour volumes were calculated using the formula [$width^2 \times length$]/2. The experiment was terminated after 30 days.

Histology and immunohistochemistry

Tumour samples from the in vivo treatment experiment were prepared for immunohistochemistry analysis as described in Supplementary Materials.

Statistical Analysis

The cell migration in trans-well layout was compared using Dunnett's multiple comparisons test and the flow data was analysed using a two-way ANOVA test with Tukey's multiple comparisons test. The values from the apoptosis array were scaled to fold-change and compared using unpaired t-tests with Holm-Sidak's correction. For the *in vivo* treatment experiment, the differences in endpoint tumour volumes were compared using the Mann-Whitney test. All other comparisons were carried out using unpaired, two-tailed t-tests. All statistical analyses were carried out using GraphPad Prism v7 (GraphPad Software, Inc.). Values presented in the Figs. represent means ± standard error mean (SEM). A two-tailed $p \leq 0.05$ was considered to be statistically significant.

Acknowledgments

We thank Bodil Hansen, Tove Johansen, Halala Sadik Saed, Berit Bølge Tysnes, Marzieh Bahador, Brith Bergum and Hege Avsnes Dale for technical assistance. Supported by The Norwegian Cancer Society, The Norwegian Research Council and Helse-Vest, Haukeland University Hospital.

Conflicts of interest

The authors declare that the research was conducted in the absence of any commercial or financial relationships that could be construed as a potential conflict of interest.

Supplementary information accompanies this article.

Figures

Fig. 1

a

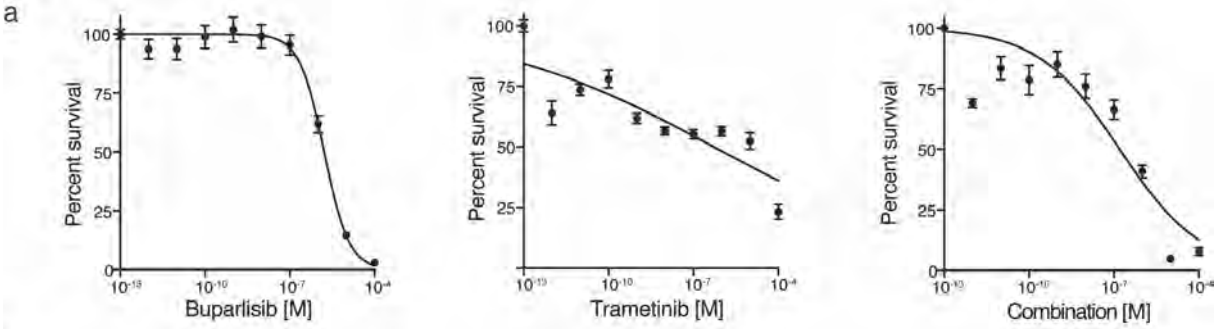

b

Cell line	Buparlisib [M]	Trametinib [M]	Combination [M]
H1	$1.52 \cdot 10^{-6} \pm 0.81 \cdot 10^{-6}$	$5.07 \cdot 10^{-6} \pm 0.59 \cdot 10^{-6}$	$0.41 \cdot 10^{-6} \pm 0.36 \cdot 10^{-6}$
H2	$1.61 \cdot 10^{-6} \pm 0.95 \cdot 10^{-6}$	$3.93 \cdot 10^{-1} \pm 5.28 \cdot 10^{-1}$	$1.58 \cdot 10^{-6} \pm 0.58 \cdot 10^{-6}$
H3	$20.32 \cdot 10^{-6} \pm 32.40 \cdot 10^{-6}$	$16.51 \cdot 10^{-6} \pm 13.21 \cdot 10^{-6}$	$0.03 \cdot 10^{-6} \pm 0.06 \cdot 10^{-6}$
H10	$0.43 \cdot 10^{-6} \pm 0.45 \cdot 10^{-6}$	$3.62 \cdot 10^{-10} \pm 5.90 \cdot 10^{-10}$	$3.18 \cdot 10^{-11} \pm 1.49 \cdot 10^{-11}$

Fig. 1 Cell survival curves of cells grown as monolayers after treatment with buparlisib and trametinib. **a** Representative graphs of H1 cells treated with increasing drug concentrations for 72 h, with either buparlisib, trametinib, or combined treatment. **b** Table showing the IC_{50} doses, the doses at which 50% of the cells were growth inhibited, for all four cell lines studied. The experiments were performed in triplicate (n = 6 per experiment per drug concentration).

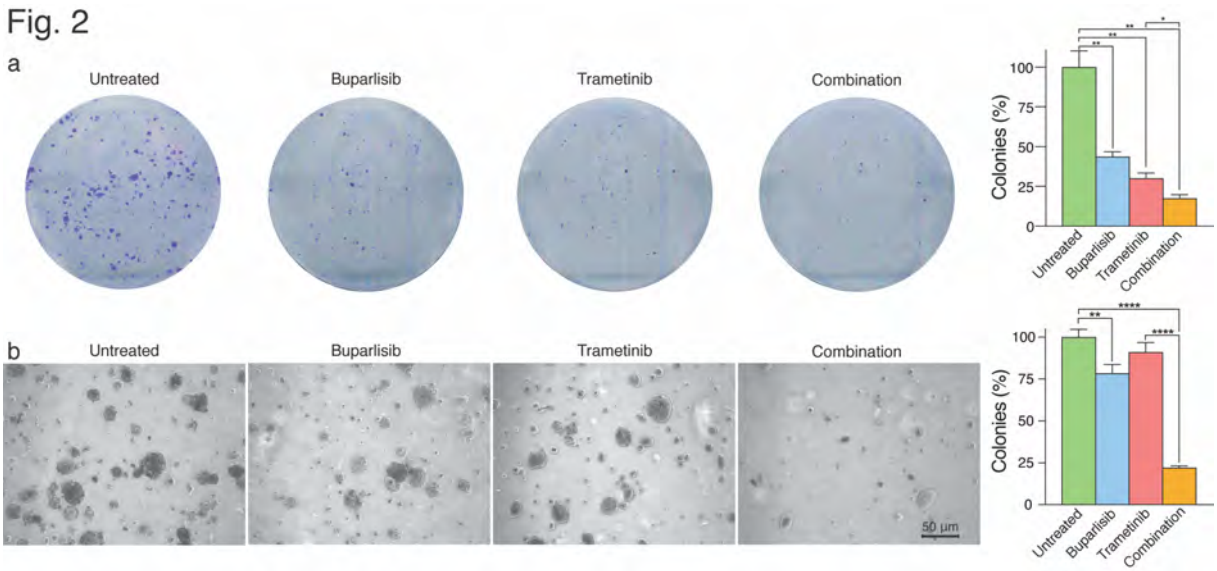

Fig. 2 ***In vitro*** **colony formation of H1 cells after pre-treatment with buparlisib and trametinib. a** Representative images of H1 cells pre-treated with 10 µM buparlisib, 10 µM trametinib or a combination (5 µM buparlisib + 5 µM trametinib) grown as colonies. The colony formation was scored and quantified as seen in the graph to the right. **b** Representative images of H1 cells pre-treated with corresponding drug concentrations seeded into low melting point agarose and incubated for 21 days. Scale bar = 50 µm. The percentage area covered by the spheroids within the total visual field was quantified as seen to the right. The experiments were performed in triplicate (n = 4 images). Abbreviations: *: $p < 0.05$, **: $p < 0.01$ and ****: $p < 0.0001$.

Fig. 3

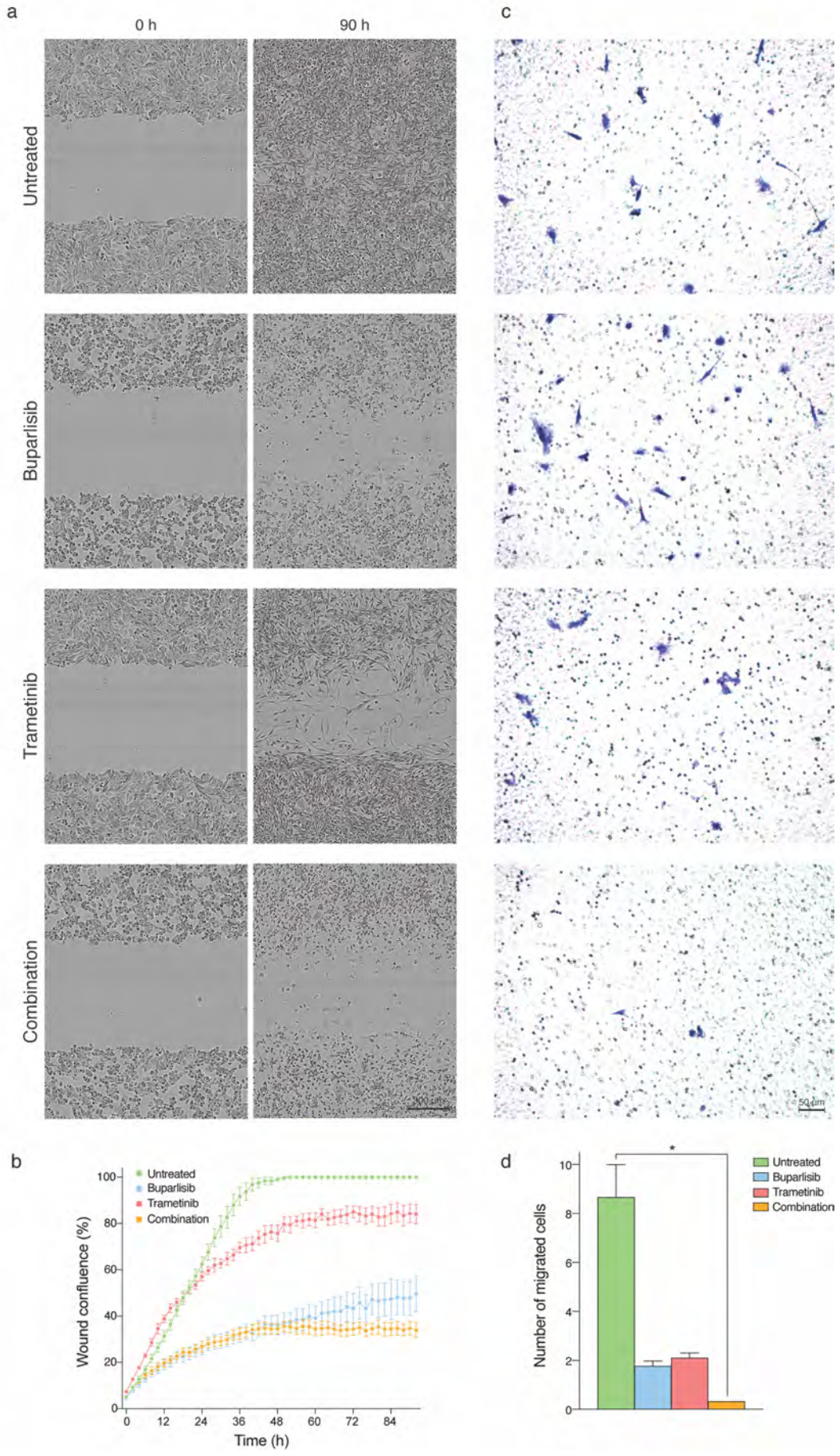
a
0 h
90 h
Untreated
Buparlisib
Trametinib
Combination
c
50 µm
b
Untreated
Buparlisib
Trametinib
Combination
Wound confluence (%)
Time (h)
d
Number of migrated cells
*

Fig. 3 Migration of H1 cells during and after pre-treatment with buparlisib and trametinib. a Representative micrographs of H1 cells before (0 h) and at completion (90 h) of the scratch-wound experiment. The drugs were added at initiation of the time-lapse experiment. Scalebar = 300 μm. **b** Quantification of wound confluence throughout the time-lapse across the different treatment groups (n = 6 per drug concentration). **c** Representative images of migrated H1 cells pre-treated with buparlisib, trametinib or a combination. Scalebar = 50 μm. **d** Quantification of H1 cells allowed to migrate towards a chemo-attractant for 48 h. The experiment was carried out in triplicate (n = 3 representative fields of view per experiment). Abbreviations: *: $p < 0.05$.

Fig. 4

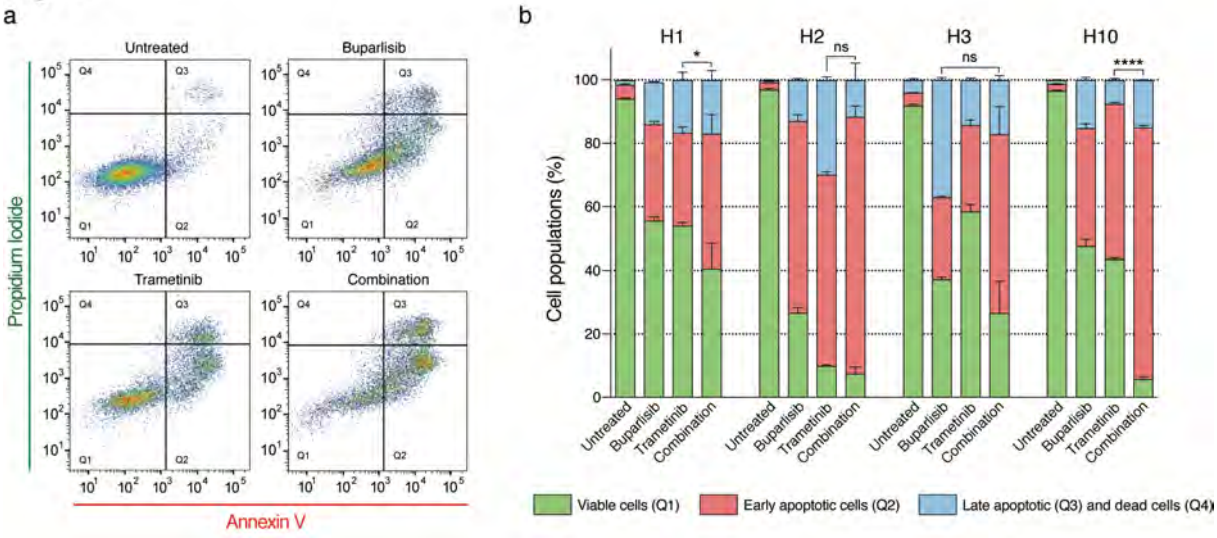

Fig. 4 Flow cytometric analysis of apoptosis after treatment of melanoma brain metastasis cells with buparlisib and trametinib. a Representative dot plots of H1 cells treated with 10 µM buparlisib, 10 µM trametinib or combination (5 µM buparlisib and 5 µM trametinib). Annexin V labels apoptotic cells, while Propidium Iodide labels necrotic cells. **b** Quantification of the percentage of viable, apoptotic and necrotic cells for the H1, H2, H3 and H10 cell lines. The experiments were done in triplicate (n = 3 per experiment per drug concentration). Abbreviations: Q1: viable cells, Q2: cells in early apoptosis, Q3: late apoptotic cells, Q4: necrotic cells, ns: not significant, *: $p < 0.05$ and ****: $p < 0.0001$.

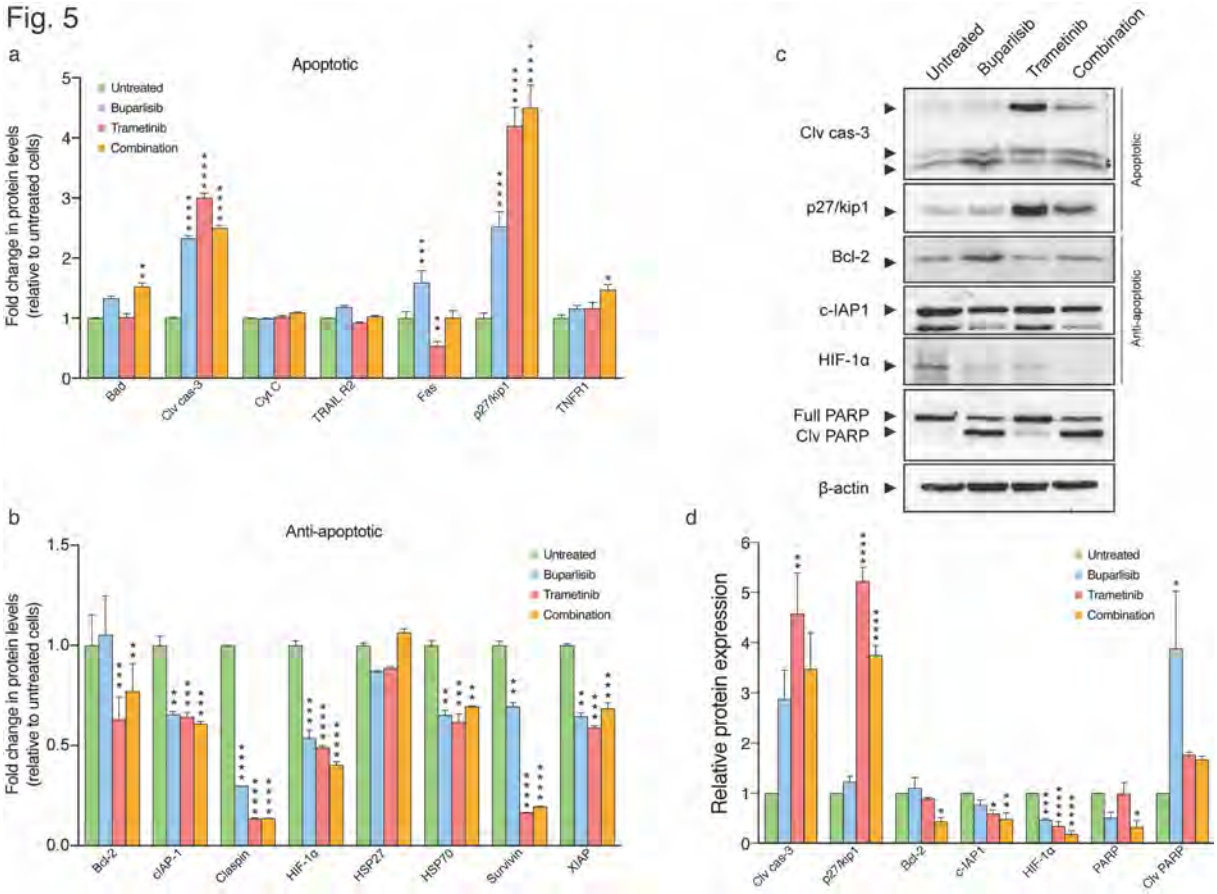

Fig. 5 Expression of apoptosis associated proteins after treatment of H1 cells with buparlisib and trametinib. a Graphic presentation of results from the apoptosis array, showing expression of key molecules involved in apoptosis in H1 cells treated with 20 μM buparlisib, 50 nM trametinib, or 10 μM buparlisib + 25 nM trametinib, for 72 h. **b** Graphic representation of key molecules involved in anti-apoptotic activity in H1 cells after buparlisib and trametinib treatment. **c** Western blots showing the expression of selected apoptotic and anti-apoptotic proteins in addition to PARP. **d** Quantification of western blot results relative to β-actin. Abbreviations: Clv cas-3: cleaved caspase-3, cyt C: cytochrome C, full: full length PARP, clv: cleaved, *: $p < 0.05$, **: $p < 0.01$, ***: $p < 0.001$ and ****: $p < 0.0001$.

Fig. 6

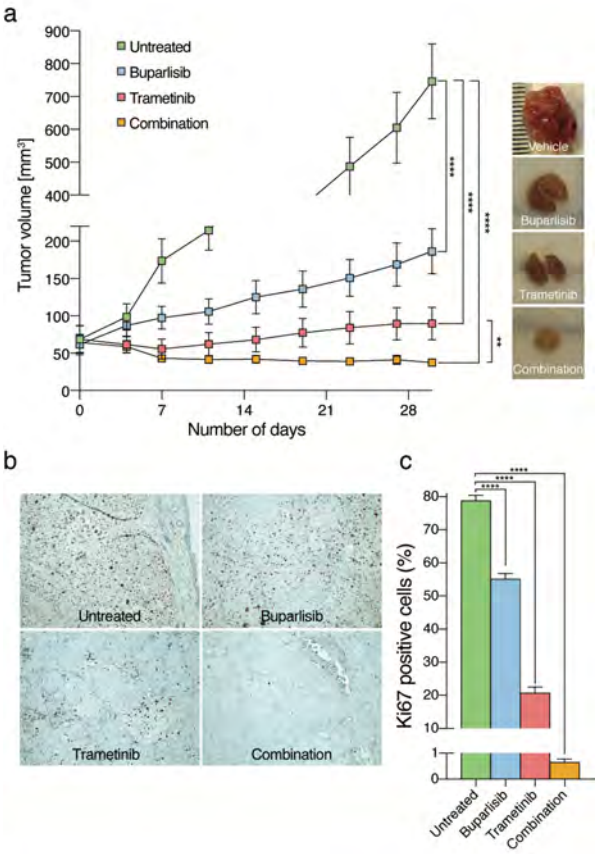

Fig. 6 Inhibition of *in vivo* tumour growth after treatment with buparlisib and trametinib. **a** Tumour volumes plotted as a function of time to assess tumour growth in response to therapy. The tumours were measured one a week and at the end-point of the experiment (30 days). Representative images of subcutaneous tumours after termination of the experiment can be seen on the right (n = 8 mice in each treatment group). **b** Immunohistochemistry sections from representative mice form each treatment group stained with antibodies against Ki67. **c** Quantification of the number of Ki67 positive cells in each treatment group. Abbreviations: **: $p < 0.01$ and ****: $p < 0.0001$.

References

1. Marks R. Epidemiology of melanoma. *Clin Exp Dermatol* 2000; **25**(6): 459-63.
2. Abate-Daga D, Ramello MC, Smalley I, Forsyth PA, Smalley KSM. The biology and therapeutic management of melanoma brain metastases. *Biochem Pharmacol* 2018; **153**: 35-45.
3. Sundstrom T, Espedal H, Harter PN, et al. Melanoma brain metastasis is independent of lactate dehydrogenase A expression. *Neuro Oncol* 2015; **17**(10): 1374-85.
4. Niessner H, Schmitz J, Tabatabai G, et al. PI3K Pathway Inhibition Achieves Potent Antitumor Activity in Melanoma Brain Metastases In Vitro and In Vivo. *Clin Cancer Res* 2016; **22**(23): 5818-28.
5. Berghoff AS, Preusser M. New developments in brain metastases. *Ther Adv Neurol Disord* 2018; **11**: 1-14.
6. Davis EJ, Johnson DB, Sosman JA, Chandra S. Melanoma: What do all the mutations mean? *Cancer* 2018; **124**(17): 3490-9.
7. Daphu I, Horn S, Stieber D, et al. In Vitro Treatment of Melanoma Brain Metastasis by Simultaneously Targeting the MAPK and PI3K Signaling Pathways. *International Journal of Molecular Sciences* 2014; **15**(5): 8773-94.
8. Leonardi GC, Falzone L, Salemi R, et al. Cutaneous melanoma: From pathogenesis to therapy (Review). *Int J Oncol* 2018; **52**(4): 1071-80.
9. Fischer GM, Vashisht Gopal YN, McQuade JL, Peng W, DeBerardinis RJ, Davies MA. Metabolic strategies of melanoma cells: Mechanisms, interactions with the tumor microenvironment, and therapeutic implications. *Pigment Cell Melanoma Res* 2018; **31**(1): 11-30.
10. Han CH, Brastianos PK. Genetic Characterization of Brain Metastases in the Era of Targeted Therapy. *Front Oncol* 2017; **7**: 230.
11. Meier F, Schittek B, Busch S, et al. The RAS/RAF/MEK/ERK and PI3K/AKT signaling pathways present molecular targets for the effective treatment of advanced melanoma. *Front Biosci* 2005; **10**: 2986-3001.
12. Isola AL, Eddy K, Chen S. Biology, Therapy and Implications of Tumor Exosomes in the Progression of Melanoma. *Cancers (Basel)* 2016; **8**(12).
13. Davies MA. The role of the PI3K-AKT pathway in melanoma. *Cancer J* 2012; **18**(2): 142-7.
14. Chen B, Tardell C, Higgins B, Packman K, Boylan JF, Niu H. BRAFV600E negatively regulates the AKT pathway in melanoma cell lines. *PLoS One* 2012; **7**(8): e42598.
15. Mabuchi S, Ohmichi M, Kimura A, et al. Inhibition of phosphorylation of BAD and Raf-1 by Akt sensitizes human ovarian cancer cells to paclitaxel. *J Biol Chem* 2002; **277**(36): 33490-500.
16. Aksamitiene E, Kiyatkin A, Kholodenko BN. Cross-talk between mitogenic Ras/MAPK and survival PI3K/Akt pathways: a fine balance. *Biochem Soc Trans* 2012; **40**(1): 139-46.
17. Mendoza MC, Er EE, Blenis J. The Ras-ERK and PI3K-mTOR pathways: cross-talk and compensation. *Trends Biochem Sci* 2011; **36**(6): 320-8.
18. Greger JG, Eastman SD, Zhang V, et al. Combinations of BRAF, MEK, and PI3K/mTOR inhibitors overcome acquired resistance to the BRAF inhibitor GSK2118436 dabrafenib, mediated by NRAS or MEK mutations. *Mol Cancer Ther* 2012; **11**(4): 909-20.
19. Gilmartin AG, Bleam MR, Groy A, et al. GSK1120212 (JTP-74057) is an inhibitor of MEK activity and activation with favorable pharmacokinetic properties for sustained in vivo pathway inhibition. *Clin Cancer Res* 2011; **17**(5): 989-1000.

20. Long GV, Fung C, Menzies AM, et al. Increased MAPK reactivation in early resistance to dabrafenib/trametinib combination therapy of BRAF-mutant metastatic melanoma. *Nat Commun* 2014; **5**: 5694.
21. Flaherty KT, Robert C, Hersey P, et al. Improved survival with MEK inhibition in BRAF-mutated melanoma. *N Engl J Med* 2012; **367**(2): 107-14.
22. Yap TA, Bjerke L, Clarke PA, Workman P. Drugging PI3K in cancer: refining targets and therapeutic strategies. *Curr Opin Pharmacol* 2015; **23**: 98-107.
23. Engelman JA. Targeting PI3K signalling in cancer: opportunities, challenges and limitations. *Nat Rev Cancer* 2009; **9**(8): 550-62.
24. Maira SM, Pecchi S, Huang A, et al. Identification and characterization of NVP-BKM120, an orally available pan-class I PI3-kinase inhibitor. *Mol Cancer Ther* 2012; **11**(2): 317-28.
25. Brachmann SM, Kleylein-Sohn J, Gaulis S, et al. Characterization of the mechanism of action of the pan class I PI3K inhibitor NVP-BKM120 across a broad range of concentrations. *Mol Cancer Ther* 2012; **11**(8): 1747-57.
26. Ando Y, Inada-Inoue M, Mitsuma A, et al. Phase I dose-escalation study of buparlisib (BKM120), an oral pan-class I PI3K inhibitor, in Japanese patients with advanced solid tumors. *Cancer Sci* 2014; **105**(3): 347-53.
27. Glitza Oliva IC, Schvartsman G, Tawbi H. Advances in the systemic treatment of melanoma brain metastases. *Ann Oncol* 2018; **29**(7): 1509-20.
28. Villanueva J, Vultur A, Lee JT, et al. Acquired resistance to BRAF inhibitors mediated by a RAF kinase switch in melanoma can be overcome by cotargeting MEK and IGF-1R/PI3K. *Cancer Cell* 2010; **18**(6): 683-95.
29. Lugowska I, Kosela-Paterczyk H, Kozak K, Rutkowski P. Trametinib: a MEK inhibitor for management of metastatic melanoma. *Onco Targets Ther* 2015; **8**: 2251-9.
30. Kim KB, Kefford R, Pavlick AC, et al. Phase II study of the MEK1/MEK2 inhibitor Trametinib in patients with metastatic BRAF-mutant cutaneous melanoma previously treated with or without a BRAF inhibitor. *J Clin Oncol* 2013; **31**(4): 482-9.
31. Wee S, Jagani Z, Xiang KX, et al. PI3K pathway activation mediates resistance to MEK inhibitors in KRAS mutant cancers. *Cancer Res* 2009; **69**(10): 4286-93.
32. Sinnberg T, Lasithiotakis K, Niessner H, et al. Inhibition of PI3K-AKT-mTOR signaling sensitizes melanoma cells to cisplatin and temozolomide. *J Invest Dermatol* 2009; **129**(6): 1500-15.
33. El Meskini R, Iacovelli AJ, Kulaga A, et al. A preclinical orthotopic model for glioblastoma recapitulates key features of human tumors and demonstrates sensitivity to a combination of MEK and PI3K pathway inhibitors. *Dis Model Mech* 2015; **8**(1): 45-56.
34. Roper J, Sinnamon MJ, Coffee EM, et al. Combination PI3K/MEK inhibition promotes tumor apoptosis and regression in PIK3CA wild-type, KRAS mutant colorectal cancer. *Cancer Lett* 2014; **347**(2): 204-11.
35. Bedard PL, Tabernero J, Janku F, et al. A phase Ib dose-escalation study of the oral pan-PI3K inhibitor buparlisib (BKM120) in combination with the oral MEK1/2 inhibitor trametinib (GSK1120212) in patients with selected advanced solid tumors. *Clin Cancer Res* 2015; **21**(4): 730-8.
36. Speranza MC, Nowicki MO, Behera P, Cho CF, Chiocca EA, Lawler SE. BKM-120 (Buparlisib): A Phosphatidyl-Inositol-3 Kinase Inhibitor with Anti-Invasive Properties in Glioblastoma. *Sci Rep* 2016; **6**: 20189.
37. Cordaro FG, De Presbiteris AL, Camerlingo R, et al. Phenotype characterization of human melanoma cells resistant to dabrafenib. *Oncol Rep* 2017; **38**(5): 2741-51.

38. Chua KN, Kong LR, Sim WJ, et al. Combinatorial treatment using targeted MEK and SRC inhibitors synergistically abrogates tumor cell growth and induces mesenchymal-epithelial transition in non-small-cell lung carcinoma. *Oncotarget* 2015; **6**(30): 29991-30005.
39. Yang E, Zha J, Jockel J, Boise LH, Thompson CB, Korsmeyer SJ. Bad, a heterodimeric partner for Bcl-XL and Bcl-2, displaces Bax and promotes cell death. *Cell* 1995; **80**(2): 285-91.
40. Huang Q, Li F, Liu X, et al. Caspase 3-mediated stimulation of tumor cell repopulation during cancer radiotherapy. *Nat Med* 2011; **17**(7): 860-6.
41. Motti ML, Califano D, Troncone G, et al. Complex regulation of the cyclin-dependent kinase inhibitor p27kip1 in thyroid cancer cells by the PI3K/AKT pathway: regulation of p27kip1 expression and localization. *Am J Pathol* 2005; **166**(3): 737-49.
42. Haydn JM, Hufnagel A, Grimm J, Maurus K, Schartl M, Meierjohann S. The MAPK pathway as an apoptosis enhancer in melanoma. *Oncotarget* 2014; **5**(13): 5040-53.
43. Siddiqa A, Long LM, Li L, Marciniak RA, Kazhdan I. Expression of HER-2 in MCF-7 breast cancer cells modulates anti-apoptotic proteins Survivin and Bcl-2 via the extracellular signal-related kinase (ERK) and phosphoinositide-3 kinase (PI3K) signalling pathways. *BMC Cancer* 2008; **8**: 129.
44. Liu X, Shi Y, Giranda VL, Luo Y. Inhibition of the phosphatidylinositol 3-kinase/Akt pathway sensitizes MDA-MB468 human breast cancer cells to cerulenin-induced apoptosis. *Mol Cancer Ther* 2006; **5**(3): 494-501.
45. Haas B, Klinger V, Keksel C, et al. Inhibition of the PI3K but not the MEK/ERK pathway sensitizes human glioma cells to alkylating drugs. *Cancer Cell Int* 2018; **18**: 69.
46. Kilic-Eren M, Boylu T, Tabor V. Targeting PI3K/Akt represses Hypoxia inducible factor-1alpha activation and sensitizes Rhabdomyosarcoma and Ewing's sarcoma cells for apoptosis. *Cancer Cell Int* 2013; **13**: 36.
47. Ramos AM, Fernandez C, Amran D, Sancho P, de Blas E, Aller P. Pharmacologic inhibitors of PI3K/Akt potentiate the apoptotic action of the antileukemic drug arsenic trioxide via glutathione depletion and increased peroxide accumulation in myeloid leukemia cells. *Blood* 2005; **105**(10): 4013-20.
48. Chatterjee M, Andrulis M, Stuhmer T, et al. The PI3K/Akt signaling pathway regulates the expression of Hsp70, which critically contributes to Hsp90-chaperone function and tumor cell survival in multiple myeloma. *Haematologica* 2013; **98**(7): 1132-41.
49. Yamada T, Horinaka M, Shinnoh M, Yoshioka T, Miki T, Sakai T. A novel HDAC inhibitor OBP-801 and a PI3K inhibitor LY294002 synergistically induce apoptosis via the suppression of survivin and XIAP in renal cell carcinoma. *Int J Oncol* 2013; **43**(4): 1080-6.
50. Zhao P, Meng Q, Liu LZ, You YP, Liu N, Jiang BH. Regulation of survivin by PI3K/Akt/p70S6K1 pathway. *Biochem Biophys Res Commun* 2010; **395**(2): 219-24.
51. Boucher MJ, Morisset J, Vachon PH, Reed JC, Laine J, Rivard N. MEK/ERK signaling pathway regulates the expression of Bcl-2, Bcl-X(L), and Mcl-1 and promotes survival of human pancreatic cancer cells. *J Cell Biochem* 2000; **79**(3): 355-69.
52. Volm M, Koomagi R. Hypoxia-inducible factor (HIF-1) and its relationship to apoptosis and proliferation in lung cancer. *Anticancer Res* 2000; **20**(3A): 1527-33.
53. Powis G, Kirkpatrick L. Hypoxia inducible factor-1alpha as a cancer drug target. *Mol Cancer Ther* 2004; **3**(5): 647-54.
54. Huang J, Lyu H, Wang J, Liu B. MicroRNA regulation and therapeutic targeting of survivin in cancer. *Am J Cancer Res* 2015; **5**(1): 20-31.
55. Altieri DC. Survivin, cancer networks and pathway-directed drug discovery. *Nat Rev Cancer* 2008; **8**(1): 61-70.

56. Boulares AH, Yakovlev AG, Ivanova V, et al. Role of poly(ADP-ribose) polymerase (PARP) cleavage in apoptosis. Caspase 3-resistant PARP mutant increases rates of apoptosis in transfected cells. *J Biol Chem* 1999; **274**(33): 22932-40.
57. Lintz M, Munoz A, Reinhart-King CA. The Mechanics of Single Cell and Collective Migration of Tumor Cells. *J Biomech Eng* 2017; **139**(2).
58. Justus CR, Leffler N, Ruiz-Echevarria M, Yang LV. In vitro cell migration and invasion assays. *J Vis Exp* 2014; (88).
59. Zhao Y, Ge CC, Wang J, et al. MEK inhibitor, PD98059, promotes breast cancer cell migration by inducing beta-catenin nuclear accumulation. *Oncol Rep* 2017; **38**(5): 3055-63.
60. Yamaguchi T, Yoshida T, Kurachi R, et al. Identification of JTP-70902, a p15(INK4b)-inductive compound, as a novel MEK1/2 inhibitor. *Cancer Sci* 2007; **98**(11): 1809-16.
61. Itamura H, Shindo T, Tawara I, et al. The MEK inhibitor trametinib separates murine graft-versus-host disease from graft-versus-tumor effects. *JCI Insight* 2016; **1**(10): e86331.
62. Yamaguchi T, Kakefuda R, Tajima N, Sowa Y, Sakai T. Antitumor activities of JTP-74057 (GSK1120212), a novel MEK1/2 inhibitor, on colorectal cancer cell lines in vitro and in vivo. *Int J Oncol* 2011; **39**(1): 23-31.
63. Liu L, Mayes PA, Eastman S, et al. The BRAF and MEK Inhibitors Dabrafenib and Trametinib: Effects on Immune Function and in Combination with Immunomodulatory Antibodies Targeting PD-1, PD-L1, and CTLA-4. *Clin Cancer Res* 2015; **21**(7): 1639-51.
64. Cho H, Matsumoto S, Fujita Y, et al. Trametinib plus 4-Methylumbelliferone Exhibits Antitumor Effects by ERK Blockade and CD44 Downregulation and Affects PD-1 and PD-L1 in Malignant Pleural Mesothelioma. *J Thorac Oncol* 2017; **12**(3): 477-90.
65. Weber JS, Flaherty KT, Infante JR, et al. Updated safety and efficacy results from a phase I/II study of the oral BRAF inhibitor dabrafenib (GSK2118436) combined with the oral MEK 1/2 inhibitor trametinib (GSK1120212) in patients with BRAFi-naive metastatic melanoma. *Journal of Clinical Oncology* 2012; **30**(15_suppl): 8510-.
66. Bissig-Choisat B, Kettlun-Leyton C, Legras XD, et al. Novel patient-derived xenograft and cell line models for therapeutic testing of pediatric liver cancer. *J Hepatol* 2016; **65**(2): 325-33.
67. de Gooijer MC, Zhang P, Buil LCM, et al. Buparlisib is a brain penetrable pan-PI3K inhibitor. *Sci Rep* 2018; **8**(1): 10784.
68. Vaidhyanathan S, Mittapalli RK, Sarkaria JN, Elmquist WF. Factors influencing the CNS distribution of a novel MEK-1/2 inhibitor: implications for combination therapy for melanoma brain metastases. *Drug Metab Dispos* 2014; **42**(8): 1292-300.
69. Eichler AF, Chung E, Kodack DP, Loeffler JS, Fukumura D, Jain RK. The biology of brain metastases-translation to new therapies. *Nat Rev Clin Oncol* 2011; **8**(6): 344-56.

Supplementary Materials

Cells

Written consent was obtained from the patients before tumour material was collected and subsequently used to prepare cell lines. The Regional Ethical Committee (REC Number 013.09) and the Norwegian Directorate of Health (NSD Number 9634) approved the tissue collection and biobank storage of tumour biopsies and derived cell lines. Cell line authentication was verified by STR fingerprinting.

The BRAF mutation status of the H1, H2, H3 and H10 cell lines was investigated by performing massive parallel sequencing of the tumour DNA, according to published protocols[1]. The H1, H2 and H10 cell lines harboured the V600E mutation, while the H3 cells were L577F mutated.

The H1 cells were transduced with two lentiviral vectors, encoding Dendra (a green fluorescent protein (GFP) variant) and luciferase to obtain the H1_DL2 cell line. Flow cytometric isolation of cells by GFP expression was performed (BD FACS Aria, Becton Dickinson, Franklin Lakes, NJ, USA).

All cells were grown in Dulbecco's modified eagles medium (DMEM; Sigma-Aldrich Inc., St. Louis, MO, USA), supplemented with 10% heat-inactivated new-born calf serum (Thermo Fischer Scientific, Waltham, MA, USA), 5 µg/mL Plasmocin (Invivogen, Toulouse, France), 2% L-glutamine (BioWhittaker, Verviers, Belgium), penicillin (100 IU/mL) and streptomycin (100 µL/mL) (BioWhittaker). The cells were cultured in a standard tissue incubator at 37 °C, 100% humidity and 5% CO_2, and trypsinated once they attained 75% confluency using 0.25% Trypsin/EDTA (BioWhittaker).

Animals

Female non-obese diabetic/severe combined immunodeficient (NOD/SCID) mice were purchased from Envigo (Gannat, France). The animals were bred and maintained in our animal facility certified by the Association for Assessment and Accreditation of Laboratory Animal Care International. They were fed a standard pellet diet and provided water *ad libitum*. The National Animal Research Authority approved all animal procedures (application #11655, approved March 7th, 2017).

Anaesthesia was induced with 3% sevoflurane (Abbott Laboratories Ltd., Berkshire, UK) in oxygen and maintained with 1.5% sevoflurane in oxygen during the injection procedures.

Cell viability assay

The cell proliferation upon combination treatment was studied using a resazurin assay, as previously described[2]. All cell lines were seeded at a density of 5×10^3 cells/well in 200 µl culture medium in 96 well plates (Nunc, Roskilde, Denmark) and treated with buparlisib or trametinib (0, 0.000001, 0.00001, 0.0001, 0.001, 0.01, 0.1, 1, 10 and 100 µM), or a combination of both these treatments for a period of 72 h. After treatment, 20 µl of 0.01 mg/ml resazurin (Sigma-Aldrich Inc.) diluted in phosphate buffered saline (PBS) was added to each well and incubated for 4 h at 37 °C. The absorbance was measured at dual mode 560/590 using a scanning multi-well spectrophotometer (Victor 3 1420 multi-label counter, Perkin Elmer, Waltham, MA, USA). Each treatment was performed in triplicate (n = 6 per experiment per drug concentration). IC_{50} concentrations were drawn from the results, i.e. the drug concentration at which 50% of the cell growth was inhibited.

Clonogenic assay

The cell lines H1, H2, H3 and H10 were seeded at a density of 5×10^6 cells/well in 2 mL culture medium in 6 well plates (Nunc) and allowed to reach 75% confluency. The cells were then treated with 20 μM buparlisib, 50 nM trametinib or combined therapy (10 μM buparlisib and 25 nM trametinib) for 72 h. The drug concentrations were optimized for this experiment. Untreated cells were maintained as controls. After treatment, the cells were washed with PBS and trypsinated using 0.25% Trypsin/EDTA. The cells were centrifuged at 900 rpm for 4 min, the supernatant was discarded and the cells were resuspended in fresh culture medium. The cells were then counted using a Countess® automated cell counter (Invitrogen) according to the manufacturers protocol. 1000 cells from each treatment were seeded in fresh 6 well culture dishes (Nunc) in 2 mL culture medium and allowed to grow for 12 days. After 12 days, the culture medium was removed from the wells and the cell layer was washed with cold PBS. The cells were thereafter fixed with prechilled methanol at -20°C for a period of 10 min. The methanol was removed and plates were left to dry. The cells were then stained using 0.5% crystal violet in 25% methanol in water for 10 min. The stain was removed, the cells were washed three times with milliQ water and the plate was allowed to dry. Colonies consisting of more than 50 cells were counted as surviving colonies. The experiment was performed in duplicate (n=3 per experiment per drug concentration).

3D colony formation assay

7.5×10^5 cells were seeded in T75 culture flasks (Nunc) and incubated until approximately 60% confluency. The culture medium was then replaced with either fresh culture medium (negative control), fresh culture medium containing 10 μM buparlisib, 10 μM trametinib or a combination of 5 μM buparlisib and 5 μM trametinib. After 72 h of incubation, the cells were washed with PBS, trypsinated and centrifuged (900 rpm for 4 min). The cell

number was adjusted to a density of 8×10^4 cells/mL and mixed 1:1 with 0.6% low melting point agarose (Sigma-Aldrich). The cells were then seeded on top of 100 µL of cooled 0.6% Difco noble agar (BD Biosciences) in a 96-well plate (Nunc) and kept at 4 °C for 20 min. The low melting point agarose layer with cells was then overlaid with 100 µL of fresh culture medium, and the plate was incubated for 21 days. Colony formation was counted using a Nikon TE2000 inverted microscope (Nikon Instruments Inc., Melville, NY, USA), and the analysis was done using GraphPad Prism v7 (GraphPad Software Inc., San Diego, CA, USA).

Cell migration

Two cell migration experiments were carried out aiming to study the migratory capacity of the cells upon combination treatment. In the first experiment, H1, H2, H3 and H10 cells were plated at a density of 5×10^5 cells/well in 2 mL culture medium in 6-well plates (Nunc). After 24 h, the cells were pre-treated with 10 µM buparlisib, 10 µM trametinib or combined therapy (5 µM buparlisib and 5 µM trametinib) for 24 h. An untreated well was maintained as a negative control. After incubation with drugs, the cells were washed twice with PBS, trypsinated and seeded at a density of 1×10^6 cells/well in Thinsert™ cell culture inserts (Greiner Bio-One GmbH, Frickenhausen, Germany) in 24 well plates (Nunc). The lower chambers were filled with 500 µL culture medium containing 30% serum as chemoattractant. After incubation in 48 h, the inserts were removed from the wells and washed with PBS to remove unbound cells. The inserts were fixed with 4% formaldehyde for 10 min followed by two times washing with PBS and staining with 0.1% crystal violet for 5 min. The inserts were then viewed using a Nikon TE2000 inverted microscope, using the 1× objective for observing the migratory capacity of the cells. The experiment was performed in triplicate. The cells were counted from each insert in all treatments to obtain the migration potential.

In the second experiment, the migratory capacity of cells was studied under constant exposure to drugs for 72 h. H1, H2, H3 and H10 cells were seeded at a density of 3.5×10^4 cells/well in Essen BioScience ImageLock 96-well plates (cat. no. 4379, Essen BioScience Ltd., Hertfordshire, UK). After 24 h, a wound-maker tool was employed to simultaneously create a consistent wound with a uniform width across all wells. All wells were then carefully washed with preheated culture medium before drug solutions were added to the wells: 10 µM buparlisib, 10 µM trametinib or combined treatment (5 µM buparlisib and 5 µM trametinib; n = 6 per treatment group). Imaging was carried out every 2 h using a 10× objective in the IncuCyte® Live Cell Imaging System (Essen BioScience Ltd.) and analysed to find the wound width in µm using the IncuCyte® Scratch Wound Cell Migration Software Module (cat. no. 9600-0012, Essen BioScience Ltd.).

Apoptosis assay

An Annexin-V flow cytometry assay was performed to assess the effects of treatment on apoptosis. The H1, H2, H3 and H10 lines were seeded at a density of 1×10^5 cells/well in 2 mL culture medium in 6 well plates (Nunc) and allowed to reach 75% confluency. The cells were then treated with 10 µM buparlisib, 10 µM trametinib or combined therapy (5 µM buparlisib and 5 µM trametinib) for 72 h. The culture medium was then removed, the cells were washed with PBS, trypsinated using 0.25% Trypsin/EDTA, collected and centrifuged (900 rpm for 4 min). Untreated cells were maintained as controls. The supernatant was discarded, and 100 µL of Annexin V binding buffer containing 2 µl of Annexin V and propidium iodide (PI; AlexaFluor®488 Annexin v/dead cell apoptosis kit; Molecular Probes, Life Technologies) was added to the cells and incubated for 20 min in the dark. The cells were placed on ice and further analysed using a flow cytometer (BD Fortessa, BD Bioscience, San Jose, CA, USA). Fluorescence in the FITC-A and PE-A channels were gated to a two-parameter histogram, and

analysed using FloJo software (Tree Star Inc., Ashland, OR, USA). The experiment was repeated three times.

Apoptosis array

A human apoptosis antibody array kit (R&D Systems, Inc., Minneapolis, MN, USA) was used to study the effects of treatment on 35 apoptosis-related proteins. 1×10^6 H1 cells were plated in 2 mL culture medium in 6 well plates (Nunc), and after reaching confluency, the cells were treated with 20 μM buparlisib, 50 nM trametinib or combined therapy (10 μM buparlisib and 25 nM trametinib) for 72 h, drug concentrations optimized for this specific experiment. Untreated wells were maintained as control. After treatment, the cells were washed and lysed using lysis buffer 17 (R&D Systems, Inc.), and protease inhibitor was added to the lysates to prevent them from degradation. The assay was performed according to the protocol provided by the manufacturer. The arrays were developed using chemi-reagent mix (HRP substrates) provided in the kit and viewed using a ChemidocTM XRS+ System (Bio-Rad laboratories AB, Oslo, Norway). The band density was analysed using ImageJ freeware version 2.0.0-rc-68/1.52g (National Institute of Health, Bethesda, MA, USA), and graphs were plotted showing the relative intensity of band density (pixels) of the various proteins. The experiment was performed once, each of the 35 proteins were spotted twice on the membrane.

Western blot analysis

H1, H2, H3 and H10 cells were seeded as monolayers at 40–50% confluency one day prior to treatment, and then treated for 72 h with 10 μM buparlisib, 10 μM trametinib, or a combination of 5 μM buparlisib and 5 μM trametinib. Control cells were left untreated. The cells were harvested, lysed in radioimmunoassay precipitation (RIPA) buffer, and subjected to Western blotting as described previously[2]. For protein detection, the following primary

antibodies were used: anti-cleaved caspase-3 (rabbit monoclonal, Cell Signaling, 1:1000), anti-p27 Kip1 (rabbit monoclonal, Cell Signaling, 1:1000), anti-PARP (rabbit polyclonal, Cell Signaling, 1:1000), anti-Bcl-2 (mouse monoclonal, NeoMarkers, 1:500), anti-c-IAP1 (mouse monoclonal, Santa Cruz, 1:100), anti-HIF-1α (mouse monoclonal, Santa Cruz, 1:200), anti- PI 3-kinase p101 (rabbit polyclonal, Santa Cruz, 1:200), anti-MEK1/2 (rabbit monoclonal, Cell Signaling, 1:1000), and anti-beta actin (rabbit polyclonal, Abcam, 1:2000). Quantification of protein bands was performed using ImageJ freeware version 2.0.0-rc-68/1.52g. Relative protein levels were first normalised against the loading control (beta actin) and then calculated and presented as a ratio of the untreated control.

Histology and immunohistochemistry

Paraffin-embedded tumours were sectioned (4 μm) and mounted on microscopic slides. Heat-induced epitope retrieval was performed in 10 mmol/L citric acid buffer at pH 7.2 preheated in a microwave and the sections were heated at 98°C for 20 min. Sections were incubated with the primary antibody Ki67 (DAKO M7240, clone MIB-1, 1:250) at 4 °C overnight, rinsed with TBST, and incubated for 1 h at room temperature with biotin-conjugated secondary antibody, followed by 30 min incubation with ABC complex (VECTASTAIN® ABC Kit, Vector laboratories). Visualization was achieved using DAB chromogen (DAKO K3468) as the substrate, and slides were counterstained with haematoxylin (CellPath) and mounted with Entellan® new (Merck 107961). Images were obtained using a Nikon TE2000 inverted microscope, and the percentages of Ki-67 positive cells were calculated, counting positive and negative cells using the point tool in the ImageJ freeware.

Bibliography

1. Bischof K, Knappskog S, Hjelle SM, et al. Influence of p53 Isoform Expression on Survival in High-Grade Serous Ovarian Cancers. *Sci Rep* 2019; **9**(1): 5244.

2. Daphu I, Horn S, Stieber D, et al. In Vitro Treatment of Melanoma Brain Metastasis by Simultaneously Targeting the MAPK and PI3K Signaling Pathways. *International Journal of Molecular Sciences* 2014; **15**(5): 8773-94.

Supplementary Figures

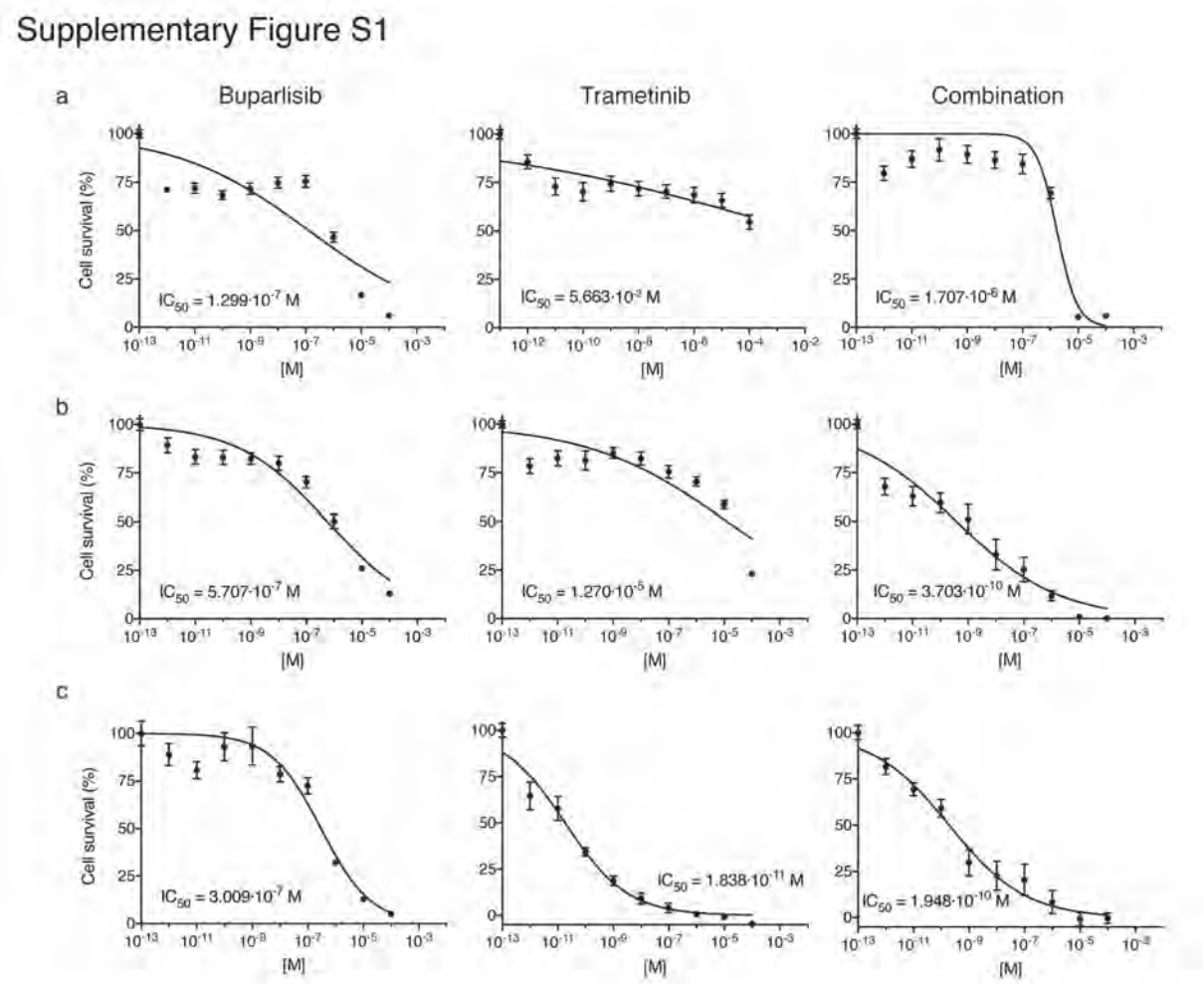

Supplementary Figure S1 Cell survival curves with indicated IC_{50} concentrations of cells grown as monolayers after treatment with buparlisib and trametinib. a $BRAF^{V600E}$ mutated H2 cells treated with buparlisib (left), trametinib (middle) and combination (right). **b** $BRAF^{L577F}$ mutated H3 cells treated with buparlisib (left), trametinib (middle) and combination (right). **c** $BRAF^{V600E}$ mutated H10 cells treated with buparlisib (left), trametinib (middle) and combination (right). The experiments were carried out in triplicate (n = 6 per drug per experiment).

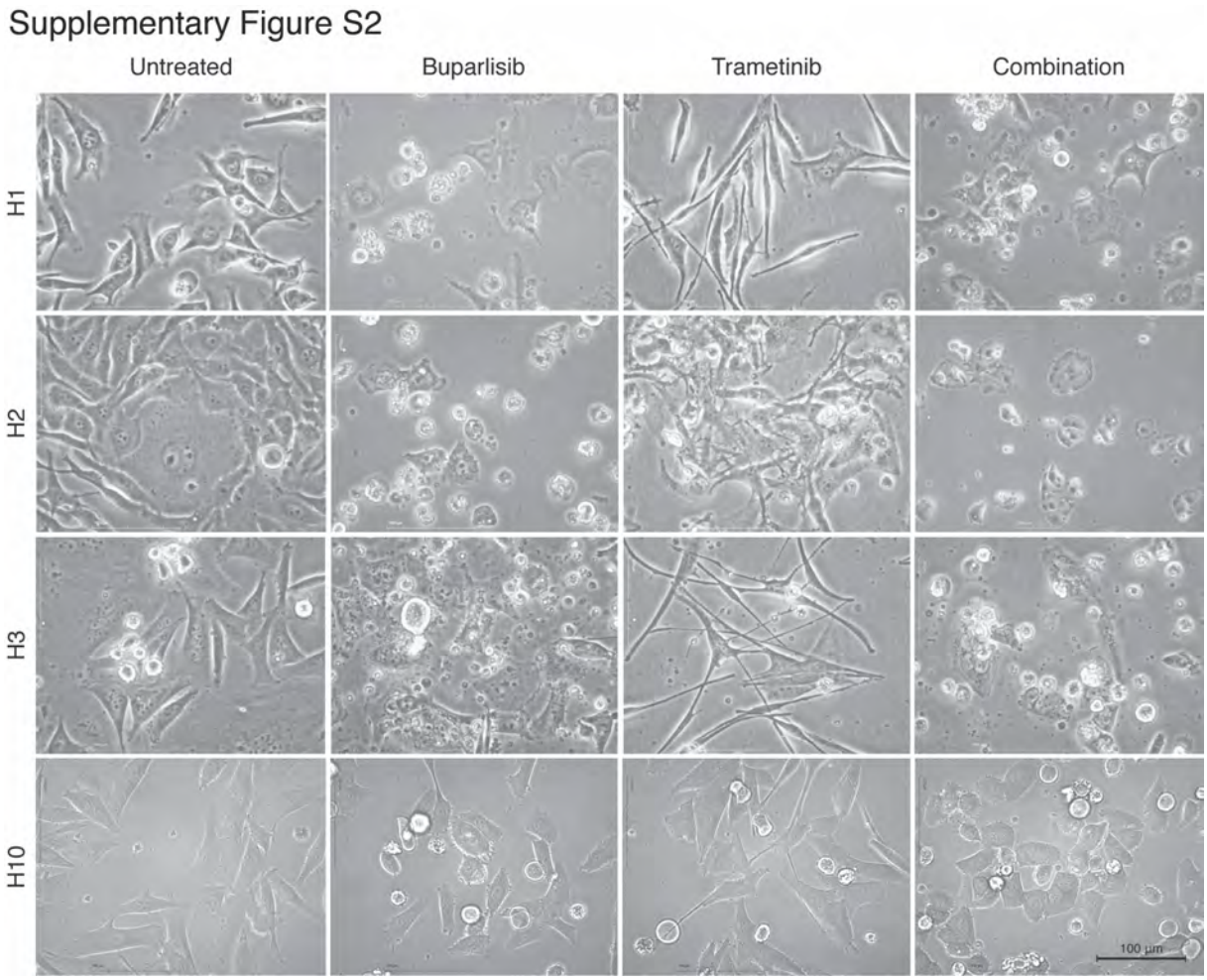

Supplementary Figure S2 Morphology of human melanoma brain metastatic cell lines after treatment with buparlisib and trametinib. Representative images of H1 ($BRAF^{V600E}$), H2 ($BRAF^{V600E}$), H3 ($BRAF^{L577F}$) and H10 ($BRAF^{V600E}$) cells can be seen from top to bottom treated with vehicle (medium), buparlisib, trametinib or a combination left to right.

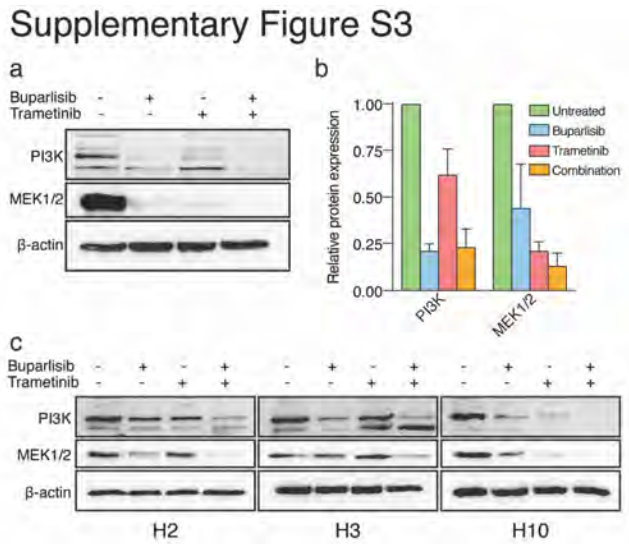

Supplementary Figure S3 Protein expression of cell lysates after *in vitro* treatment with 10 µM buparlisib, 10 µM trametinib or combination (5 µM + 5 µM). a Western blots of lysates from H1 cells showing the expression of PI3K and MEK1/2. **b** Quantification of PI3K and MEK1/2 expression relative to β-actin. **c** Protein expression of lysates from H2 ($BRAF^{V600E}$), H3 ($BRAF^{L577F}$) and H10 ($BRAF^{V600E}$) cells after drug treatment.

Supplementary Figure S4

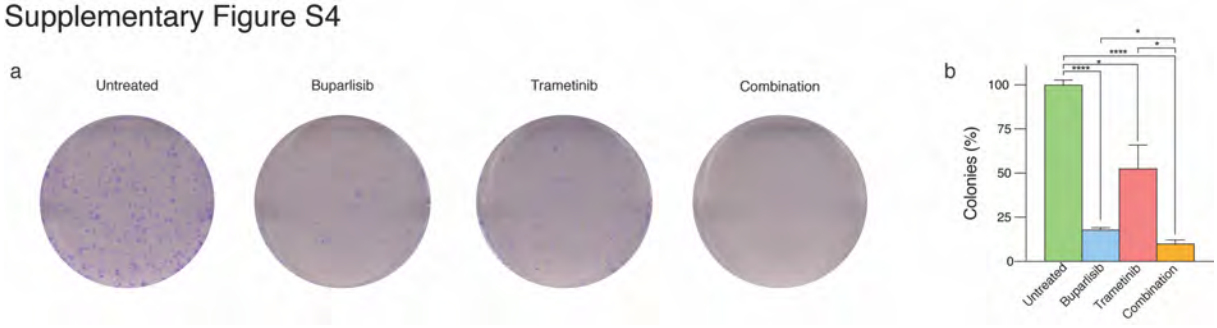

Supplementary Figure S4 *In vitro* colony formation of H2 cells pre-treated with buparlisib and trametinib. **a** Representative images of H2 cells pre-treated with 10 μM buparlisib, 10 μM trametinib or a combination (5 μM + 5 μM trametinib) grown as colonies. **b** The colony formation was scored and quantified as seen in the graph. The experiments were performed in triplicate. Abbreviations: *: $p < 0.05$, and ****: $p < 0.0001$.

Supplementary Figure S5

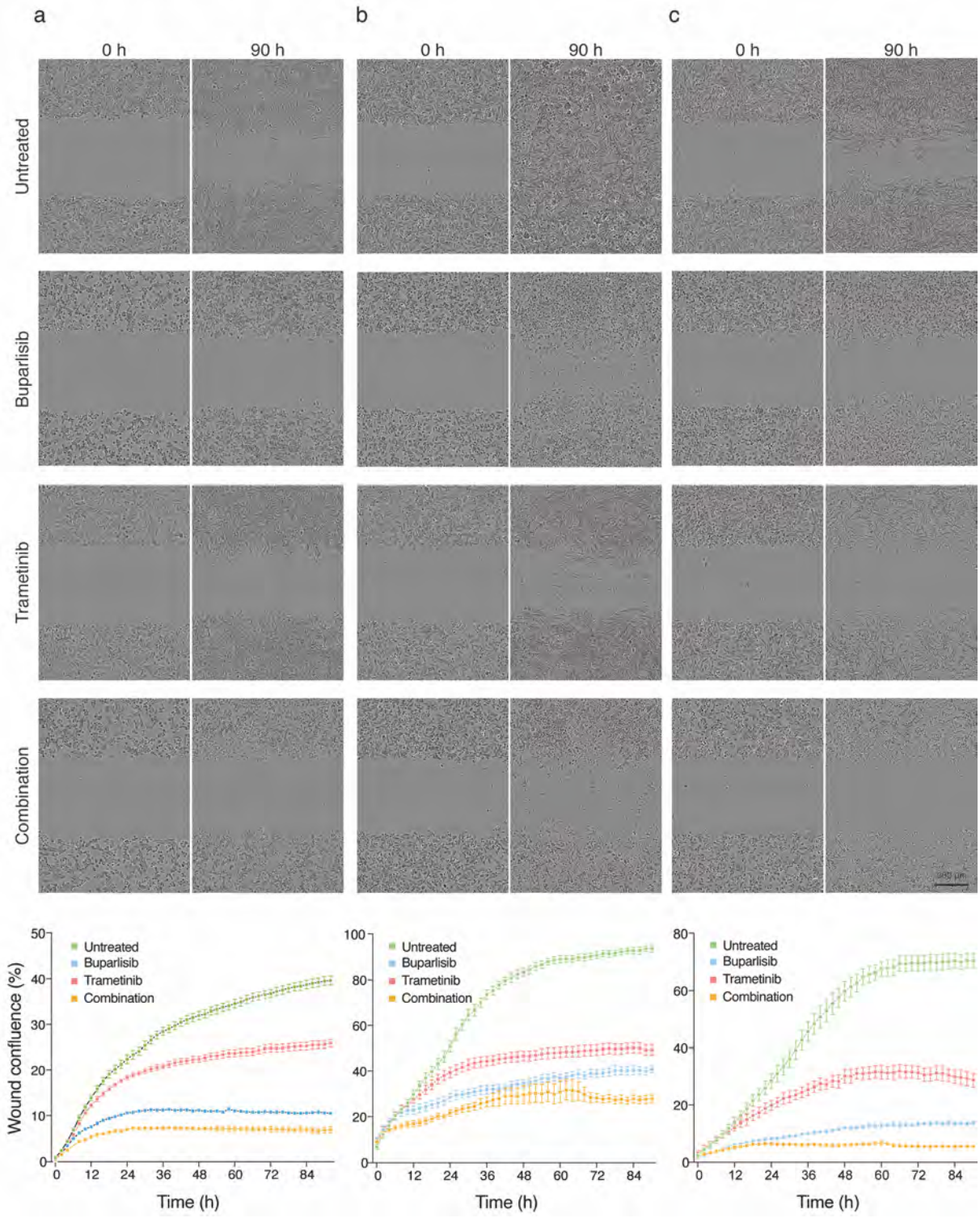

Supplementary Figure S5 Migration of brain metastatic melanoma cells during and after pre-treatment with buparlisib and trametinib. a Representative micrographs of H2 ($BRAF^{V600E}$), **b** H3 ($BRAF^{L577F}$) and **c** H10 ($BRAF^{V600E}$) cells before (0 h) and at completion (90 h) of the scratch-wound experiment. The respective wound confluences were quantified and placed below each cell line (n = 6 per drug concentration). Scalebar = 300 µm.

Supplementary Figure S6

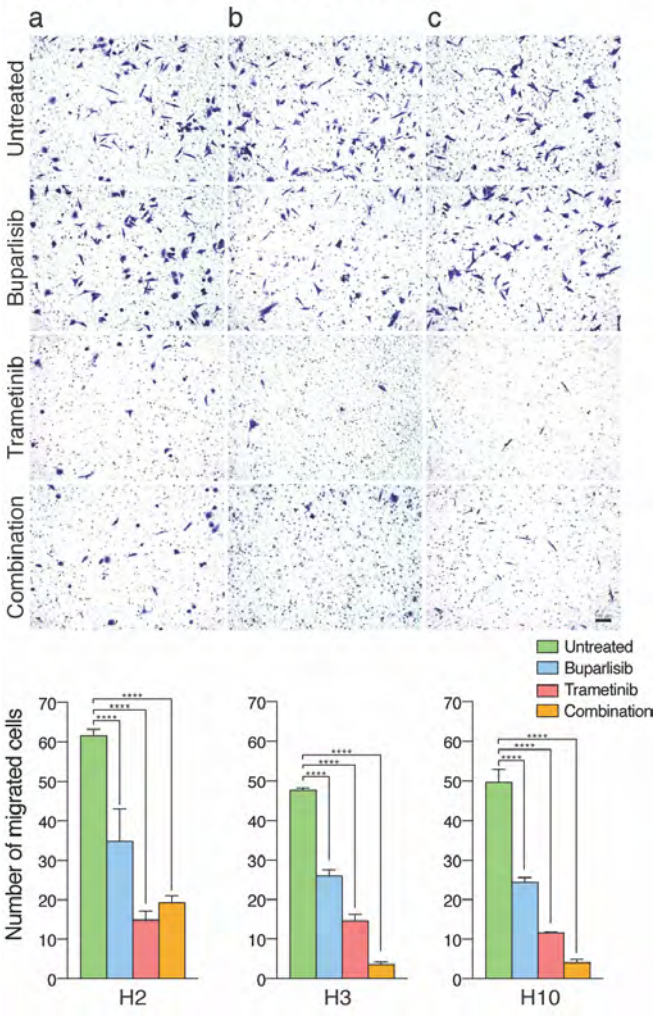

Supplementary Figure S6 Cell migration towards a chemoattractant. Representative images of migrated a H2 ($BRAF^{V600E}$), **b** H3 ($BRAF^{L577F}$) and **c** H10 ($BRAF^{V600E}$) cells. The number of cells were quantified based on three fields of view and placed below each cell line in the figure. The experiment was performed in triplicate. Abbreviations: ****: $p < 0.0001$.